

INFORMATION TO USERS

While the most advanced technology has been used to photograph and reproduce this manuscript, the quality of the reproduction is heavily dependent upon the quality of the material submitted. For example:

- Manuscript pages may have indistinct print. In such cases, the best available copy has been filmed.
- Manuscripts may not always be complete. In such cases, a note will indicate that it is not possible to obtain missing pages.
- Copyrighted material may have been removed from the manuscript. In such cases, a note will indicate the deletion.

Oversize materials (e.g., maps, drawings, and charts) are photographed by sectioning the original, beginning at the upper left-hand corner and continuing from left to right in equal sections with small overlaps. Each oversize page is also filmed as one exposure and is available, for an additional charge, as a standard 35mm slide or as a 17"x 23" black and white photographic print.

Most photographs reproduce acceptably on positive microfilm or microfiche but lack the clarity on xerographic copies made from the microfilm. For an additional charge, 35mm slides of 6"x 9" black and white photographic prints are available for any photographs or illustrations that cannot be reproduced satisfactorily by xerography.



Order Number 8726806

**Nonlinear and magneto-optic effects on long-range surface
plasmon polaritons**

Hickernell, Robert Kerr, Ph.D.

The University of Arizona, 1987

U·M·I
300 N. Zeeb Rd.
Ann Arbor, MI 48106

PLEASE NOTE:

In all cases this material has been filmed in the best possible way from the available copy. Problems encountered with this document have been identified here with a check mark .

1. Glossy photographs or pages _____
2. Colored illustrations, paper or print _____
3. Photographs with dark background _____
4. Illustrations are poor copy _____
5. Pages with black marks, not original copy
6. Print shows through as there is text on both sides of page _____
7. Indistinct, broken or small print on several pages _____
8. Print exceeds margin requirements _____
9. Tightly bound copy with print lost in spine _____
10. Computer printout pages with indistinct print _____
11. Page(s) _____ lacking when material received, and not available from school or author.
12. Page(s) _____ seem to be missing in numbering only as text follows.
13. Two pages numbered _____. Text follows.
14. Curling and wrinkled pages _____
15. Dissertation contains pages with print at a slant, filmed as received _____
16. Other _____

University
Microfilms
International



NONLINEAR AND MAGNETO-OPTIC EFFECTS
ON LONG-RANGE SURFACE PLASMON POLARITONS

by

Robert Kerr Hickernell

A Dissertation Submitted to the Faculty of the
COMMITTEE ON OPTICAL SCIENCES (GRADUATE)

In Partial Fulfillment of the Requirements
For the Degree of

DOCTOR OF PHILOSOPHY

In the Graduate College

THE UNIVERSITY OF ARIZONA

1 9 8 7

THE UNIVERSITY OF ARIZONA
GRADUATE COLLEGE

As members of the Final Examination Committee, we certify that we have read
the dissertation prepared by Robert Kerr Hickernell

entitled Nonlinear and Magneto-optic Effects on Long-range
Surface Plasmon Polaritons

and recommend that it be accepted as fulfilling the dissertation requirement
for the Degree of Doctor of Philosophy.

D. Sivil

6-2-87
Date

H. C. Macleod

6-3-87
Date

J. Bunker

6-3-87
Date

Date

Date

Final approval and acceptance of this dissertation is contingent upon the
candidate's submission of the final copy of the dissertation to the Graduate
College.

I hereby certify that I have read this dissertation prepared under my
direction and recommend that it be accepted as fulfilling the dissertation
requirement.

D. Sivil
Dissertation Director

6-3-87
Date

STATEMENT BY AUTHOR

This dissertation has been submitted in partial fulfillment of requirements for an advanced degree at The University of Arizona and is deposited in the University Library to be made available to borrowers under rules of the Library.

Brief quotations from this dissertaion are allowable without special permission, provided that accurate acknowledgment of source is made. Requests for permission for extended quotation from or reproduction of this manuscript in whole or in part may be granted by the head of the major department or the Dean of the Graduate College when in his or her judgment the proposed use of the material is in the interests of scholarship. In all other instances, however, permission must be obtained from the author.

SIGNED: Robert K. Hickenell

ACKNOWLEDGMENTS

This work would not have been possible without the encouragement, support, and patience of a number of people. First, I wish to thank my advisor, Professor Dror Sarid, for the research ideas and the tools with which to carry them out. I appreciate him giving me the opportunity to be involved in a variety of projects, and trusting me to go the distance with them.

Credit is also due the guys in the group who have put up with me over the years. They have allowed me to "borrow" equipment, unravelled me from computer tangles, moved me from lab to lab to lab, given me good advice on technical problems, and tolerated my overzealous proofreading. Alan Craig, Grieg Olson, and Richard Booman pioneered the experimental study of the long-range surface plasmon and wrote the data-acquisition software. Ralph Jameson was a comrade in the early struggles which are not represented in this work. Wayne Gibbons has been a good colleague and a good friend, a source of advice on matters scientific and otherwise. Brian McGinnis always listened and usually came up with a solution. Merritt Deeter shared equipment and a crowded room with me, and participated in fruitful discussions regarding surface magnetoplasmons.

I extend my thanks to Professor Jim Burke for his critical reading and clarifying discussions of the manuscript.

Finally, I wish to express my great appreciation for my family, whose love, support, and prayers have been a constant encouragement. Mom has always believed in me, and has patiently endured the idiosyncrasies of a family of physicists. Dad inspired my early interest in science and my later interest in waveguide optics;

he has been an enviable example of a great scientist and a great father (not to mention the supply of nickel film samples).

And a big thank you to Beth, who was brave enough to marry a graduate student. My late nights, absentmindedness, and perfectionism were met with her patience, constructive comments, and dedication.

TABLE OF CONTENTS

| | Page |
|--|------|
| LIST OF ILLUSTRATIONS | viii |
| LIST OF TABLES | xii |
| ABSTRACT | xiii |
| 1. INTRODUCTION | 1 |
| 1A. Background to Optical Surface Waves | 2 |
| 1B. Organization of the Dissertation | 6 |
| 2. SURFACE PLASMON POLARITONS — THEORETICAL FRAMEWORK | 8 |
| 2A. General Description and Historical Background | 8 |
| 2B. TM-Polarized Fields in Layered Media | 14 |
| 2C. Bound Surface Plasmon Polaritons — Dispersion Relations | 22 |
| 2C.1. Single-Interface Plasmon Polariton | 23 |
| 2C.2. Double-Interface Plasmon Polaritons | 25 |
| 2D. Prism Coupling to Surface Plasmon Polaritons | 34 |
| 2D.1. Prism-Coupling Geometries | 36 |
| 2D.2. Prism Coupling to the Long-Range Surface Plasmon Polariton | 42 |
| 3. THEORY OF PRISM COUPLING TO NONLINEAR SURFACE PLASMON POLARITONS | 45 |
| 3A. Introduction | 45 |
| 3B. Prism Coupling of an Infinite Plane Wave to TM-Polarized Nonlinear Guided Waves | 50 |
| 3C. Analysis of Approximations in Nonlinear Wave Theory | 55 |
| 3C.1. Infinite, Incident Plane-Wave Approximation | 55 |
| 3C.2. Small Change in Dielectric Constant | 56 |
| 3C.3. Uniaxial Approximation | 57 |
| 3D. Alternative Models | 58 |
| 3E. Optical Bistability with Prism Coupling to Nonlinear Surface Plasmon Polaritons | 60 |
| 3F. Long-Range Surface Plasmon Polaritons Near Cutoff | 72 |
| 3F.1. Comparison of Negative and Positive, Substrate Nonlinearity | 73 |
| 3F.2. Coupling-Layer-Thickness Dependence | 76 |
| 3F.3. Comparison of Nonlinear Theories | 80 |
| 3G. Nonlinear Coupling Layer | 82 |
| 3H. Experimental Difficulties | 84 |

TABLE OF CONTENTS—Continued

| | Page |
|--|------|
| 4. THEORY OF SURFACE MAGNETOPLASMON POLARITONS | 89 |
| 4A. Background to Magneto-Optic Effects | 89 |
| 4B. Background to Surface Magnetoplasmon Polaritons | 93 |
| 4C. TM-Polarized Waves in Layered Media with a Transversely-Applied Magnetic Field | 97 |
| 4D. Bound Surface Magnetoplasmon Polaritons — Dispersion Relations . | 103 |
| 4D.1. Single-Interface Magnetoplasmon Polariton | 103 |
| 4D.2. Long-Range Surface Magnetoplasmon Polariton | 104 |
| 4E. Prism Coupling to Surface Magnetoplasmon Polaritons | 108 |
| 4E.1. Effect of Modal Properties on Differential Reflectance . | 112 |
| 4E.2. Comparison of Single-Interface and Long-Range Modes . | 116 |
| 5. EXPERIMENTAL APPARATUS FOR THE STUDY OF SURFACE MAGNETOPLASMON POLARITONS | 119 |
| 5A. Bare Sample Reflectance Measurements | 120 |
| 5A.1. Apparatus | 120 |
| 5A.2. Alignment and Calibration | 125 |
| 5A.3. Experimental Problems and Solutions | 126 |
| 5B. Prism-Coupled Sample Reflectance Measurements | 128 |
| 5B.1. Apparatus | 128 |
| 5B.2. Alignment and Calibration | 134 |
| 5B.3. Experimental Problems and Solutions | 140 |
| 6. EXPERIMENTAL OBSERVATION OF LONG-RANGE SURFACE MAGNETOPLASMON POLARITONS IN NICKEL FILMS . | 144 |
| 6A. Sample Preparation | 145 |
| 6B. Reflectance and Differential Reflectance from Bare Samples | 146 |
| 6C. Reflectance from Prism-Coupled, Long-Range Surface Plasmon Polaritons | 151 |
| 6D. Differential Reflectance from Prism-Coupled, Long-Range Surface Magnetoplasmon Polaritons | 157 |
| 6E. Measurement of the Phase of the Magneto-Optic Coefficient | 160 |
| 6F. Effect of Sample Parameters on Reflectance and Differential Reflectance | 170 |
| 6F.1. Nickel Thickness | 171 |
| 6F.2. Coupling-Layer Thickness | 174 |
| 6F.3. Coupling-Layer Refractive Index | 176 |

TABLE OF CONTENTS—Continued

| | Page |
|---|------|
| 7. CONCLUSION | 181 |
| APPENDIX A: MATERIAL CHARACTERIZATION USING EXPERIMENTAL PRISM-COUPLER REFLECTANCE | 187 |
| LIST OF REFERENCES | 201 |

LIST OF ILLUSTRATIONS

| Figure | Page |
|---|------|
| 2.1. Multiple-layer geometry | 15 |
| 2.2. Propagation lengths of surface plasmon polaritons | 26 |
| 2.3. Normalized propagation constants of double-interface plasmon polaritons in silver | 28 |
| 2.4. Magnetic-field profile of double-interface plasmon polaritons | 30 |
| 2.5. Normalized propagation constant of the long-range surface plasmon polariton for asymmetric bounding | 31 |
| 2.6. Propagation constant of the long-range surface plasmon polariton in lossy metals | 33 |
| 2.7. Prism-coupling geometries for single-interface plasmon polaritons | 37 |
| 2.8. Prism-coupling geometry for double-interface plasmon polaritons | 38 |
| 2.9. Reflectance and plasmon field for different prism-coupling geometries -- nickel film | 40 |
| 2.10. Reflectance and plasmon field for different prism-coupling geometries -- silver film | 41 |
| 3.1. Resonance detuning for optical bistability | 62 |
| 3.2. Optical bistability with prism-coupled, nonlinear long-range surface plasmon | 63 |
| 3.3. Intensity enhancement parameters | 66 |
| 3.4. Loss parameters | 68 |
| 3.5. Optical bistability for single-interface and long-range surface plasmon polaritons | 69 |
| 3.6. Switching intensity parameters | 71 |
| 3.7. Bistable switching characteristics for positive and negative substrate nonlinearities | 74 |

LIST OF ILLUSTRATIONS--Continued

| Figure | Page |
|---|------|
| 3.8. Simple homogeneous-index model | 75 |
| 3.9. Power-limiting effects | 78 |
| 3.10. Self-focussing effects | 79 |
| 3.11. Nonlinear wave theory vs perturbation theory | 81 |
| 4.1. Shift of the normalized propagation constant of the long-range surface magnetoplasmon polariton | 105 |
| 4.2. Shift of the normalized propagation constant for asymmetric bounding . | 109 |
| 4.3. Shift of surface magnetoplasmon reflectance resonance | 111 |
| 4.4. Differential reflectance of the prism-coupled, long-range surface magnetoplasmon | 113 |
| 4.5. Differential reflectance in single-interface and long-range mode geometries | 118 |
| 5.1. Bare reflectance measurement apparatus | 121 |
| 5.2. Transverse, magnetic-field application schemes | 123 |
| 5.3. Prism-coupled, reflectance measurement apparatus | 130 |
| 5.4. Prism-coupler sample holder | 133 |
| 5.5. Detector calibration curve | 139 |
| 6.1. Reflectance of bare nickel sample | 148 |
| 6.2. Differential reflectance of bare nickel sample | 150 |
| 6.3. TM reflectance from prism-coupled, long-range surface plasmon polariton -- wide angular range | 153 |
| 6.4. TM reflectance from prism-coupled, long-range surface plasmon polariton -- narrow angular range | 154 |
| 6.5. TE reflectance in prism-coupled, long-range surface plasmon geometry . | 155 |

LIST OF ILLUSTRATIONS--Continued

| Figure | Page |
|---|------|
| 6.6. Prism-coupled excitation of long-range surface magnetoplasmon polariton -- wide angular reflectance scan | 158 |
| 6.7. Prism-coupled excitation of long-range surface magnetoplasmon polariton -- narrow angular reflectance scan | 159 |
| 6.8. Linearity of differential reflectance with applied magnetic field | 161 |
| 6.9. Differential reflectance as a function of magneto-optic coefficient phase | 163 |
| 6.10. Cermet-layer model of nickel differential reflectance -- cermet layer added to reflectance-determined nickel thickness | 164 |
| 6.11. Cermet-layer model of nickel differential reflectance - model matches prism-coupled, Fresnel reflectance | 165 |
| 6.12. Inert-layer model of nickel differential reflectance | 169 |
| 6.13. Prism-coupled, long-range surface magnetoplasmon as a function of nickel thickness | 172 |
| 6.14. Prism-coupled, long-range surface magnetoplasmon as a function of coupling-layer thickness | 175 |
| 6.15. Prism-coupled reflectance and differential reflectance as a function of bounding asymmetry: $n_{\text{COU}} > n_{\text{SUB}}$ | 177 |
| 6.16. Prism-coupled reflectance and differential reflectance as a function of bounding layer asymmetry: $n_{\text{COU}} < n_{\text{SUB}}$ | 179 |
| A.1. Theoretical dependence of bare sample reflectance on nickel dielectric constant | 190 |
| A.2. Theoretical dependence of bare sample reflectance on nickel thickness and substrate refractive index | 191 |
| A.3. Theoretical dependence of reflectance from prism-coupled, long-range surface plasmon on nickel thickness | 192 |
| A.4. Theoretical dependence of reflectance from prism-coupled, long-range surface plasmon on real part of nickel dielectric constant | 193 |

LIST OF ILLUSTRATIONS--Continued

| Figure | Page |
|---|------|
| A.5. Theoretical dependence of reflectance from prism-coupled, long-range surface plasmon on imaginary part of nickel dielectric constant . . . | 194 |
| A.6. Theoretical dependence of reflectance from prism-coupled, long-range surface plasmon on coupling-layer thickness | 195 |
| A.7. Theoretical dependence of reflectance from prism-coupled, long-range surface plasmon on coupling-layer refractive index | 196 |
| A.8. Theoretical dependence of reflectance from prism-coupled, long-range surface plasmon on substrate refractive index | 197 |

LIST OF TABLES

| Table | Page |
|--|------|
| 3.1. Theoretical bistable switching intensities | 85 |
| 6.1. Experimentally-determined sample parameters | 147 |
| A.1. Unknown sample parameters and features of TM reflectance curves | 188 |
| A.2. Degree of dependence of prism-coupled TM reflectance features on sample parameters | 199 |

ABSTRACT

The properties of surface plasmon polaritons which propagate in optically nonlinear or magnetic media are investigated. Expressions for the electromagnetic fields of a multilayer stack are derived by modification of the Fresnel reflection coefficients. Original research on prism-coupled, nonlinear, long-range surface plasmon polaritons, and on bound and prism-coupled, long-range surface magnetoplasmon polaritons in a transversely-applied magnetic field, is compared to previous research on single-interface plasmon polaritons.

The reflectance from prism-coupled, nonlinear surface plasmons is analyzed using the infinite plane-wave approximation and a substrate nonlinearity which depends on the square of the transverse-electric field. Bistable switching requires incident intensities two orders of magnitude smaller for the long-range mode than for the single-interface mode. The regime in which the approximations are valid is shown to extend beyond that of first-order perturbation theory to guided waves that are very near cutoff. The sign and location of the nonlinearity become significant for these waves. For positive nonlinearities, nonlinear wave analysis indicates an additional branch of the reflected intensity curve, due to self-focussing of the guided wave. Positive and negative nonlinearities exhibit different switching intensities.

The propagation constant of the long-range surface plasmon of a magnetic metal film is shifted by the application of a transverse magnetic field. The sign and magnitude of the shift are highly dependent on the metal thickness and the refractive indices of the bounding media. The shift is manifested experimentally as a resonant modulation of the reflectance from the prism-coupled surface plasmon due to changes

in the angular position and width of the plasmon resonance. Experimental prism-coupling to the long-range surface magnetoplasmon in thin nickel films confirms the theoretical expectations for a wide variety of sample parameters. The phase of the magneto-optic coefficient is determined from the angular profile of the reflectance modulation. Although the shift of the propagation constant may be two orders of magnitude smaller for the long-range mode, the modulation signal is the same order of magnitude for long-range and single-interface magnetoplasmons.

CHAPTER 1

INTRODUCTION

The past two decades have seen a rapid accumulation of knowledge concerning optical waves guided by thin films and interfaces. A major impetus for this research has been a realization of the technological potential for using guided waves in all-optical signal processing applications, as is already being demonstrated by fiber optics. The study of the physics and chemistry of, and at, surfaces has also influenced the research. As the demand has increased for higher quality and more sophisticated material structures in optics as well as electronics, so too has the demand for an understanding of their surface properties. A third impetus for optical guided-wave research has been the enhancement of incident electromagnetic fields by thin film structures, which enhances phenomena such as magneto-optic and nonlinear optic effects. Nonlinear directional couplers, optical limiters, optically bistable switching elements, and magneto-optic data storage devices are a few of the current research topics which may play an important role in future technology.

This work concerns the nonlinear and magneto-optic properties of a particular type of surface wave -- the surface plasmon polariton. Surface plasmon polaritons are electromagnetic modes guided at the interfaces between an electron plasma, or plasma-like medium, and other media. In this chapter the general topics which form the foundations of the research are introduced, and reference is made to important pioneering and review articles. Later chapters present further background information relevant to the specific topics of the study.

1A. Background to Optical Surface Waves

As an electromagnetic wave travels through a polarizable medium, it excites internal degrees of freedom in the medium, inducing a polarization, which in turn affects the propagation of the wave [1, 2]. This coupled mode is called a "polariton", a term originally introduced to classify "polarization field particles analogous to photons" [3]. The current use of the term to imply the interaction of an electromagnetic wave and an elementary excitation is explained by Mills and Burstein, who provide a good review of the research up to the mid-1970's [4]. Polaritons are specified by the type of polar excitation which is coupled to the electromagnetic wave, for example phonons, plasmons, excitons, or magnons. With such a range of phenomena, it is easy to imagine the diversity of research possible in the study of polaritons [5].

Surface polaritons are photons coupled to electric-dipole and/or magnetic-dipole excitations at the interfaces between media [6, 7]. They are manifested as electromagnetic modes propagating in a wave-like manner along the interfaces but exponentially decreasing in amplitude away from the interfaces. The existence of surface electromagnetic waves has been appreciated since the early 1900's, when Zenneck [8] and Sommerfeld [9] showed theoretically that radio-frequency electromagnetic waves can be bound to the interface between a lossy medium, characterized by a large imaginary part of the dielectric constant, and a lossless medium. Many years later Fano realized that, at optical frequencies, electromagnetic surface waves will propagate along an interface between a medium with a negative real part of its dielectric constant (a "metal") and a lossless medium [10]. The wavevector of the bound mode is greater than that of a bulk wave in the medium.

Fano also noted that the Zenneck-Sommerfeld waves, the metal-air modes now called Fano modes, and the Brewster-angle condition at lossless dielectric interfaces represent the same mathematical case. In all three, the solution to the boundary conditions at the interface between two isotropic, dissimilar media can be met by a pair of plane waves, one in each medium. The allowed waves are transverse-magnetic (magnetic field parallel to the interfaces and perpendicular to the wavevector) for the case of linear, nonmagnetic media.

Various classification schemes have been used to distinguish the types of electromagnetic surface modes [6, 11-14]. Many authors consider only Fano modes to be true polaritons, since they are the only surface normal modes, not requiring losses to bind them to the interface, as do the Zenneck-Sommerfeld and Brewster modes [13]. The propagation wavevector of Fano modes has a component parallel to the interfaces which is mostly real (sinusoidal propagation) and a component perpendicular to the interfaces which is mostly imaginary (evanescent confinement).

Tamir has classified four types of electromagnetic waves that are supported by planar boundaries: surface waves, leaky waves, the lateral wave and radiation modes [14]. Surface waves include surface polaritons (Fano modes) and thin-film optical waveguide modes. Leaky waves are modal solutions which leak energy into the media surrounding the guiding region at a definite angle. These coupled waves are closely associated with surface waves and represent a simple method for studying their properties, as in prism excitation. The lateral wave occurs only for a beam of finite width incident from one medium at its interface with a rarer medium, at an angle near the critical angle. The so-called "Goos-Haenchen shift" [15] of the reflected beam from its geometrical optics path is a consequence of the lateral wave.

Radiation modes support fields which are not guided by the interfaces, and whose angular spectrum is continuous. Although this work focusses on surface and leaky waves, the lateral wave and radiation modes must be understood when exciting surface polaritons with a finite beam and when analyzing the complete angular spectrum of prism excitation.

The development of the attenuated total reflection (ATR) technique was the pivotal point in the modern-day study of surface polaritons. Although the technique was demonstrated as early as 1947 [16], Otto in 1968 was the first to show that ATR could be used to launch surface plasmon polaritons at a single interface and to measure their dispersive properties [17]. Kretschmann and Raether presented an alternate ATR geometry of exciting the waves and used it to measure the optical constants of thin metal films [18, 19]. Since then, the ATR technique has generated a great deal of information about many types of surface polaritons. A hybrid of the Otto and Kretschmann geometries methods is utilized in this study to investigate coupled, double-interface plasmon polaritons.

As mentioned above, one of the catalysts for the study of surface waves has been the use of waveguide optics in signal processing, a field known as integrated optics [20]. The study of optical waveguides is tied very closely to that of surface polaritons, since the same formalism is used to analyze both planar waveguides and surface polaritons, the basic difference being the dielectric properties of the media. Because, in almost all cases, optical signals are converted to and from electrical signals for output and input, a particular emphasis is placed on materials which are constituents of both integrated circuits and optical waveguides. This includes metals and semiconductors. A thin metallic film is necessary for the propagation of surface

plasmons discussed in this work, and the examples presented for the nonlinear surface plasmon theory rely heavily on semiconductor optical nonlinearities. Tien and coworkers introduced the prism-coupling concept to planar waveguide optics [21] shortly after Otto applied it to the study of surface plasmons. Although integrated optical devices often use an endfire method of coupling light, and gratings provide a compact in-plane method for coupling out-of-plane light, the prism-coupler offers a simple, nondestructive means of testing waveguide materials and concepts.

The central theme of the research presented here is the surface plasmon polariton which propagates along the interface(s) between a metal and media having a positive, real dielectric constant. The metal, having a negative, real part of the dielectric constant, is called the surface-active medium, and the other media are the surface-inactive media [11]. The focus of the study will be on original research involving two special cases: 1) surface-inactive media whose dielectric constants depend on the square of the electric-field component which is normal to the interfaces, giving rise to nonlinear surface plasmons, and 2) a magnetic surface-active medium, giving rise to surface magnetoplasmons. Two types of modes will be studied: freely-propagating surface plasmons which are uncoupled from bulk radiation, and prism-loaded surface plasmons which are studied by the methods of attenuated total reflection. As is the case in the literature, the terms "surface plasmon", "surface plasmon polariton", and "surface plasma wave" will be used interchangeably. The research results for double-interface modes are original, but the results for single-interface modes are also presented for the sake of completeness and, in the case of the surface magnetoplasmon, to correct a previous misinterpretation.

1B. Organization of the Dissertation

Chapter 2 presents a theoretical framework for the study of surface plasmon polaritons, based on previous research. Expressions are derived for the reflectance from, and electromagnetic fields in, a multiple-layer material stack which is nonmagnetic and optically linear. They are applied to the analysis of freely-propagating and prism-coupled surface plasmon modes. The theory for nonlinear surface plasmons and surface magnetoplasmons in subsequent chapters is a modification of these expressions.

In Chapter 3 a theory of prism coupling to the nonlinear surface plasmon is developed, and the conditions for its applicability are analyzed. Examples of different material geometries and properties are given, and the results are compared to related studies. Reasons are given for the difficulty in investigating the nonlinear surface plasmon experimentally.

A theoretical analysis of surface magnetoplasmons involving transversely-magnetized metallic media is presented in Chapter 4. The properties of the long-range surface magnetoplasmon polariton guided by a thin metal film are described as a function of material parameters. Appropriate modification of the Fresnel reflection coefficients indicates a modulation of the reflectance from the prism-coupled surface magnetoplasmon when a modulated, external magnetic field is applied. The results are compared to previous studies of the single-interface magnetoplasmon polariton. Chapter 5 describes the experimental apparatus used to measure material parameters and to verify the theoretical expectations of the prism-coupled, long-range surface magnetoplasmon. Details are given of the experimental setups used for light incident on the samples from air and from the prism-coupler. Chapter 6 presents the data

and analysis of the experimental verification of theory using thin nickel films. The dependence of the differential reflectance on the various experimental parameters is plotted and compared with theory. The influence of the magnetic surface properties on the prism-coupled, long-range surface magnetoplasmon polariton is discussed.

Conclusions from the present study are drawn in Chapter 7, and areas for further study are suggested. Appendix A describes the method used to infer material parameters from the measured reflectance data from both experimental setups.

CHAPTER 2

SURFACE PLASMON POLARITONS -- THEORETICAL FRAMEWORK

This chapter presents a framework for the understanding of surface plasmon polaritons at metal interfaces. The linear, non-magnetic properties of the waves are developed theoretically to provide a basis for discussing the nonlinear and magneto-optic properties in subsequent chapters. Two cases are considered here -- non-radiative surface modes not coupled to the bulk, and prism-coupled leaky modes which are a source of experimental data on surface plasmons. A history of the study of surface plasmons is given first, in a mostly chronological fashion. It is followed by a derivation of the electromagnetic theory for TM-polarized waves in multiple-layer media. Finally, the bound and prism-coupled waves are discussed in turn.

2A. General Description and Historical Background

An unbounded, homogeneous, free-electron plasma is characterized by the dielectric function $\epsilon = 1 - \omega_p^2 / \omega^2$, in which spatial dispersion (the dependence of ϵ on the wavevector) has been neglected. The plasma supports a collective, longitudinal oscillation of electrons at the plasma frequency, ω_p [22]. The quantum of oscillation is called a volume plasmon, and the wavevector of the oscillation is purely real, indicating a bulk wave. With the introduction of a surface, the symmetry of the system is broken and the wavevector, k , may be complex, giving rise to electron oscillations which are localized at the surface. This mode of oscillation is the single-interface, surface plasmon. In the electrostatic approximation, all interactions are

taken to be instantaneous, and $\nabla \times \mathbf{E} = 0$, equivalent to setting the speed of light to infinity. In this approximation, valid for large wavevectors, the surface plasmon oscillation is longitudinal and has an angular frequency of $\omega_p/\sqrt{2}$ [23].

When the full set of Maxwell's equations are considered, the complete dispersion relation is derived as $k = (\omega/c)[\epsilon/(\epsilon+1)]^{1/2}$ for a semi-infinite metal bounded by vacuum [24]. At large wavevectors the surface plasmon angular frequency, ω , approaches the limit $\omega_p/\sqrt{2}$, the oscillation being purely longitudinal or plasma-like. For shorter wavevectors, when the phase velocity, ω/k , is comparable to the speed of light, c , the oscillation acquires a transverse nature and coupling to electromagnetic radiation becomes significant. The coupled mode is the surface plasmon polariton. As the wavevector approaches zero, the wave is photon-like, and the dispersion curve is asymptotic to the light line.

In his pioneering paper, Ritchie predicted that surface plasma waves could be excited along a metal surface by incident, fast electrons [23]. Experimental confirmation was obtained by measuring the energy loss of the reflected electrons in the long-wavevector region of the dispersion curve [25]. In the short-wavevector region, the surface waves excited by electrons are detected by radiation to the bulk if the surface is not planar, as in the case of statistical surface roughness [26] or a periodic grating [27]. Roughness has also been used to excite surface plasma waves with incident light [28].

The method of attenuated total reflection was introduced to the study of surface plasmon polaritons in two different geometries. Otto's geometry consisted of a prism separated from the metal surface by a gap region [17]. The geometry of

Kretschmann and Raether, usually referred to as the Kretschmann geometry, had a thin metal film deposited on the base of the prism, and the surface plasmon mode was excited at the opposite surface [18]. Both have the advantage that the surface on which the mode propagates is as smooth as the fabrication method allows, so that the properties of the mode are closely associated with the nonradiative mode guided by the planar interface between two semi-infinite media.

The inclusion of damping effects to describe surface plasmon polaritons in real metals requires a complex dielectric constant and therefore a complex dispersion relation. Either the frequency, wavevector, or both, can be considered complex. In the electron energy-loss experiments, and in ATR coupling techniques where the frequency is scanned, the width of the excitation resonance can be expressed in terms of the imaginary part of the frequency. This describes a temporal decay of the surface plasmon. In an angular ATR scan, the resonance width corresponds to the imaginary part of the wavevector, describing a spatial decay of the plasmon [17]. Some researchers have suggested that it is appropriate to consider both the frequency and wavevector as complex for frequency scans [29, 30]. In the visible and infrared regions of the electromagnetic spectrum considered in this work, all three conventions produce similar results. The convention of a complex wavevector and a real frequency will be used here.

The prism-coupling resonance of a surface plasmon is highly sensitive to the dielectric properties and the surface condition of the metal interfaces. This is one of the main reasons why surface plasmon polaritons have gained so much research attention. As mentioned, Kretschmann and Raether's original work emphasized the measurement of the dielectric constants of thin metal films via the surface plasmon resonance [18]. Surface roughness increases the resonance angle and width [31], that

is it increases both the real and imaginary part of the surface plasmon wavevector. A simple but effective model for a small degree of roughness uses a cermet theory to describe the dielectric constant near the surface of the metal [32].

The early studies of surface plasmon polaritons dealt with the modes guided by a single interface between a metal and a dielectric. In the late 1960's, the surface plasmon dispersion relations for the multiple-interface, coupled modes of thin films were expressed in terms of real propagation wavevectors [33, 34]. The frequency splitting due to the coupling was experimentally verified with electron energy-loss experiments [35]. However, it took several years before coupled surface plasmon modes were optically excited. In the interim, the two decoupled, single-interface modes at the surfaces of a thin metal film were observed using an ATR geometry which was a hybrid of the Otto and Kretschmann geometries, having both a coupling layer and a thin metal film [36]. An additional metal layer allowed the experimental study of the coupling of two single-interface plasmon modes across a dielectric gap region [37]. Plots of the energy flow, current distribution, and surface charge density in the layered structure illustrate the surface-guiding properties and coupled charge oscillation of the modes.

A thin metallic film will support at least one surface plasmon mode whose electromagnetic fields are coupled between the two metal surfaces even if the media bounding the metal are very dissimilar [38]. Both the real and imaginary components of the modal propagation constant increase with decreasing metal thickness. Kovacs considered a symmetrically-bounded indium layer and found that two coupled surface-plasmon modes occur in this case [39, 40]. For one mode, the components of the propagation constant decrease with metal thickness, and for the other they increase with metal thickness. With the appropriate coupling-layer and

film thicknesses, a prism-coupled reflectance resonance was observed for both modes, each at a different angle and with a different resonance width, corresponding to the different real and imaginary components of the propagation constant, respectively. Other researchers expressed these properties in terms of a complex frequency, so that the lifetime varied as a function of thickness in opposite directions for the two modes. It was noted that the penetration of the evanescent fields into the bounding dielectrics is deeper for the longer-lived surface plasmon polariton, which carries more of its energy in the low-loss dielectrics and less in the absorbing metal than the shorter-lived mode [41]. Sarid showed that a slightly asymmetric structure can support both modes, and that for a 20-nm-thick silver film, the mode with the near-symmetric, transverse magnetic-field profile propagates a distance which is longer by more than an order of magnitude than that of the single-interface plasmon [42]. He coined the term "long-range" surface plasmon for this mode. The mode with the anti-symmetric magnetic-field profile propagates a shorter distance than the single-interface mode, and hence was termed the "short-range" mode. Because the long-range mode is less lossy than the short-range and single-interface modes, the electromagnetic fields excited at the metal surfaces by a prism-coupled, long-range surface plasmon will be enhanced relative to the other modes [43]. The combined effects of a longer propagation distance and enhanced fields make the long-range surface plasmon mode more attractive for nonlinear optics applications [44, 45].

Further theoretical investigations of the dispersion relations for double-interface plasmon polaritons have exposed interesting details. The degree of asymmetry between the bounding media can be chosen to increase the propagation length substantially when the mode is close to cutoff [46]. Growing and leaky surface waves may also exist in the asymmetric case [47]. Birefringence in the

bounding media is found to have a minimal effect on the propagation constants of long-range surface plasmon polaritons [48]. Structures with two metal films have been analyzed for electro-optics applications [49].

The long- and short-range surface plasmon polaritons have been experimentally excited in silver and aluminum films via prism-coupling, and the dependence of metal thickness on the propagation constants has been verified [50 - 52]. Measurements of the modal properties were extracted from the total reflectance from the coupler as a function of angle. Due to prism-loading, the propagation constants measured by this method are not exactly those of the unbounded structure. In particular, the losses contributing to the width of the reflectance resonance are due both to dissipation in the metal film and to energy reradiation into the prism. Analysis of the spatial profile of a finite beam reflected from the prism in a coupling geometry allows the separation of these two contributions [53]. Experimental results from prism-coupled, long-range surface plasmons in thin silver films confirmed the theoretical analysis [54].

Two alternate methods for coupling bulk radiation to surface plasmon polaritons are grating coupling and endfire coupling. Grating coupling represents the special case of surface roughness with a periodic profile. Because surface plasmon polaritons have a high electromagnetic field intensity at the metal interfaces, even a small grating depth induces significant coupling to the modes [31, 55]. Endfire coupling to the single-interface plasmon was investigated numerically, and an optimum coupling efficiency of close to 90% was estimated [56]. The advantages of endfire coupling over the other two methods include broadband coupling, which is limited by the frequency selectivity of grating and prism coupling, and the coupling of high optical energies, which is difficult for the distributed coupling techniques,

particularly in an optically nonlinear material. Experimental verification of endfire coupling to surface plasmons has yet to be reported.

2B. TM-Polarized Fields in Layered Media

The structure considered in this study, as in most studies of planar waveguiding, is the multiple-layer material stack shown in Fig. 2.1, in which homogeneous layers and planar interfaces are assumed. The top (0^{th}) and bottom (n^{th}) layers are taken to be semi-infinite, representing thick bounding media in actual experiments. Two types of studies are made of this structure -- the theoretical study of bound surface waves which do not interact with bulk waves, and the study of leaky surface waves by direct optical measurements. Both types of studies can be made using the theoretical formalism presented in this section.

The standard optical measurements made of a multilayer structure are the reflectance and transmission as a function of incident angle, polarization, and light intensity. The measurements are dependent on the material parameters of the stack, namely the thickness and dielectric constant of each of the layers. By modelling the structure and applying the principles of electromagnetic wave theory, relationships between the optical measurements and the material parameters can be derived. Depending on one's starting point -- theoretical or experimental -- either the optical measurements or material parameters can be determined if the other is known. The theoretical Chapters 2, 3, and 4 present examples of optical measurements derived from material parameters. In Chapter 6, a model of material parameters is varied to match experimental measurements.

In Figure 2.1, the x-z plane is the plane of incidence. The x-direction is parallel to the layer boundaries and the z-direction is perpendicular to the interfaces,

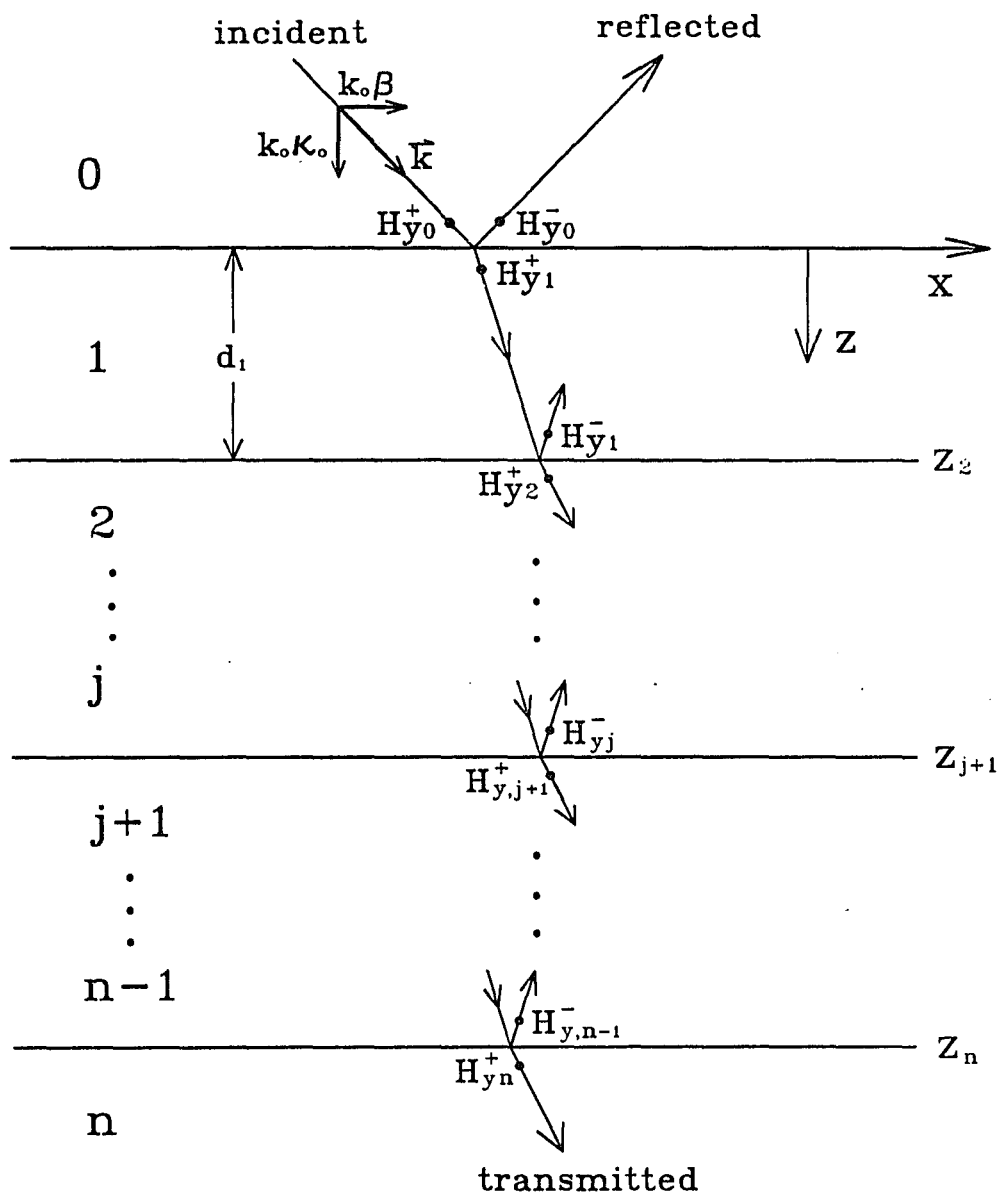


Fig. 2.1. Multiple-layer geometry.

Layers 0 and n are semi-infinite.

with its origin at the top interface. The j^{th} layer is characterized by a thickness, d_j , and an isotropic, relative dielectric constant, $\epsilon_j \equiv \epsilon_j' + i\epsilon_j''$, at a given free-space wavelength, λ_0 . (The nonlinear and magnetic media discussed in later chapters are not isotropic, as will be noted.) The dielectric properties can be expressed equivalently in terms of the refractive index, $n_j \equiv n_j' + in_j'' = (\epsilon_j)^{1/2}$. (The dielectric constant of the 0^{th} layer is expressed as n_0^2 to avoid confusion with the free-space dielectric permittivity, ϵ_0 .) The relative magnetic permeability, μ , is taken to be unity. In the following and subsequent discussions, all quantities, except frequency ω , time t , and variables with units of length, are considered complex, with the real part denoted by a single prime and the imaginary part denoted by a double prime.

Electromagnetic waves in the layered media are considered planar in phase and of infinite extent. Because of symmetry, only the x - and z -dependences of the field amplitudes are discussed. The electric- and magnetic-field vectors are assumed to have the usual form:

$$\mathbf{A} = \frac{1}{2} [\mathbf{A}(x,z) \exp(-i\omega t) + \mathbf{A}^*(x,z) \exp(i\omega t)] . \quad (2.1)$$

For TM polarization, $\mathbf{E}(x,z) = E_x \mathbf{x} + E_z \mathbf{z}$ and $\mathbf{H}(x,z) = H_y \mathbf{y}$, where \mathbf{x} , \mathbf{y} , and \mathbf{z} are unit vectors in their respective directions. Maxwell's equations, for the case of no current or charge density, are

$$\nabla \cdot (\epsilon \cdot \mathbf{E}) = 0 , \quad (2.2)$$

$$\nabla \times \mathbf{H} = \epsilon_0 \epsilon \cdot \frac{\partial \mathbf{E}}{\partial t}, \quad (2.4)$$

and

$$\nabla \times \mathbf{E} = -\mu_0 \frac{\partial \mathbf{H}}{\partial t}, \quad (2.5)$$

where ϵ_0 and μ_0 are the free-space dielectric permittivity and magnetic permeability, respectively, and ϵ is written as a tensor for generality, as required in subsequent chapters. For the isotropic media of this chapter, Eqs. (2.4) and (2.5) lead to

$$E_x = -\frac{i}{\omega \epsilon_0 \epsilon} \frac{\partial H_y}{\partial z}, \quad (2.6)$$

$$E_z = \frac{i}{\omega \epsilon_0 \epsilon} \frac{\partial H_y}{\partial x}, \quad (2.7)$$

and

$$H_y = \frac{i}{\omega \mu_0} \left[\frac{\partial E_z}{\partial x} - \frac{\partial E_x}{\partial z} \right]. \quad (2.8)$$

Eliminating E_x and E_z from the equations, the wave equation in terms of the transverse magnetic field, H_y , can be derived as

$$\frac{\partial^2 H_y}{\partial x^2} + \frac{\partial^2 H_y}{\partial z^2} + k_0^2 \epsilon H_y = 0, \quad (2.9)$$

where $k_0 = \omega/c = 2\pi/\lambda_0$.

The solution to the TM wave equation in layer j is well-known:

$$H_{yj}(x,z) = H_{yj}^+ \exp[ik_0[\beta x + \kappa_j(z-z_j)]] + H_{yj}^- \exp[ik_0[\beta x - \kappa_j(z-z_{j+1})]], \quad (2.10)$$

where

$$\beta^2 + \kappa_j^2 = \epsilon_j . \quad (2.11)$$

and the coefficients $H_{y_j}^+$ and $H_{y_j}^-$ are illustrated in Fig. 2.1. The superscripts + and - indicate the direction of wave propagation perpendicular to the layer interfaces. β is the normalized propagation constant in the x-direction (also called the "effective refractive index"), identical in each material layer by virtue of the continuity of tangential fields. It is related to the complex angle of propagation, θ_j , in each layer by

$$\beta = n_j \sin \theta_j . \quad (2.12)$$

κ_j is the normalized propagation constant of layer j in the z-direction, dependent on each layer's optical properties. z_j is the low-z interface of the j^{th} layer, and z_{j+1} is the high-z interface of the j^{th} layer.

By definition, the relative optical impedance of medium j is

$$Z_j \equiv \frac{c\epsilon_0 E_{x_j}^+}{H_{y_j}^+} = - \frac{c\epsilon_0 E_{x_j}^-}{H_{y_j}^-} = \frac{\kappa_j}{\epsilon_j} . \quad (2.13)$$

Boundary conditions demand that E_x and H_y be continuous at each interface, that is

$$Z_j H_{y_j}^+ \exp(ik_0 \kappa_j d_j) + Z_j H_{y_j}^- = Z_{j+1} H_{y_{j+1}}^+ + Z_{j+1} H_{y_{j+1}}^- \exp(ik_0 \kappa_{j+1} d_{j+1}) \quad (2.14)$$

$$H_{y_j}^+ \exp(ik_0 \kappa_j d_j) + H_{y_j}^- = H_{y_{j+1}}^+ + H_{y_{j+1}}^- \exp(ik_0 \kappa_{j+1} d_{j+1}) . \quad (2.15)$$

Letting $\gamma_j = ik_0\kappa_j d_j$, which is the phase change across layer j , and defining $d_0 \equiv 0$, the boundary conditions reduce to the form

$$H_{y_j}^+ = \frac{1}{2Z_j} \left[(Z_j + Z_{j+1}) H_{y_{j+1}}^+ + (Z_j - Z_{j+1}) H_{y_{j+1}}^- \exp(\gamma_{j+1}) \right] \exp(-\gamma_j) \quad (2.16)$$

$$H_{y_j}^- = \frac{1}{2Z_j} \left[(Z_j - Z_{j+1}) H_{y_{j+1}}^+ + (Z_j + Z_{j+1}) H_{y_{j+1}}^- \exp(\gamma_{j+1}) \right]. \quad (2.17)$$

Consider a single interface between semi-infinite layers j and $j+1$. No wave is incident from layer $j+1$, such that $H_{y_{j+1}}^- = 0$. The single-interface, amplitude reflection coefficient for the magnetic field is then

$$r_{j,j+1} \equiv \frac{H_{y_j}^-}{H_{y_j}^+} \exp(-\gamma_j) = \frac{Z_j - Z_{j+1}}{Z_j + Z_{j+1}} \quad (2.18)$$

and the single-interface transmission coefficient is

$$t_{j,j+1} \equiv \frac{H_{y_{j+1}}^+}{H_{y_j}^+} \exp(-\gamma_j) = \frac{2Z_j}{Z_j + Z_{j+1}}. \quad (2.19)$$

The phase term, $\exp(-\gamma_j)$, is irrelevant for the single interface but is included in expressions for multiple-layer reflection because of the convention used to label the field components (see Fig. 2.1).

If a second interface between layers $j+1$ and $j+2$ is present in the structure, Eqs. (2.16) and (2.17) can be rewritten, using the definitions of (2.18) and (2.19) to express the fields in layer $j+1$ in terms of the fields in layer $j+2$. The result is:

$$H_{y_j}^+ = \frac{1}{2Z_j} [(Z_j + Z_{j+1}) + (Z_j - Z_{j+1}) r_{j+1,j+2} \exp(-\gamma_{j+1})] \frac{H_{y_{j+2}}^+}{t_{j+1,j+2}} \exp(-\gamma_j - \gamma_{j+1}) \quad (2.20)$$

$$H_{y_j}^- = \frac{1}{2Z_j} [(Z_j - Z_{j+1}) + (Z_j + Z_{j+1}) r_{j+1,j+2} \exp(-\gamma_{j+1})] \frac{H_{y_{j+2}}^+}{t_{j+1,j+2}} \exp(-\gamma_{j+1}) \quad (2.21)$$

From these equations it can be shown that the three-layer reflection coefficient for layers j through $j+2$ is given by

$$\rho_{j,j+2} \equiv \frac{H_{y_j}^-}{H_{y_j}^+} \exp(-\gamma_j) = \left[\frac{r_{j,j+1} + r_{j+1,j+2} \exp(2\gamma_{j+1})}{1 + r_{j,j+1} r_{j+1,j+2} \exp(2\gamma_{j+1})} \right] \quad (2.22)$$

The inclusion of additional layers produces a similar expression, such that, by defining $\rho_n \equiv 0$, the multilayer, amplitude reflection coefficient ρ_j between the j^{th} layer and the bottom, semi-infinite n^{th} layer is given recursively by

$$\rho_j \equiv \frac{H_{y_j}^-}{H_{y_j}^+} \exp(-\gamma_j) = \left[\frac{r_{j,j+1} + \rho_{j+1} \exp(2\gamma_{j+1})}{1 + r_{j,j+1} \rho_{j+1} \exp(2\gamma_{j+1})} \right] \quad (2.23)$$

The intensity reflectance of the entire stack is $R \equiv |\rho_0|^2$. The multilayer, amplitude transmission coefficient between layers j and $j+1$ (in the presence of the complete multilayer stack) is

$$\tau_{j,j+1} = \frac{H_{y_{j+1}}^+}{H_{y_j}^+} \exp(-\gamma_j) = \frac{t_{j,j+1}}{1 + r_{j,j+1} \rho_{j+1} \exp(2\gamma_{j+1})} \quad (2.24)$$

Amplitude transmission through the entire stack is calculated as the product of

successive $\tau_{j,j+1}$. The electric fields for each layer j are of the form of Eqs. (2.1) and (2.10), with coefficients given by Eqs. (2.6) and (2.7) as

$$E_{Xj}^+ = \frac{\kappa_j}{c\epsilon_0\epsilon_j} H_{Yj}^+, \quad (2.25a)$$

$$E_{Xj}^- = -\frac{\kappa_j}{c\epsilon_0\epsilon_j} \rho_j \exp(\gamma_j) H_{Yj}^+, \quad (2.25b)$$

$$E_{Zj}^+ = -\frac{\beta}{c\epsilon_0\epsilon_j} H_{Yj}^+, \quad (2.25c)$$

and

$$E_{Zj}^- = -\frac{\beta}{(c\epsilon_0\epsilon_j)\rho_j} \exp(\gamma_j) H_{Yj}^+. \quad (2.25d)$$

An important property of multilayer structures is the intensity enhancement in the intermediate layers relative to the incident intensity in the bulk. In experimental geometries such as a prism-coupling geometry, the incident light enters medium 0 from air at an interface which is not necessarily parallel to the other interfaces. For example, with the hemispherical coupler used as medium 0 in the present work, the incident beam is always normal to the coupler face and the reflection losses are constant with angle in the prism. Assuming normal incidence and neglecting reflection losses at the prism face, the total incident intensity in air is given by

$$I_{in} = \frac{1}{2c\epsilon_0 n_0^2} |H_{Y0}^+|^2. \quad (2.26)$$

The guided intensity, (the x-component of the Poynting vector) at the layer m side of the j,j+1 interface is

$$I_{x,m}(z_{j+1}) = \frac{\beta}{2c\epsilon_0} \operatorname{Re} \left[\frac{1}{\epsilon_m} \right] |H_{y_j}(z_{j+1})|^2, \quad (2.27)$$

where $m=j$ or $j+1$. The interfacial, guided-intensity enhancement is $I_{x,m}/I_{in}$. The z-component of the Poynting vector is

$$I_{z,m}(z_{j+1}) = \frac{1}{2c\epsilon_0} \operatorname{Re} \left[\frac{\kappa_m}{\epsilon_m} \right] |H_{y_j}(z_{j+1})|^2, \quad (2.28)$$

which is zero in the n^{th} medium at incident angles greater than the critical angle, where surface plasmons are excited.

2C. Bound Surface Plasmon Polaritons -- Dispersion Relations

The dispersion relation for a guided surface mode is derived by restricting the fields in each of the two outer semi-infinite layers to the single wave which travels away from the stack and decays to zero. A common method of expressing these conditions is to take the limit of the reflectance from the layered stack as it approaches infinity, that is to find a complex pole, β , of the reflectance. This implies that, although no light is incident from outside the stack, the structure supports finite electromagnetic fields. Since the multilayer reflectance is expressed as a quotient in Eq. (2.23), the pole is found by solving for the zero of the denominator of the reflectance coefficient, ρ_0 . The geometries of interest are the two-layer stack, which supports the single-interface mode, and the three-layer stack,

which supports the double-interface modes. Note that in the discussion of bound modes, β is a discrete, complex solution of the dispersion equation. In the discussions of prism coupling, β is a real value in a continuous spectrum.

2C.1. Single-Interface Plasmon Polariton

Consider the case of a surface plasmon polariton bound to the single interface between a semi-infinite metal (medium 2) and a semi-infinite dielectric with a positive, real dielectric constant (medium 1). The normalized propagation constant, β , is the pole of the single-interface reflectance coefficient for TM-polarized light, as expressed by the dispersion equation

$$\frac{\kappa_1}{\epsilon_1} + \frac{\kappa_2}{\epsilon_2} = 0, \quad (2.29)$$

The solution is analytical for the single-interface mode and, from Eq. (2.11), it is given by

$$\beta = \left[\frac{\epsilon_1 \epsilon_2}{\epsilon_1 + \epsilon_2} \right]^{1/2}. \quad (2.30)$$

To insure that the mode is a bound Fano mode, evanescently decaying with distance away from the interface, the perpendicular, normalized propagation constants, κ_1 and κ_2 , must both be mostly imaginary; the requirement $\beta^2 > \epsilon_j$ must be met for each of the media, according to Eq. (2.11). Therefore, from Eq. (2.30), the dielectric constants must satisfy the condition, $-\epsilon'_2 > \epsilon'_1 > 1$. This constitutes the definition of an "active" medium 2 necessary for the existence of Fano modes. Materials other than metals may satisfy the condition in certain spectral regions, and metals do not satisfy the condition above the plasma frequency.

The length of the evanescent "wing" of the guided intensity, normal to the interface, is given by

$$\Gamma_j = \frac{\lambda_0}{4\pi\kappa_j''} . \quad (2.31)$$

Γ_j is highly dependent on the magnitude of the metal's dielectric constant. With increasing $|\epsilon_2'|$, β^2 approaches ϵ_1 , causing the wing length in the surface inactive medium 1 to increase, via Eq. (2.11), and the mode to become less confined to the surface. The distance that the bound surface plasmon travels before decaying to 1/e of its initial intensity is termed the propagation length, l , and is given by

$$l = \frac{\lambda_0}{4\pi\beta''} . \quad (2.32)$$

Equation (2.30) indicates that if $\epsilon_1'' = \epsilon_2'' = 0$, β is purely real, so that the surface plasmon mode experiences no decay as it propagates along the interface. The damping in real metals ($\epsilon_2'' \neq 0$) induces decay in the propagation of the surface plasmon polariton. Kretschmann has shown that the decay term, β'' , varies as $\epsilon_2''/|\epsilon_2'|$ as long as $|\epsilon_2'| \gg \epsilon_1$ [19]. According to the Drude model for the dielectric constants of metals [57],

$$\epsilon_2' = \epsilon_\infty - \frac{\omega_p^2}{\omega^2 + \omega_\tau^2} \quad (2.33)$$

$$\epsilon_2'' = \frac{\omega_p^2 \omega_\tau}{\omega^3 + \omega\omega_\tau^2} \quad (2.34),$$

where ϵ_∞ is the high-frequency dielectric constant, ω_p is the plasma frequency, ω_τ

is the damping frequency, and ω is the frequency of light. Since at visible and infrared wavelengths $\omega_T \ll \omega < \omega_p$ for most metals, $|\epsilon_2'|$ varies as the second power of wavelength, and ϵ_2'' varies as the third power of wavelength. Therefore, in wavelength regions where certain metals can be modelled according to the Drude theory, β'' of the single-interface plasmon for these metals is expected to depend inversely on wavelength. This produces an increase of the propagation length, l , to the second power of wavelength. Schoenwald et al. predicted macroscopic propagation lengths for surface plasmon polaritons at a copper-air interface in the infrared, and measured $l = 1.9$ cm at a wavelength of $10.6 \mu\text{m}$ [58]. Silver, commonly used in the study of surface plasmon polaritons, is a good example of a Drude metal in the near and middle infrared ($\lambda_0 = 0.75$ to $20 \mu\text{m}$) [59, 60]. Figure 2.2 displays the calculated dependence of l on wavelength, which is, on the average, slightly higher than the second power in this wavelength region.

Note that if the electromagnetic wave is TE-polarized, the dispersion equation is $\kappa_1 + \kappa_2 = 0$, which does not allow a solution since the imaginary part of both κ_1 and κ_2 must be positive for evanescent decay. It is well-known that a single interface between linear, nonmagnetic media cannot support a TE-polarized guided wave.

2C.2. Double-Interface Plasmon Polaritons

Consider now the case of a surface plasmon polariton coupled between the two interfaces of a thin metal film (layer 2) bounded by two semi-infinite dielectrics with positive, real dielectric constants (layers 1 and 3). The dispersion equation expresses the condition for a pole of the three-layer Fresnel reflectance for TM-polarized light,

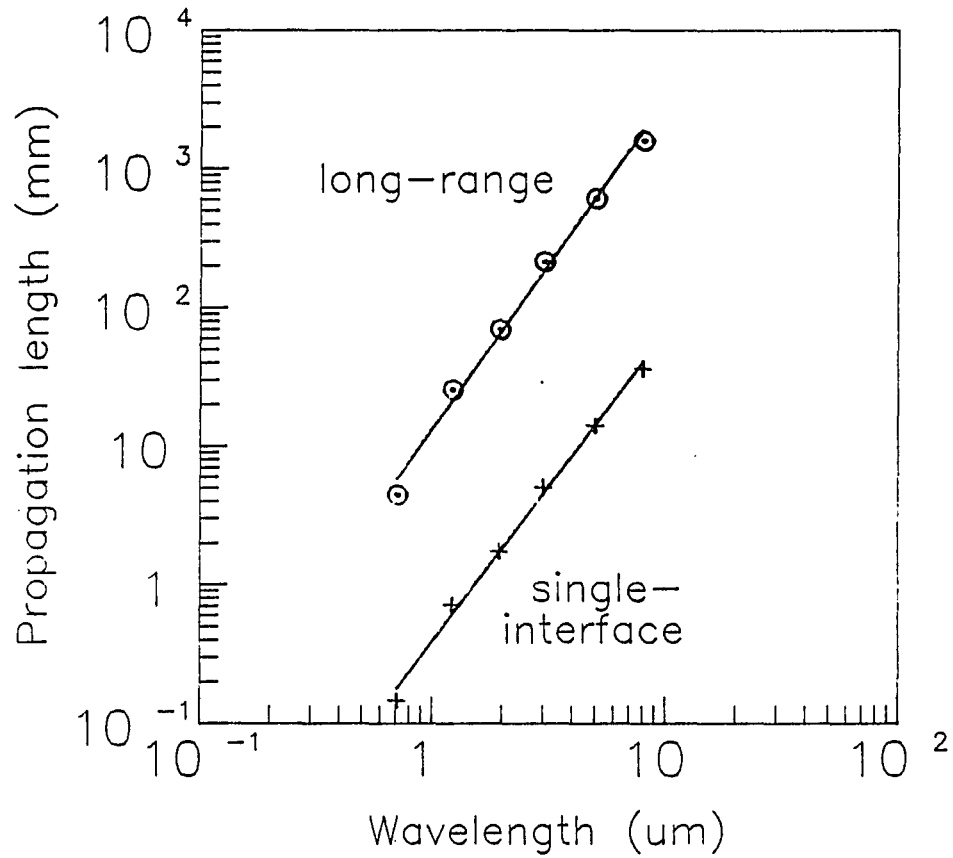


Fig. 2.2. Propagation lengths of surface plasmon polaritons

theoretical calculations for single-interface and long-range modes in silver bounded by air as a function of wavelength; silver dielectric constants are from Refs. [59] and [60], and silver thickness for the long-range mode is 20 nm.

$$1 + r_{12} r_{23} \exp(2ik_0\kappa_2d_2) = 0 \quad (2.35)$$

This is a transcendental equation which must be solved numerically to find β . For a large metal film thickness ($d_2 \rightarrow \infty$) it reduces to the dispersion equations for the single-interface plasmon at each of the two metal interfaces, Eq. (2.29). Equation (2.35) for the coupled, double-interface modes has two roots if $|n_1 - n_3| > \beta'_{\infty\min} - n_{\min}$, where n_{\min} is the index of the rarer medium bounding the metal, and $\beta'_{\infty\min}$ is the real part of the single-interface mode's, normalized propagation constant at the rarer interface. The two roots represent the long- and short-range surface plasmon polaritons mentioned in the introduction.

The real (dispersive) and imaginary (absorptive) part of the normalized propagation constant of the double-interface modes are plotted in Fig. 2.3 as a function of silver layer thickness at a wavelength of 632.8 nm. The dielectric constant of silver is taken to be $\epsilon = -18.5 + 0.47i$ [60], and lossless glass of index 1.5 constitutes both bounding media. The notable feature of these plots is that as the metal film thickness is decreased, both the real and imaginary parts of the propagation constant of the long-range mode decrease, and those of the short-range mode increase. In other words, the propagation length, l , of the long-range mode increases and l of the short-range mode decreases with decreasing metal thickness, hence the names of the modes. This behavior can be understood in terms of the distribution of power carried by the mode. For the long-range mode, as β approaches the index of the bounding media with decreasing metal thickness, the evanescent wing lengths in the bounding media increase, according to Eqs. (2.31) and (2.11). Consequently, more of the power is carried by the wings in the low-loss bounding media, and less is carried in the metal, which has significant losses. The

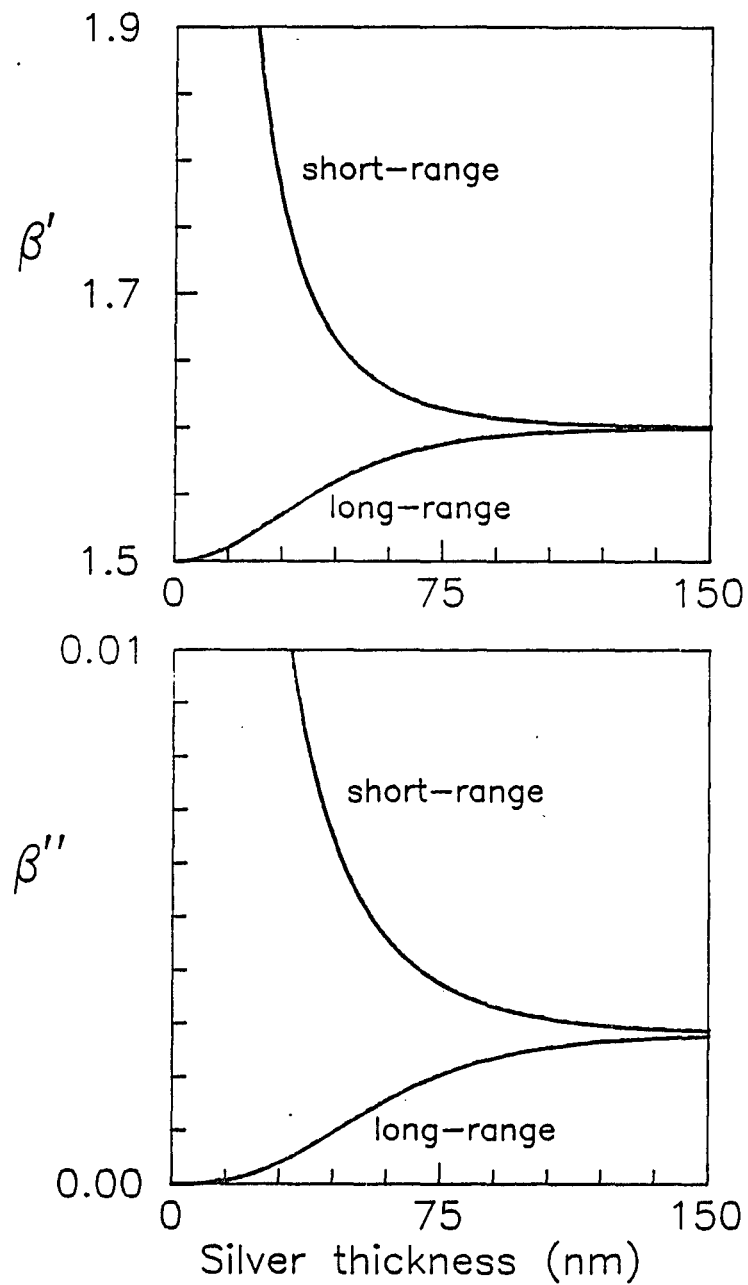


Fig. 2.3. Normalized propagation constants of double-interface plasmon polaritons

dispersive (β') and absorptive (β'') parts of β at a wavelength of 632.8 nm as a function of silver ($\epsilon_1 = -18.5 + i0.47$) thickness; both bounding media are lossless glass ($n_0 = n_2 = 1.5$).

opposite is true of the short-range mode, which explains why it decays in a shorter length than the long-range mode. Profiles of the magnetic field for the two modes, calculated from the equations of Sect. 2B for a silver thickness of 50 nm, are shown in Fig. 2.4. The modes have opposite symmetries of their fields, the magnetic field of the long-range mode being symmetric about the center of the metal film, and the magnetic field of the short-range mode being anti-symmetric.

The theoretical propagation length of the long-range surface plasmon of a 20 nm silver layer bounded by glass is plotted in Fig. 2.2 vs wavelength. Compared to the single-interface plasmon, the long-range mode is predicted to propagate more than an order of magnitude farther. The experimentally achievable propagation length is limited by surface roughness, variation of the silver-film thickness, and losses in the bounding media. However, the enhanced propagation length and guided intensity of the long-range mode motivates the study of nonlinear surface plasmon polaritons in the infrared, which is the subject of Chapter 3.

When the media bounding the metal film are identical, the long-range surface plasmon exists for any metal thickness down to zero. Note from Fig. 2.3 that the two limiting solutions for the long-range mode are the single-interface mode for an infinitely thick metal, as mentioned, and a plane wave in the bounding media for no metal. However, if the bounding media have different indices of refraction, with decreasing metal thickness the wave solution in the denser medium approaches a plane wave while the solution in the rarer medium is still bound to the surface. Consequently the mode is cut off at a finite metal thickness with its normalized propagation constant equal to the denser (higher) index; thinner films will not support the long-range mode. This behavior is illustrated in Fig. 2.5, where the normalized propagation constant of the long-range mode is plotted vs silver layer thickness for

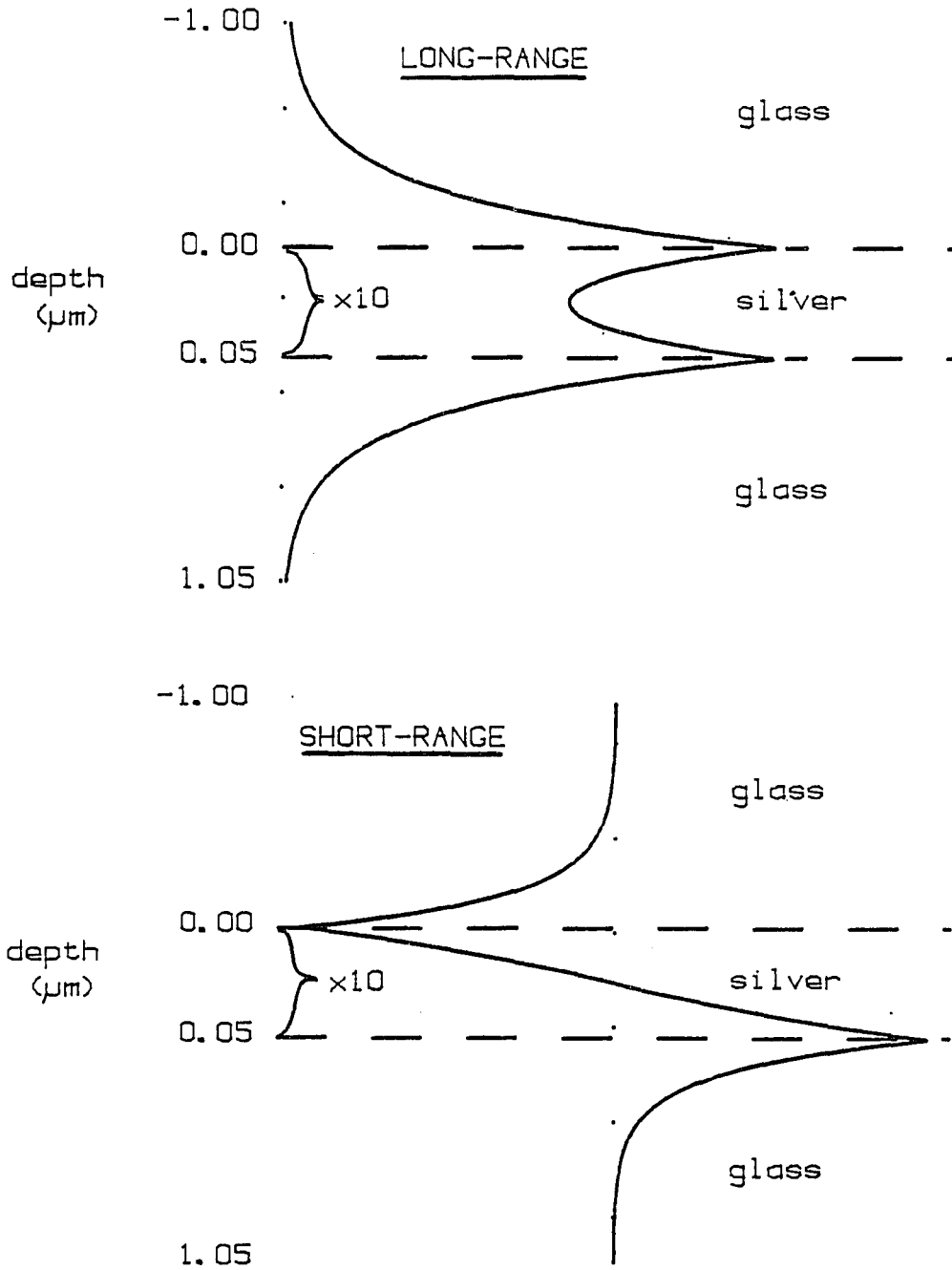


Fig. 2.4. Magnetic-field profile of double-interface plasmon polaritons

H_y calculated in 50 nm silver film bounded by glass; $\lambda_0 = 632.8$ nm; distance in the silver is expanded $\times 10$.

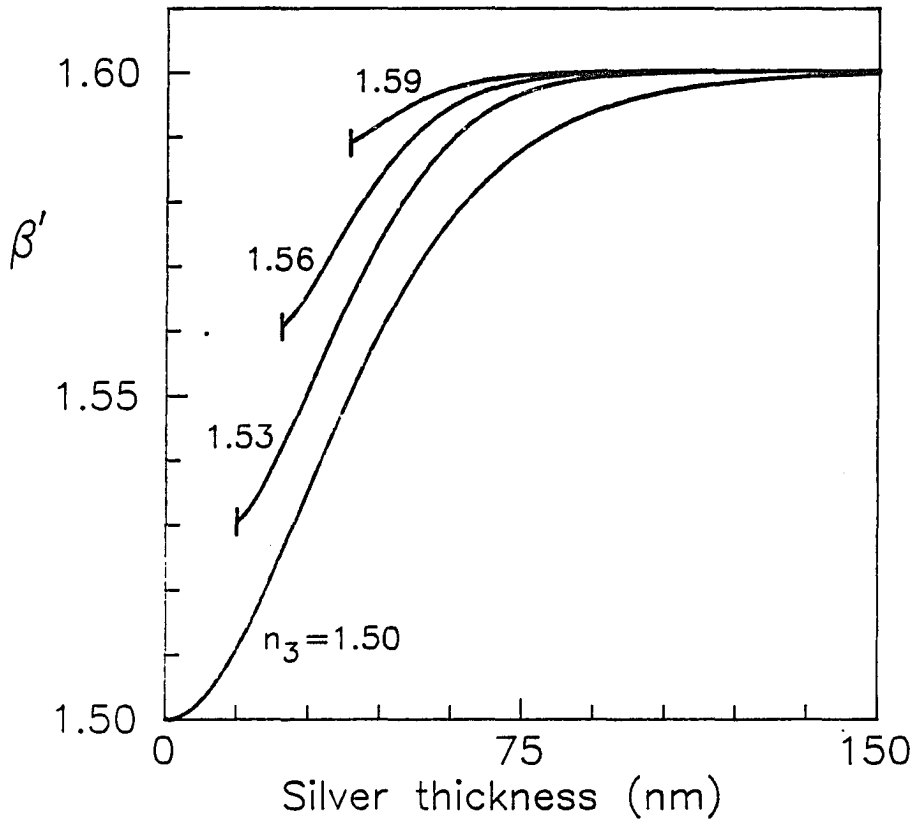


Fig. 2.5. Normalized propagation constant of the long-range surface plasmon polariton for asymmetric bounding

dispersive part of β as a function of silver film thickness; $\lambda_0 = 632.8$ nm, $n_1 = 1.5$, n_3 is as labelled.

one bounding medium of index 1.5 and different values of index for the other bounding medium. The thick-metal limit of the long-range mode is the single-interface mode between the metal and the rarer medium, while the thick-metal limit of the short-range mode is the single-interface mode between the metal and the denser medium.

The long-range modes of asymmetric geometries have been analyzed for their enhanced propagation lengths near cutoff [46]. Another application, of interest to this study, is the excitation of nonlinear long-range surface plasmons. Note in Fig. 2.5 that if one of the bounding refractive indices changes, β for a given metal thickness is shifted. One means of changing the refractive index is by changing the intensity in a nonlinear optical medium. Although an accurate description of nonlinear media in surface plasmon geometries requires the solution of the nonlinear wave equation, as discussed in Chapter 3, a simple theory which provides qualitative insight into the problem is based on the equations of this chapter. The essential elements of such a theory are given in Sects. 3F.1 and 3G.

The behavior of surface plasmons has been described up to this point using the example of silver. Silver and the other noble metals have the lowest optical losses of metals in the visible and near infrared; the real part of their dielectric constants is large in magnitude compared to the imaginary part. Consequently, they will produce the narrow resonances and long propagation lengths necessary for the study of nonlinear effects with surface plasmons. On the other hand, metals producing significant magneto-optic effects, such as the ferromagnets nickel and iron, are quite lossy and exhibit surface-plasmon properties which differ from those of the noble metals. Figure 2.6 illustrates the differences for the long-range surface plasmon, using nickel ($\epsilon = -13 + i16$) and iron ($\epsilon = -1.0 + i17.8$) [61] films at a

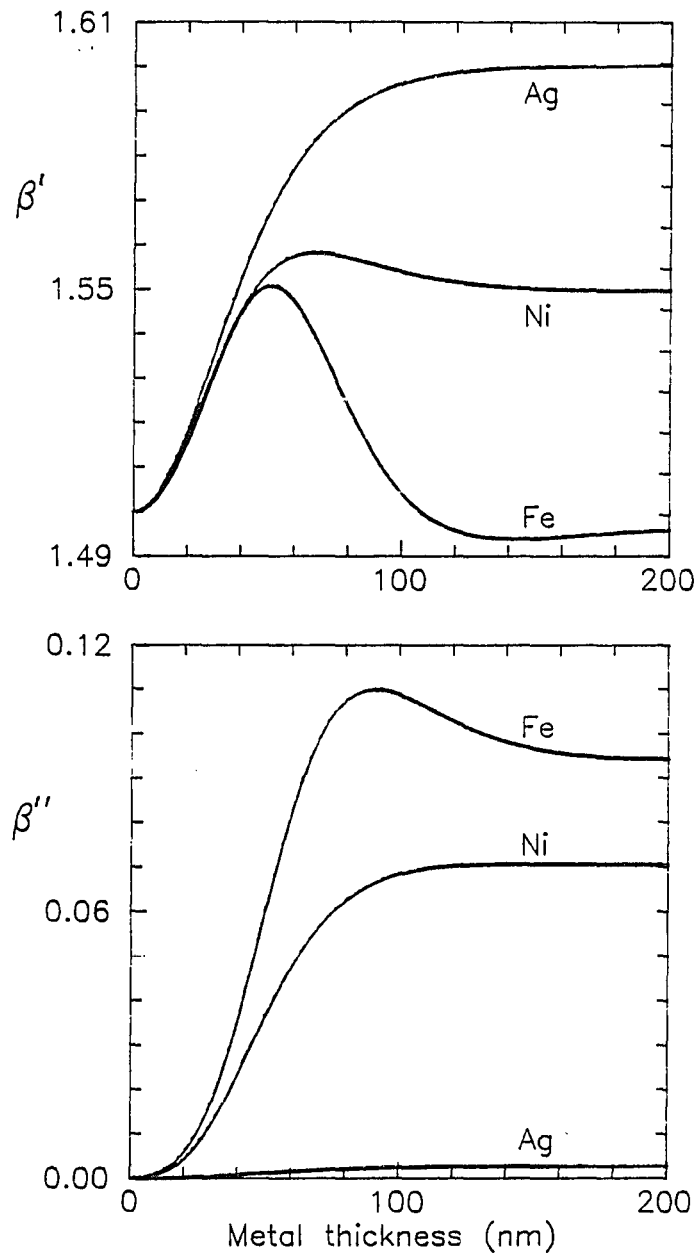


Fig. 2.6. Normalized propagation constant of the long-range surface plasmon polariton in lossy metals

nickel ($\epsilon = -13 + i16$) and iron ($\epsilon = -1.0 + i17.8$) at a wavelength of 632.8 nm; silver data from Fig. 2.3 is shown for comparison.

wavelength of 632.8 nm. Instead of increasing monotonically with increasing metal thickness, as in the case of silver, β of the long-range mode for lossy metals exhibits a local maximum and then decreases to that of the single-surface mode. In fact, for iron β' exhibits a local minimum below the index of the bounding media. At these large thicknesses, the surface guiding is caused by the large dielectric loss of the metal, such that the type of surface wave is between the Zenneck-Sommerfeld regime and the Fano regime. Although the ability to verify these properties experimentally is doubtful since they occur at large thicknesses, they are mentioned here as background to the magnetoplasmon study of Chapters 4-6.

2D. Prism Coupling to Surface Plasmon Polaritons

Since the surface plasmon polaritons discussed above are waves bound to the interfaces, with electromagnetic fields decaying into the bounding media, they will not interact with a bulk optical wave in the bounding media. The normalized propagation constant, or effective index, of the modes is always greater than that of the bounding media, hence the wavevector of the modes is greater than that of the bulk wave. Prisms and gratings are two means of compensating for the difference in wavevector in order to couple light to surface waves. Gratings add to the wavevector of the bulk by interrupting the surface in a periodic way. A prism allows for longer wavevectors by having a refractive index larger than that of the mode index and having nonparallel sides for light input. The angle of incidence of the wave in the prism can be adjusted above the critical angle to produce a longitudinal component of the wavevector which matches the wavevector of the surface mode. Excitation of the mode is accomplished by the fields evanescent from the prism base. This method is often called "attenuated total reflection" or "ATR

coupling". In this work, the term "prism" is used for any high-index medium used as an ATR coupler, regardless of its shape.

Prism coupling to TM-polarized, guided waves can be analyzed using the equations of Section 2B for a multilayer stack. The top, semi-infinite layer is the prism, and any number of remaining layers constitute the waveguide and coupling layers. The modelling of an infinite plane wave which is incident from the prism medium is valid in experimental geometries if the width of the incident beam at the base of the prism is much larger than the propagation length of the surface plasmon [53]. This is certainly true of the experimental study presented in Chapters 4-6 of this work, in which the nickel films guide long-range surface plasmons with propagation lengths less than $10 \mu\text{m}$. The plane-wave approximation is discussed in Chapter 3 in reference to prism-coupled, nonlinear surface plasmons.

Whereas it is the complex pole of the reflectance which solves the dispersion equation for bound surface modes, prism coupling to surface modes manifests itself as a reflectance minimum. A Lorentzian-like reflectance resonance is observed as the angle of light incidence is varied. On resonance, the light energy is coupled to the surface wave and dissipated. If the prism is sufficiently distant from the guiding surfaces and the mode has relatively low loss, the reflectance minimum is very close to the pole of the bound mode. It is therefore a good measure of the dispersive part of the modal, normalized propagation constant, via the expression

$$\beta' \equiv n_0 \sin \theta_{\min}, \quad (2.36)$$

where n_0 is the prism refractive index and θ_{\min} is the angle of the resonance minimum, measured in the prism. The width of the resonance is a measure of the losses in the wave, consisting of the absorptive part, β'' , of the modal, normalized

propagation constant and the radiative damping due to the presence of the prism [17]. The total, normalized decay constant of the prism-coupled mode, $\hat{\beta}''$, relates to the full-width of the reflectance resonance at half-depth, $\delta\theta$, by the expression [62, 63]

$$\hat{\beta}'' = \frac{n_0}{2} \delta\theta \sin\theta_{\min} \cos\theta_{\min}. \quad (2.37)$$

References [62] and [53] provide a detailed analysis of the shift of the resonance minimum due to prism loading.

2D.1. Prism-Coupling Geometries

Three basic geometries have been used to prism couple light into surface plasmon polaritons and to study their properties. They are pictured in Figs. 2.7 and 2.8. As mentioned earlier, the Otto geometry separates the metal surface from the prism by a coupling layer, and is used to excite single-interface plasmon polaritons [17]. The Kretschmann geometry has a thin metal film adjacent to the prism, and single-interface plasmon polaritons are excited on the opposite surface of the film [18]. A hybrid of these geometries, shown in Fig. 2.8, includes a coupling layer and a thin metal film for coupling to double-interface modes. Figures 2.7 and 2.8 include a typical profile of the magnetic field of the prism-coupled surface plasmon across the multilayer for each of the prism geometries.

It has been noted that ATR data from coupling to surface plasmons using the Otto or Kretschmann geometry may be misleading in the case of lossy metals such as nickel [64]. Metals exhibit a pseudo-Brewster effect which manifests itself as a broad minimum in the TM reflectance. This effect can mask or skew the minimum

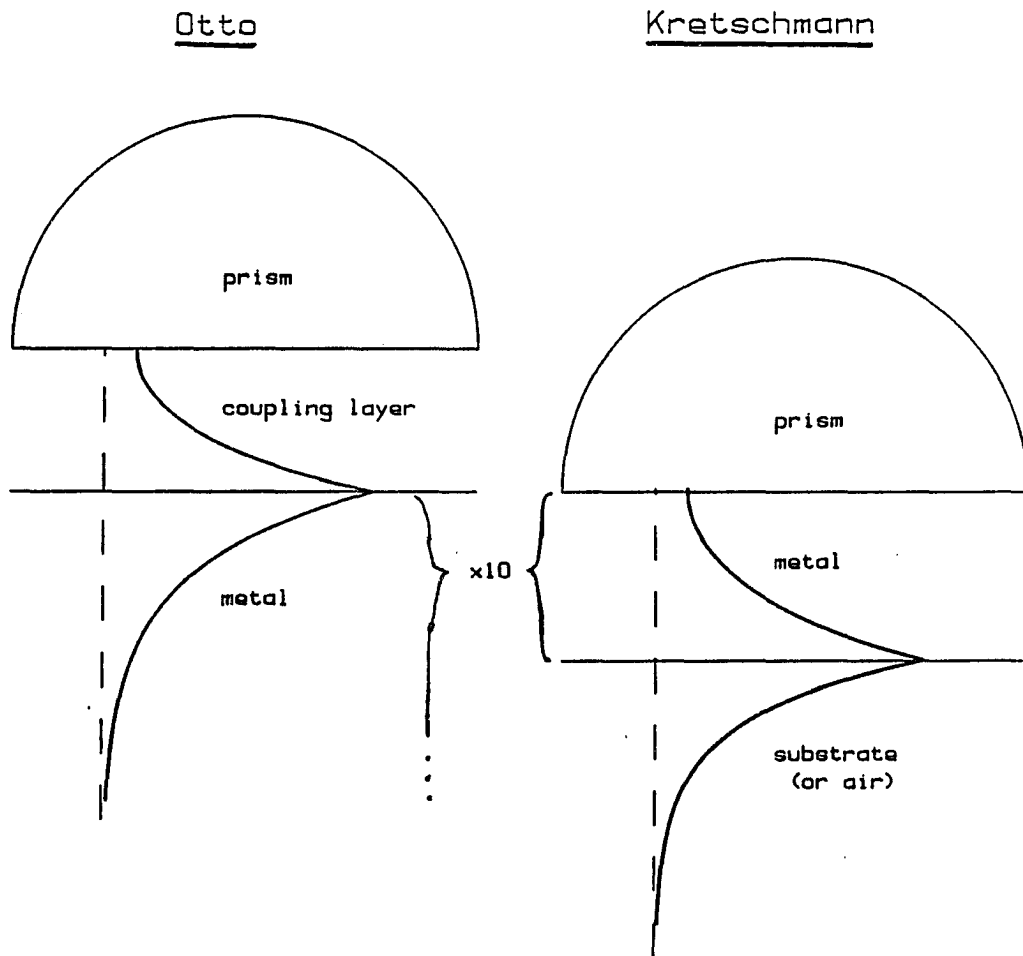


Fig. 2.7. Prism-coupling geometries for single-interface plasmon polaritons

typical excited magnetic-field (H_y) profiles are also shown; distance in metal is expanded $\times 10$.

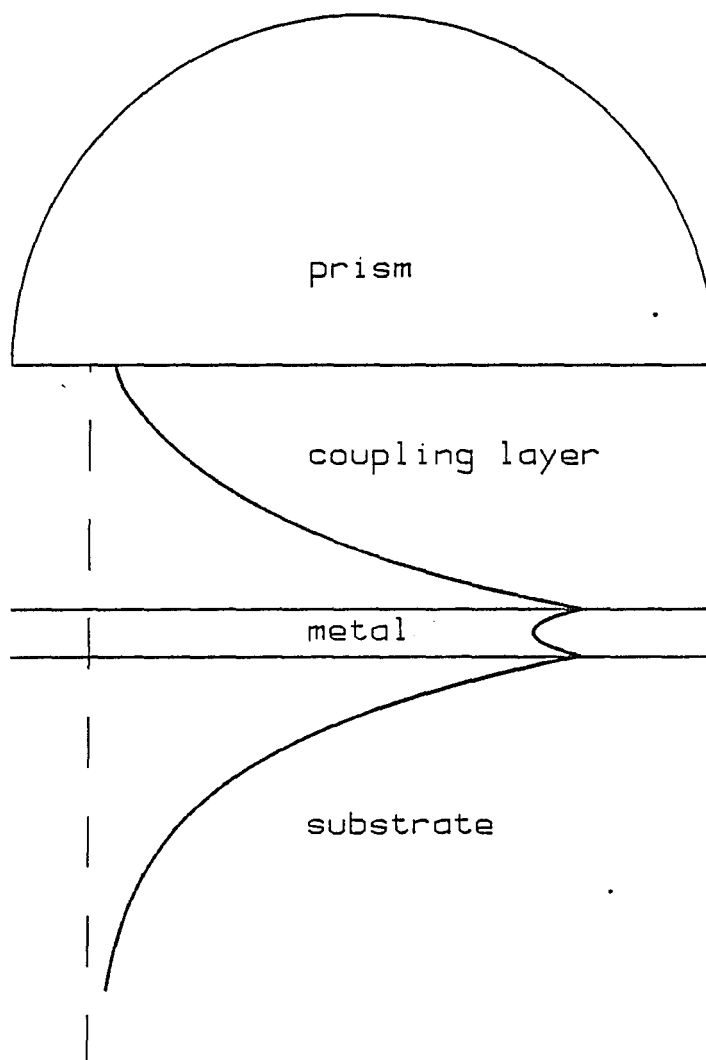


Fig. 2.8. Prism-coupling geometry for double-interface plasmon polaritons

typical excited magnetic-field (H_y) profile for long-range mode is also shown; distance in metal is expanded $\times 10$.

of reflectance associated with the excitation of a single-surface plasmon. For lossy metals, the reflectance minimum may be separated from the peak excitation of the surface plasmon by tens of degrees in angle [65]. The accurate method of determining the peak excitation of the plasmon is to calculate the angle at which the peak field is excited at the surface, or measure it using the enhancement of another process such as second harmonic generation.

An example of the discrepancy of reflectance minimum and plasmon excitation is given in Fig. 2.9, in which TM reflectance is plotted for the three prism-coupling geometries as a function of angle above the critical angle. Nickel is the surface active medium and the wavelength is 632.8 nm. The nickel thickness is 20 nm for the Kretschmann and double-interface (or long-range) geometries, the bounding media have an index of 1.5, and the coupling-layer thickness is 0.25 μm for the Otto geometry and 0.5 μm for the double-interface geometry. Also plotted is the relative, transverse magnetic-field strength at the nickel surface where the surface plasmon is excited. It is seen that for the Otto and Kretschmann geometries, the peak field excitation is separated by several degrees from the reflectance minimum, whereas for the long-range surface plasmon, the angular positions nearly coincide. This indicates that the enhancement of the Kerr magneto-optic effect in nickel, as discussed in later chapters, may not necessarily be attributed to the excitation of a surface plasmon in the single-interface geometries.

To contrast with the results for nickel, the prism-coupler reflectance and magnetic-field strength are plotted in Fig. 2.10 for silver. The silver thickness is 55 nm for the Kretschmann geometry and 20 nm for the long-range geometry, the coupling-layer thickness is 0.45 μm for the Otto geometry and 1.05 μm for the long-range geometry, and the coupling layer and substrate have an index of 1.5. Because

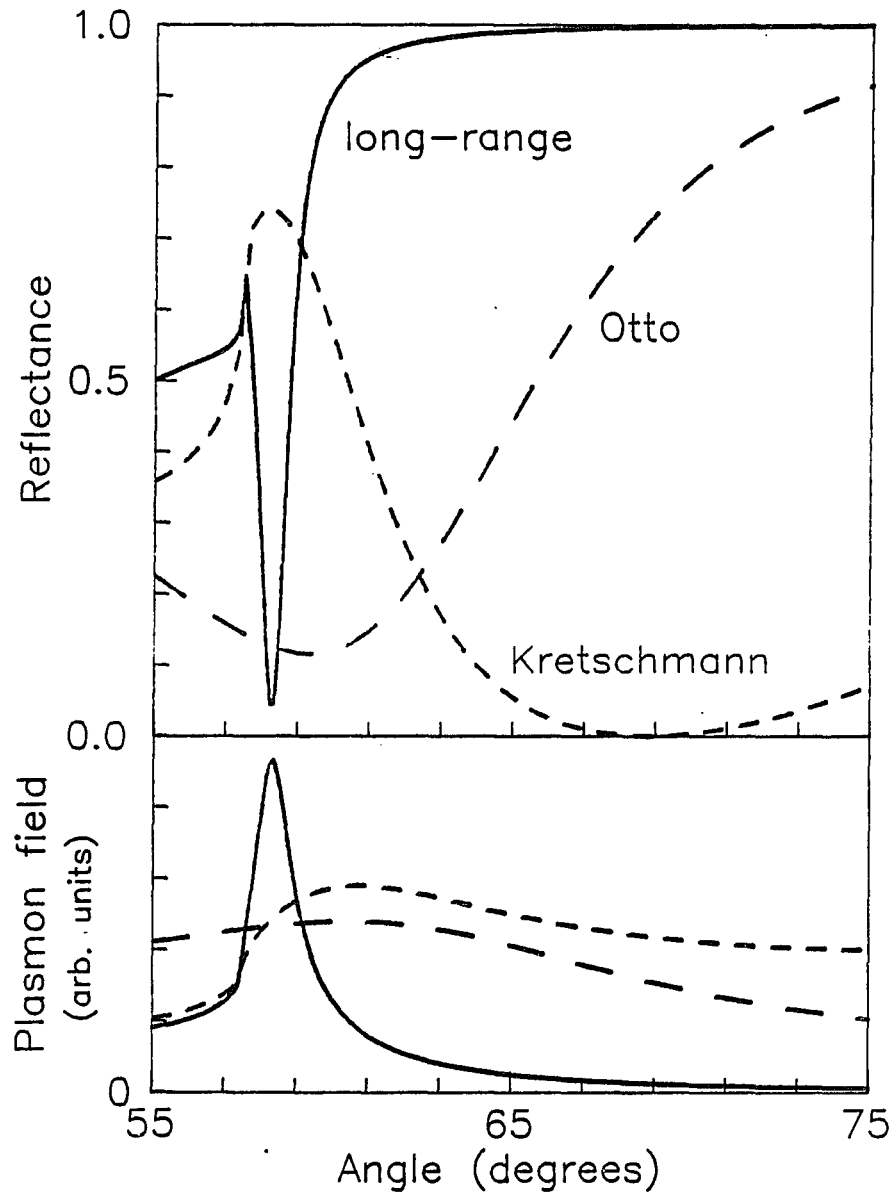


Fig. 2.9. Reflectance and plasmon field for different prism-coupling geometries -- nickel film

plasmon field is H_y , calculated at nickel interface; $\lambda_0 = 632.8$ nm, $n_0 = 1.7788$, and $n_1 = n_3 = 1.5$ (when applicable). For the Kretschmann geometry (short-dashed line), $d_1 = 0$ and $d_2 = 20$ nm; for the Otto geometry (long-dashed line), $d_1 = 0.25$ μm ; and for the long-range geometry (solid line), $d_1 = 0.5$ μm and $d_2 = 20$ nm.

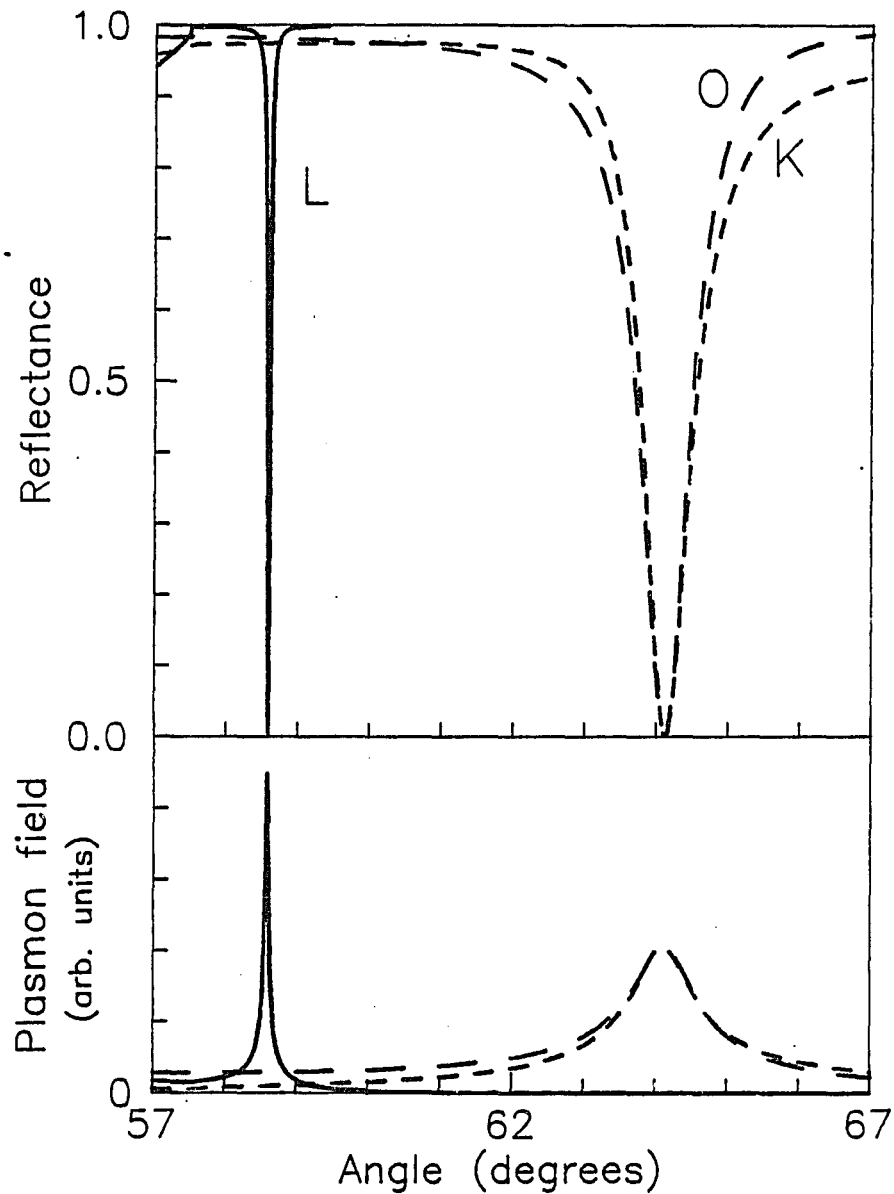


Fig. 2.10. Reflectance and plasmon field for different prism-coupling geometries -- silver film

plasmon field is H_y , calculated at silver interface; $\lambda_0 = 632.8$ nm, $n_0 = 1.7788$, and $n_1 = n_3 = 1.5$ (when applicable). For the Kretschmann (K) geometry (short-dashed line), $d_1 = 0$ and $d_2 = 55$ nm; for the Otto (O) geometry (long-dashed line), $d_1 = 0.45$ μm ; and for the long-range (L) geometry (solid line), $d_1 = 1.05$ μm and $d_2 = 20$ nm.

silver is a low-loss metal, the single-interface plasmon geometries exhibit well-defined reflectance resonances which correspond to the peak excitation of the plasmon field at the silver interface. The reflectance and magnetic-field excitation for the Otto and Kretschmann geometries are very similar, unlike the case of the lossy nickel film.

2D.2. Prism Coupling to the Long-Range Surface Plasmon Polariton

As background to the experimental study of prism coupling to the long-range surface magnetoplasmon, it is helpful to examine the properties of the prism-coupled reflectance as a function of sample parameters. Figures and discussion illustrating these properties are presented in Appendix A and Chapter 6, and only a summary will be given here. The basic features of a reflectance vs angle plot, as seen in Fig. A.4 are the coupling-layer resonances at angles less than the critical angle between the prism and substrate, the surface plasmon resonance at an angle greater than the critical angle, and the peak in reflectance occurring at the critical angle. The coupling layer resonances depend on the index and thickness of the coupling layer, the Fresnel reflectivity of the prism interface, and the reflectivity of the metal film. The critical angle depends solely on the relative refractive indices of the prism and substrate.

Of most interest to this study are the properties of the surface plasmon resonance. They parallel the properties of the bound mode, discussed in Section 2C.2, with some modifications due to the asymmetric nature of the prism coupler. Since the real and imaginary parts of the normalized propagation constant β increase with an increase in the thickness of the metal film, so too will the angle and width of the resonance minimum, as indicated by Eqs. (2.36) and (2.37). The dielectric

constant of the metal affects the resonance similarly; the resonance angle and width are larger for lossier metals, although this effect is small for the range of the dielectric constant used in Appendix A.

The presence of the prism and finite coupling layer causes the prism-coupling geometry to be a perturbation of the three-layer structure for bound double-interface modes. The reflectance resonance as a measure of the normalized propagation constant of the surface plasmon is thus affected. Increasing the coupling-layer thickness brings the resonance angle and width closer to the unperturbed properties, but makes the depth shallower and more difficult to detect. Decreasing the thickness shifts the resonance to smaller angles and increases the resonance width due to reradiation losses [53]. Below a certain coupling-layer thickness the resonance depth decreases due to over-damping by the prism. For a sufficiently thin coupling layer, the reflectance behaves like that of the Kretschmann geometry. The optimum thickness for experimental study is usually an intermediate one where a deep resonance is observed. A complete modelling of the reflectance properties, as in Appendix A, enables an accurate measurement of the sample parameters and avoids the approximation in Eqs. (2.36) and (2.37).

Because the prism-coupled surface plasmon is a leaky wave, bound only on the substrate side, the effect of the substrate and coupling layer refractive indices on the reflectance resonance will be dissimilar. If the coupling layer index is decreased relative to the substrate index (or equivalently the substrate index is increased relative to the coupling layer index), the resonance will shift in the direction of the varying index and eventually be cutoff by the lower index. This behavior is in accord with that of the bound mode discussed in Section 2C.2. However, if the coupling layer index is increased relative to the substrate index (or its equivalent), no

cutoff occurs. Instead, the excited intensity changes from the relatively symmetric distribution which peaks at the two metal interfaces to a single-surface mode distribution which peaks at the metal-substrate interface. The single-surface mode couples to a leaky waveguide mode in the coupling layer, yielding a hybrid mode. The reflectance resonance is shifted by the change in index and broadened by the larger loss of the single-surface plasmon and the waveguide leakage. Although the resonance is not cut off, it is no longer associated with a coupled, long-range surface plasmon. This topic is discussed further in the next chapter in regard to nonlinear bounding media.

CHAPTER 3

THEORY OF PRISM COUPLING TO NONLINEAR SURFACE PLASMON POLARITONS

The term "nonlinear" as used in this study applies to materials whose dielectric constants depend on the square of the optical electric-field strength, i.e. Kerr-type nonlinear materials. If one or more of the layers constituting a planar optical waveguide is nonlinear, the propagation constants of the guided wave depend on the power carried by the wave [66, 67], and the reflectance and dispersion equations derived in the previous chapter must be modified to describe the waveguiding properties. Unique properties and device concepts are possible due to the nonlinearity. Examples are an optical transistor or transphasor, power limiting, power threshold discrimination, and optical bistability. The optically bistable device has been the topic of most interest to researchers in nonlinear optics in recent years, owing to its promise as a switching element for all-optical signal processing. Consequently, although the theme of this chapter is prism coupling to the nonlinear long-range surface plasmon, the properties of optical bistability in this context are a focal point. The other applications of prism coupling to nonlinear waveguide modes are extensions of the theory.

3A. Introduction

Optical bistability requires a nonlinearity and feedback. In the case of a guided wave, feedback may affect the guided wave itself or may occur in the efficiency of coupling to the wave. In the first feedback mechanism, a power-

dependent phase shift is produced by propagation along the guide. Reflective feedback is provided, for example, by a grating etched perpendicular to the propagation direction. The resulting, nonlinear Fabry-Perot resonances cause bistability in the reflected and transmitted, guided power [68]. The early theoretical research on nonlinear guided waves analyzed the phase shifts necessary for this method, as produced by bound surface waves [66, 69, 70].

In experimental situations, the optical power must be coupled into the waveguide. This is the basis for a second feedback mechanism for achieving bistability. It has been shown that the light reflected from a prism or grating coupler should exhibit bistability when one of the waveguide media is nonlinear [71-75]. Since the propagation wavevector of a nonlinear guided wave is power-dependent, the coupling resonance position varies with the coupled power. As the power changes, the coupler tunes in or out of resonance and the coupling efficiency changes, giving rise to feedback and a bistable region.

As mentioned previously, waveguide coupling is usually accomplished by a prism, a grating, or by endfire coupling. Endfire coupling involves matching the field distribution of a guided wave at the edge of the waveguide with the field distribution of a laser beam or a mode from another waveguide, such that the overlap integral is non-zero. Although the propagation wavevector is power-dependent in a nonlinear waveguide, significant changes in the field distribution occur only if the optically induced refractive index change is comparable to the low-intensity difference between the index of one of the guiding media and the effective index of the waveguide mode [70]. Unless this is the case, the endfire coupling efficiency should remain relatively constant with incident power.

Grating and prism couplers operate by matching the component of the incident wavevector parallel to the surface with the wavevector of the guided mode. Both exhibit an angular resonance in coupling efficiency and thus produce feedback in the coupling mechanism. The grating, by nature of its periodic structure, also produces distributed feedback as the guided wave propagates. The prism coupler involves only the feedback of coupling efficiency so that it allows a separate analysis of the two feedback methods.

Prism coupling into dielectric waveguides [71] and single-interface plasmon [72-74] geometries involving nonlinear media has been studied theoretically. The power calculated to observe bistable switching with a prism-coupler was at least an order of magnitude less than that calculated for light incident on an equivalent, single nonlinear interface [76]. Early prism-coupling calculations, however, were based on approximate theories using the linear Fresnel relations and an intensity-dependent index of refraction. They either assumed a fixed field-enhancement in the guide, regardless of intensity [71], or a uniform index of refraction in the nonlinear medium [72, 74], or they used iterative, numerical techniques to assure self-consistency of the field distribution [73]. (Note that the case of a nonlinear prism [74], although it exhibits bistability, is not a nonlinear waveguide in the definition used here; the incident wavevector is intensity-dependent, not the guided wavevector.

For TE-polarized waves, exact analytic expressions have been developed for the reflectance of a plane wave incident upon a nonlinear medium [77-78]. Exact analysis has also been made of the dispersion relations and guided power of uncoupled, bound waves at nonlinear interfaces [79, 80], and in thin-film waveguides

involving nonlinear media [81-84, 70]. The analysis has been used to investigate bistability in an attenuated total reflection (ATR) waveguide-coupling geometry [86].

For TM-polarized waves, exact solutions for uncoupled waves have been derived if the dielectric constant is assumed to be linearly dependent on the square of the longitudinal electric-field component, E_x , only [87-91]. However, many waveguide geometries sustain modes that are near cutoff, such as the surface plasmon. Having properties approaching those of the plane wave, E_x is small compared to the transverse electric-field component, E_z . It was shown that a more physically reasonable uniaxial approximation assumes a nonlinearity which is dependent upon the square of the transverse electric-field component [92-94]. The approximation leads to TM wave solutions that behave similarly to those found for the TE case, since it is equivalent to defining the nonlinear index in terms of the magnetic field. The wave equation for a TM nonlinear surface polariton at a single interface has been solved exactly in quadratures for an arbitrary dependence of the dielectric function on intensity [95].

The theme of this chapter is an ATR prism-coupling geometry used to excite TM guided waves in a structure whose substrate has an intensity-dependent refractive index. Assuming an infinite, incident plane wave and a dielectric constant dependent on the square of the transverse electric-field component, the nonlinear wave equation is derived and solved to calculate the fields in the layered structure. Optical bistability in the reflected intensity is predicted by an expression for the parametric dependence of reflected and incident intensity. Approximations made in the derivation are discussed. The regime in which the equations apply is analyzed and compared to homogeneous index theories using the linear Fresnel relations or

first-order perturbation theory. Bistable switching intensities for the long-range surface plasmon polariton are compared theoretically to those of the single-interface plasmon. The switching behavior of a long-range mode which is very near cutoff is shown to depend on the sign of the nonlinearity, and power-limiting for a positive nonlinear substrate is given as an example. The differences between a nonlinear substrate and a nonlinear coupling layer are estimated using perturbation theory and a homogeneous index theory.

Much research has been published on this "hot" topic since the author developed the results discussed here [96]. During the author's preparation of Ref. 96, a conference poster paper was presented which used essentially the same theoretical framework to study prism coupling to nonlinear surface plasmons [97]. Preliminary results were given for bistability with the long-range surface plasmon polariton using CS_2 as the nonlinearity at a wavelength of $1.06 \mu\text{m}$. More recently, the same authors applied the exact analysis of Leung [95] to the problem, and they show that the exact analysis produces results for the long-range mode that are virtually identical to the approximate theory used in their previous study and this work [98]. A concern that has been raised in regard to the infinite, incident plane-wave approximation is that it does not accurately portray experimental reality. Some unpublished sources predict that no hysteresis will occur in the reflected intensity with a Gaussian incident beam. However, bistability has been calculated for the case of a square-wave input to a prism-coupled, TE waveguide with a nonlinear substrate [99]. The analysis indicates switching at the same intensities as those indicated by the plane-wave treatment, but with a lower reflectance contrast. Different parts of the beam exhibit different reflectance contrasts, but all parts switch at the same intensities. These results imply that the theory presented here is

valid for estimating switching intensities, although possibly not for estimating absolute reflectances, which depend on the width of the incident beam relative to the propagation length of the surface wave. Further discussion is presented in Section 3C.1.

3B. Prism Coupling of an Infinite Plane Wave to TM-polarized Nonlinear Guided Waves

The multilayer structure introduced in Chapter 2, Fig. 2.1, is again considered, and Eqs. (2.1) - (2.5) are applicable. In this chapter, however, the dielectric tensor of a nonlinear medium is diagonal but anisotropic, with elements ϵ_x , ϵ_y , and ϵ_z . Equations (2.6) - (2.8) are then more generally written as

$$E_x = - \frac{i}{\omega \epsilon_0 \epsilon_x} \frac{\partial H_y}{\partial z} \quad (3.1)$$

$$E_z = \frac{i}{\omega \epsilon_0 \epsilon_z} \frac{\partial H_y}{\partial x} \quad (3.2)$$

$$H_y = \frac{i}{\omega \mu_0} \left[\frac{\partial E_z}{\partial x} - \frac{\partial E_x}{\partial z} \right] \quad (3.3)$$

The uniaxial approximation is made such that the optical nonlinearity depends only on the transverse electric field [92]:

$$\epsilon_z = \epsilon_{z0} + \alpha E_z^2 \quad (3.4)$$

where $\alpha = c \epsilon_0 \epsilon_z n_{2,I}$, and $n_{2,I}$ is the nonlinear index with respect to intensity. The linear components of the dielectric constants are assumed equal for simplicity:

$$\epsilon_x = \epsilon_y = \epsilon_{z0} \equiv \epsilon. \quad (3.5)$$

For the steady state considered here, there is no variation of intensity in the propagation direction, so that the x-dependence of the electromagnetic field is given by Eq. (2.10) as

$$A(x) = \exp(ik_0\beta x). \quad (3.6)$$

Eliminating E_x and E_z from the above equations, the wave equation in terms of H_y can be derived. Using Eqs. (3.2) and (3.4),

$$E_z(z)[\epsilon + \alpha E_z^2(z)] = -\frac{\beta}{c\epsilon_0} H_y(z) \quad (3.7a)$$

$$\begin{aligned} E_z(z) &= -\frac{1}{\epsilon} \left[\frac{\beta}{c\epsilon_0} H_y(z) + \alpha E_z^3(z) \right] \\ &= -\frac{\beta}{c\epsilon_0\epsilon} H_y(z) \left[1 - \frac{\beta^2\alpha}{c^2\epsilon_0^2\epsilon_z^3(z)} H_y^2(z) \right]. \end{aligned} \quad (3.7b)$$

Applying Eqs. (3.1), (3.3), and (3.7), and simplifying, one obtains the wave equation,

$$\frac{\partial^2 H_y(z)}{\partial z^2} + k_0^2 \kappa^2 H_y(z) + k_0^2 \alpha' H_y^3(z) = 0, \quad (3.8)$$

where $\kappa^2 = \epsilon - \beta^2$ and $\alpha' = \alpha\beta^4 [c^2\epsilon_0^2\epsilon_z^3]^{-1}$. Note that Eq. (3.8) has the form of the linear wave Equation (2.9) with the addition of a third term, which contains the factor $\epsilon_z^3 = (\epsilon_3 + \Delta\epsilon_z)^3$, where $\Delta\epsilon_z$ is the intensity-dependent departure of the

dielectric constant from its low-intensity value. In real materials and experimental geometries there is a limit on $\Delta\epsilon_z$, such that the approximation $\epsilon_z = \epsilon_{z0} \equiv \epsilon$ can be made in the third term to enable the analytic solution of the equation. This approximation is discussed in Section 3C.3.

The solutions to the TM nonlinear wave equation (the same form as the solutions to the TE equation) are well-known [77-78]:

$$H_y(z) = \left| \frac{2}{\alpha'_j} \right|^{1/2} \frac{-i\kappa_j}{\cosh[-ik_0\kappa_j(z-z_j-\xi_j)]} \quad \text{for } \alpha_j > 0 \quad (3.9a)$$

$$H_y(z) = \left| \frac{2}{\alpha'_j} \right|^{1/2} \frac{-i\kappa_j}{\sinh[-ik_0\kappa_j(z-z_j-\xi_j)]} \quad \text{for } \alpha_j < 0 \quad (3.9b)$$

in the region $z > 0$, where z_j is the low- z interface of the nonlinear layer j . ξ_j is the offset of the center of field symmetry from the boundary. At $z = z_j + \xi_j$ the field has a maximum if $\alpha_j > 0$ (see Fig. 3.10) and a zero if $\alpha_j < 0$, as long as $z_j + \xi_j$ lies within the j^{th} layer. The field decays exponentially to zero at large $|z - z_j - \xi_j|$, as in a linear waveguiding medium. (Note that the solutions are usually expressed in terms of the transverse decay constant, q , where $q^2 = \beta^2 - \epsilon^2$; this is equivalent to the use of $-i\kappa$, which is consistent with the rest of this work.)

The boundary conditions are now applied to the multilayer stack of Fig. 2.1. Each linear material layer supports a magnetic field of the form of Eq. (2.10),

$$H_{y_j}(z) = H_{y_j}^+(z) \exp[ik_0\kappa_j(z-z_j)] + H_{y_j}^-(z) \exp[-ik_0\kappa_j(z-z_{j+1})], \quad (3.10)$$

Note that once the normalized propagation constant, β , is fixed, for each linear layer of finite thickness there are two parameters to be determined, $H_{y_j}^+$ and $H_{y_j}^-$. For any nonlinear material there is only one parameter, the peak field offset ξ_j . In prism coupling, the top, semi-infinite layer has both the incident and reflected fields as parameters, while the bottom, semi-infinite layer has only the transmitted field. The total number of field parameters for a prism-coupling stack of n layers is computed as follows: $2n-1$, if all layers are linear; minus m for m nonlinear layers of finite thickness; plus one for the normalized propagation constant, β , for a total of $2n-m$. Since there are $2n-2$ boundary conditions, the number of parameters that can be chosen freely is $2-m$. For prism coupling to nonlinear layers, one wishes to retain both β and the incident intensity as experimentally chosen parameters. Hence, nonlinear layers may not have finite thickness to allow an analytic solution, so that only the substrate may be nonlinear. The case studied here is a nonlinear substrate, layer 3, and linear layers 0, 1, and 2, in the double-interface coupling geometry of Fig. 2.8. (In the analysis of bound, uncoupled waves, a layer of finite thickness may be nonlinear; however, β and the guided-wave power are then interdependent [88, 91].)

The nonlinear substrate, for the case of a positive nonlinearity ($\alpha_3 > 0$), will support the fields

$$H_{y_3}(z) = H_{y_3}^+(z) = \left| \frac{2}{\alpha_3} \right|^{1/2} \frac{-ik_3}{\cosh[-ik_0\kappa_3(z-z_3-\xi_3)]} \quad (3.11a)$$

$$E_{x_3}(z) = \frac{\kappa_3}{c\epsilon_0 n_3^2} \tanh[-ik_0\kappa_3(z-z_3-\xi_3)] H_{y_3}(z) \quad (3.11b)$$

$$E_{z3}(z) = -\frac{\beta}{c\epsilon_0 n_3^2} \left[1 - \frac{\alpha_3'}{\beta^2} H_{y3}^2(z) \right] H_{y3}(z) . \quad (3.11c)$$

The relative optical impedance for linear media ($j=0,1,2$) is given by Eq. (2.15) as

$$Z_j \equiv \frac{c\epsilon_0 E_{xj}^+}{H_{yj}^+} = \frac{\kappa_j}{n_j^2} \quad (3.12)$$

For nonlinear medium 3, an equivalent nonlinear impedance can be defined as

$$Z_3 \equiv \frac{c\epsilon_0 E_{xj}^+}{H_{yj}^+} = \frac{\kappa_3 \tanh(ik_0 \kappa_3 \zeta_3)}{n_3^2} . \quad (3.13)$$

After this definition, the application of boundary conditions and the derivation of reflection coefficients is identical to the linear case presented in Chapter 2, such that Eqs. (2.16) - (2.28) are applicable. The one exception is that the electric-field coefficients for the linear media are given by Eq. (2.25), while the electric fields for the nonlinear substrate are given by Eq. (3.11) above. The case of a nonlinear material with a negative nonlinear index ($\alpha_3 < 0$) is handled by replacing the hyperbolic functions "cosh" with "sinh," and "tanh" with "coth" in all equations. After fixing the parallel component, $k_0\beta$, of the incident wavevector, a range of incident intensities and corresponding reflected intensities are calculated parametrically by varying the peak field offset, ζ_3 . The incident intensity is calculated in air, assuming normal incidence on the prism and neglecting reflection losses at the prism face, and is given by Eq. (2.26).

3C. Analysis of Approximations in Nonlinear Wave Theory

Three approximations have been made in the solution to the TM nonlinear wave equation. To define the regions in which the solution is valid, this section discusses the limits of each approximation.

3C.1. Infinite, Incident Plane-Wave Approximation

The first approximation is the modelling of the incident wave as an infinite plane wave, which continuously supplies a fixed power to the waveguide. Two consequences of this approximation are apparent. In the case of a finite input beam, the coupling properties change along the length of the beam as power is coupled into the nonlinear medium [100]. Therefore, the reflectance varies across the beam length. However, as already mentioned, recent calculations indicate that a square-wave incident beam switches as a whole at discrete intensities [99]. The finiteness of the beam was shown to affect only the high-to-low contrast of the two stable reflectances. The leading parts of the beam display a larger reflectance contrast than the trailing parts because guided power has built up in the waveguide. Narrower beams produced smaller contrast than wide beams, and when the beam projection on the base of the prism was 1.7 mm for a waveguide mode with a propagation length of 1.76 mm, bistability was essentially eliminated. The conclusion is that the beam projection must be greater than the propagation length of the mode for the present results to apply, which is the same condition stated for the linear reflectance results in Chapter 2. In all examples given in this chapter, the surface plasmon polariton propagation length is less than 1 cm, implying that with an incident beam of reasonable width, experimental results should agree at least qualitatively with the nonlinear model discussed here.

Because the incident wave is assumed cw, the waveguide has a "memory" of the field distribution and associated dielectric function. However, in actual experiments a pulsed laser source is often used due to the high powers necessary to induce a significant change in the local dielectric constant. If the relaxation time of the nonlinearity is smaller than the pulse repetition time, the system is not expected to demonstrate optical switching [73]. The relevance of these consequences merits further investigation.

3C.2. Small Change in Dielectric Constant

Another approximation made in the theory is that the change, $\Delta\epsilon_z$, in the dielectric function, ϵ_z , is small enough that ϵ_z can be replaced by its linear value ϵ_3 in the third term of the nonlinear wave equation, Eq. (3.8). ϵ_z enters the equation as ϵ_z^3 which, when expanded as $\epsilon_z^3 = \epsilon_3^3 + 3\epsilon_3^2\Delta\epsilon_z + \dots$, requires that $3\Delta\epsilon_z/\epsilon_3 \ll 1$ in order to justify the approximation. In most materials this will be satisfied by saturation effects, which limit $\Delta\epsilon$ to under 0.1. In general, from Eq. (3.7),

$$\begin{aligned} \frac{3\Delta\epsilon_z}{\epsilon_3} &= \frac{3\alpha_3}{\epsilon_3} E_{z3}^2(z) \\ &= \frac{-6\kappa_3^2}{\beta^2 \cosh^2[-ik_0\kappa_3(z-z_3-\zeta_3)]} \left[1 + \frac{2\kappa_3^2}{\beta^2 \cosh^2[-ik_0\kappa_3(z-z_3-\zeta_3)]} \right] \end{aligned} \quad (3.14)$$

for $\alpha_3 > 0$. For experimental systems of interest, the waveguide mode is relatively close to cutoff, in which case $-\kappa_3^2 \equiv \beta^2 - n_3^2 < \beta^2/2$. Then $3\Delta\epsilon_z/\epsilon_3 < -6\kappa_3^2/\beta^2$ for all z and ζ_3 (remember $\kappa_3^2 < 0$). Therefore, a sufficient condition for validity of this third approximation is that

$$\frac{-\kappa_3^2}{\beta^2} \ll 0.16 . \quad (3.15)$$

In the limit of a thick metal film on glass, for good conductors such as gold or silver, $-\kappa_3^2/\beta^2 \cong 0.05$ for the single-interface plasmon modes at a wavelength of $1 \mu\text{m}$. At longer wavelengths and for thinner films, $-\kappa_3^2/\beta^2$ decreases substantially, since the mode approaches cutoff. Hence, for a positive nonlinearity, the approximation of a small change in dielectric constant is valid for all long-range surface plasmon geometries, as well as dielectric waveguides near cutoff.

For a negative nonlinearity, with the appropriate changes made to the equations, the term $3\Delta\epsilon_z/\epsilon_3$ diverges for small $z-z_3-\zeta_3$, but exponentially decays to zero at large, positive values of z and $-\zeta_3$. $-\zeta_3$ is usually large in the region of prism coupling to long-range surface plasmons, so that the approximation is valid.

3C.3. Uniaxial Approximation

The uniaxial approximation assumes that the longitudinal electric-field component, E_x , is small compared to the transverse component, E_z . Thus the nonlinearity can be expressed as dependent only on the transverse electric field, as in Eq. (3.4). The imposed condition is

$$\frac{|E_x(z)|^2}{|E_z(z)|^2} \ll 1 . \quad (3.16)$$

For a positive nonlinearity,

$$\frac{|E_{X_3}(z)|^2}{|E_{Z_3}(z)|^2} = \frac{|\kappa_3 \tanh[-ik_0 \kappa_3 (z - z_3 - \xi_3)] H_{Y_3}(z)|^2}{\left| \beta \left[1 + \frac{2\kappa_3^2}{\beta^2 \cosh^2[-ik_0 \kappa_3 (z - z_3 - \xi_3)]} \right] H_{Y_3}(z) \right|^2} \quad (3.17)$$

As shown above, the approximation of a small change in dielectric constant imposes the strictest sufficient condition: $-\kappa_3^2/\beta^2 \ll 0.16$. Under this condition,

$$\frac{|E_{X_3}(z)|^2}{|E_{Z_3}(z)|^2} < \frac{-\kappa_3^2}{\beta^2} \ll 1, \quad (3.18)$$

such that the condition imposed by the uniaxial approximation is met automatically. For a negative nonlinearity, with the hyperbolic functions appropriately exchanged in Eq. (3.17), the parameter $|E_{X_3}|^2/|E_{Z_3}|^2$ has a singularity at a value of $z - z_3 - \xi_3$ near unity. However, it decreases exponentially to $-\kappa_3^2/\beta^2$ at large, positive values of z and $-\xi_3$. Individual cases must be considered separately in order to insure the validity of the uniaxial approximation for a negative nonlinearity.

3D. Alternative Models

Other approximate models have been used to calculate the behavior of nonlinear guided waves. The simplest model is to assume an intensity-dependent change in the refractive index of the nonlinear medium, calculate the field strengths at the nonlinear interface necessary to produce the change, and then work back through the layers using the linear Fresnel equations to calculate the input intensity [71, 72]. This model does not account for any variation in intensity across the

nonlinear medium, particularly the evanescent decay away from the interface, which is the distinguishing characteristic of guided waves. However, it can be helpful in explaining some of the qualitative features of nonlinear waves and optical switching.

First-order perturbation theory has been used to calculate changes in the propagation wavevector of a nonlinear guided wave [66, 69, 70]. Applicable to any field distribution, it is valid if the distribution is not significantly altered by the nonlinear change in index. Since this study addresses the case of a fixed incident wavevector, perturbation theory could be used to calculate the change in index of the nonlinear medium, which effectively changes the wavevector of the guided wave. The index change is given by [69, 70]

$$\Delta n_j = \frac{n_j}{\beta} \Delta\beta = \frac{\pi c^2 \epsilon_0^2 n_j^2 n_{2,I}}{4P_j} \int_{z_j}^{z_{j+1}} dz \left[\frac{2}{3} [|E_{xj}(z)|^2 + |E_{zj}(z)|^2]^2 + \frac{1}{3} |E_{xj}^2(z) + E_{zj}^2(z)|^2 \right], \quad (3.19)$$

where P_j is the guided-wave power in the nonlinear medium and $n_{2,I}$ is the nonlinear index. For a purely evanescent field in a nonlinear substrate, the induced index change is exactly one-half of that induced by a uniform field with the same amplitude at the interface. Consequently, the features calculated from perturbation theory tend to occur at twice the intensity calculated from the simple homogeneous index theory.

Like the simple homogeneous index theory, perturbation theory assumes a uniform index in the nonlinear medium. It has been shown that perturbation theory is valid for changes in index that are small compared to the difference between the normalized propagation constant, β , and the substrate index, n_3 [70]. If β is near n_3 (near cutoff), as the refractive index of the substrate increases with intensity, the

transverse field decay constant, $-i\kappa_3 \equiv (\beta^2 - n_3^2)^{1/2}$, decreases rapidly. In this case, uniform index models indicate that the evanescent fields tend toward radiation into the substrate, while nonlinear wave theory accounts for changes in field distribution and a non-uniform index, which tend to maintain waveguiding. Note that while perturbation theory is applicable to changes in the propagation constant but not in the field distribution, the nonlinear wave theory is applicable to both changes. In fact, Eq. (3.15) indicates that for positive nonlinearities, the approximations made in the nonlinear wave theory are most easily validated by guided waves close to cutoff, where the field distribution changes most with a variation in index.

Another approach used in analyzing TM nonlinear guided waves has been a solution of the nonlinear wave equation assuming a nonlinearity dependent on the square of the longitudinal electric-field component, E_x [87-91]. As mentioned previously, this approach does not produce physically reasonable results for modes near cutoff, such as surface plasmon polaritons [92]. Therefore, it will not be considered here.

3E. Optical Bistability with Prism Coupling to Nonlinear Surface Plasmon Polaritons

The theory developed in Section 3B can be used to analyze prism coupling to single-interface and long-range, nonlinear surface plasmon polaritons. Regardless of the theoretical approach, the nonlinear behavior can be described qualitatively in terms of the linear behavior of the modal dispersion equation and prism-coupling properties discussed in Chapter 2 and Appendix A. At low intensities, the prism-coupled reflectance exhibits a resonance with angle corresponding to the resonant excitation of an optical field decaying away from the metal interfaces. If one of the materials surrounding the metal is nonlinear, a change in the strength of the surface

plasmon field changes the index of the bounding material. This shifts the propagation constant of the mode and the resonance angle of the prism-coupler, as explained in Sections 2C.2 and 2D.2 and Appendix A.

Now suppose that the light in the prism is fixed at an incident angle off of resonance, specifically at the angle $\theta_{\min} + \Delta\theta$, where $\Delta\theta > 0$ for a positive nonlinearity, as in Fig. 3.1. If the incident intensity is increased, the increasing internal fields shift the surface plasmon toward resonance with the incident light. The internal fields are increased even more by the positive feedback mechanism of resonant excitation. Because of the nonlinearity and feedback, the plasmon is swept through resonance at a certain incident intensity, and the reflectance switches to a lower value on the opposite side of the resonance curve ("switch-down"). A further increase in the incident intensity forces the plasmon further from resonance, to higher reflectance. Subsequently, if the intensity is decreased, the plasmon will shift back into resonance and remain resonant to a lower incident intensity than the switch-down intensity, due to the resonant field enhancement. "switch-up" occurs when the incident intensity is too low to sustain the internal fields necessary to hold the plasmon in resonance. The prism-coupling geometry exhibits optical bistability, having two possible reflected intensities for the same incident intensity, depending on the history of the incident intensity. A theoretical example of this behavior is shown in Fig. 3.2 for a prism-coupled, long-range surface plasmon in silver bounded by a substrate of carbon disulfide (CS_2) at a wavelength of $1.06 \mu\text{m}$. The calculation was carried out using the nonlinear wave theory of Section 3B; the dashed line traces an unstable region of the solution, and the vertical lines with arrows have been added to indicate the switching which would occur in an actual experiment.

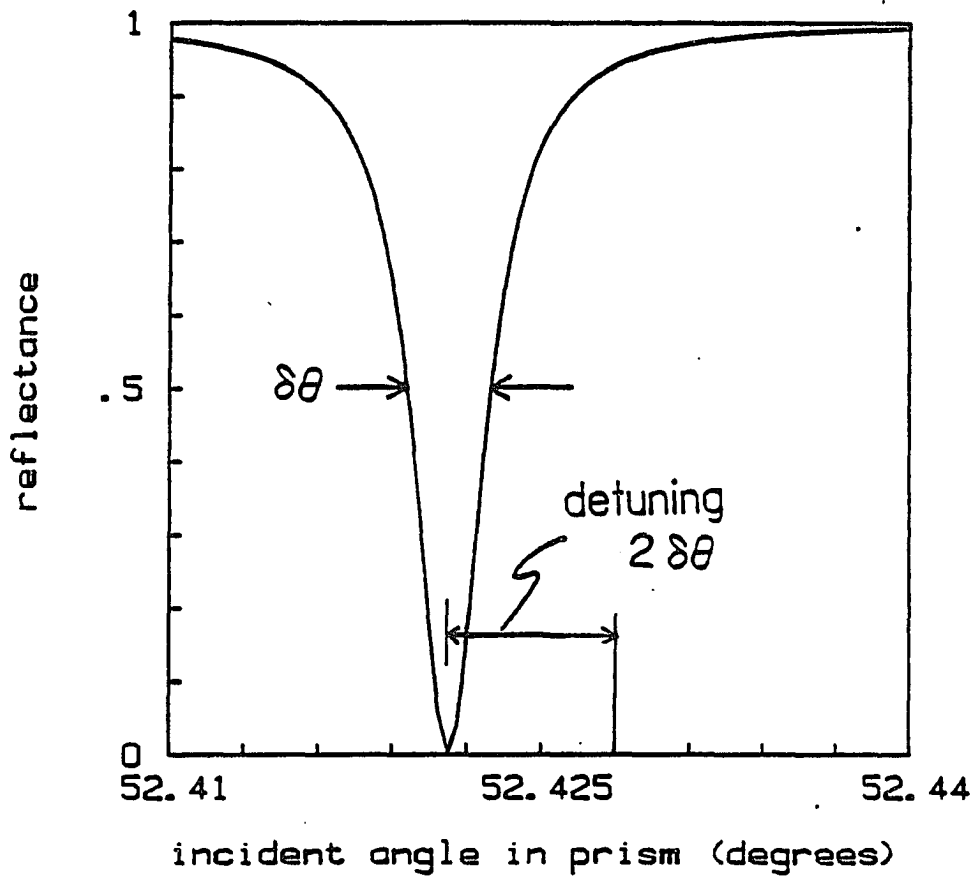


Fig. 3.1. Resonance detuning for optical bistability

detuning shown is for a positive nonlinearity; detuning is $-2\delta\theta$ for a negative nonlinearity.

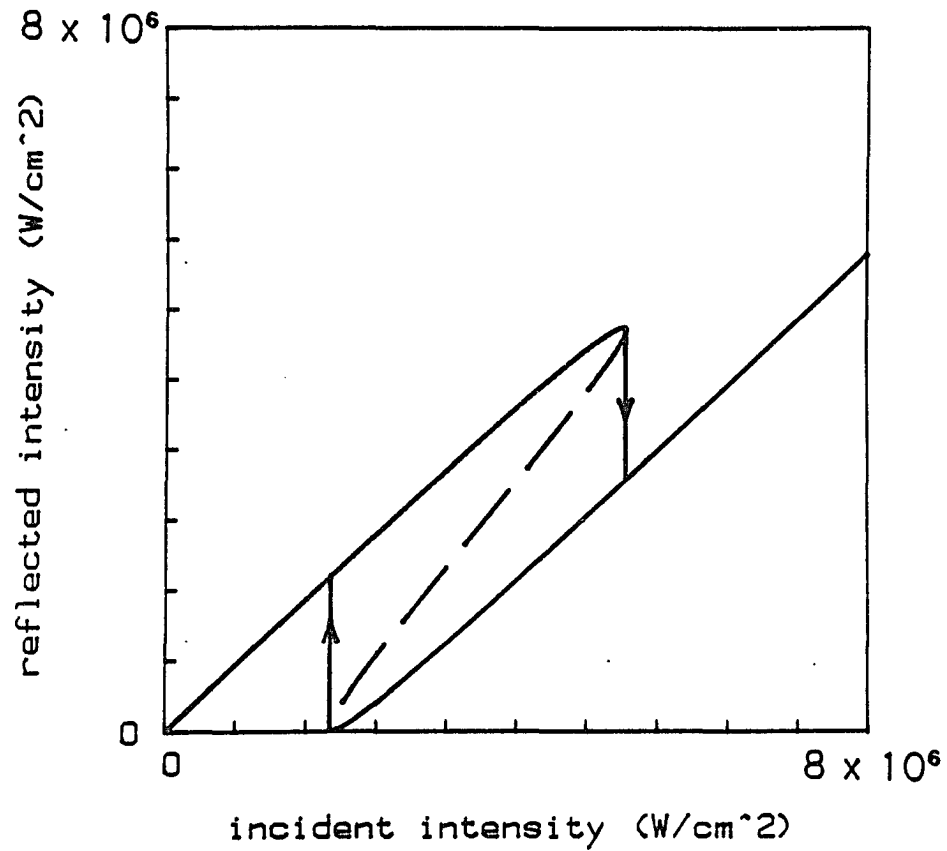


Fig. 3.2. Optical bistability with prism-coupled, nonlinear long-range surface plasmon

theoretical curve for 20-nm silver film ($\epsilon_2 = -57.8 + i0.6$) with CS₂ nonlinearity in the substrate -- $n_3 = 1.5 + (3 \times 10^{-18} \text{ cm}^2/\text{W})I$, at 1.06 μm . Dashed curve is an unstable solution. $n_1 = 1.5$, $d_1 = 3.8 \mu\text{m}$ and $d_2 = 20 \text{ nm}$.

Different theoretical approaches yield different switching intensities, and in some cases different shapes of the bistable reflectance curves. These are illustrated in the sections that follow. For comparison purposes, the angular detuning, $\Delta\theta$, is standardized to a value of two times the full-width at half-depth of the reflectance resonance relative to unity ($2\delta\theta$, see Fig. 3.1), except where noted. This produces hysteresis curves which are similar in shape for different geometries and materials. When quantified, the angular detuning is that measured in the prism, and for the small detunings considered here, it is equivalent to a detuning in β' of twice the resonance width.

Two parameters determine the incident intensity necessary to observe bistable switching -- the intensity enhancement due to excitation of the surface plasmon polariton, and the angular detuning, which is directly proportional to the angular resonance width. These parameters of the prism-coupled surface mode are related directly to parameters of the bound surface mode, such that relative switching intensities can be predicted before performing the actual calculations.

Considering the prism-coupled surface plasmon as a lossy resonator, the integrated intensity (stored energy) in the resonator is proportional to the input intensity divided by the resonator loss, that is

$$\int_0^{\infty} I(z) dz \sim \frac{I_{in}}{\beta''}, \quad (3.20)$$

where β'' is the normalized decay constant of the surface plasmon. Since most of the power is carried in the evanescent wings of the mode,

$$\begin{aligned}
\int_0^{\infty} I(z) dz &\cong \int_0^{z_2} I_{X_1}(z_2) \exp[-ik_0\kappa_1(z-z_2)] dz + \int_{z_3}^{\infty} I_{X_3}(z_3) \exp[ik_0\kappa_3(z-z_3)] dz \\
&\cong \frac{1}{k_0} \left[\frac{I_{X_1}(z_2)}{\kappa_1''} + \frac{I_{X_3}(z_3)}{\kappa_3''} \right], \tag{3.21}
\end{aligned}$$

for the long-range surface plasmon. This assumes small prism-loading, such that $\exp(-k_0\kappa_1''d_1) \cong 0$. Then the average intensity enhancement at the metal interfaces due to excitation of a surface plasmon polariton is related to the normalized propagation constants of the mode by the relationship

$$\frac{I_{X_1} + I_{X_3}}{2I_{in}} \sim \frac{\kappa_3''}{2\beta''}, \tag{3.22}$$

where $I_{X_1} \equiv I_{X_1}(z_2)$ and $I_{X_3} \equiv I_{X_3}(z_3)$ are the intensities at the two metal interfaces, and it is assumed that $\kappa_1'' \cong \kappa_3''$.

Figure 3.3 plots the calculated ratio of absorptive decay constants, κ_3''/β'' , for the single-interface plasmon polariton and as a function of silver film thickness for the long-range surface plasmon. The wavelength is $1.06 \mu\text{m}$, the dielectric constant of silver is $\epsilon = 57.8 + i0.6$ [60], and the bounding media have a refractive index of 1.5. Also plotted is the prism-coupled, resonant intensity enhancement at the bottom metal interface, I_{X_3}/I_{in} , for a coupling-layer thickness theoretically optimized to the highest coupling efficiency. The identical dependence of I_{X_3}/I_{in} and κ_3''/β'' on silver thickness confirms relationship (3.22). Both quantities depend approximately on the inverse second power of silver thickness for thicknesses less than 60 nm. Note that

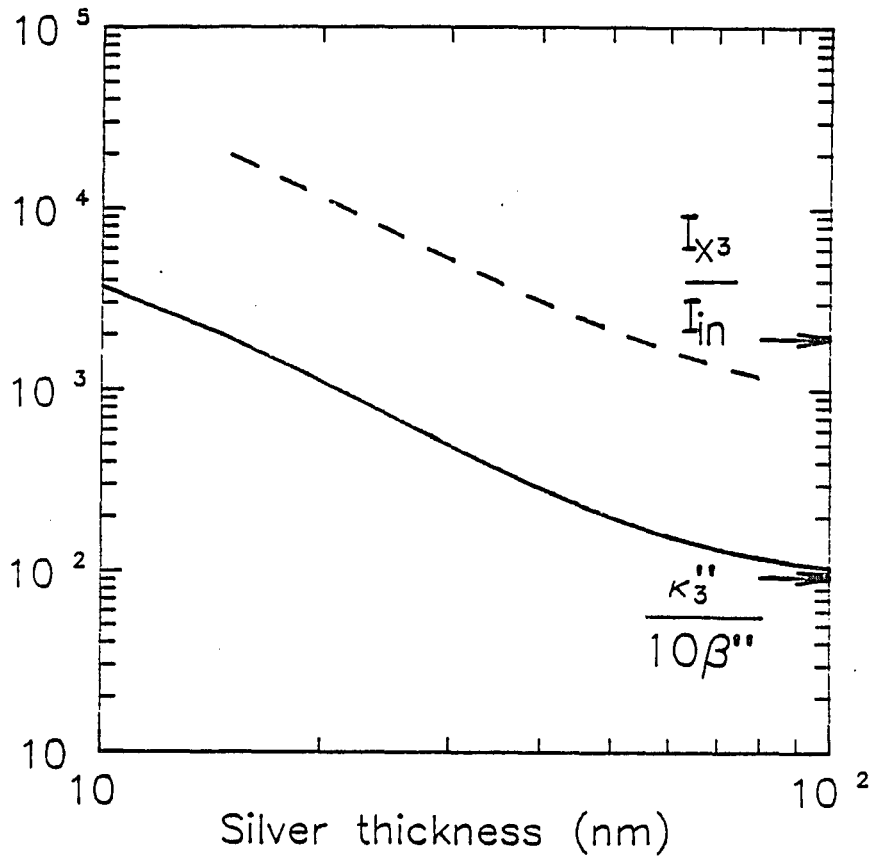


Fig. 3.3. Intensity enhancement parameters

Identical dependence of κ_3''/β_3'' for a bound surface plasmon (solid line) and on-resonance intensity enhancement, I_{x3}/I_{in} , in the substrate of a prism-coupled surface plasmon (dashed line) at low incident intensity ($n_1=n_3=1.5$). Long-range surface plasmon parameters are for the geometry of Fig. 3.2; single-interface plasmon parameters (arrows) are for a Kretschmann geometry: $d_1=0$ and $d_2=62.5$ nm.

while the single-interface mode guides power in a single dielectric medium, the long-range mode guides power in both surrounding media. This accounts for the additional factor of two between I_{X3}/I_{IN} and κ_3''/β'' of the single-interface mode. A Kretschmann geometry with a 62.5-nm-thick silver film was used to calculate I_{X3}/I_{IN} for the single-interface mode.

As mentioned in Section 2D, the reflectance resonance width, $\delta\theta$, depends directly on the absorptive part, β'' , of the normalized propagation constant of the surface plasmon. These two quantities are plotted in Fig. 3.4 for the single-interface and long-range surface plasmon, illustrating their identical dependence on silver thickness approximately to the 2.5 power for thicknesses less than 60 nm.

The direct dependence of I_{X3}/I_{IN} on κ_3''/β'' , and $\delta\theta$ on β'' , implies that the incident intensities I_{\uparrow} (switch-up) and I_{\downarrow} (switch-down) for observing bistable switching exhibit the dependence

$$I_{\uparrow\downarrow} \sim \frac{\delta\theta}{I_{X3}/I_{IN}} \sim \frac{\beta''^2}{\kappa_3''}. \quad (3.23)$$

From Figs. 3.3 and 3.4, the switching intensities for the long-range surface plasmon polariton are expected to depend on silver thickness to greater than the fourth power, for thicknesses smaller than 60 nm. Comparing a long-range mode for a 20 nm silver thickness with the single-interface mode, including the factor of two mentioned above, the observation of optical bistability with prism-coupling to the long-range mode is expected to require 0.012 times the intensities required for the single-interface, Kretschmann geometry. The calculated reflectance curves for the two modes, shown in Fig. 3.5, verifies the expectation. The factor β''^2/κ_3'' is plotted in

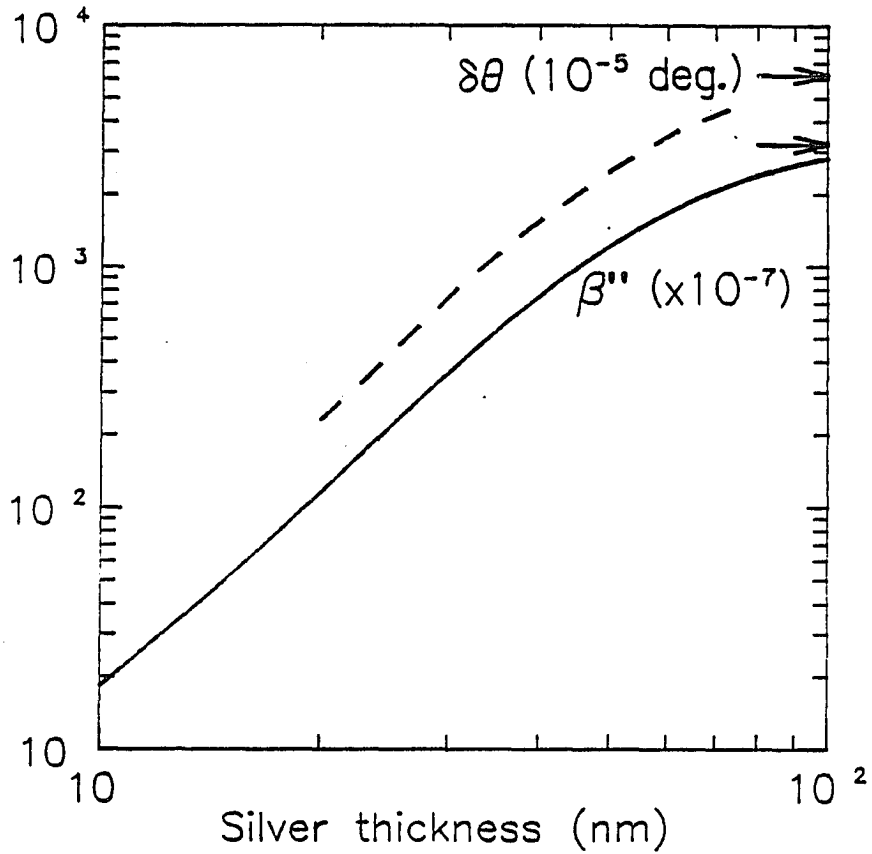


Fig. 3.4. Loss parameters

Identical dependence of β'' for a bound surface plasmon (solid line) and the angular width, $\delta\theta$, of the prism-coupled reflectance resonance (dashed line) at low incident intensity. Long-range surface plasmon parameters are for the geometry of Fig. 3.2; single-interface plasmon parameters (arrows) are for a Kretschmann geometry as in Fig. 3.3.

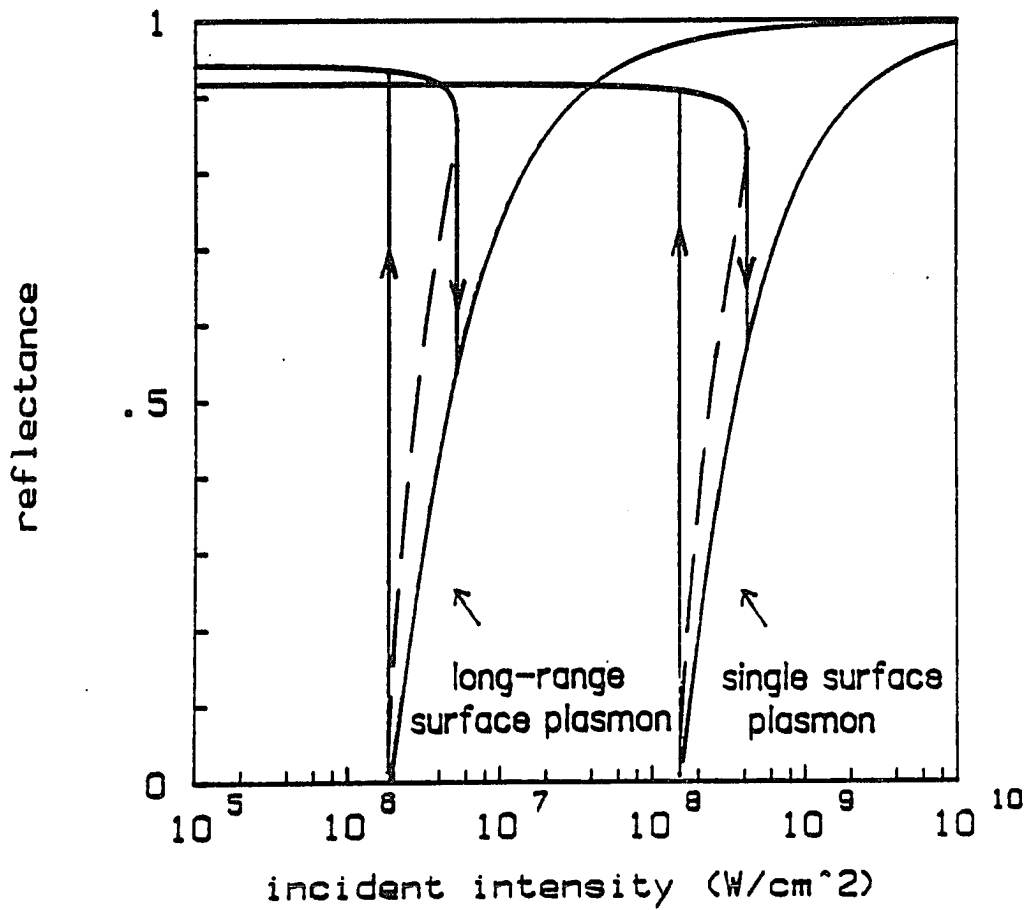


Fig. 3.5. Optical bistability for single-interface and long-range surface plasmon polaritons

Theoretical reflectance vs incident intensity of 1.06- μm radiation coupled to surface plasmons in silver, with a CS_2 nonlinearity in substrate. The single surface plasmon curve is for the Kretschmann geometry as in Fig. 3.3; other parameters are the same as in Fig. 3.2.

Fig. 3.6 alongside the switching intensities calculated using the nonlinear TM wave theory, for a nonlinearity of magnitude similar to that of CS_2 ($n_2,1 = 3 \times 10^{-14} \text{ cm}^2/\text{W}$ at $1.06 \mu\text{m}$ wavelength) [101]. Their interrelationship is confirmed, which provides an approximate method for assessing the merits of different materials and geometries for surface plasmon optical bistability, using relationship (3.23). Calculations at other wavelengths and for other metals agree with the results presented here, within a factor of two, allowing direct comparison of switching intensities for various material systems. Some differences occur due to prism loading, and the intensities must be scaled with the magnitude of the nonlinearity.

Sections 2C.1 and 2C.2 explained that at longer wavelengths, surface plasmon modes become less lossy, such that β'' varies inversely with wavelength for metals which behave according to the Drude theory. κ_3'' varies approximately inversely with wavelength. Therefore, bistable switching intensities are expected to depend inversely on wavelength, assuming lossless nonlinear media. In actuality, nonlinear materials are not perfectly transparent. For example, in semiconductors for which the bandgap-resonant nonlinearity is large, the nonlinearity is accompanied by significant absorption, which increases β'' of the surface plasmon. The example of InSb in the next section includes absorption, and therefore the switching intensities do not scale inversely with wavelength and nonlinearity when compared to the example of CS_2 in this section.

For comparison to the nonlinear wave theory, the two alternative models discussed in Section 3D are used to calculate reflectance vs incident intensity for prism-coupling to the single-interface and long-range surface plasmon polaritons. Using simple homogeneous index theory, for which the change in index depends on the interfacial intensity, similarly-shaped bistable curves are produced, but at

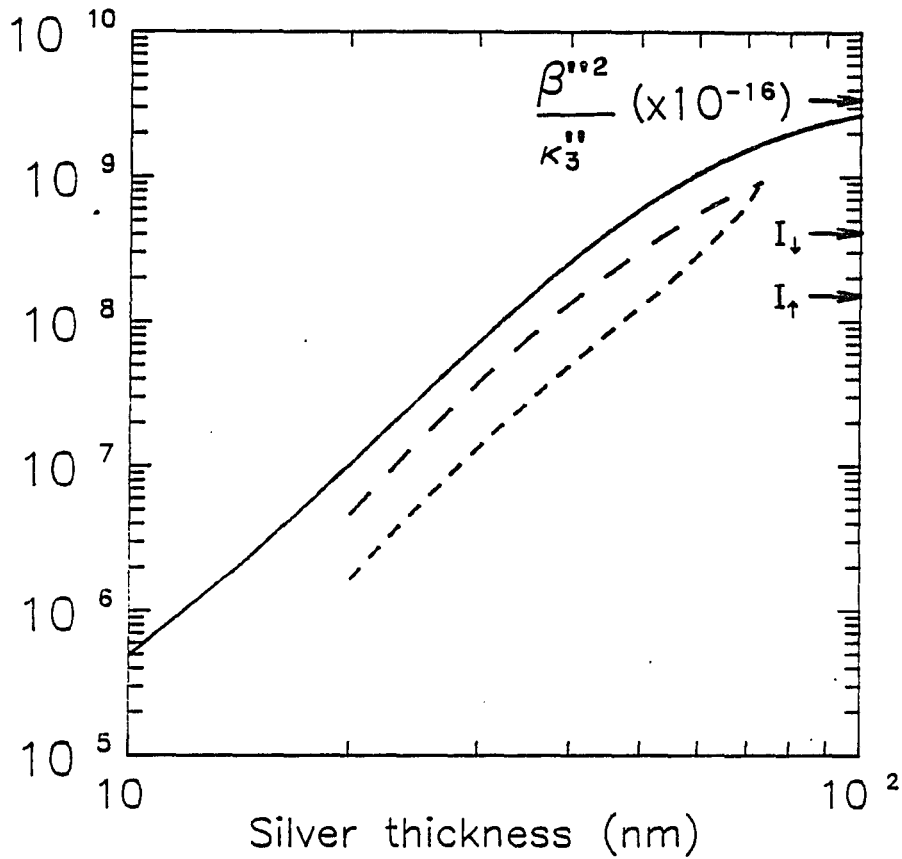


Fig. 3.6. Switching intensity parameters

Switch-up (short-dashed line) and switch-down (long-dashed line) intensity (in W/cm^2) for bistability with the prism-coupled, long-range surface plasmon, and the parameter β''^2/κ_3'' (solid line) predicting switching-intensity dependence. Single-interface plasmon parameters are shown with arrows. Material geometries are the same as in Fig. 3.3, except $n_3 = 1.5 + (3 \times 10^{-18} \text{ cm}^2/\text{W}) I$.

intensities half of those derived from the nonlinear wave theory. The first-order perturbation theory matches the nonlinear wave theory exactly. This agreement is expected, since the parameter ζ_3 remains less than $-3\lambda_0$ throughout the bistable loop of the long-range mode. It implies that the field in the nonlinear medium is almost identical to the exponentially decaying field calculated from linear wave theory for this material system. This is not necessarily the case for modes closer to cutoff, as is seen in the following sections.

Throughout the bistable loop of the single-interface mode, the parameters $|E_{x3}(z)|^2/|E_{z3}(z)|^2$ and $3\Delta\epsilon_z/\epsilon_3$ remain less than 0.043 and 0.028, respectively. These values imply conformity with the approximations made in the nonlinear wave theory, as discussed in Section 3C. The long-range mode, being closer to cutoff, conforms more easily with the approximations than does the single-interface mode.

3F. Long-range Surface Plasmon Polaritons Near Cutoff

To discuss the unique properties exhibited by modes close to cutoff, the nonlinear wave theory is applied to the case of a silver film bounded by indium antimonide (InSb) at a wavelength of $5.6 \mu\text{m}$. InSb is a material of technological interest because of its large nonlinearity near the bandgap. It has a negative nonlinear index; however, for generality, a positive nonlinear index will also be considered. The magnitude of the nonlinear index is $|n_{2,I}| = 7 \times 10^{-5} \text{ cm}^2/\text{W}$ at $5.6 \mu\text{m}$ and 77 K [102]. The linear refractive index is taken to be that of the bulk material, $4.0 + i0.00016$. Experimentally, prism coupling to the long-range mode of an InSb-bounded metal film is difficult because of the high refractive index of InSb and the difficulty in growing optical-quality thin films. For the purpose of illustrating the theory, a prism index of 5.0 and no air gaps between any of the

layers are assumed. The experimental difficulties will be discussed in further detail in Sect. 3H.

3F.1. Comparison of Negative and Positive, Substrate Nonlinearity

Figure 3.7 shows the calculated reflectance curves for positive and gative InSb nonlinearities, a silver ($\epsilon_2 = -1600 + i130$ at $5.6 \mu\text{m}$ [60]) thickness of 20 nm, and an index-matched coupling layer optimized to a thickness of $d_1 = 6 \mu\text{m}$ for maximum coupling. Both curves are shaped like the curves of the CS_2 example. However, the case of a negative nonlinearity exhibits switching at intensities lower than the case of a positive nonlinearity -- about 6% lower for switch-down and about 22% lower for switch-up.

This behavior can be understood qualitatively using a simple homogeneous index model of the nonlinearity, as portrayed in Fig. 3.8 for the InSb geometry. The dispersive part of the normalized propagation constant of the long-range surface plasmon polariton is plotted for a homogeneous change in the refractive index of either bounding medium, corresponding to a change in the coupled intensity in the medium. $\hat{\beta}'_1$ and $\hat{\beta}'_3$ correspond to the prism-loaded long-range mode for changes in the index of medium 1 or medium 3, respectively. $n_1(\Delta n_1)$ is the varying index of medium 1, and $n_1(\Delta n_3)$ is the fixed index of medium 1 as the index of medium 3 varies. β'_1 is the uncoupled normalized propagation constant for an index change in either medium. The positions of constant detuning for a positive or negative nonlinear medium are β'_d and β'_d , respectively, as shown in Fig. 3.8. For a positive nonlinearity, β'_d is greater than the resonance value, $\hat{\beta}'$, while for a negative nonlinearity, β'_d is less than $\hat{\beta}'$, in order to shift $\hat{\beta}'$ toward β'_d with increasing

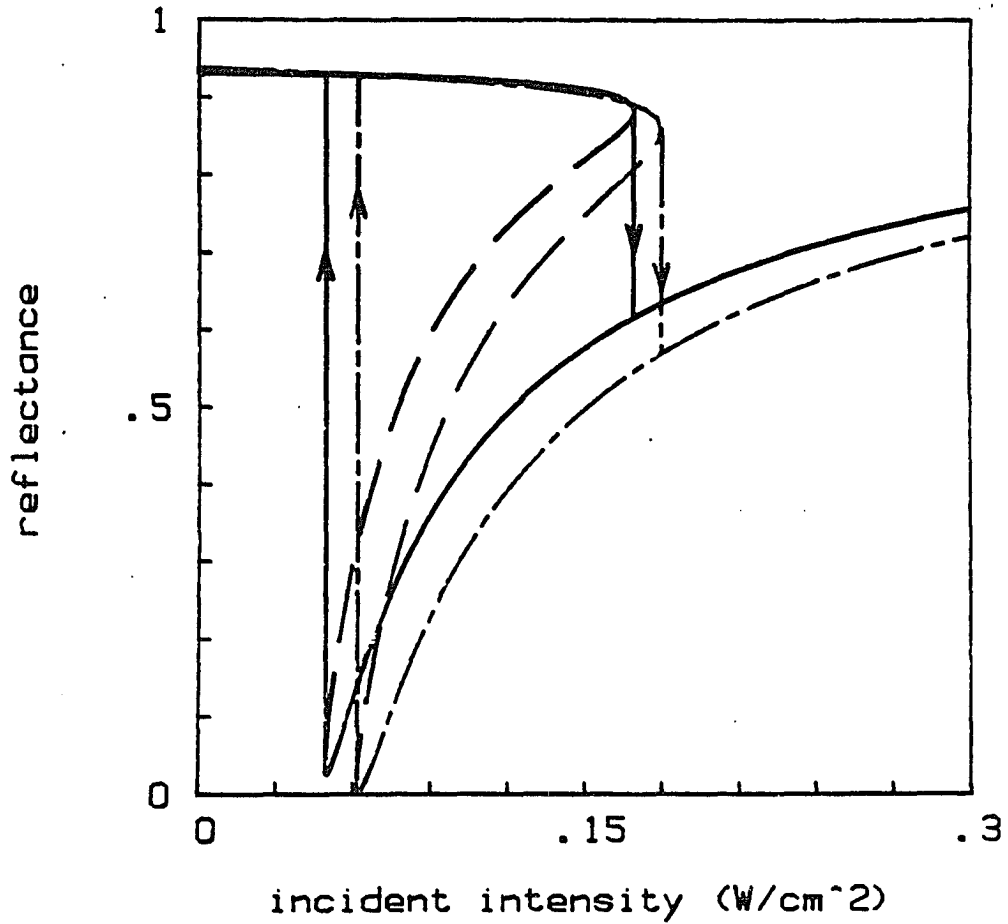


Fig. 3.7. Bistable switching characteristics for positive and negative substrate nonlinearities

prism-coupled long-range surface plasmon for positive (long- and short-dashed line) and negative (solid line) substrate nonlinearities of the magnitude of InSb at $\lambda_0=5.6 \mu\text{m}$ and 77 K ($n_3 = 4.0 + i0.00016 + 7 \times 10^{-5} \text{ cm}^2/\text{W}$ I). $n_0 = 5.0$, $n_1 = 4.0 + i0.00016$, $d_1 = 6 \mu\text{m}$, and $d_2 = 20 \text{ nm}$.

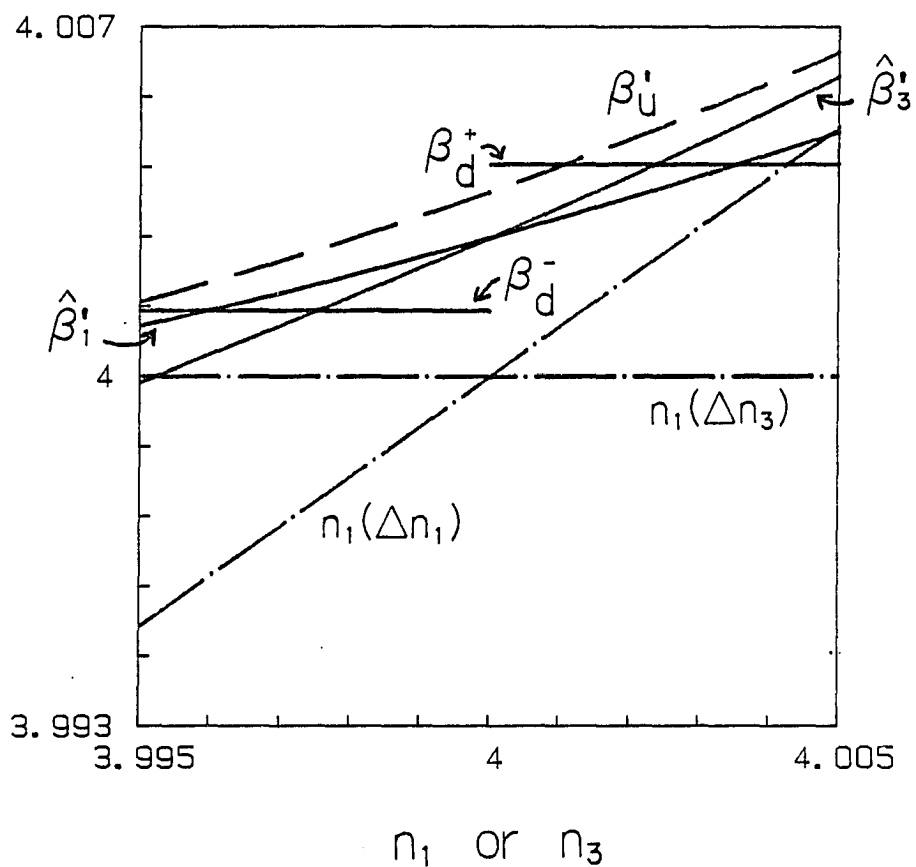


Fig. 3.8. Simple homogeneous-index model

geometry of Fig. 3.7 for prism-coupling to the nonlinear long-range surface plasmon. $\hat{\beta}_j'$ is the dispersive part of the normalized propagation constant of the prism-coupled mode in silver for a change in the index of layer j ; $\hat{\beta}_U'$ is the dispersive part of the normalized propagation constant of the bound mode; $n_j(\Delta n_k)$ is the index of layer j for changes in the index of layer k ; and β_d^+ and β_d^- are the detuning positions for positive and negative index changes, respectively.

intensity. Switch-up occurs approximately at the intersection of $\hat{\beta}'$ and β_d , and switch-down occurs for a smaller Δn .

The difference in switching intensities for a positive and negative nonlinearity is due primarily to the difference between the coupled-intensity enhancement, I_X/I_{IN} , for the two cases. For on-resonance coupling to the surface plasmon, the coupled intensity depends directly on the coupling factor, $h = \exp(-k_0\kappa_1''d_1)$, where $\kappa_1'' \cong (\hat{\beta}'^2 - n_1^2)$. If the nonlinearity in the substrate (medium 3) is positive, an increase in the incident intensity increases n_3 and therefore increases $\hat{\beta}'_3$, as illustrated in Fig. 3.8. The difference between $\hat{\beta}'_3$ and $n_1(\Delta n_3)$ increases, so that less intensity is coupled into the mode at resonance, assuming a fixed coupling-layer thickness, d_1 . The opposite is true for a negative nonlinearity, which shifts $\hat{\beta}'_3$ closer to n_1 , increasing the coupled-intensity enhancement. Consequently, a prism-coupling geometry with a negative, substrate nonlinearity will tend to switch at lower incident intensities than a geometry with a positive, substrate nonlinearity, since it is the coupled intensity which drives the bistable behavior. A larger percentage difference in switching intensities is observed for switch-up than for switch-down because switch-up occurs at a larger $|\Delta n_3|$.

3F.2. Coupling-Layer-Thickness Dependence

If the prism-coupled, long-range surface plasmon is more heavily loaded by decreasing the coupling-layer thickness, d_1 , there is an increase in the loss of the guided power due to reradiation into the prism. The mode shifts toward cutoff, and the reflectance dip broadens and becomes more shallow [53]. While the approximations of the nonlinear wave theory remain valid for this geometry, first-order perturbation theory is no longer applicable.

Figure 3.9 shows the reflectance calculated from the nonlinear wave theory for a coupling-layer thickness of $3.4 \mu\text{m}$, a positive nonlinearity, and a detuning of 0.05° in the prism. Bistable behavior is still evident; however, there is a limit to the incident intensity that can be supported by the structure. Power limiting, a well-established property of nonlinear guided waves, is due to a maximum of the field in the interior of the nonlinear substrate ($\zeta_3 > 0$), arising from Eq. (3.9). It is not predicted by homogeneous index approximations which assume an evanescent field decaying away from the interface. With a larger ζ_3 the field maximum is further from the interface, and consequently a smaller input intensity is required to excite the field profile. The guided-wave intensity in the direction of propagation, $I_x(z)$, is shown in Fig. 3.10 for an input intensity of 0.27 W/cm^2 on the upper branch of Fig. 3.9. It illustrates the self-focussing that occurs in this regime, and is in conceptual agreement with the results for uncoupled, nonlinear surface waves [93-94]. Since the curve of Fig. 3.9 is a multivalued function which is derived parametrically, it is not apparent whether the self-focussed intensity profile of Fig. 3.10 can be excited experimentally by prism coupling. The question of stability, which was not covered by this research, should be addressed [103].

Because the guided wave for the material parameters of Fig. 3.9 has a propagation constant very near cutoff, analysis of bistability for a negative nonlinearity would require a detuning angle which was less than the critical angle of the prism. The wave would no longer be bound to the metal/substrate interface; therefore, it will not be considered in this work.

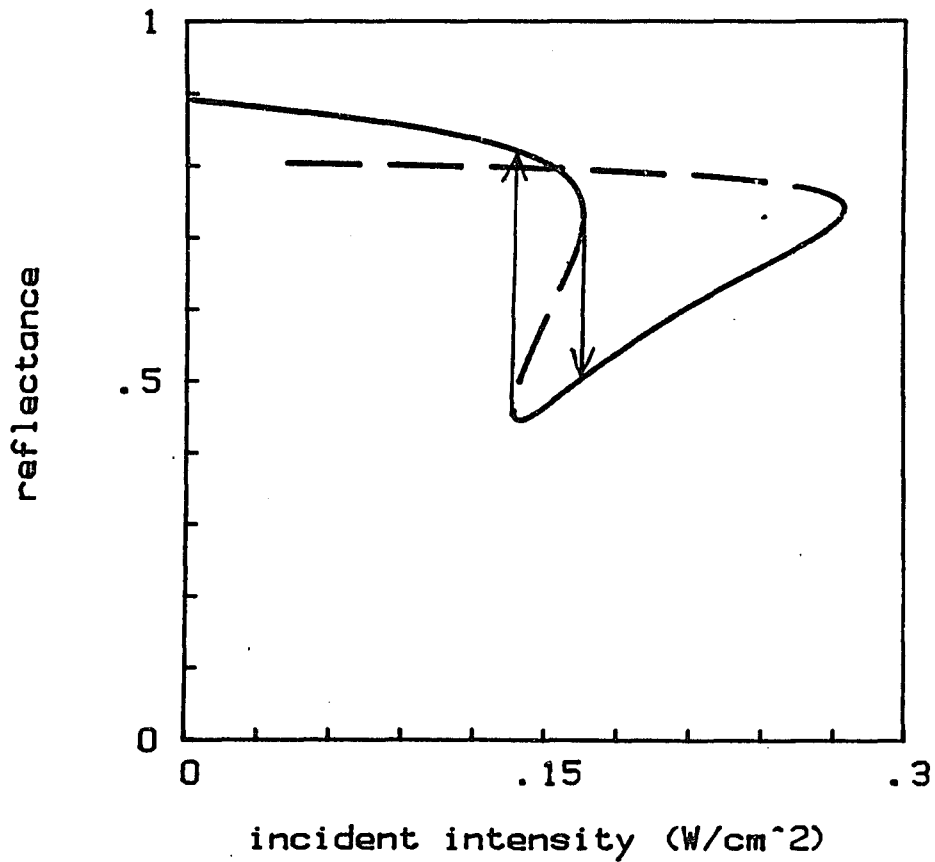


Fig. 3.9. Power-limiting effects

Reflectance vs incident intensity predicted by nonlinear wave theory for thinner-than-optimum coupling layer ($d_1=3.4 \mu\text{m}$) in the long-range mode geometry. $\lambda_0=5.6 \mu\text{m}$, $n_1=4.0 + i0.00016$, $n_3=4.0 + i0.00016 + (7 \times 10^{-5} \text{ cm}^2/\text{W}) I$, $d_2=20 \text{ nm}$, and the detuning = 0.05° in prism.

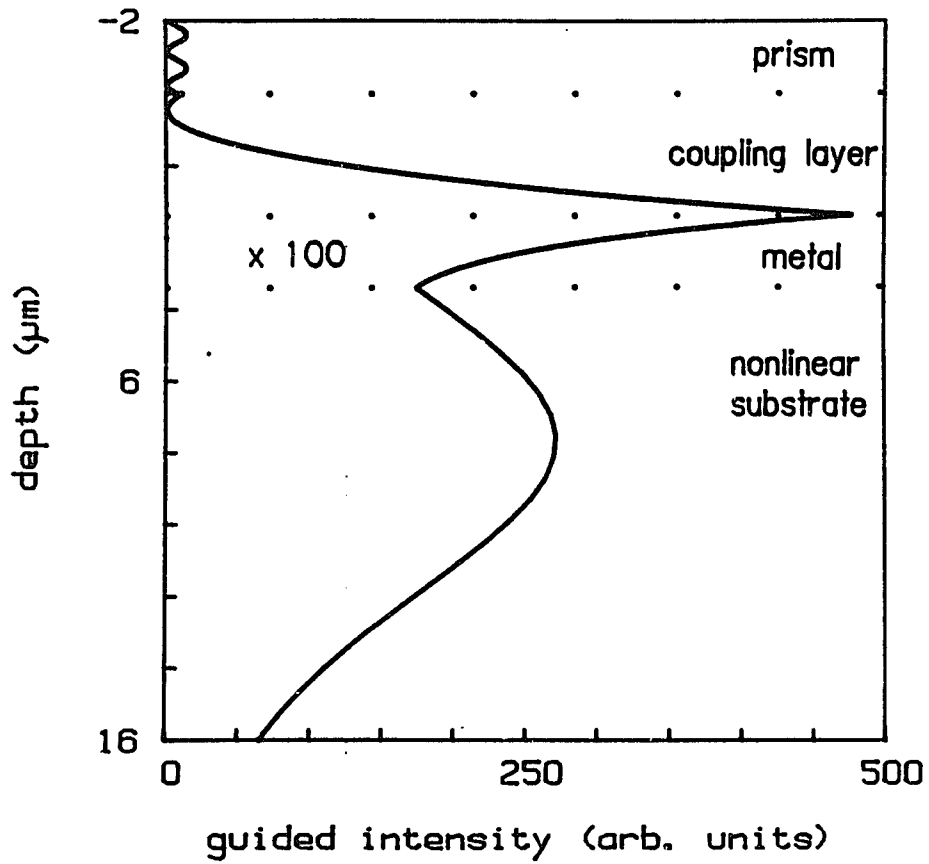


Fig. 3.10. Self-focussing effects

Theoretical guided intensity profile for geometry of Fig. 3.8 at $I_{in} = 0.27 \text{ W/cm}^2$ on the upper branch. Depth and intensity in the metal film are expanded $\times 100$. Self-focussing in the nonlinear substrate is evident.

3F.3. Comparison of Nonlinear Theories

Figure 3.11 accentuates the most common difference between the results of the perturbation (dot-dashed line) and the nonlinear wave (solid line) models for prism-coupled, nonlinear surface waves close to cutoff. The geometry consists of a 15-nm silver film sandwiched between an InSb substrate and an index-matched coupling layer. In the perturbation theory, as the index of the entire substrate is changed by an increase in input intensity, the wave is forced toward radiation into the substrate by the asymmetry of the guide, which broadens the resonance and the shape of the bistable curve. In the nonlinear wave theory a gradient index profile exists, which decreases away from the nonlinear interface. This gradient maintains the field decay and, therefore, the wave guiding. Since there is a very large field enhancement for this thin metal film, the reflectance is driven through resonance with a much smaller change in intensity. The bistable curve is more compressed than that of previous examples for the same relative detuning.

It should be noted that materials such as InSb, whose nonlinearity arises from the photoexcitation of charge carriers, may not be able to maintain a large gradient refractive index due to carrier diffusion. The effects of carrier diffusion have been analyzed for the case of a semiconductor waveguide with a nonlinear core [104]. Carrier diffusion has little effect on the nonlinear response of modes close to cutoff, since the field profile is relatively flat across the core. For the case of a semiconductor nonlinearity in the substrate, carrier diffusion would tend to wash out the self-guiding properties of the gradient index, and one might expect the prism-coupled waveguide behavior to be an average between the calculations of the nonlinear theory and a uniform index theory.

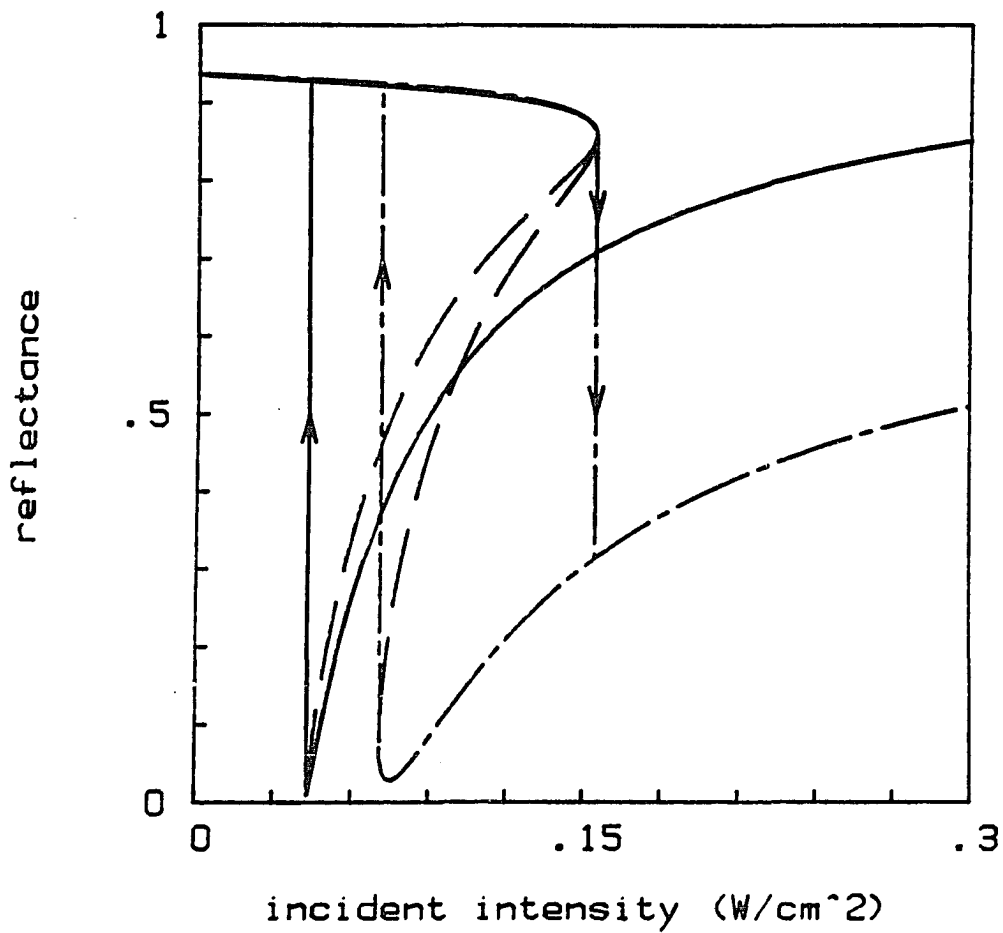


Fig. 3.11. Nonlinear wave theory vs perturbation theory

Theoretical reflectance vs incident intensity of nonlinear long-range surface plasmon for 15-nm silver film and InSb-like positive nonlinearity in the substrate at $5.6 \mu\text{m}$ and 77 K. Solid line is based on nonlinear wave theory and long- and short-dashed line is based on first-order perturbation theory.

3G. Nonlinear Coupling Layer

As explained in Section 3B, the nonlinear wave theory in a prism-coupling context can be developed only for a nonlinearity in the substrate, and not in the coupling layer. In experimental geometries, however, one may want to use a nonlinear liquid such as CS_2 in the coupling layer. Perturbation theory, which can be applied to a nonlinearity in either medium, agrees well with the nonlinear wave theory for a nonlinear substrate at a wavelength of $1.06 \mu\text{m}$. Applying perturbation theory to a nonlinear coupling layer, it is seen that the switching intensities agree to within a few percent. For this lower wavelength, the excited resonance is far from cutoff, relative to the amount it is shifted for bistable switching. Therefore, the change induced by the nonlinearity is mostly a change in propagation constant, not in field distribution, and the prism-coupled, nonlinear resonance follows the behavior of β' for a bound mode in a structure with a varying bounding index, as discussed in reference to Fig. 2.5.

At longer wavelengths, where the long-range mode resonance is closer to cutoff, prism loading has a stronger effect on the field distribution and, therefore, a stronger effect on the nonlinear behavior of the resonance. Perturbation theory is less accurate in this regime, and there is a larger difference between the cases of a nonlinear coupling layer and of a nonlinear substrate. The two primary factors which determine the bistable switching intensities are the nature of the field profile of the prism-coupled mode, which depends upon the refractive index of the layers; and the magnitude of the coupled-intensity enhancement.

Consider the InSb geometry of Section 3F.1 and the homogeneous index model of Fig. 3.8. Note that the slope of $\hat{\beta}'_1$ for a nonlinear coupling layer is smaller

than that of $\hat{\beta}'_3$ for a nonlinear substrate. For a positive Δn_1 , the field profile of the prism-loaded, long-range surface plasmon tends to have mixed properties -- those of a leaky waveguide mode in layer 1 and of a single-interface plasmon at the 2-3 interface. The plasmon character dominates for small Δn_1 , and, since the index of medium 3 is fixed, $\hat{\beta}'_1$ changes slowly with Δn_1 . For a positive Δn_3 , the prism-loaded mode retains its double-interface-guided field profile, and with increasing Δn_3 , $\hat{\beta}'_3$ tends to that of the uncoupled mode, β'_{u3} , and eventually to cutoff due to the asymmetry. For a negative Δn_1 , the long-range surface plasmon also retains its character, with $\hat{\beta}'_1$ tending to β'_{u1} and then to cutoff. For a negative Δn_3 , the field shape tends to a mixed mode, and $\hat{\beta}'_3$ changes rapidly with Δn_3 as the 2-3 interface plasmon dominates for small Δn_3 . Because the slope of $\hat{\beta}'_1$ is smaller than the slope of $\hat{\beta}'_3$, the index change needed to shift $\hat{\beta}'$ into resonance with the incident light at β_d is about 50% more for a nonlinear medium 1 than for a nonlinear medium 3. Therefore, the switching intensities are expected to be higher for nonlinear medium 1 relative to those for nonlinear medium 3.

The coupled-intensity enhancement, I_x/I_{in} , depends on the sign and location of the nonlinearity. The intensity in the coupling layer depends roughly on the coupling factor, h , but note that for a nonlinearity in the coupling layer, κ_1'' depends on the difference between $\hat{\beta}'_1$ and $n_1(\Delta n_1)$. I_x/I_{in} increases with incident intensity for a positive nonlinearity and decreases with incident intensity for a negative nonlinearity, such that the case of a positive, coupling-layer nonlinearity switches at lower intensities than the case of a negative, coupling-layer nonlinearity. This is in direct contrast to the case of a nonlinearity in the substrate, as discussed in Section 3F.1.

When the effects of the coupled intensity are taken into account, they reduce the difference between the switching intensities expected for a positive, substrate nonlinearity and a positive, coupling-layer nonlinearity. They increase the difference between the switching intensities expected for a negative, substrate nonlinearity and a negative, coupling-layer nonlinearity. Table 3.1 lists the switching intensities for a prism-coupled, nonlinear long-range surface plasmon in InSb, as calculated from nonlinear theory and from perturbation theory for the various nonlinear cases. They are in qualitative agreement with the results predicted by the graphic analysis of Fig. 3.8.

3H. Experimental Difficulties

The experimental evidence for cw optical bistability with resonant coupling to a nonlinear waveguide has been very limited. Laval et al. have observed bistability near the resonance of a single-interface plasmon due to thermally-induced index changes in CS₂ used as a nonlinear prism [105]. Other researchers have noted shifts in the resonance angle of grating-coupled, nonlinear single-interface plasmons as the incident intensity was changed [106]. Prism coupling to a ZnS waveguide was shown to exhibit increasing absorption bistability, due to a thermal nonlinearity [107]. Bistability of the prism-coupled light was also observed with a liquid crystal as the nonlinear coupling layer [108]. The effect was also thermal in origin, producing a longitudinal feedback due to heat transfer. No observation has yet been made of cw optical bistability with prism coupling to a waveguide which has an electronic nonlinearity. The basic problem is the lack of materials with sufficiently large nonlinearities so that reasonable intensities can be used for switching. Although the intensity enhancement of a waveguide lowers the requirements for

Table 3.1. Theoretical bistable switching intensities

Prism-coupled, nonlinear long-range surface plasmon in a 20-nm silver film bound by an InSb-like nonlinearity at 77 K and a wavelength of 5.6 μm .

| Nonlinear medium | Sign of nonlinearity | Nonlinear wave theory | | Perturbation theory | |
|------------------|----------------------|-------------------------------------|---------------------------------------|-------------------------------------|---------------------------------------|
| | | I_{\uparrow} (W/cm ²) | I_{\downarrow} (W/cm ²) | I_{\uparrow} (W/cm ²) | I_{\downarrow} (W/cm ²) |
| substrate | + | 0.056 | 0.18 | 0.066 | 0.18 |
| substrate | - | 0.047 | 0.16 | 0.052 | 0.16 |
| coupling layer | + | ----- | ----- | 0.068 | 0.20 |
| coupling layer | - | ----- | ----- | 0.099 | 0.26 |

input intensity, the high guided intensity in thin material layers is prone to induce damage, particularly in a metal film.

One solution is to move to longer wavelengths where, as seen in Section 3E, the intensity requirements decrease due to the decrease in the dielectric losses of metals and the existence of surface plasmon modes closer to cutoff. There also are more choices of nonlinear materials, including the compound semiconductors such as InSb, with large, bandgap-resonant nonlinearities in the infrared. However, more difficulties arise with these materials at longer wavelengths. The most prominent difficulties are the sensitivity to asymmetry in the media bounding the metal film, the sensitivity to air gaps in the layered structure, the lack of index-matching fluids in the infrared, and the scarcity of prism materials with a sufficiently high index of refraction to couple to surface plasmon modes in high-index media. These difficulties are illustrated by the case of the long-range surface plasmon polariton in a silver film bounded by InSb at a wavelength of $5.6 \mu\text{m}$, which is discussed in the following paragraphs.

The discussion of Section 2C.2 indicates that a difference in the refractive indices of the two media surrounding the metal film will cut off the long-range surface plasmon mode at a certain minimum metal thickness. If the bounding index difference, $|n_1 - n_3|$, is greater than the difference between the smaller index and the mode index, β'_{∞} of the single-interface plasmon, then no long-range mode will be allowed, regardless of metal thickness. For a silver film and InSb at $5.6 \mu\text{m}$, $\beta'_{\infty} - n = 0.025$ for the single-interface mode, and $\beta' - n = 0.0037$ for the long-range mode on a 20-nm-thick film. The implication is that in manufacturing the sandwich structure of InSb-silver-InSb, the index of the top InSb layer must be within 0.025 of the index of the InSb substrate just for a long-range mode to exist. This is a tight

tolerance, especially since the deposition of optical-quality InSb films is still in its infancy. Experimental observation of a long-range surface plasmon polariton on a 20-nm film is a very difficult task, since the index-matching tolerance is an order of magnitude smaller.

If such a sandwich structure could be fabricated, the next problem to be faced is the scarcity of high-index prism materials. The prism index must be larger than the surface plasmon mode index, which is always slightly higher than the index of the bounding media, 4.0 in this case. The only common transparent material with a higher index is tellurium, with an index of between 4.85 and 6.3, depending on the crystal orientation [109]. Tellurium is quite brittle, so it would be difficult to cut and polish as a prism. Replacing InSb with another nonlinear semiconductor would allow for more choices of prism materials, but consideration must be given to the relative bandgaps of the materials.

A final difficulty is encountered in attempting to optically contact adjacent layers of solid materials in the prism-coupling structure. If the surfaces are not perfectly smooth, an air gap will exist between the layers. At middle-infrared wavelengths, liquids tend to have large absorption due to molecular vibration modes, such that they cannot be used as index-matching fluids as they are in the visible. Because of the high prism refractive index and surface plasmon mode index, gaps with a moderate refractive index will cause a large evanescent decay in the excitation fields and extinguish the prism coupling. As an example, for the geometry of Section 3F.1 and Fig. 3.7, the existence of an air gap of only 25 nm between the prism and the InSb coupling layer would reduce the coupled intensity by 75% and produce a resonant minimum reflectance of only 0.75. Gaps between other layers are even more serious, as they relate to the index symmetry condition discussed

above. Only 1 nm of air between the silver film and adjacent InSb would totally prevent coupling to the long-range mode.

Although the difficulties listed here are sizable, the progress being made in thin-film deposition and materials research holds promise for the eventual observation of nonlinear effects with long-range surface plasmon polaritons. New discoveries and a balance between the wavelength, the magnitude of the nonlinearity, and the metal thickness will hopefully combine to provide experimental data for the testing of theories such as the one presented here.

CHAPTER 4

THEORY OF SURFACE MAGNETOPLASMON POLARITONS

Surface magnetoplasmon polaritons are excited in layered media in the presence of an applied magnetic field or material magnetization. This chapter concerns the theory of surface magnetoplasmon polaritons which propagate in magnetic metal films bounded by dielectric media when a magnetic field is applied perpendicular to the guided wavevector in the plane of the interfaces. A short introduction to magneto-optic effects is presented first, followed by a history of the study of surface magnetoplasmon polaritons. The equations describing the behavior of TM-polarized waves in layered media with a transversely-applied magnetic field are derived. They are used to explain the properties of the bound, single-interface magnetoplasmon and long-range surface magnetoplasmon of a magnetic metal. Prism coupling is discussed as a tool for studying surface magnetoplasmons experimentally. The manner in which the modal properties of the surface magnetoplasmon affect the transverse Kerr reflectance signal are described, and comparison is made between prism coupling to single-interface and long-range modes. Chapters 5 and 6 present the experimental apparatus and data from the study of the long-range surface magnetoplasmon polariton, including additional theoretical explanation.

4A. Background to Magneto-optic Effects

Magneto-optics has played a major role in the development of both electromagnetic theory and atomic physics [110]. The first magneto-optical phenomenon to be discovered was the Faraday effect, in which the polarization

direction of linearly polarized light propagating in glass was rotated by the application of a magnetic field. The effect was a confirmation of the electromagnetic nature of light. John Kerr discovered a similar rotation upon reflection from a magnetic material, an effect which is named after him. Both effects can be understood phenomenologically in terms of Maxwell's equations and a non-diagonal dielectric tensor.

A microscopic explanation of magneto-optical phenomena came with the observation of the Zeeman effect, a frequency splitting of emission lines into two circularly polarized components when the emission was viewed along the direction of an applied magnetic field. The splitting could be explained using the classical Lorentz theory of electron motion. A static magnetic field exerts a force on the electrons perpendicular to their oscillation in the optical electric field. As a result, the susceptibility of a medium exhibits a frequency shift of approximately $\omega_c/2$, where $\omega_c = eB/m$ is the cyclotron frequency, B is the static magnetic induction, and e and m are the charge and mass of the electron, respectively. The absorption and dispersion spectra of the medium are affected by the shift. The normal modes of the medium are right and left circularly polarized light, so that the Kerr and Faraday effects are understood in terms of both circular dichroism and circular birefringence.

Whereas the magneto-optical properties of the more common diamagnetic materials originate from the Lorentz force on an electron, the properties of paramagnetic and ferromagnetic materials originate from the spins of unpaired electrons and their coupling with the electron orbital angular momentum. Since only electrons with opposite spins may occupy the same orbit, the magnetic moment of an atom due to electron spin is zero unless some of the electrons are unpaired. The spin moment of unpaired electrons interacts with the orbital angular moment to

produce energy states described by the total angular momentum. The spin-orbit interaction is 100-1000 times larger in ferromagnetic materials and nonmetallic paramagnetic materials than the direct effect of the magnetic field [111].

In paramagnetic materials, an applied magnetic field acts to bring the spin moments into alignment from their random thermal orientation. In ferromagnetic materials, adjacent magnetic dipoles are locked into alignment by quantum-mechanical exchange forces. The cooperative behavior results in a very large magnetic moment at temperatures below the Curie temperature. Curie temperatures of the ferromagnets iron and nickel are 1043 K and 631 K, respectively [112, p. 12], above which the metals act paramagnetically. Groups of aligned atoms exist in microscopic domains. An applied magnetic field turns the direction of magnetization inside each domain, or causes the growth of domains with preferred alignment at the expense of other domains. A saturation magnetization is reached when the applied field is strong enough to align the domains of the entire sample in the same direction. The off-diagonal elements of the dielectric tensor of paramagnetic and ferromagnetic materials are determined by the macroscopic magnetization, M . At low magnetic field strengths, for paramagnets and non-magnetized ferromagnets, the off-diagonal elements depend directly on the applied magnetic field, H .

Nickel, cobalt, and iron are the common ferromagnetic metals of most interest to researchers because of their large saturation magnetization. Nickel films were used in the study of surface magnetoplasmon polaritons presented here. To completely understand ferromagnetism and magneto-optical effects in the ferromagnetic metals, the energy band structure of the outer bands must be determined. The magneto-optic Kerr effect has played a major role in this determination. In the so-called "3d metals", the outer 3d band overlaps the 4s band

such that fractional filling of the states occurs. For example, the Bohr magneton number, a measure of the number of unpaired spins which contribute to ferromagnetism, is measured in nickel to be 0.6 instead of the value of 2 expected from a single nickel atom [112, p. 12]. The magnitude of the off-diagonal dielectric tensor elements in the optical region depends on the electron transitions between bands and sub-bands. In the visible part of the spectrum, the primary contribution is from indirect, interband transitions [113]. Complex methods have been developed to calculate the band structure of the 3d metals, but there exists no satisfactorily complete theory [114]. Further discussion is beyond the scope of this study, and the dielectric tensor elements used here for comparison purposes are taken from direct measurements cited in the literature.

The magnetic properties of non-ferromagnetic metals and semiconductors depend to differing degrees on both electron-orbital effects and spin-orbit coupling, according to the material and wavelength region [111]. The low-loss noble metals, which are often used in non-magnetic surface plasmon studies, exhibit a very small magneto-optic effect because they have no unpaired electrons. Semiconductors may exhibit a substantial magneto-optic effect due to the small effective mass of their charge carriers, upon which the cyclotron frequency has an inverse dependence. Indium antimonide, for example, has an effective electron mass of 0.015 times the mass of the electron [115]. It was used in many of the original magnetoplasmon studies.

This research concerns the Kerr magneto-optic effect of ferromagnetic metals in surface plasmon geometries. There are three standard orientations of the applied magnetic field or inherent magnetization for the Kerr effect -- the polar, longitudinal and transverse orientations. In the polar orientation the applied field is

perpendicular to the reflecting interfaces. In the longitudinal orientation the applied field is parallel to the interfaces and in the plane of incidence of the light. Both orientations give rise to a rotation of the plane of polarization upon reflection. No rotation occurs for the transverse orientation, for which the applied field is parallel to the interfaces but perpendicular to the plane of incidence. However, there is a change in reflectance due to the magnetic field. This study focusses on the transverse orientation, which is the simplest of the three to analyze.

4B. Background to Surface Magnetoplasmon Polaritons

Progress in the study of surface plasma waves and bulk magnetoplasma waves led to interest in surface magnetoplasma waves in the early 1970's. Chiu and Quinn developed the dispersion relations for single-surface magnetoplasma waves on a metal or degenerate semiconductor with a high-frequency dielectric constant of unity [116, 117]. They showed that, for the polar and longitudinal orientations of the applied magnetic field in the short-wavelength limit, the frequency of a surface plasma wave is shifted from the value given by $\omega^2 = \omega_p^2/2$ to the value given by $\omega^2 = (\omega_p^2 + \omega_c^2)/2$, assuming an interface with vacuum. In the long-wavelength limit of the polar configuration, surface plasma wave frequencies below the cyclotron frequency are not allowed since the magnetic field allows helicon waves to propagate in the bulk, and surface excitations do not exist. For the transverse orientation, the surface plasma wave frequency is split into two branches for positive and negative magnetic fields. The size of the splitting increases with decreasing wavelength, and has a short-wavelength limit of $\Delta\omega = \pm\omega_c/2$.

Kaplan and coworkers studied the excitation of single-surface magnetoplasmon polaritons in the Otto prism-coupling geometry [118]. At a fixed

angle they calculated ATR spectra as a function of frequency for the longitudinal and transverse magnetic field orientations. Their calculations and experimental results with InSb in the transverse orientation agree with the bound mode dispersion curves. The reflectance resonance position was shifted by the applied field, indicating a splitting of the surface-plasmon frequency which depended on the direction of the field. Calculations for the longitudinal orientation show a downshift in frequency with the application of the field. There is also a coupling of TM-polarized incident light into TE-polarized reflected light, and vice versa, indicating cyclotron motion of the electron plasma out of the plane of incidence.

The excitation of single-surface magnetoplasmon polaritons on the surface of ferromagnetic metals was first observed in nickel and iron films using the Kretschmann geometry and a transversely-applied magnetic field [119, 120]. In this experiment, the frequency of excitation was fixed while the angle of incidence was varied. With an alternating magnetic field, a resonant enhancement of the transverse Kerr magneto-optic effect (a modulated or "differential" reflectance) was detected. The enhancement was attributed to a shift in the propagation constant of the surface plasmon polariton. However, two errors were made in the analysis of the results. The dispersion curves of Ref. 119 for the prism-coupled surface magnetoplasmon were apparently calculated incorrectly; they display a value of the shift in the propagation constant which is more than two orders of magnitude larger than that derived later in this chapter. In addition, the angular positions of the resonant maximum and minimum of the differential reflectance signal were interpreted as being directly associated with the excitation of the two magnetoplasmons for oppositely-directed, applied fields. The separation of the extrema was several

degrees [118], agreeing qualitatively with the inaccurate calculation of the propagation constant shift.

As will be demonstrated in this chapter (see Section 4E and Fig. 4.4), the characteristic shape of the differential reflectance is actually due to a much smaller shift of a reflectance resonance, on the order of one-hundredth of a degree in angle. Furthermore, as discussed in Section 2D.1 and Fig. 2.9, the reflectance resonance in single-interface plasmon geometries involving lossy magnetic metals is located at an angle which is much larger than that of the excitation resonance of the surface plasmon; the reflectance resonance is primarily due to the pseudo-Brewster effect. Thus, the enhancement of the differential reflectance cannot be attributed to the single-interface magnetoplasmon. In the double-interface geometry, which is the focus of this study, the enhancement is directly related to excitation of the long-range surface magnetoplasmon.

Recently, researchers have measured the differential reflectance of single-interface magnetoplasmons in nickel and Permalloy samples for both the transverse and longitudinal configurations of a Kretschmann geometry [121, 122]. However, the errors in interpreting the data were perpetuated. To this author's knowledge, a full explanation of the differential reflectance due to surface magnetoplasmon excitation was not presented in the literature until the present work, which is summarized in Ref. 123.

The preceding discussion points out an important consideration in the ATR enhancement of the Kerr magneto-optic effect from magnetic metals, namely whether the enhancement is associated with the excitation of a surface mode or with other phenomena [64]. The traditional measure of the Kerr magneto-optic effect for a transversely-applied magnetic field is the normalized reflectance difference $\Delta R/R$.

$\Delta R/R$ is a measure of the ac-to-dc signal ratio in an experimental setup where the magnetic field is modulated, and it may be the best measure when considering device applications. However, attenuated total reflectance can be extremely small for certain material constants and angles of incidence, so that $\Delta R/R$ can be very large solely due to the normalization [65]. Since a reflectance minimum may not occur at the angle of maximum excitation of a surface magnetoplasmon polariton in a magnetic metal, the enhancement is doubly deceiving. The present work focusses on the physics of surface magnetoplasmon polaritons; therefore, unnormalized ΔR is used here as a more physical measure of the enhancement of the transverse Kerr magneto-optic effect due to the surface magnetoplasmon polariton [65].

Until recently, research on surface magnetoplasmons was limited to modes at a single interface. Sarid developed the theory of the freely-propagating, double-interface magnetoplasmons of a thin, nonmagnetic metal film bounded by a magnetic semiconductor [124, 125]. The propagation lengths, l , of the short- and long-range modes were plotted for InSb as a function of thickness, for different applied magnetic field strengths. l was shown to decrease substantially with magnetic field, particularly for the long-range mode. This was attributed to a destruction of symmetry of the three-layer structure, as induced by the magnetic field, and a corresponding decrease in the coherence length between the two coupled, single-surface modes. The associated electromagnetic fields became asymmetric with the application of the dc field.

This work considers the case of a thin, magnetic metal film bounded by two nonmagnetic dielectric media with equal or nearly equal refractive indices. The geometry differs from previous studies in two significant ways. First, because the

metal is thin, it is a double-interface geometry which allows for long- and short-range surface magnetoplasmon polaritons. Second, because it is the metal which is magnetic, and not the bounding media, the magneto-optic phase change across the metal affects the properties of the magnetoplasmon polaritons.

The properties of both freely-propagating and prism-coupled surface magnetoplasmons are considered here. The theoretical framework is the same for the two cases, consisting of a modification of the Fresnel reflection coefficients which were derived in Section 2B for a nonmagnetic, multiple-layer system. A transversely-applied magnetic field is assumed. The electromagnetic field is of transverse-magnetic polarization, as required for the surface plasmon, so that the magnetic field of the light is parallel to the applied magnetic field. Derivation of the relevant theory mirrors the derivation in Section 2B.

4C. TM-Polarized Waves in Layered Media with a Transversely-Applied Magnetic Field

It should be understood that the following derivation is valid for material layers whose dielectric tensors can be written in the general form of Eq. (4.1). The relative sign and magnitude of the dielectric constants of the various layers determines whether a guided surface wave can be excited in any given structure. In the examples that follow, only the cases in which one of the media has a negative real part of the dielectric constant are considered. However, the reflection coefficients are general for any material constants, unless specifically stated otherwise.

Referring to the geometry of Fig. 2.1, if a material layer has a permanent magnetization in the y -direction or an induced magnetization due to a transversely-applied magnetic field (in the y -direction), then the dielectric tensor of the material

can be written in the form [126]

$$\epsilon = \epsilon_0 \begin{bmatrix} \epsilon_{11} & 0 & -iQ\epsilon_{11} \\ 0 & \epsilon_{22} & 0 \\ iQ\epsilon_{11} & 0 & \epsilon_{11} \end{bmatrix} \quad (4.1)$$

and the relative magnetic permeability is taken to be unity. Q is the magneto-optic coefficient, a complex quantity much less than unity which is often described in terms of magnitude and phase: $Q = Q_0 \exp(i\phi)$. The cases of a permanent magnetization or one induced by an applied magnetic field are treated in the same manner. ϵ_{11} and ϵ_{22} are even functions of the magnetic field, H , and Q is an odd function of H [126]. The effect of the applied magnetic field on TE-polarized light is only to the second power of Q through the term ϵ_{22} , whereas the effect on TM-polarized light is to couple the two components of the electric field through the off-diagonal tensor elements, which are essentially linear in Q . Therefore, the larger effect is on TM-polarized light, and TE polarization will not be treated here. Although it is straightforward to consider the general case of a non-zero Q for all layers, for simplicity in the examples given below only the metal layer is taken to have a non-zero Q .

Because of the anisotropy in ϵ , the wave equation is more easily written in terms of the electric fields. Maxwell's equations, Eqs. (2.4) and (2.5), lead to the wave equation,

$$\nabla \times \nabla \times \mathbf{E} = -\mu_0 \frac{\partial^2 \mathbf{D}}{\partial t^2}. \quad (4.2)$$

Assuming TM-polarized fields of the form of Eq. (2.10) with the time dependence of

Eq. (2.1), the two sides of the wave equation are given by

$$\begin{aligned}\nabla \times \nabla \times \mathbf{E} &= ik_0(\kappa \mathbf{E}_X - \beta \mathbf{E}_Z) \nabla \times [\mathbf{y} \exp[ik_0(\kappa z + \beta x) - i\omega t]] \\ &= k_0^2(x\kappa - z\beta) (\kappa \mathbf{E}_X - \beta \mathbf{E}_Z) \exp[ik_0(\kappa z + \beta x) - i\omega t]\end{aligned}\quad (4.3a)$$

and

$$-\mu_0 \frac{\partial^2 \mathbf{D}}{\partial t^2} = \mu_0 \epsilon_0 \epsilon_{11} \omega^2 [x(\mathbf{E}_X - iQ\mathbf{E}_Z) + z(\mathbf{E}_Z + iQ\mathbf{E}_X)] \exp[ik_0(\kappa z + \beta x) - i\omega t]. \quad (4.3b)$$

Equating the x- and y-components of the two sides leads to

$$(\epsilon_{11} - \kappa^2) E_X + (\kappa\beta - iQ\epsilon_{11}) E_Z = 0 \quad (4.4a)$$

$$(\kappa\beta + iQ\epsilon_{11}) E_X + (\epsilon_{11} - \beta^2) E_Z = 0. \quad (4.4b)$$

The solution of this set of equations requires a null determinant of the coefficients, yielding [127]

$$\beta^2 + \kappa^2 = \epsilon_{11}(1 - Q^2) \quad (4.5)$$

Comparison of Eq. (4.5) with Eq. (2.11) indicates that the normalized propagation constants are shifted by the applied magnetic field.

From Equation (2.4),

$$\mp \kappa H_y^\pm = -c\epsilon_0\epsilon_{11} \left(E_X^\pm - iQE_Z^\pm \right) \quad (4.6a)$$

$$\beta H_y^\pm = -c\epsilon_0\epsilon_{11} \left(iQE_X^\pm + E_Z^\pm \right). \quad (4.6b)$$

resulting in the expression for the relative optical impedance of the j^{th} layer:

$$Z_j^\pm \equiv \frac{c\epsilon_0 E_{xj}^\pm}{H_{yj}^\pm} = \frac{\pm\kappa_j - iQ_j\beta}{\epsilon_j(1-Q_j^2)}, \quad (4.7)$$

where ϵ_j is the element ϵ_{11} of the dielectric tensor for the j^{th} layer. Note that $Z_j^+ \neq -Z_j^-$ for magnetic media, contrary to the case of nonmagnetic media since the optical fields depend on the relative directions of the wavevector and the applied magnetic field.

Boundary conditions are applied in the same manner as in Chapter 2 to derive expressions for the reflection, transmission, and fields in the layers of the multilayer stack; however, the nondegenerate impedances must be distinguished for the case of magnetic media. The boundary conditions equivalent to Eqs. (2.14) and (2.15) are

$$Z_j^+ H_{yj}^+ \exp(ik_0\kappa_j d_j) + Z_j^- H_{yj}^- = Z_{j+1}^+ H_{y,j+1}^+ + Z_{j+1}^- H_{y,j+1}^- \exp(ik_0\kappa_{j+1} d_{j+1}) \quad (4.8)$$

and

$$H_{yj}^+ \exp(ik_0\kappa_j d_j) + H_{yj}^- = H_{y,j+1}^+ + H_{y,j+1}^- \exp(ik_0\kappa_{j+1} d_{j+1}), \quad (4.9)$$

which give rise to

$$H_{yj}^+ = \frac{1}{-Z_j^- + Z_j^+} \left[\left(-Z_j^- + Z_{j+1}^+ \right) H_{y,j+1}^+ + \left(-Z_j^- + Z_{j+1}^- \right) H_{y,j+1}^- \exp(\gamma_{j+1}) \right] \exp(-\gamma_j) \quad (4.10)$$

and

$$H_{\bar{y}j} = \frac{1}{-Z_j^- + Z_j^+} \left[\left(Z_j^+ - Z_{j+1}^+ \right) H_{\bar{y},j+1}^+ + \left(Z_j^+ - Z_{j+1}^- \right) H_{\bar{y},j+1}^- \exp(\gamma_{j+1}) \right] \quad (4.11)$$

mirroring Eqs. (2.16) and (2.17). The single-interface, magnetic-field amplitude reflection coefficients between layer j and $j+1$ are given by

$$r_{j,j+1}^+ \equiv \frac{H_{\bar{y}j}^- \exp(-\gamma_j)}{H_{\bar{y}j}^+} = \frac{Z_j^+ - Z_{j+1}^+}{-Z_j^- + Z_{j+1}^+} \quad (4.12)$$

$$-r_{j,j+1}^- \equiv -\frac{H_{\bar{y},j+1}^+ \exp(\gamma_j)}{H_{\bar{y},j+1}^-} = \frac{Z_j^- - Z_{j+1}^-}{-Z_j^- + Z_{j+1}^+}, \quad (4.13)$$

where + and - indicate the direction in which the wave is incident on the interface. It is seen that $r_{j,j+1}^+ \neq -r_{j,j+1}^-$; the application of a magnetic field lifts the degeneracy of the reflection since the handedness of the applied field is opposite for reflection from the two sides of the interface. The single-interface amplitude transmission coefficient is

$$t_{j,j+1}^+ = \frac{H_{\bar{y},j+1}^+ \exp(-\gamma_j)}{H_{\bar{y}j}^+} = \frac{Z_j^+ - Z_j^-}{-Z_j^- + Z_{j+1}^+}. \quad (4.14)$$

Taking the $j+2$ interface into account yields the expressions

$$H_{\bar{y}j}^+ = \frac{\exp(-\gamma_j)}{-Z_j^- + Z_j^+} \left[\frac{\left(-Z_j^- + Z_{j+1}^+ \right) \exp(-\gamma_{j+1}) + \left(-Z_j^- + Z_{j+1}^- \right) r_{j+1,j+2}^+ \exp(\gamma_{j+1})}{t_{j+1,j+2}^+} \right] H_{\bar{y},j+1}^+ \quad (4.15)$$

$$H_{y_j}^- = \frac{1}{-Z_j^- + Z_j^+} \frac{\left[\left(Z_j^+ - Z_{j+1}^+ \right) \exp(-\gamma_{j+1}) + \left(Z_j^+ - Z_{j+1}^- \right) r_{j+1,j+2}^+ \exp(\gamma_{j+1}) \right] H_{y_{j+1}}^+}{t_{j+1,j+2}^+} \quad (4.16)$$

The multilayer, amplitude reflection coefficient between the j^{th} layer and the bottom semi-infinite layer is then given in a form similar to that for reflectance from nonmagnetic layers (see Eq. (2.23)):

$$\rho_j^+ = \frac{H_{y_j}^-}{H_{y_j}^+} \exp(-\gamma_j) = \frac{r_{j,j+1}^+ + s_{j,j+1} \rho_{j+1}^+ \exp(2\gamma_{j+1})}{1 + r_{j,j+1}^- \rho_{j+1}^+ \exp(2\gamma_{j+1})}, \quad (4.17)$$

where $\gamma_j = ik_0 \kappa_j d_j$. $s_{j,j+1}$ is an indicator of the asymmetry induced by the applied field, and is defined as

$$s_{j,j+1} = \frac{Z_j^+ - Z_{j+1}^-}{-Z_j^- + Z_{j+1}^+}. \quad (4.18)$$

The reflectance, $R = |\rho_j^+|^2$, of the entire stack can be calculated recursively from Eq. (4.17), starting with the bottom interface. The transmission coefficient between layers j and $j+1$ in the presence of the complete multilayer is

$$\tau_{j,j+1} = \frac{H_{y_{j+1}}^+}{H_{y_j}^+} \exp(-\gamma_j) = \frac{t_{j,j+1}^+}{1 + r_{j,j+1}^- \rho_{j+1}^+ \exp(2\gamma_{j+1})}, \quad (4.19)$$

and multilayer transmission is calculated as the product of coefficients for adjacent layers.

The electric fields for each layer j are of the form of Eq. (2.10), with coefficients derived from Eqs. (4.6) and (4.7):

$$E_{Xj}^+ = \frac{\kappa_j - iQ_j\beta}{c\epsilon_0\epsilon_j(1-Q_j^2)} H_{Yj}^+ \quad (4.20a)$$

$$E_{Xj}^- = \frac{-\kappa_j + iQ_j\beta}{c\epsilon_0\epsilon_j(1-Q_j^2)} \rho_j \exp(\gamma_j) H_{Yj}^+ \quad (4.20b)$$

$$E_{Zj}^+ = -\frac{\beta + iQ_j\kappa_j}{c\epsilon_0\epsilon_j} H_{Yj}^+ \quad (4.20c)$$

$$E_{Zj}^- = -\frac{\beta - iQ_j\kappa_j}{c\epsilon_0\epsilon_j} \rho_j \exp(\gamma_j) H_{Yj}^+ \quad (4.20d)$$

4D. Bound Surface Magnetoplasmon Polaritons -- Dispersion Relations

4D.1 Single-Interface Magnetoplasmon Polariton

Following the methods of Section 2C, the modal dispersion relations for the bound surface magnetoplasmon polaritons of a single interface and a double interface can be derived. Letting the amplitude reflection coefficient at the single interface between a nonmagnetic dielectric (medium 1) and a magnetic metal (medium 2) approach infinity, the dispersion equation for the single-interface magnetoplasmon polariton is found to be [127]

$$\kappa_2\epsilon_1 + \kappa_1\epsilon_2(1-Q^2) - i\beta Q\epsilon_1 = 0. \quad (4.21)$$

Q can be positive or negative, representing the two opposite directions of mode

propagation relative to the perpendicular, applied magnetic field. Unlike the case of no applied field, the equation must be solved numerically to determine the normalized propagation constant, β . With the application of an external magnetic field, β shifts from its nonmagnetized value, β_0 , by the amount $\Delta\beta = \beta - \beta_0$. The direction of the shift depends on the sign of the applied field, and its magnitude is approximately equal for equal and opposite fields. As indicated in Fig. 4.1, $\Delta\beta = (4.3 + i4.3) \times 10^{-4}$ for the single-interface magnetoplasmon polariton of nickel ($\epsilon = -13 + i16$) with its saturated magneto-optic coefficient of approximately $Q = 1.08 \times 10^{-2} \exp[i(-33.7^\circ)]$ at a wavelength of 632.8 nm [128]; glass is the bounding medium. (Note: measurements of the magneto-optic coefficient of nickel vary significantly in the literature [113, 128]. A typical value is used for the theoretical examples, and the experimental data of this study is reported in Chapter 6.)

4D.2. Long-Range Surface Magnetoplasmon Polariton

For the case of a double-interface magnetoplasmon polariton, consider a magnetic metal layer bounded by two nonmagnetic dielectrics. When the reflection coefficient for the three-layer stack is set to infinity, the dispersion equation is given by

$$1 + r_{21}^- r_{23}^+ \exp(2ik_0\kappa_2 d_2) = 0 . \quad (4.22)$$

The two solutions to this transcendental equation are the long-range and short-range surface magnetoplasmon polaritons. Nickel at visible wavelengths is quite lossy; therefore, the short-range mode has extremely high attenuation, and it will not be considered here. The shift of the normalized propagation constant of the long-range mode due to a saturating magnetic field is plotted vs nickel thickness in Fig. 4.1.

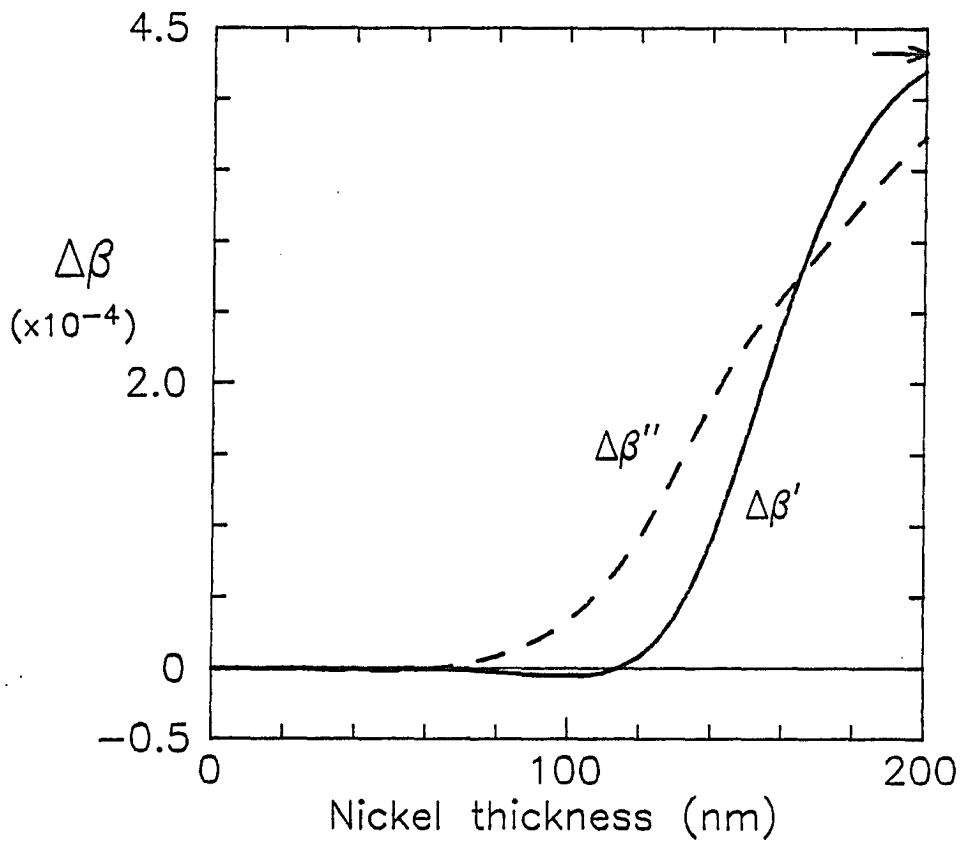


Fig. 4.1. Shift of the normalized propagation constant of the long-range surface magnetoplasmon polariton

Dispersive ($\Delta\beta'$) and absorptive ($\Delta\beta''$) parts of the shift for nickel ($\epsilon_2 = -13 + i16$) due to a saturating magnetic field -- $Q = 1.08 \times 10^{-3} \exp[i(-33.7^\circ)]$. $\Delta\beta'$ and $\Delta\beta''$ for the single-interface magnetoplasmon polariton are approximately equal and are indicated with an arrow. $\lambda_0 = 632.8$ nm, and the refractive index of the bounding medium is 1.5.

The most noticeable feature of Fig. 4.1 is that the induced shift, $\Delta\beta$, of the long-range surface plasmon is much smaller than that of the single-interface plasmon -- more than two orders of magnitude for nickel thicknesses less than 60 nm. In contrast to $\Delta\beta$ of the nonlinear surface plasmon, discussed in Chapter 3, $\Delta\beta$ of the surface magnetoplasmon does not increase with the enhanced optical fields of the long-range mode. It depends on the induced reflectivity perturbation at the metal interfaces and the magneto-optic phase shift across the metal layer. The dependence is investigated by expanding the dispersion equation, Eq. (4.22), in terms of the magneto-optic coefficient, Q , as follows.

The transverse decay constant of the nickel layer can be written as

$$\kappa_2 = (\epsilon_2^2 - \beta^2 - Q^2\epsilon_2)^{1/2} \cong \kappa_2 - \frac{Q^2\epsilon_2}{2\kappa_2}, \quad (4.23)$$

where $\kappa_2 \equiv (\epsilon_2 - \beta_0^2)^{1/2}$ is the unperturbed value of κ_2 , and terms of order Q^3 and higher have been neglected. Equation (4.23) indicates that the phase across the magnetic metal layer is affected to the second power of Q . Reflectivity at the metal interfaces is expanded from Eqs. (4.12) and (4.13) as

$$\Gamma_{23}^+ = \frac{\kappa_3\epsilon_2 - \kappa_2\epsilon_3 - iQ\beta\epsilon_2}{\kappa_3\epsilon_2 + \kappa_2\epsilon_3 + iQ\beta\epsilon_2} \cong \frac{\tilde{r}_{23} - \frac{iQ\beta\epsilon_2}{\kappa_3\epsilon_2 + \kappa_2\epsilon_3}}{1 + \frac{iQ\beta\epsilon_2}{\kappa_3\epsilon_2 + \kappa_2\epsilon_3}} \cong (\tilde{r}_{23} - q_{23})(1 - q_{23}) \quad (4.24)$$

where \tilde{r}_{23} is the single-interface, amplitude reflection coefficient for no applied field and

$$q_{23} = \frac{iQ\beta_0\epsilon_2}{\kappa_3\epsilon_2 + \kappa_2\epsilon_3}, \quad (4.25)$$

which is neglected to order higher than two. Similarly,

$$r_{21}^- \cong (r_{21} + q_{21})(1 + q_{21}) \quad (4.26)$$

such that the reflectivity term in Eq. (4.16) is

$$r_{21}^- r_{23}^+ \cong r_{21}^- r_{23}^+ + [q_{21} r_{23}^- - q_{23} r_{21}^-] + [q_{21}^2 r_{23}^- + q_{23}^2 r_{21}^-] \quad (4.27)$$

If the metal film is symmetrically bounded, the second term of (4.27), of order q , is zero, and the shift of the magnetoplasmon propagation constant depends on q only to the second power, that is to the second power of Q . Asymmetry in the indices of the bounding media causes a first-order dependence on Q . The dependencies based on the expansion have been confirmed using the complete calculation.

For small metal thicknesses, the modal solution to the dispersion equation depends on both the reflectivity and phase terms, which change with Q to only the second power for a symmetric structure. For large thicknesses, the phase term becomes very small due to decay in the metal, and the solution is dominated by one of the reflection coefficients approaching infinity, the limit of a single-interface plasmon polariton. Since a single reflection coefficient depends on Q to the first power, the shift, $\Delta\beta$, of the normalized propagation constant is expected to be much larger for large metal thicknesses and for the single-interface mode than for the long-range mode. Fig. 4.1 confirms this behavior.

In the case of the symmetrically bounded metal film, the normalized propagation constants of the long-range surface magnetoplasmon polariton is

independent of the sign of the magnetic field, since there exist equivalent right-handed and left-handed reflections at the two metal interfaces. Asymmetry of the bounding indices lifts the degeneracy, and the respective shifts, $\Delta\beta^+$ and $\Delta\beta^-$, are usually opposite but not necessarily equal for positive and negative magnetic fields. Fig. 4.2 plots the shifts for different asymmetries, showing that asymmetry enables a much larger effect because the normalized propagation constant depends directly on Q rather than on Q^2 .

Note from Fig. 4.1 that for the symmetrically-bounded nickel film of a certain thickness, β' of the long-range surface plasmon is not shifted by a magnetic field. For another nickel thickness, β'' is not shifted; however, $\Delta\beta''$ does not cross zero for the asymmetric geometries of Fig. 4.2. The zero-crossings are highly material-dependent, but do not exist for both $\Delta\beta'$ and $\Delta\beta''$ at the same thickness nor at periodic intervals of thickness, due to the interdependence of reflectivity, β , and κ_2 . Unfortunately, the zero-crossings cannot be verified by prism-coupling experiments, since the large nickel thicknesses at which they occur make the modes too lossy. In addition, the presence of the prism affects the observable modal properties, as will be discussed in the following section.

4E. Prism Coupling to Surface Magnetoplasmon Polaritons

Surface magnetoplasmon polaritons can be studied in a prism-coupling geometry. The shift of the normalized propagation constant accompanying the application of a transverse, external magnetic field should appear as a change in the angular reflectance resonance. The shift of β' changes the angular position of the resonance relative to that of the unperturbed plasmon, and the shift of β'' changes the width of the resonance. Direct measurement of these changes are very difficult,

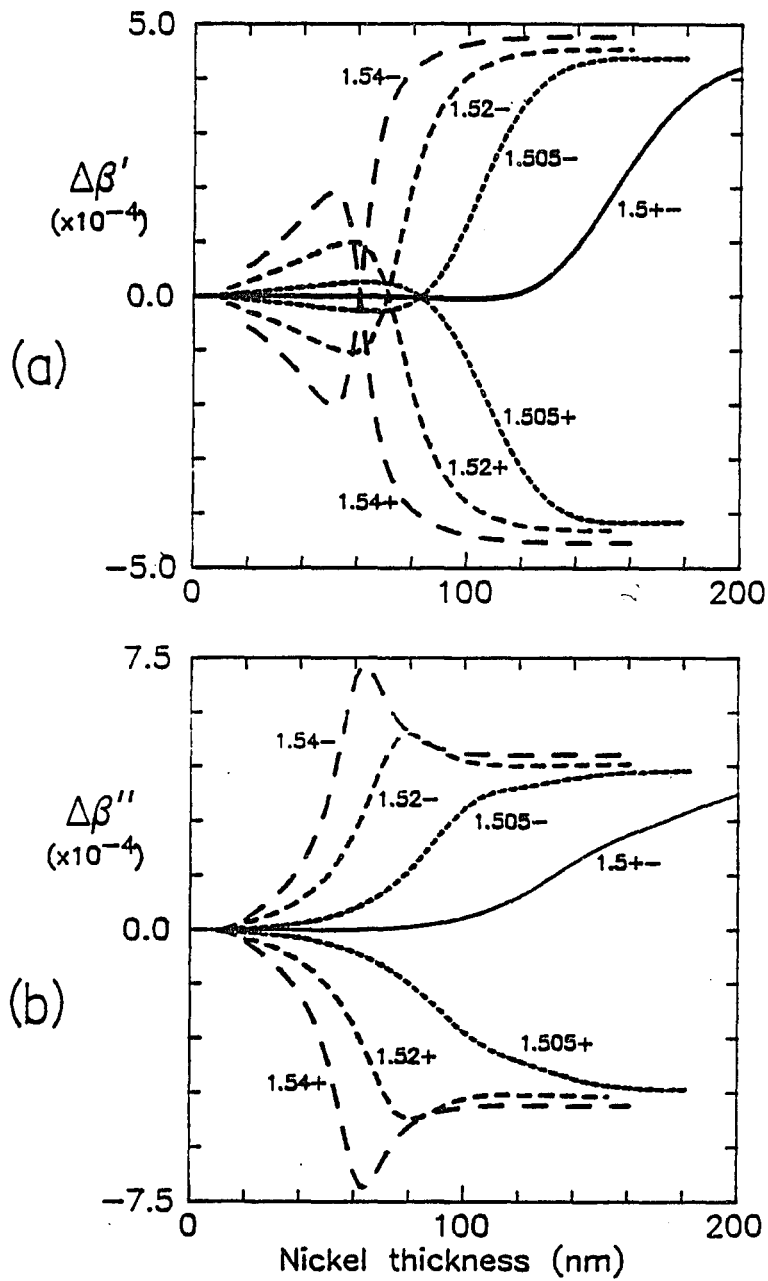


Fig. 4.2. Shift of the normalized propagation constant for asymmetric bounding

Dispersive (a) and absorptive (b) parts of the shift, $\Delta\beta_{\pm} = \beta_{\pm} - \beta_0$, for the long-range surface magnetoplasmon in nickel due to positive (+) and negative (-) saturating magnetic field; $n_3 = 1.5$ and n_1 is as labelled; parameters are otherwise the same as in Fig. 4.1.

however, since the normalized changes, $\Delta\beta'/\beta'$, $\Delta\beta'/\beta''$ and $\Delta\beta''/\beta''$, for an actual magnetic metal are quite small. This difficulty is illustrated in Fig. 4.3, in which the theoretical, prism-coupled reflectance resonance of the long-range surface plasmon and of the two long-range surface magnetoplasmons are plotted on an expanded scale for a 20-nm-thick nickel film bounded by a refractive index of 1.5. R_0 , R_+ and R_- are the respective reflectances for no magnetization and for positive and negative saturation magnetization, Q . Shifts in the resonance position are larger than those predicted from the bound mode properties, due to the inherent asymmetry of the prism-coupling geometry (discussed later), but they are still very small relative to the obtainable measurement sensitivities. The figure indicates that in order to directly distinguish the relative positions of the resonance dips, a sensitivity in reflectance of at least 10^{-5} and in angular position of at least 0.0005° would be necessary.

Indirect measurement of the properties of surface magnetoplasmon polaritons is possible, however, through measurement of the modulation in reflectance due to modulation of the applied magnetic field. Referring to Eqs. (4.7) - (4.18) for a multilayer stack, of which at least one layer is magnetic, the reflectance is changed with the application of a transverse, external magnetic field. In an experimental geometry, if the magnetic field is modulated between zero and a finite value, or between positive and negative values, then a reflectance modulation should be measured at the same modulation frequency. The shifts in position and width of the angular resonance appear indirectly as changes in reflectance, which can more easily be measured by lock-in detection techniques.

To simulate the differential reflectance measurements, the quantities $\Delta R_+ \equiv R_+ - R_0$ and $-\Delta R_- \equiv -(R_- - R_0)$ are calculated in the angular vicinity of a

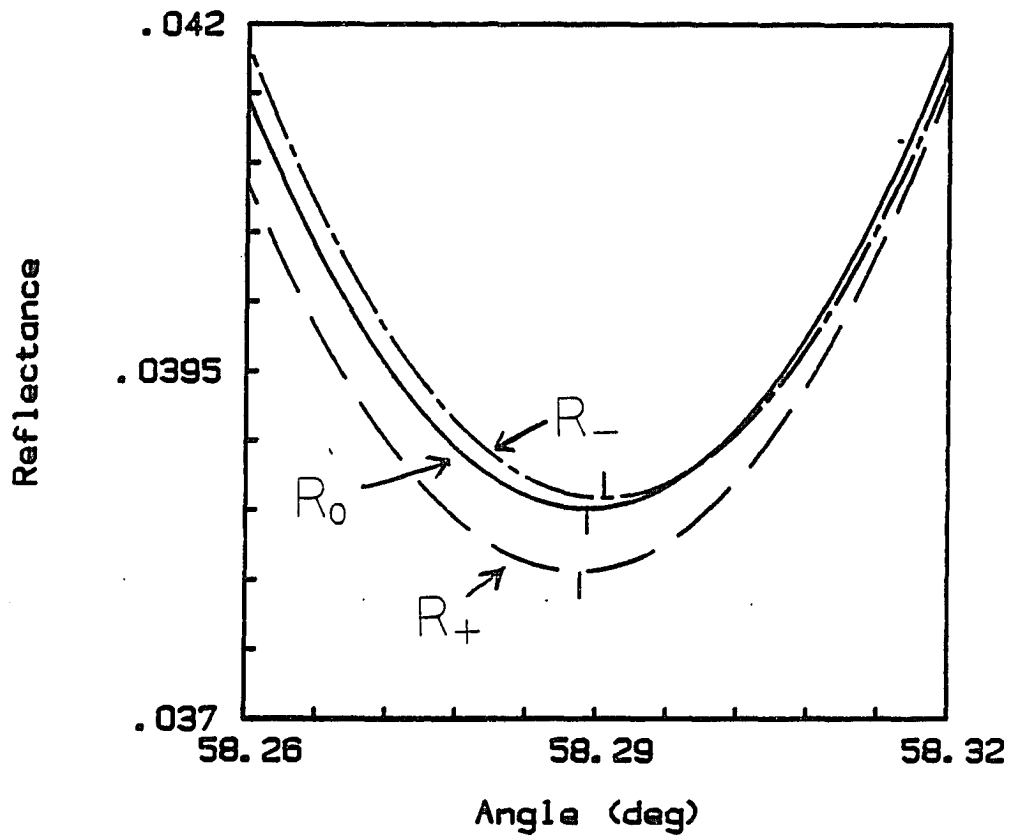


Fig. 4.3. Shift of surface magnetoplasmon reflectance resonance

Highly expanded theoretical plot of reflectance vs angle from prism-coupled, long-range surface magnetoplasmon in nickel for positive (R_+), negative (R_-), and no (R_0) saturating magnetic field. $n_0 = 1.7788$, $n_1 = n_3 = 1.5$, $d_1 = 0.5 \mu\text{m}$, $d_2 = 20 \text{ nm}$, and the other parameters are as in Fig. 4.1.

prism-coupled, long-range surface plasmon resonance. They are plotted in Fig. 4.4 for the same geometry as that used for Fig. 4.3. Also plotted is R_0 , which demonstrates the resonant nature of the differential reflectance around the surface plasmon resonance. Figures 4.3 and 4.4 illustrate the origin of the differential reflectance as a shift in both the position and width of the plasmon resonance and a change in the minimum reflection due to a change in coupling efficiency. The figures also show how the finiteness of the coupling layer and the addition of a semi-infinite prism layer cause asymmetry in the otherwise symmetric, double-interface plasmon geometry, producing behavior in the differential reflectance that is dissimilar for the two directions of the applied magnetic field. In Chapter 6 the differential reflectance term $\Delta R_{\pm} = R_{+} - R_{-}$ is used to compare theoretical with experimental results, since the experimentally applied field was modulated sinusoidally about zero.

4E.1. Effect of Modal Properties on Differential Reflectance

Because the surface magnetoplasmon polariton in a magnetic metal is quite lossy, its properties are significantly affected by the presence of the prism. Consequently, the behavior of the differential reflectance depends only qualitatively on the propagation constants of the freely-propagating mode described in Sect. 4D. A better understanding is developed using the constants of the prism-coupled mode.

Just as the propagation constant of a bound surface plasmon mode for a three-layer stack is a pole of the three-layer reflectance, the propagation constant of a leaky, prism-coupled plasmon mode is a pole of the four-layer reflectance. Near the resonance angle, the reflectance from the prism coupler can be approximated by the expression [129]

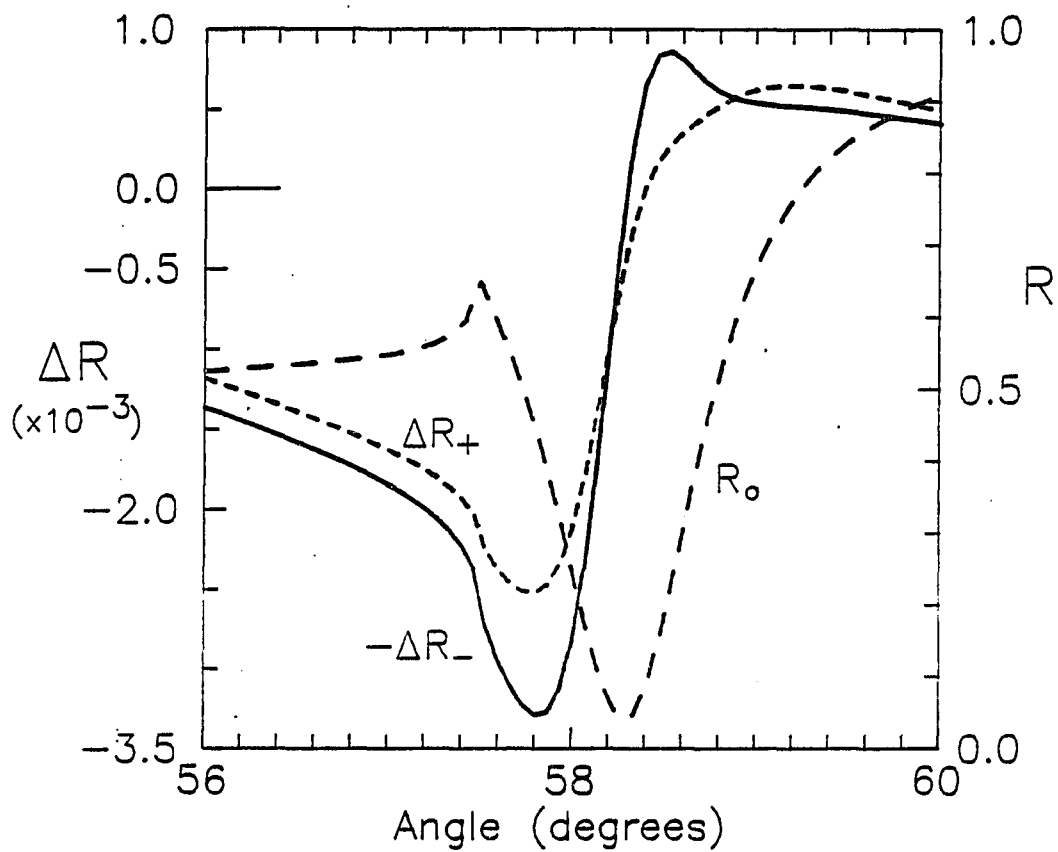


Fig. 4.4. Differential reflectance of the prism-coupled, long-range surface magnetoplasmon

Calculated for material parameters of Fig. 4.3; $\Delta R_+ = R_+ - R_0$ and $\Delta R_- = R_- - R_0$; Fresnel reflectance, R_0 , is shown with dotted line.

$$R(\theta) = |\rho_0|^2 \cong K_0 \left| \frac{\beta - \beta_z}{\beta - \beta_p} \right|^2, \quad (4.28)$$

where $\beta = n_0 \sin \theta$, K_0 is a constant, and β_z and β_p are the complex zero and pole of the reflectance, respectively. An applied magnetic field induces changes in β_z , β_p and K_0 which affect the reflectance resonance. A simplified view of the resonance indicates that the differential reflectance depends on three factors: the angular shift of the resonance center, $\Delta\theta_{\min}$, as a fraction of the resonance width, $\delta\theta$; the relative change in the resonance width, $\Delta(\delta\theta)/\delta\theta$; and a change in the minimum reflectance, $\Delta\tilde{R}_{\min}$. From Eqs. (4.28), (2.36) and (2.37), these quantities are related approximately to the zero and pole of the reflectance by the expressions

$$\sin\theta_{\min} \cong \frac{\beta'_z}{n_0} \quad (4.29)$$

and

$$\delta\theta \cong \frac{2\beta''_p}{n_0 \sin\theta_{\min} \cos\theta_{\min}} \quad (4.30)$$

for the usual case of $\beta''_p \gg \beta''_z$, such that

$$\Delta\theta_{\min} \cong \frac{\Delta\beta'_z}{n_0 \cos\theta_{\min}} \quad (4.31)$$

and

$$\Delta(\delta\theta) \cong \frac{2\Delta\beta''_p}{n_0 \sin\theta_{\min} \cos\theta_{\min}}. \quad (4.32)$$

The profile of ΔR as a function of angle is essentially the difference between two Lorentzians of slightly different widths which are shifted both in angle

and depth. This combination can take a variety of shapes depending on the sign and magnitude of the three factors, but usually it is a resonant curve with a positive local extremum on one side of the angle of minimum Fresnel reflectance and a negative local extremum on the other side, as in Fig. 4.4. It resembles a skewed derivative of the resonance. The maximum extent of $\Delta R(\theta)$, i.e. the difference between the two extrema, varies roughly as

$$|\Delta R|_{\max} \sim \frac{\Delta\theta_{\min} + \Delta(\delta\theta)}{\delta\theta} \sim \frac{\Delta\beta'_z \sin\theta_{\min} + 2\Delta\beta''_p}{2\beta''_p}. \quad (4.33)$$

$\Delta\tilde{R}_{\min}$ is usually small compared to $|\Delta R|_{\max}$ and primarily affects the mean value of the $\Delta R(\theta)$ curve.

Other factors which affect $|\Delta R|_{\max}$ but are difficult to quantify apart from exact calculation are the depth of the reflectance resonance and the overlapping of the resonance with the critical angle. The resonance depth depends on the prism-coupling efficiency, and a smaller depth is expected to yield a smaller $|\Delta R|_{\max}$, all other factors being equal. Near the critical angle between the prism and substrate, κ of the substrate is very nearly zero, so that the optical impedance given by Eq. (4.7) is also very small, and the reflectivity between the substrate and metal is dominated by the properties of the metal. The effect of an applied magnetic field on the metal's impedance is enhanced in the expression for reflectivity. This can cause the magnitude of the differential reflectance to be larger on the low-angle side of the resonance than on the high-angle side, as seen in Fig. 4.4.

Because of the inherent asymmetry of the prism-coupled surface magnetoplasmon polariton, the differential reflectance does not exhibit the same dependence on the magneto-optic coefficient, Q , as that of the bound mode.

Considering the expression for reflectance, Eq. (4.17), it is seen that the single-interface reflection coefficients enter individually, not just in tandem as in the dispersion equation, Eq. (4.22). As a result, the magnitude, $|\Delta R|_{\max}$, of the differential reflectance depends to the first order on Q_0 . However, the angular profile of ΔR retains essentially the same relative shape independent of Q_0 , due to the standard Lorentzian shape of the reflectance resonance and to its large width compared to the field-induced shifts. The extrema of ΔR are located at angles where the slope of the reflectance is greatest. Different shapes are seen for different phases, ϕ , of Q , which will be discussed in Chapter 6 in connection with experimental measurements.

4E.2. Comparison of Single-Interface and Long-Range Modes

As mentioned earlier, other researchers have experimentally excited the single-interface magnetoplasmon polariton on magnetic metal films via prism coupling in the Kretschmann geometry, and have measured the accompanying differential reflectance [119-122]. They interpreted the angular positions of the two differential reflectance extrema as measures of β' of the surface magnetoplasmon polaritons for oppositely-directed magnetization. From the discussions above, this is seen to be an incorrect interpretation, since the shift of the normalized propagation constant for the single-surface mode is on the order of 10^{-4} and is proportional to Q_0 . According to the previous interpretation, the extremum would be separated by several hundredths of degrees in angle, not several degrees as they are experimentally. In addition, the extremum positions of ΔR are independent of Q_0 , and are observed even for a dc-biased, modulated magnetic field.

The Kretschmann and Otto geometries may be used to excite the single-interface magnetoplasmon. Their Fresnel reflectance properties for surface plasmons on nickel were presented in Section 2D.1 and Fig. 2.9, showing that the reflectance minima for the single-surface geometries are dominated by the pseudo-Brewster effect of a lossy metal, which washes out the plasmon resonance. In Fig. 4.5 the theoretical, differential reflectance properties are compared for the same material systems. R_{\pm} exhibits resonant behavior around the reflectance minimum, and the magnitude of the effect is similar for long-range and single-interface geometries. Although the single-interface geometries are dominated by the pseudo-Brewster effect, there is qualitative agreement with the dependence of $|\Delta R|_{\max}$ on the modal properties expressed in Eq. (4.33).

The differential reflectance of the prism-coupled, long-range surface magnetoplasmon polariton depends strongly on the material parameters of the metal film, coupling layer and substrate. Since Chapter 6 presents experimental data from magnetoplasmon polaritons for a variety of material parameters, the theoretical discussion is continued there.

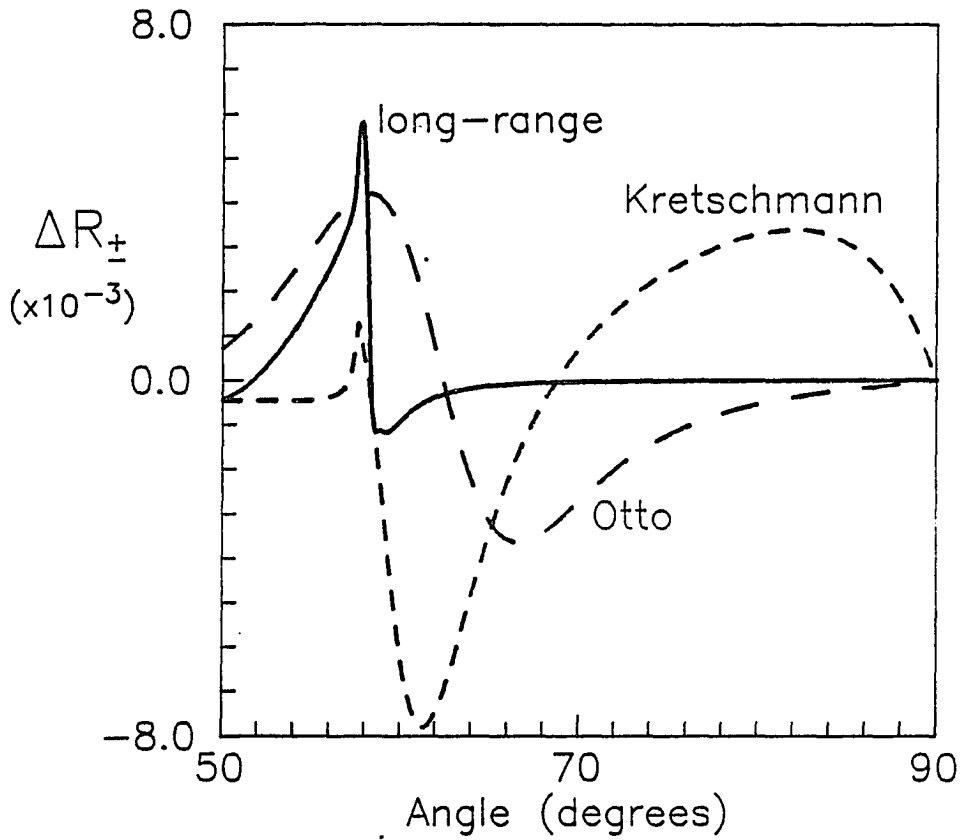


Fig. 4.5. Differential reflectance in single-interface and long-range mode geometries

$\Delta R_{\pm} \equiv R_{+} - R_{-}$ for prism-coupled magnetoplasmons in Kretschmann (short-dashed), Otto (long-dashed) and long-range (solid) geometries. Material parameters are the same as in Fig. 2.10, and $Q = 1.08 \times 10^{-3} \exp[i(-33.7^{\circ})]$.

CHAPTER 5

EXPERIMENTAL APPARATUS FOR THE STUDY OF SURFACE MAGNETOPLASMON POLARITONS

Experimental verification of prism coupling to the long-range surface magnetoplasmon polariton was accomplished using the apparatus described in this chapter. In the process, the relevant optical parameters of the material systems under investigation were characterized. Two different experimental layouts were used for the measurement of reflectance and differential reflectance from two types of samples, as a function of angle. The first sample type consisted of a thin nickel film on a glass substrate, for which the reflectance at the metal-air interface was measured. The second type sample consisted of a high-index prism-coupler, a liquid coupling layer, and a thin nickel film on a glass substrate, for which the reflectance from the base of the coupler was measured. This chapter details the two experimental setups in turn. Components which were common to both setups are discussed in the first section. The methods of calibrating the experimental data for comparison with theory are described. For each of the setups, some of the general difficulties encountered in data-taking and the solutions to the difficulties are discussed. Details of the sample properties and additional discussion of the experiment are included in Chapter 6.

5A. Bare Sample Reflectance Measurements

5A.1. Apparatus

Historically, the early transverse Kerr-effect measurements were performed with light incident from air onto a magnetic material. In order to duplicate this measurement for the samples used in the present research and to characterize the optical constants of the nickel, the setup shown in Fig. 5.1 was assembled. A 15 mW He-Ne laser, Spectra Physics model 124B, was used as the source of light at 632.8 nm wavelength. A half-wave plate permitted rotation of the polarization, and a periscoping mirror pair enabled the vertical positioning of the beam.

The samples were aligned on a shaft centered on the axis of an Aerotech model ARS 304 rotation stage. The rotation stage had a 0.004° resolution. Two orthogonal translation stages in the horizontal plane aided the alignment. A sprocket with 24 teeth was attached to the shaft, and another sprocket, with 17 teeth, was free to turn around the shaft, suspended by an aluminum collar and teflon sleeve. An identical set of sprockets, their relative positions reversed and both attached to another shaft, were connected to the first set by plastic link chain. Since $(24)^2 \cong 2(17)^2$, the net effect was a rotation of the second sprocket on the rotation stage at twice the angle of the first sprocket. An arm carrying a lens and p-i-n silicon detector was attached to the second sprocket so that, with proper alignment, the light specularly reflected from the sample was collected by the detector. For differential reflectance measurements, the detected signal was sent through an Ithaco current-to-voltage preamplifier to an Ithaco, model 393, lock-in amplifier. Output from the lock-in amplifier was measured by a digital voltmeter. For Fresnel reflectance measurements, the detector signal was sent through the preamplifier directly to the voltmeter.

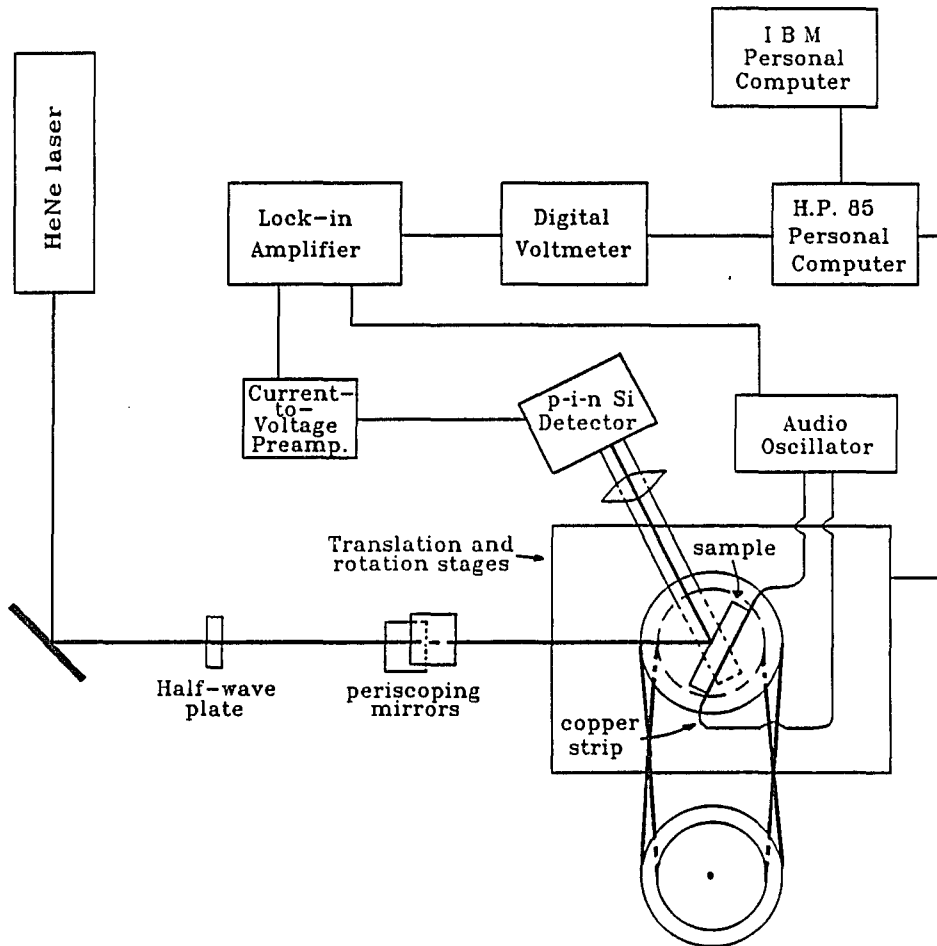


Fig. 5.1. Bare reflectance measurement apparatus

Control of the experiment was centered in a Hewlett-Packard 85 personal computer, which directed the rotation stage to set the angular position of the sample and collected data from the digital voltmeter. The computer was connected to the other equipment via IEEE-488 interface buses. Software in the BASIC language was written by colleagues Allan Craig, Grieg Olson, and Richard Booman, and was modified by the author; it automated the collection and storage of data.

Data files were transferred to an IBM Personal Computer for calibration, plotting, and comparison with the theoretical results. On the IBM PC, the experimental curves were matched to theoretical ones, using software written by the author, in order to measure the sample parameters and to verify the excitation of the long-range surface magnetoplasmon polariton.

As discussed in Chapter 4, a reflectance modulation is induced by an external magnetic field applied to the nickel film. Various schemes for applying the field were tested until a suitable one was found. They are depicted in Fig. 5.2. The first consisted of a C-shaped, iron-core electromagnet with a radius of 2.5 cm, approximately 90 turns of copper wire, and a gap of 5 mm. Fringing magnetic fields in the gap region were expected to induce the transverse Kerr magneto-optic effect. Because the nickel films were deposited on microscope slides with a width of one inch and a length of one to three inches, the samples could not be placed directly between the poles of the magnet. They were placed on the face of the "C", in the weaker fringing fields. With the laser beam directed at the sample area in front of the pole space, and an ac current of 1.0 amp rms in the electromagnet, only a very small and noisy differential reflectance signal was detected through the lock-in amplifier. The setup was also bulky and would not allow an easy transfer from the transverse to the longitudinal magnetic-field configuration.

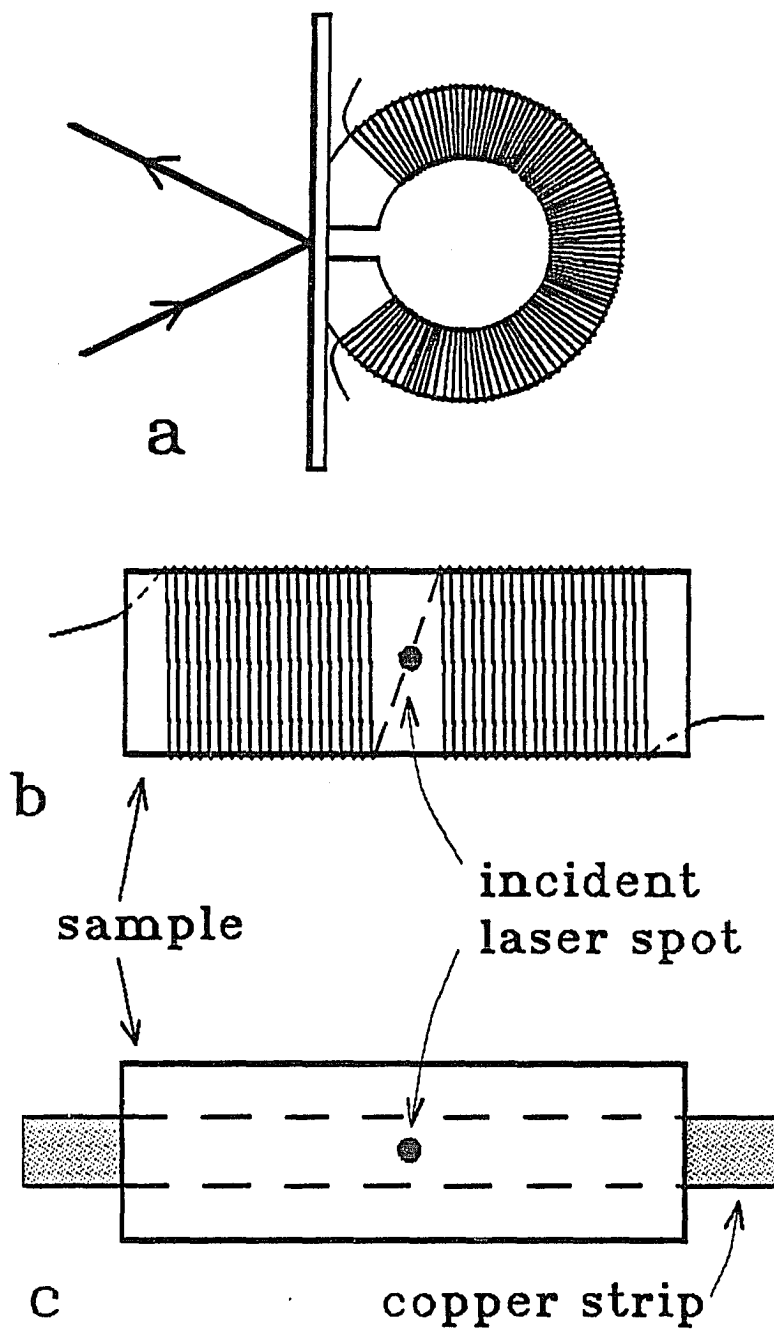


Fig. 5.2. Transverse, magnetic-field application schemes

a) C-shaped electromagnet, b) solenoid, c) conducting strip (used in this work).

The second scheme for applying a magnetic field to the sample was a solenoid configuration with the sample as the core. Approximately 100 turns of copper wire were wound around the glass substrate and deposited nickel film. At the sample center, two adjacent turns were separated by about 6 mm to allow reflection of the laser beam. A 1.0-amp ac current was passed through the wire, which produced a magnetic field in the plane of the metal film. In this scheme the signal-to-noise ratio of the differential reflectance was larger, and the apparatus was lighter than in the first scheme. However, the small separation of wire turns at the sample center, which was necessary to insure a uniform transverse field, did not allow for a prism on top of the sample, as required by the second experimental setup. A separation of 20 mm was attempted, but it produced a signal which was weaker and which had angular characteristics that did not match previous measurements or theoretical calculations. Polar fringing fields at the center of the sample were suspected to be the cause, due to the large wire separation.

The third applied-field scheme resulted in the optimal configuration for both experimental setups. A 30- μm -thick copper strip was attached to the back of the substrate with double-sided tape, and an ac current was passed through it [130]. As long as the strip was wide relative to the laser spot on the sample, the magnetic field which encircled the strip was uniform and parallel to the sample over the area of the spot. The length of the strip was approximately 7.5 cm., giving it a resistance of between 0.13 and 0.077 Ω , depending on the strip width, which was between 7 mm and 12 mm. Most of the measurements were taken using the 7-mm strip. A current of up to 5.0 amps rms (the limit of the source) could be passed through it, with manageable resistive heating. From an Ampere's Law analysis, the dc magnetic field (in amperes/meter) induced a distance s away from the center of a conducting strip

is $H = (I/\pi w) \tan^{-1}(w/2s)$, where w is the width of the strip and I is the dc current in the strip. A narrow strip produced the largest field, and thus the best signal-to-noise ratio, which required the shortest time constant at the lock-in amplifier. For the 7-mm-wide strip and the 5.0-amp rms current used for most of the measurements, the peak, induced magnetic field was calculated to be approximately 420 amps/m, or 5.2 Oe.

The current was supplied by an audio oscillator which produced an approximately sinusoidal signal. A frequency of 3.0 kHz was chosen because it resulted in a low noise level and a fairly good sine-wave signal. A pure sinusoidal reference signal from the oscillator was sent to the lock-in amplifier.

5A.2. Alignment and Calibration

Careful alignment of the optical system and sample was performed to maintain the tracking of the detector with the reflected laser beam over a large angular range. First, the top periscoping mirror was adjusted to insure a horizontal beam path between the mirror and sample and a vertical centering of the beam spot on the sample. Next, the beam was tilted downward and rotated from the top periscoping mirror to center it on the shaft of the rotation stage. It was then returned to horizontal.

To center the sample on the rotation shaft, the sample was mounted parallel to one of the two orthogonal translation stages and initially aligned perpendicular to the incident beam. After being centered horizontally in the beam, the sample was rotated 90° and adjusted by the other translation stage such that the beam was centered on the sample edge. Because of the finite size of the laser beam and the sample, the largest angle at which the beam remained completely on the sample was

about 85° . The angular zero (normal incidence) was set by reflecting the incident light back through a pinhole placed in the beam path 120 cm from the sample. This insured an angular precision of approximately $.02^\circ$.

The final step in alignment of the optical system was the positioning of the detector. The detector arm could be disengaged from the secondary sprocket to allow for the initial alignment procedures. The sample was then rotated to an arbitrary position between 0° and 90° , and the detector was locked into intersection with the reflected beam. Due to slack in the sprocket chains, the detector usually had to be readjusted slightly after an initial rotation of the stage. Detection of the whole beam was checked over the entire angular range of the measurements, and the automated measurements were taken only with increasing angle to eliminate backlash problems. Recently the chains have been replaced by gears to eliminate most of the backlash. Vignetting of the incident beam by the detector arm limited the incident angle to above about 7° . At the end of a set of measurements on a given sample, the sample was removed and the detector arm was rotated into coincidence with the beam path to measure the incident power of the laser beam, enabling a reflectance calibration.

5A.3. Experimental Problems and Solutions

The accurate measurement of incident power in the bare reflectance setup was made difficult by the nature of the detector assembly. Because the sample holder had to be disconnected from the shaft of the rotation stage prior to the measurement, the detector arm was loosened such that it required manual positioning in the incident beam path. Nonuniformity across the detector surface created an uncertainty in the detected power. Consequently, some of the data was

re-normalized based upon the known properties of TE and TM reflectance as a function of angle. Section 6B discusses the correction. The detector was stationary in the prism-coupling setup described in Section 5B, alleviating the normalization problem.

A succession of trials and errors by the author led to the detection method used for differential reflectance measurements in the first experimental setup. The history is recounted here to inform the experimenter who may try similar measurements, although no claim is made that the end result is the absolute optimum configuration. The majority of the problems stemmed from the fact that the differential reflectance measurement involves the detection of a small ac signal on a large dc bias. In contrast to the polar and longitudinal Kerr magneto-optic effects, the transverse effect cannot be separated from the Fresnel reflectance by a crossed polarizer. Because some types of noise are proportional to the strength of the total signal, a fundamentally greater problem is encountered with the transverse orientation than with the other two. A second disadvantage of a large dc signal is the saturation of the detection system.

The preamplifier converted current from the silicon detector to a corresponding voltage for input to the lock-in amplifier. Preamplifier settings were 10^4 , 10^6 , and 10^8 V/A. At the two higher preamplifier settings, the total detection noise increased with laser power at a rate lower than the amplified dc signal. However, the laser power could only be increased to about 0.1 mW before saturating the preamplifier at the middle setting and quenching the signal. To counteract this problem, a simple RC high-pass filter was inserted after the detector to prevent dc current from flowing to the preamplifier.

It was then discovered that the lock-in amplifier was saturating, and an additional high-pass filter was inserted between the preamplifier and lock-in amplifier. Although this resolved the saturation problems, a spurious signal was detected by the lock-in amplifier. The signal also occurred when light was reflected from a nonmagnetic metal sample, but not in the dark current from the detector. It was postulated that the false signal originated from direct modulation of electron flow at the face of the detector due to the fringing, applied magnetic field, which was intended only for the sample. Upon removing the filter from between the detector and preamplifier, the false signal disappeared. This confirmed the hypothesis that the filter, which prevented dc current flow, was causing a high density of photoelectrons to accumulate on the detector face, close enough to the sample to allow interaction with the magnetic field. The detector arm was necessarily short to decrease the torque it exerted on the center rotation shaft. Attempts at shielding the detector did not alleviate the crosstalk. Because of the original saturation problem, the only solution was to return to the lower (10^4 V/A) preamplifier setting and use a long time-constant in the lock-in amplifier to average out the noise. As will be seen in the next section, the second experimental setup eliminated the spurious signal problem by having the detector far removed from the sample.

5B. Prism-Coupled Sample Reflectance Measurements

5B.1. Apparatus

The second experimental setup used in the present study served the same basic function as the first, that of measuring reflectance and differential reflectance as a function of angle. However, the addition of a prism-coupler and fluid coupling

layer to the sample allowed this setup to detect the presence of the long-range surface magnetoplasmon polariton. The three major changes from the first setup were the prism-coupler, the sample holder, and the position of the detector. They are described in this section. The experimental setup is pictured in Fig. 5.3.

Most experiments involving prism coupling to waveguide modes rely on a prism with a triangular-shaped cross-section. Those that require measurement of the exit light beam, composed of specularly reflected and reradiated components, often use an isocles prism so that the incident and exit optical paths are symmetric. With these prisms, the difficulty remains that as the incident angle is changed, the exit angle also changes. A tracking mechanism must be devised to keep the detector aligned in the beam. The presence of the prism makes tracking even more difficult than for a reflection in air since the beam walks along the prism base as the angle is scanned, due to refraction at the prism face. If this cannot be compensated by collection optics at the detector, the tracking mechanism must be fairly complex. An additional uncertainty lies in the fact that a different part of the sample is probed at different angles of incidence. If the sample, substrate, or coupling-layer properties vary along their length, an accurate measurement cannot be made.

Both of the difficulties encountered with a triangular coupling prism are eliminated by the use of a hemispherical retroreflecting prism-coupler [131]. Developed by the author's colleagues for the study of long-range surface plasmon polaritons, the hemispherical retroreflecting prism-coupler has been used successfully in several research programs including the present one [50, 54, 123]. As mentioned earlier, the term "prism" is applied here to the hemispherical coupler because of its purpose, not its shape. The hemisphere, polished from SF56 glass, was cut in half and polished on the cut surfaces. A thick aluminum film was deposited on each of

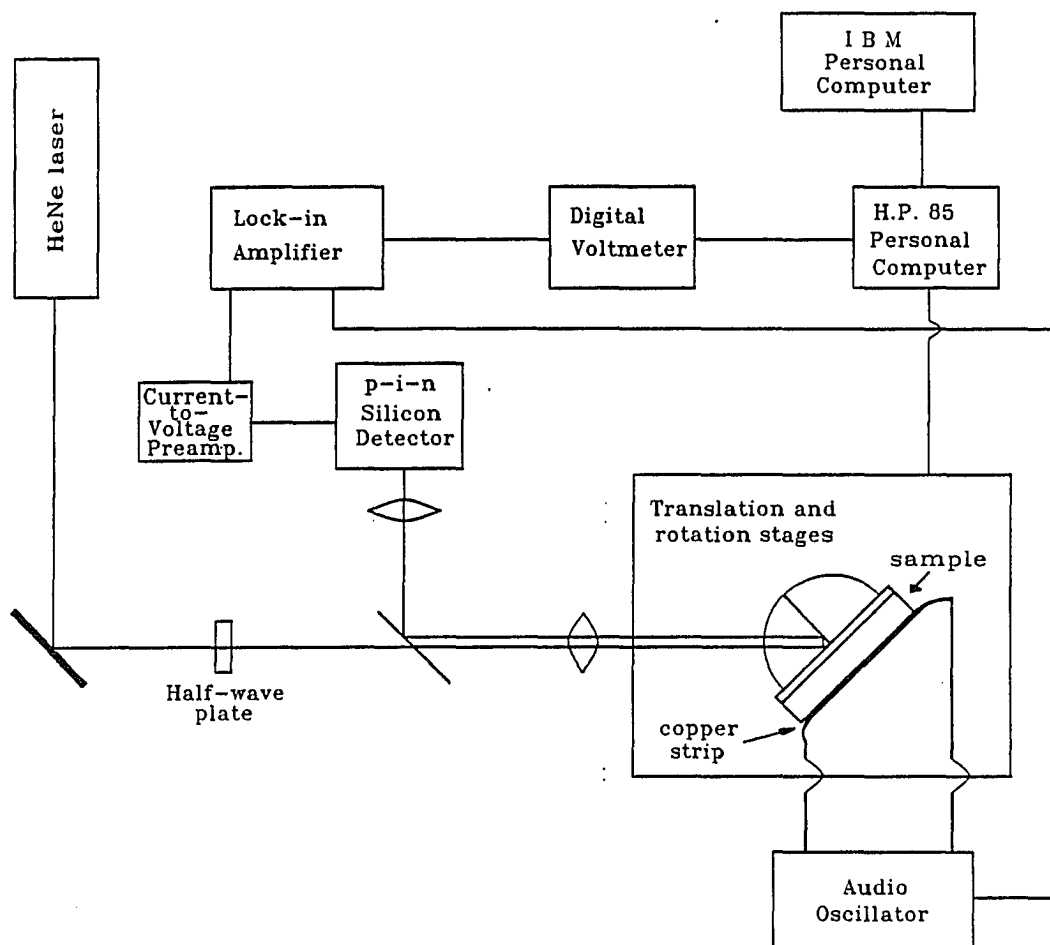


Fig. 5.3. Prism-coupled, reflectance measurement apparatus

the cut surfaces, and the halves were rejoined with cement. Final polishing of the hemisphere base assured a smooth coupling surface. The radius of the hemisphere is 11.8 mm.

The resulting prism, when accompanied by the compensating lens mentioned below, produces a retroreflection of the laser beam after it reflects from the prism base. Because of the hemispherical shape, incident and reflected beams are not refracted significantly at the air-prism interface, as long as the beam is aimed at or near the center of the prism base. The retroreflected beam returns parallel to the incident beam path, regardless of the angular position of the sample. Thus, a beam splitter can be inserted in the two parallel paths to split off the reflected beam for measurement by the detector. The advantages of this setup are as follows, assuming the beam is centered: 1) the incident and exit angle of the central ray are the same in both air and prism, allowing direct angular calibration; 2) reflection losses at the air-prism interface are constant regardless of angle; 3) there is no walkoff of the beam along the sample and, consequently, no beam walkoff on the detector; and 4) the detector is fixed, requiring no tracking mechanism. These advantages make the measurement of optical properties via prism coupling simpler and more accurate. Although the hemispherical retroreflecting prism-coupler is not a stock item and is more expensive than the traditional triangular prisms, several years of use have proven it to be well worth the cost.

Because the prism has a curved surface, it focusses a collimated incident beam. This was compensated by a lens in front of the prism which focusses the collimated incident beam to the focal point of the prism so that it is collimated again inside the prism. After reflection from the prism base, the beam is retroreflected at the thick aluminum film and retraces an equivalent path back through the prism,

emerging collimated from the lens. A shearing plate in the retroreflected, beamsplit beam monitored the degree of collimation while the lens position was adjusted. The respective focal lengths of the lens and prism, 15 mm and approximately 65 mm, produce a 4.3-times reduction in the beam diameter inside the prism. The 3-mm-diameter beam from the laser as it enters the lens becomes approximately 0.7 mm inside the prism. The beam width projected onto the prism base was between 0.8 mm and 4 mm for the incident angles of 30-80° scanned in reflectance measurements, and approximately 1.3 mm at the surface plasmon excitation angle. Further details of the lens and prism system can be found in Ref. 19.

The coupling layer was one of three Cargille index-matching liquids, a drop of which was placed on the sample surface before the prism was contacted. Its refractive index at 25° C and a wavelength of 632.8 nm could be extrapolated from the manufacturer's data at .5893 μm and .6563 μm . However, the sample was heated approximately 11° above ambient temperature by resistive heating of the copper strip and an additional 4° by the rotation stage. This resulted in a change in the refractive index. Although the sample temperature could not be measured accurately, the coupling liquid's index was accurately inferred from the reflectance measurement, as described in Appendix A.

The sandwiched prism, coupling liquid, and sample were held on an Aerotech rotation stage by a machined holder designed to maintain the coupling layer at a fixed thickness with a spring-loaded micrometer, as shown in Fig. 5.4. The micrometer head pressed against an aluminum shim holding a 2-mm-diameter cylindrical piece of rubber, onto which the sample and prism were mounted. The rubber piece distributed pressure evenly along its length to insure a fairly uniform coupling-layer thickness. Support for the prism apex was provided by a teflon cup.

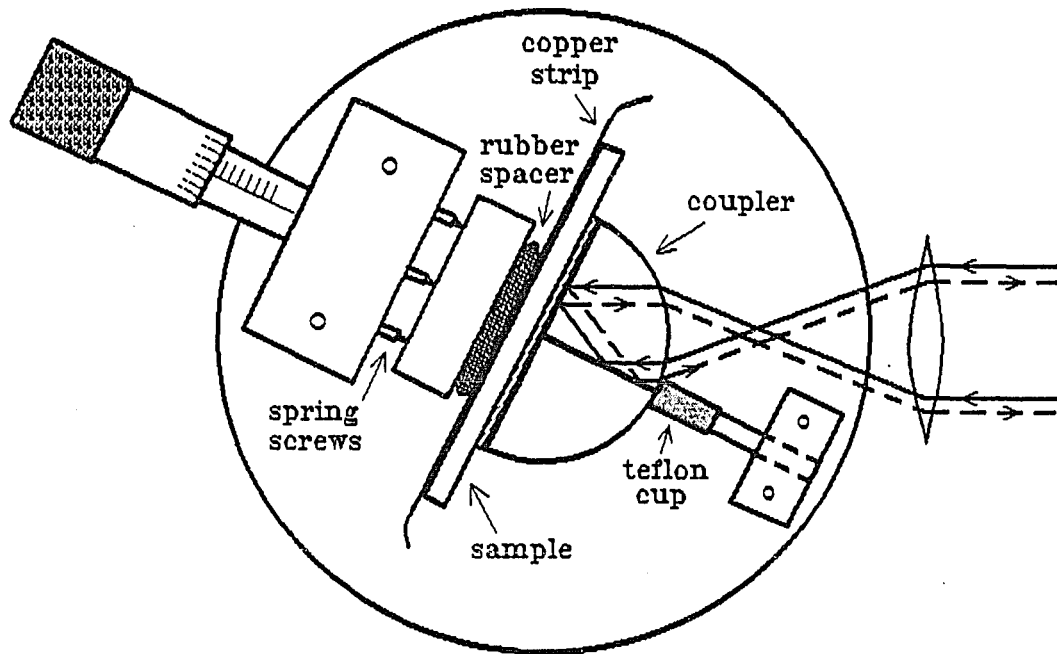


Fig. 5.4. Prism-coupler sample holder (not to scale)

It was adjusted perpendicular to the prism base to center the prism, but was then fixed for successive sample changes.

Laser speckle around the incident beam was blocked by an adjustable aperture. A pellicle beamsplitter was inserted in the laser beam path to split off the retroreflected beam for detection. Light was focussed onto the p-i-n silicon detector by a 5:1-power microscope objective. The stability of the detector output while moving the detector around its central position indicated that the entire beam was collected.

5B.2. Alignment and Calibration

To prevent walkoff of the beam on the sample and on the detector as the angular position changed, the retroreflecting prism corner was centered on the rotation axis of the stage, and the laser beam was aligned through that axis. Alignment was made easier by the symmetry of the two sides of the prism. The prism-sample mount was designed so that a line between the micrometer and the teflon mounting cup passes through the rotation axis. Only minor adjustment had to be made perpendicular to the line. Most of the alignment consisted of centering the prism along the line, moving the entire rotation stage and prism mount horizontally relative to the beam, and tilting the prism to keep the retroreflected beam from walking vertically. Instructions for the procedure are outlined as follows:

- 1) Rotate the prism to an arbitrary angle, θ , on the right side of the prism as seen by the incoming beam (considered to be a positive angle for the purpose of discussion).

2) Center the incident beam spot at the corner of the retroreflector (center of the prism base) using the translator which moves the whole rotation stage perpendicular to the beam.

3) Note the position of the retroreflected spot which is beamsplit to the detector.

4) Rotate to the equivalent $-\theta$ on the left side of the prism and note the position of the retroreflected, beamsplit spot.

5) If the position of the spot is different for the angles θ and $-\theta$ then the retroreflecting corner is not centered or tilted properly. Rotate the prism back to the positive angles and scan a large range of increasing angle while watching the position of the spot at the detector position. Adjustment is made by one or both of the following methods, depending on whether movement of the spot is in a horizontal or vertical direction:

a) horizontal movement: if the spot moves right as angle increases, adjust the micrometer to move the prism and sample toward the micrometer; if the spot moves left, move the sample away from the micrometer.

b) vertical movement: if the spot moves up as angle increases, tilt the prism up at the side towards the micrometer; if the spot moves down, tilt the prism down.

6) Re-center the incident spot at the retroreflecting corner as in instruction (2) and note the amount and direction of translation needed.

7) Repeat instructions (1) - (6) until alignment is achieved. The differences in beam spot position and the degree of adjustment should decrease with each iteration.

The ideal vertical position of beam incidence on the prism is at the center of the hemisphere, where the retroreflected path is identical to the incident path. However, at this position of normal incidence, some of the light reflected from the face of the prism is collected by the detector as a spurious signal in the Fresnel

reflectance measurements. The lens was translated slightly in the vertical direction to cause the stray light to be deflected from the incident beam path.

Due to the presence of the prism and holder, reflection at normal incidence could not be used to zero the angular rotation stage as a calibration. The most prominent and stable feature of the angular reflectance profile which could be used for calibration was located at the critical angle between the prism and the thick substrate, $\theta_c = \sin^{-1}(n'_{\text{sub}}/n'_{\text{pr}})$. As this angle is approached from lower angles, the reflectance increases toward unity. For lossy metals such as nickel, in the coupling geometry for the long-range surface plasmon, the reflectance does not reach unity near θ_c . However, due to the large plasmon resonance width and the proximity of the resonance to cutoff, the reflectance exhibits a well-defined local maximum at θ_c for a near-symmetrically-bounded metal film. In fact, theory shows the maximum to be a sharp cusp, unlike the other reflectance features. Theoretical calculations and experimental plots demonstrate that even for a refractive index difference, $\Delta n = n_{\text{cou}} - n_{\text{sub}}$, on the order of ± 0.02 between the coupling layer and substrate, the cusp remains at θ_c , tied to the substrate refractive index. If the refractive index of the coupling layer is significantly larger than that of the substrate, or if the nickel film is fairly thick, the local maximum at the critical angle is broadened as the resonance shifts to higher angles away from the critical angle. If the refractive index of the coupling layer is significantly smaller than that of the substrate, the resonance associated with the surface plasmon is shifted "through" θ_c toward lower angles, becoming a coupling-layer resonance. In the transition, roughly $-0.025 > \Delta n > -0.045$ for a 20-nm nickel film, the feature at θ_c is a rounded step, decreasing in reflectance with angle. For approximately $-0.045 > \Delta n > -0.075$ the feature is a local minimum, and for a larger asymmetry it is a rounded step to

higher reflectance at the critical angle. The sharpness of the critical angle feature is affected by the coupling layer index, but its position is not.

Similarly, variations in the other parameters (index or thickness) of the four-layer prism-coupling stack do not alter the position of the critical angle feature, with the obvious exception of the prism refractive index (see Appendix A for illustration). This enables a definitive measurement of the substrate index if the prism index is known and the critical angle is measured. The angular position of normal incidence to the sample was determined as the midpoint between the positions of the critical angle feature on each side of the symmetric, retroreflecting prism. A digital readout of the rotation stage angle made this a simple procedure. Depending on the sample parameters, normal incidence was determined to within a maximum uncertainty of 0.02° .

In the hemispherical, retroreflecting prism-coupler geometry, the reflectance from the prism base is modified by reflection from the retroreflecting aluminum film. Reflectance from a thick aluminum layer was calculated, as a function of angle, from the dielectric constant of aluminum, $-46.4 + i16.7$ at a wavelength of 632.8 nm [132]. Experimental reflectance measurements were adjusted by multiplying the reflectance at each incident angle by the inverse reflectance of aluminum at the incident angle's complement, since the aluminum film is oriented 90° to the prism base. All other reflection losses are essentially constant, regardless of angle, and were ignored.

The measurement of the effective incident power, which was used to normalize the experimental reflectance data, relied on the properties of the prism coupler. Because the prism is in an attenuated total reflection geometry, the reflectance approaches unity at large incident angles. The reflected power measured

at an angle much larger than the critical angle should be an accurate value for the effective incident power, after adjustment for the retroreflection. In practice, vignetting of the beam occurs at large angles near grazing incidence, due to the finite size of the prism and of the beam. Particulate matter or coupling fluid at the edge of the prism face may also affect the reflectance at large angles. Therefore, in this study the maximum reflected power measured above the critical angle was used for normalization, and the method was very accurate for most cases. Greater uncertainty was encountered with the thicker nickel samples and for a large coupling-layer index. The surface plasmon resonance is wider for these cases and the reflectance approaches unity at larger angles, at which the measurement was prone to inaccuracy. In the few cases where the maximum reflected power was obviously inconsistent with other data, the average from the other data was used.

After experiencing some difficulties in understanding the experimental reflectance data in terms of the theoretical model, it was discovered that the p-i-n silicon detector signal was not linear with laser power. A calibration curve was constructed using a United Detector Technologies model 350 optometer. Fig. 5.5 plots the actual detected power, P , measured by the optometer, vs the preamplified detector voltage, V . To make conversion of the computer data files simpler, an algorithm which related P to V was sought. Two possible relationships were hypothesized:

$$P = K \frac{V}{1-aV} \quad (5.1a)$$

and
$$P = K V \exp(bV) \quad (5.1b)$$

where P is given in milliwatts, V is given in volts, and K , a , and b are constants.

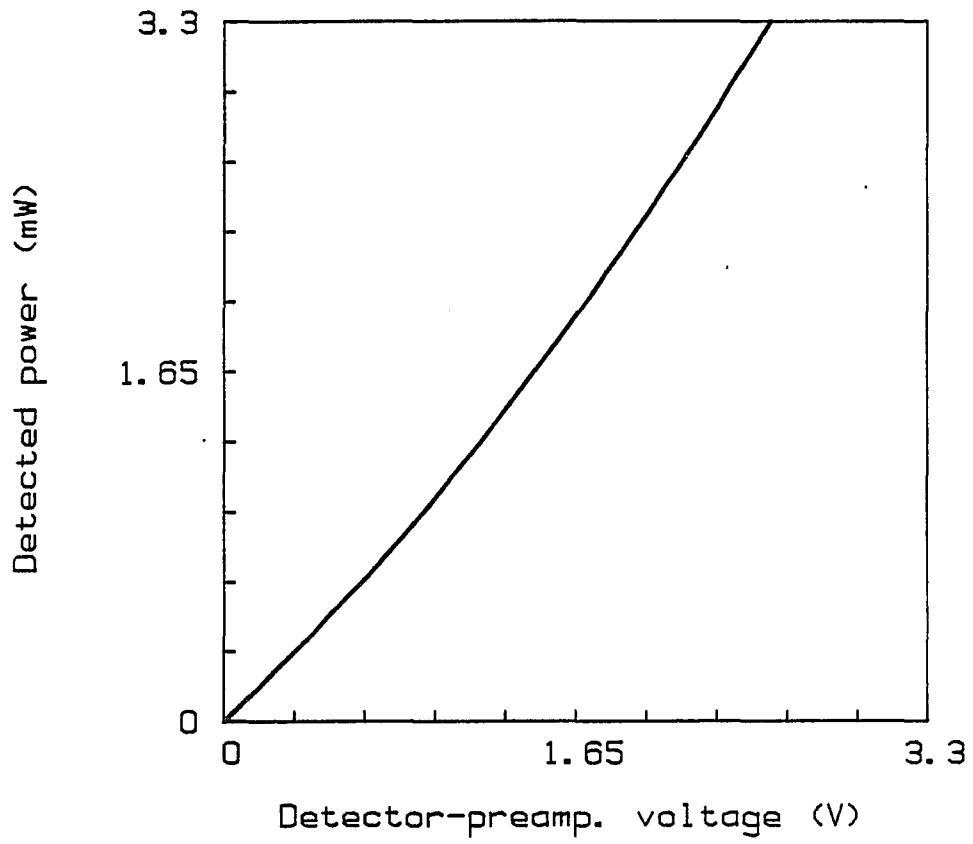


Fig. 5.5. Detector calibration curve

Both of these relationships were tested, and the constants were determined which yielded the lowest average relative deviation of calculated power from measured power over the range of measurement. Relationship (5.1a) produced the best fit, having a 1.4% average deviation, compared with 1.8% deviation using relationship (5.1b). The best-fit constants were $K = 1.0$ and $a = 0.0866$. They were used to convert the voltage data into laser power data using (5.1a). With the conversion, the experimental and theoretical results matched very well, as discussed in Chapter 6.

5B.3. Experimental Problems and Solutions

Several questions and difficulties were dealt with in the experimentation phase of this research. The development of a solid theoretical foundation and a computer model of the relevant parameters prior to the experiment greatly aided the interactive research process, which involved seesawing between experiment and theory. This section presents various side issues of the experimental procedure which were essential to correct interpretation of and confidence in the results described in the next chapter.

As mentioned above, fellow researchers used similar apparatus to study long-range surface plasmon polaritons in thin silver films. Their research showed that the angular resolution required to properly measure the width of reflectance resonances necessitated spatial filtering and re-collimation of the laser beam before it entered the lens and prism system. However, because nickel is quite lossy, the angular resonance width associated with excitation of the long-range surface plasmon in a nickel film is about 30 times larger than that for a silver film at the wavelength of 632.8 nm. In the present study, reflectance measurements were made with and without a spatial filter and collimating lens. The results were virtually identical in

the two cases, indicating that any irregularities in the spatial profile or divergence of the beam did not affect the reflecting properties of the prism-coupled plasmon, and the measurements could be interpreted as if the input beam was an infinite plane wave. This allowed the use of the total power available from the laser, which was important in collecting differential reflectance data with a low signal-to-noise ratio in a reasonable amount of time.

Accurate and repeatable measurements of the reflective properties of the sample depended on the stability of its material parameters. The parameters most prone to change were the refractive index of the sample layers as a function of temperature, and the thickness of the fluid coupling layer. The coupling-layer thickness depended on the position of the spring-loaded micrometer on the sample holder; because the fluid was somewhat viscous, the thickness took time to reach its steady state after the micrometer was adjusted. A steady-state condition was observed by monitoring the reflectance at a sensitive angular position such as the surface-plasmon resonance dip. Material parameters were inferred from the reflectance measurements using the methods of Appendix A.

An important aspect of the research was demonstrated during the measurement of differential reflectance from the prism-coupled sample. For Fresnel reflectance measurements, the incident beam was aligned at the center of the retroreflecting corner -- which corresponded with the rotation axis of the rotary stage -- in order to insure the accuracy of angle calibration. In this configuration, half of the incident beam reflects from the sample stack first and then reflects from the thick aluminum film; the other half reflects from the two interfaces in the opposite order. This configuration is suitable for the measurement of Fresnel reflectance, since both halves of the beam are incident at the same angle at each

interface, and both trace an equivalent beam path. However, as discussed in Chapter 4, magneto-optic reflectance depends on the relative directions of the applied magnetic field and of the wavevector of the incident light. The induced changes in reflectance are usually opposite in sign for opposite field directions, though not equal for the inherently asymmetric prism-coupling structure. With a beam incident at the corner of the retroreflecting prism, the two halves "see" the magnetic field applied to the sample in opposite directions. When the halves are recombined, the magneto-optic effects cancel each other. To measure the desired differential reflectance signal, the entire beam must encounter the reflectances in the same order. In the present study, the sample holder was translated horizontally off-center for the differential reflectance measurements, and Fresnel reflectance measurements were made for both centered and decentered beams. This permitted a reliable angular calibration and the measurement of any wedge in the coupling layer.

The reflectance data of centered and decentered beams inferred slightly different coupler-layer thicknesses. The largest thickness difference for any of the samples was $0.05 \mu\text{m}$, measured at angles near the plasmon resonance. The sample was translated by approximately 0.75 mm to decenter the beam at an angle of 60° , such that for this sample the coupling layer wedge (slope) was calculated to be approximately 4.3×10^{-5} . A decentered beam of width 0.7 mm in the prism produces a spot of width 1.4 mm at the prism base, such that the largest variation of coupling-layer thickness across the beam was $0.06 \mu\text{m}$ at angles near the surface plasmon resonance. The primary effect of a small change in coupling-layer thickness is to scale the reflectance at the plasmon resonance but not to significantly change the angular position of the resonance. Theoretical calculations have shown that a small wedge in the coupling layer results in a reflectance profile that is

virtually identical to the reflectance of a uniform layer of average thickness. Therefore, the presence of a coupling layer wedge did not significantly affect the data presented in this study.

Because the measurement of differential reflectance required the incident laser beam to be moved off of the prism center, some of the advantageous qualities of the hemispherical retroreflecting prism appear to be forfeited. As the angle is scanned from 30° to 80° , the beam walks roughly 2 mm across the sample and there is a slight variation in the air-prism reflection loss for the reflected beam. Walking of the beam and a wedged coupling layer is evidenced in the wide angular reflectance scan, but the deviation is very small for the narrow surface plasmon resonance scan, which is of greatest interest. Any walkoff of the reflected beam is handled by the microscope objective in front of the detector. Overall, the hemispherical retroreflecting prism coupler remains an excellent tool for simple and accurate surface wave research.

CHAPTER 6

EXPERIMENTAL OBSERVATION OF LONG-RANGE SURFACE MAGNETOPLASMON POLARITONS IN NICKEL FILMS

In this chapter the experimental data obtained from a study of prism coupling to the long-range surface magnetoplasmon polariton is presented and analyzed. The topics discussed, in their approximate order, are as follows. The deposition of thin nickel film samples is outlined. Reflectance and transverse Kerr differential reflectance from the bare samples are reported for comparison with the results of other researchers. In an attenuated total reflection geometry involving a prism and a coupling liquid, reflectance from the nickel samples shows the presence of the long-range surface plasmon polariton as a resonant minimum in the TM reflectance. Analysis of the surface plasmon polariton resonance and other reflectance features as a function of angle provides a measurement of the unknown dimensions and optical properties of the multilayer structure. With an external, oscillating magnetic field applied transversely to the nickel film, the differential reflectance signal is enhanced due to the presence of the long-range surface plasmon polariton. The experimental data is shown to confirm the theory developed in Chapter 4 when the magnetic properties of the nickel surface are understood. Data from several film samples is presented, allowing a comparison of measurements for varying nickel thickness, coupling-layer thickness, and coupling-layer refractive index.

6A. Sample Preparation

The nickel film samples used in this study were deposited with an electron-beam, vacuum deposition system and supplied by Fred Hickernell of Motorola Inc. [133]. The target material consisted of high-purity (99.999%), "VP grade" nickel slugs, 1/4-inch in diameter and 1/2-inch long. The slugs were held in carbon crucibles approximately 15 inches from the substrate holder, which rotated at 180 revolutions per minute to insure uniform film thickness. The Temescal 270-degree electron-beam gun was operated at 10 kilovolts. The substrates were glass microscope slides, measuring 1 in. x 3 in. x 1 mm. They were cleaned prior to the deposition with an alconox scrub, a deionized water rinse, and a spin dry.

The deposition system was pumped down to a background pressure of 2×10^{-6} Torr, and the substrates were heated to 280 ± 10 °C by quartz lamps. Pre-evaporation conditioning of the target lasted 55 seconds and involved a power-up of the electron-beam source, a pre-heat of the source material, and stabilization at the deposition power level. The deposition rate was approximately 1 nm/sec, and the film thickness was monitored by a quartz crystal mass sensor, with an accuracy of about ± 2.5 nm. A cooling period of at least 30 minutes was allowed before removal of the samples from the bell jar. Three separate depositions produced nickel films of nominally 10-nm, 20-nm, and 40-nm thickness. The films were extremely adhesive to the glass surface and appeared uniform in thickness. Samples #2 and #3 were from the 20-nm deposition, sample #4 was nominally 10-nm thick, and sample #5 was nominally 40-nm thick.

Reflectance measurements reported in this chapter provided an accurate determination of the nickel film thicknesses and substrate refractive index, as well as other parameters, when analyzed according to the methods of Appendix A. The

material parameters are listed in Table 6.1 for each data set. The refractive index of the substrate varied from sample to sample, and was between 1.510 and 1.514.

6B. Reflectance and Differential Reflectance from Bare Samples

The experimental apparatus shown in Fig. 5.1 was used to measure the TE and TM reflectance of the bare nickel films on glass substrates at a wavelength of 632.8 nm. Because of the alignment problems associated with this setup, as described in Section 5A.3, the measurement of incident power in certain data was suspect. Since it is known that reflectance approaches unity at grazing incidence and that TE and TM reflectance are identical at normal incidence, the suspect data were re-calibrated to fit these extrapolations of the measurements. As an example, reflectance data from sample #4 is plotted in Fig. 6.1 as a function of incident angle. The value of TE-polarized incident power has been adjusted by 1%.

Since the transmission through the nickel films is quite low (approximately 1% through a 20-nm film), reflection from the substrate's rear surface can be ignored, and the sample reflectance can be treated as being from a thin nickel film on a semi-infinite substrate. As shown in Appendix A, the reflectance from a thin metal film has a negligible dependence on the substrate refractive index. The shape of the reflectance curve as a function of angle depends primarily on the imaginary part, ϵ'' , of the metal dielectric constant. The magnitude of the reflectance depends on the real part, ϵ' , of the metal dielectric constant and on the metal thickness in a similar fashion, such that these two sample properties cannot both be independently determined from a bare reflectance measurement. Therefore, the information gathered from the bare film reflectances was ϵ'' and a set of paired values of ϵ' and nickel thickness, assuming an approximate substrate index of 1.5. Unique values

Table 6.1 Experimentally-determined sample parameters

| data set | d_{Ni} ± 0.5 (nm) | ϵ_{Ni} $\pm .5 \pm i1$ | n_{sub} $\pm .01$ | n_{cou} $\pm .0005$ | d_{cou} $\pm .001$ (μm) | ϕ ± 2 (deg.) | d_{in} ± 0.3 (nm) |
|----------|-------------------------------|------------------------------------|------------------------|--------------------------|--|-----------------------------|-------------------------------|
| 2a | 22.0 | -12+i16 | 1.5107 | 1.507 | .545 | -35 | 0.0 |
| 2b | 22.0 | -12+i16 | 1.5107 | 1.509 | .363 | -35 | 0.0 |
| 3a | 24.5 | -12+i16 | 1.514 | 1.507 | .56 | -34 | 1.2 |
| 3b | 24.3 | -12+i16 | 1.514 | 1.507 | .46 | -35.5 | 1.2 |
| 3c | 24.5 | -12+i16 | 1.514 | 1.506 | .30 | -37.5 | 1.2 |
| 3d | 24.5 | -12+i16 | 1.514 | 1.507 | .18 | -37.5 | 1.2 |
| 3e | 24.5 | -12+i16 | 1.514 | 1.507 | .13 | -35 | 1.2 |
| 3f | 24.5 | -12+i16 | 1.514 | 1.507 | .295 | -37.5 | 1.2 |
| 3g | 24.5 | -12+i16 | 1.514 | 1.508 | .295 | -37.5 | 1.2 |
| 3h | 24.5 | -12+i16 | 1.514 | 1.509 | .295 | -37.5 | 1.2 |
| 3i | 24.5 | -12+i16 | 1.514 | 1.509 | .295 | -37.5 | 1.2 |
| 3j | 25.5 ± 1.0 | -12+i16 | 1.512 $\pm .002$ | 1.647 $\pm .005$ | .40 | -33 | 1.2 |
| 3k | 25.5 ± 1.0 | -12+i16 | 1.514 $\pm .001$ | 1.457 | .42 | -33 | 1.2 |
| 4a | 13.0 | -12+i15 | 1.5115 | 1.506 | .94 | -37.5 | 1.3 |
| 5a | 45.0 | -12+i17 | 1.5137 | 1.506 | .315 | -33 | 1.8 |

Notes: a) inert layer thickness, d_{in} , is top layer of total nickel thickness, d_{Ni} .
b) data sets 3f - 3i are for different ac currents of 5.0, 2.5, 1.0, and 0.5 amps rms, respectively, in the copper strip; all other data sets are for 5.0 amps.

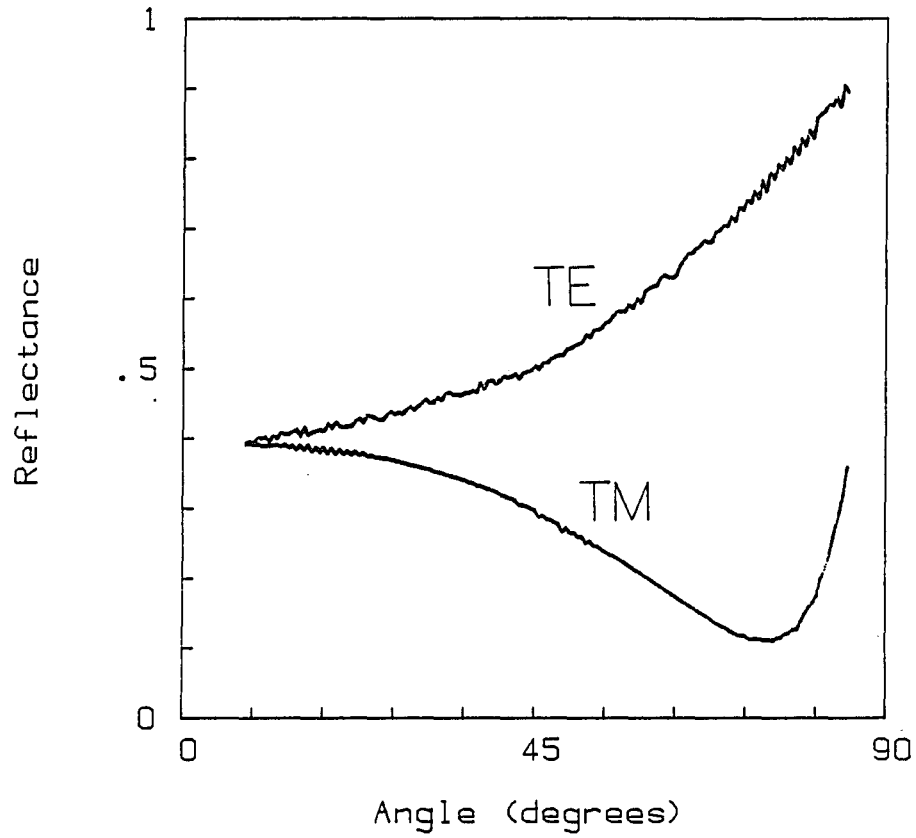


Fig. 6.1. Reflectance of bare nickel sample
sample #4; $\lambda_0 = 632.8$ nm, nickel thickness is 13.0 nm.

were determined from subsequent measurements of attenuated total reflectance from the prism-coupled, long-range surface plasmon, and are given in Table 6.1. Sample #2 was the only sample for which the value $\epsilon'' = 12$ determined from bare reflectance data did not agree with $\epsilon'' = 16$ determined from ATR data. Since the bare reflectance data and ATR data of samples other than sample #2 were consistent, and since the parameters of sample #2 determined from ATR data were consistent with the other samples, the ATR-determined $\epsilon'' = 16$ was considered to be the most accurate value.

Transverse Kerr differential reflectance measurements were made of the bare samples using the setup described in Section 5A. An oscillating, transverse magnetic field was applied to the nickel film at a frequency of 3.0 kHz, and the absolute differential reflectance, $|\Delta R| \sim |R_+ - R_-|$, was measured as a function of angle via the lock-in detection technique. The absolute value of ΔR was measured experimentally because it avoided the problem of phase mismatch between detected and reference signals in the lock-in amplifier. Some direct measurements of ΔR were made to confirm its sign and zero crossings, so that the data presented in this chapter is ΔR inferred from the measurement of $|\Delta R|$. Note that if the reflectance varies sinusoidally, the dc output of the lock-in amplifier is $1/\pi$ times the difference between the peak and trough of the reflectance. This factor is used when comparing the experimental ΔR with the theoretical $\Delta R_{\pm} \equiv R_+ - R_-$, where the magnetization is assumed to vary linearly with the applied field.

A typical ΔR measurement from bare sample #3 is shown in Fig. 6.2. The shape of the curve is similar to those of previous measurements from thick nickel films [121, 122], but the magnitude is 0.017 times that expected from a nickel film driven to magnetic saturation, based on the reported magneto-optic coefficient,

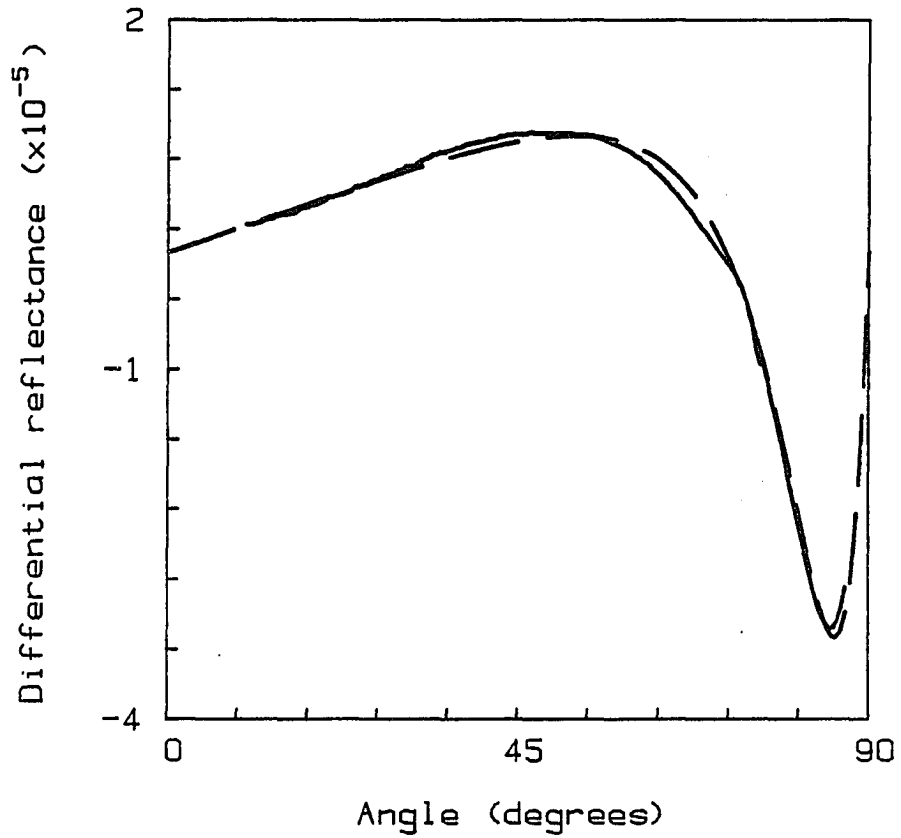


Fig. 6.2. Differential reflectance of bare nickel sample

sample #3; TM-polarized light; peak, applied magnetic field is approximately 0.017 times saturation strength; experimental curve is solid, theoretical curve is dashed.

$Q = 1.08 \times 10^{-2} \exp[i(-33.7^\circ)]$ [128]. This is in agreement with an applied magnetic field of approximately 5.2 Oe, calculated in Section 5A.1, and a reported coercivity of a 25-nm-thick nickel film of approximately 310 Oe [134]. Measurements with a weaker applied magnetic field were virtually identical in shape and were proportional to the applied field in magnitude, confirming the fact that the magnetization of the nickel film was not saturated by the applied field (see Sect. 6D and Fig. 6.8 for further discussion). Since the current through the copper strip was the largest that could be applied with the available current source, and since the generation of a magnetic field 60 times larger using the existing apparatus would cause severe resistive heating, it was concluded that the saturation threshold could not easily be reached.

The saturation magnitude, Q_0 , of the magneto-optic coefficient could not be measured in this experiment. However, since the magnitude of ΔR is directly proportional to Q_0 and the angular profile of ΔR is dependent on the phase ϕ of Q , ϕ could be determined by matching the experimental ΔR with the theoretical model of Chapter 4. Using the material parameters of sample #3 based on subsequent reflectance measurements, the theoretical match of Fig. 6.2 yields a magneto-optic coefficient phase of -31.5° . This is in fair agreement with the value of -34° reported for thick nickel films at a wavelength of 632.8 nm [128]. The prism-coupled, differential reflectance data presented in Section 6E produces a more accurate measure of ϕ .

6C. Reflectance from Prism-Coupled, Long-Range Surface Plasmon Polaritons

The prism-coupling geometry discussed in Section 5B was used to make measurements of the attenuated total reflectance from the nickel samples. It made

possible the observation of the long-range surface magnetoplasmon polariton and the determination of unknown sample properties. Typical experimental reflectance curves for TM-polarized light are shown in Figs. 6.3 and 6.4 for sample #2 (data set #2a) with a coupling layer having a refractive index near that of the substrate. The data of Fig. 6.3 constitutes a wide angular range, displaying the Fabry-Perot resonances of the coupling layer at angles less than the critical angle. Also evident is a reflectance cusp at the critical angle, $\theta_c = 58.13^\circ$, as discussed in Section 5B.2.

The Lorentzian-like reflectance resonance located at an angle slightly greater than the critical angle marks the excitation of a surface plasmon polariton. The resonance is plotted from data of higher angular resolution in Fig. 6.4. A TE-polarized reflectance scan is shown in Fig. 6.5 for the same geometry. It has no features above the critical angle, confirming the fact that surface plasmons are excited only by TM-polarized light. The width and angular position of the reflectance resonance were seen to increase with an increase in nickel film thickness, as presented later in Section 6F.1 and Fig. 6.13. This provided proof of the excitation of the long-range surface plasmon polariton.

Assuming homogeneous media, plane parallel interfaces, and losses only for the metal, the experimental reflectance was matched theoretically to determine the unknown sample parameters. Appendix A details the steps in this process. From the reflectance data of Figs. 6.3 and 6.4, the nickel thickness was found to be 22.0 ± 0.5 nm, and the nickel dielectric constant was $\epsilon = -12 + i16 \pm (0.5+i1)$. This is in good agreement with the dielectric constant of nickel reported in the literature, $\epsilon = -13 + i16$ at a wavelength of 632.8 nm [61]. The refractive index of the coupling liquid was determined to be 1.507 ± 0.001 . The measurement agrees with the nominal index of 1.5115 at 25^o C, interpolated from the manufacturer's data, a

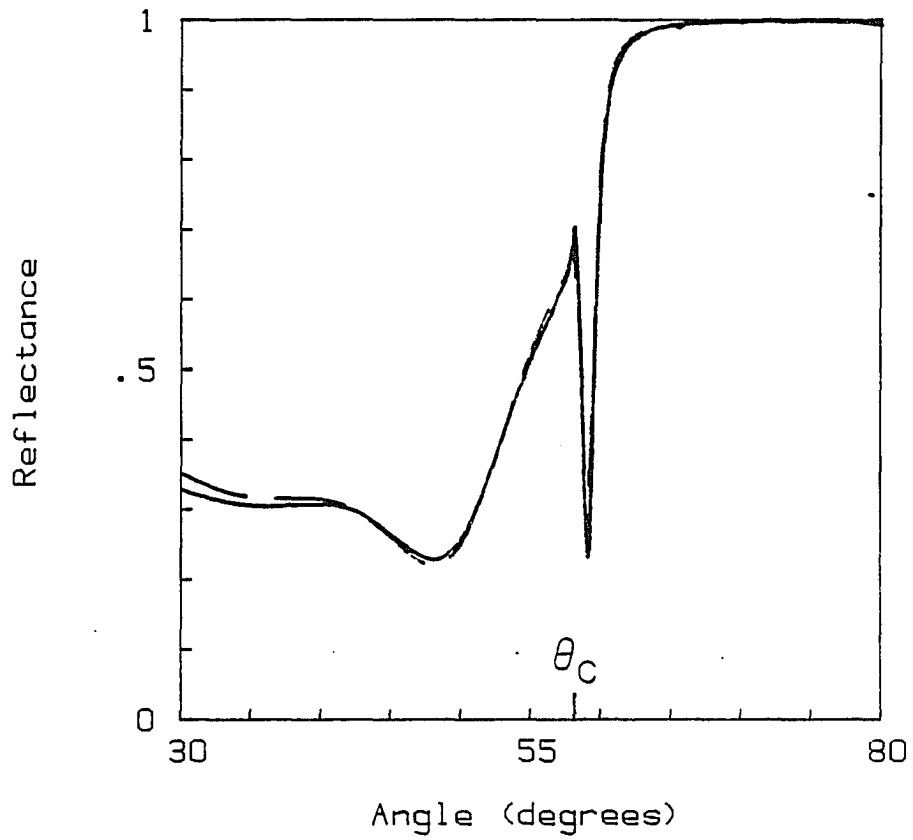


Fig. 6.3. TM reflectance from prism-coupled, long-range surface plasmon polariton
-- wide angular range

data set #2a; incident angle is measured in prism; experimental curve is solid,
theoretical curve is dashed.

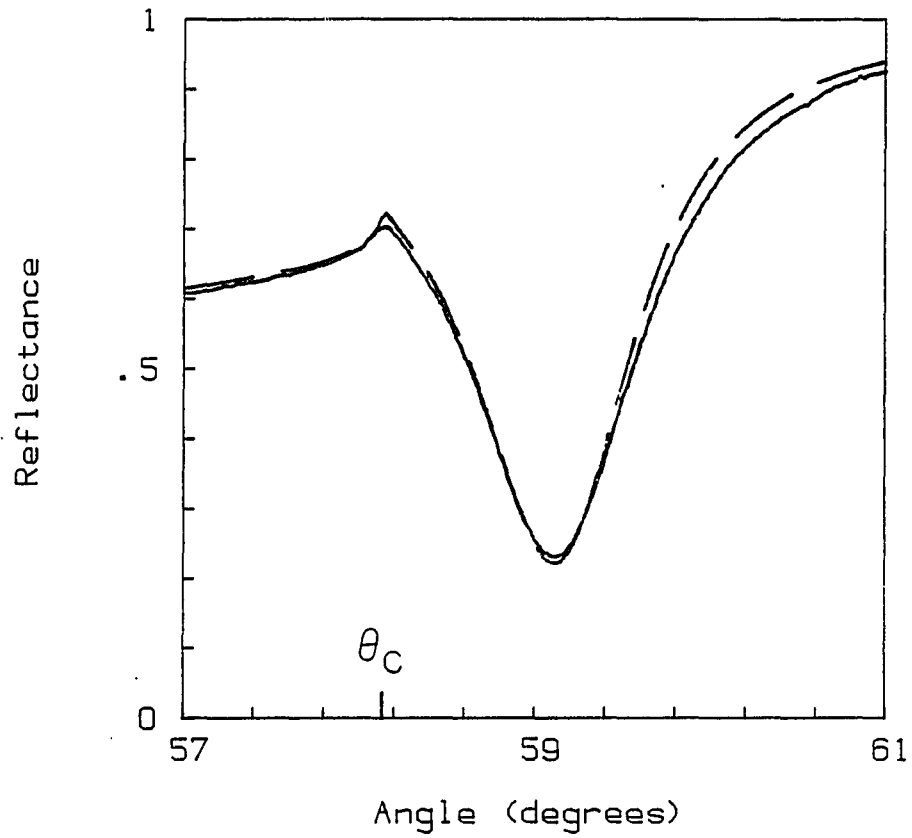


Fig. 6.4. TM reflectance from prism-coupled, long-range surface plasmon polariton
-- narrow angular range

data set #2a; experimental curve is solid, theoretical curve is dashed.

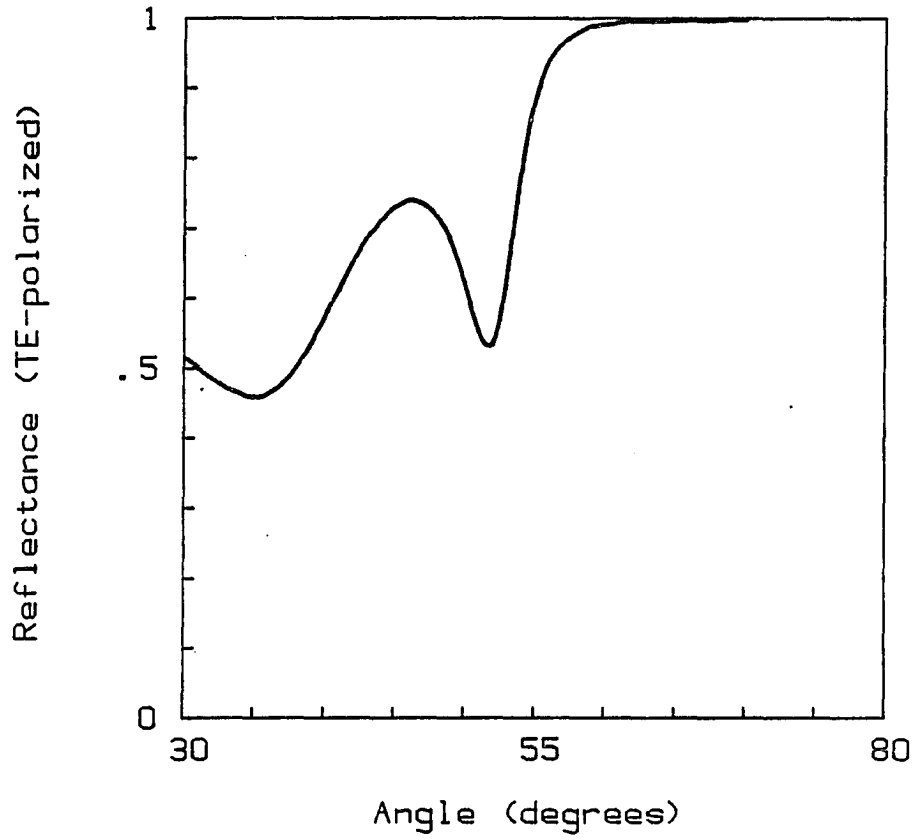


Fig. 6.5. TE reflectance in prism-coupled, long-range surface plasmon geometry data set #2a.

listed temperature coefficient of $\Delta n/\Delta T = 0.0004/^\circ\text{C}$, and an approximate sample temperature of 38°C measured with a thermocouple. Refractive index measurements of the other two coupling liquids used in this study yielded similar agreement, although the index varied slightly for different data due to changes in room temperature. The coupling-layer thickness for this data set was $0.55 \pm 0.01\ \mu\text{m}$, and the local substrate index was 1.5107 ± 0.0005 .

Figures 6.3 and 6.4 overlap the experimental reflectance data with the theoretically modelled reflectance. The deviation from theory at low angles for the wide scan was common to all samples. Because the laser spot was necessarily de-centered, the spot walked across the slightly wedged coupling layer as the incident angle was varied, thus causing the deviation. In the narrow angular scan the smoothing of the reflectance peak at the critical angle is due to the angular spread of the incident beam. The average root-mean-squared deviation of the measured reflectance from the theoretically expected reflectance was 0.011 for the wide scan (Fig. 6.3), and 0.019 for the narrow scan (Fig. 6.4).

Similar reflectance data were observed for all the samples and configurations studied. For each data set, the material parameters were derived from a modelling of the reflectance; they are given in Table 6.1. Averaged over all sets of data, the root-mean-squared deviation of the measured reflectance from the theoretically expected reflectance was 0.012 for the wide angular scan, below the critical angle, and 0.015 for the narrow angular scan. The experimental dependence of reflectance on the sample parameters is discussed in Section 6F.

6D. Differential Reflectance from Prism-Coupled, Long-Range Surface Magnetoplasmon Polaritons

With a transverse magnetic field applied to the nickel film, the TM-polarized differential reflectance from several prism-coupled samples was measured. Typical ΔR data for sample #2 (data set #2b) is plotted in Figs. 6.6 and 6.7 above the corresponding Fresnel reflectance for comparison. The prominent characteristic of ΔR in the prism-coupling geometry is a resonance around the surface plasmon resonance angle. The magnitude of the peak signal near the critical angle was 10 times the magnitude of the signal plateau between 30° and 50° . It was 1.4 times the maximum $|\Delta R|$ from the bare nickel film (Fig. 6.2); in theory it should have been 3.8 times for a comparable system. However, the copper strip attached to sample #2 was wider than that of the other samples, inducing a smaller magnetic field. In contrast to the broad features of ΔR for the bare nickel film, the prism-coupled, long-range surface magnetoplasmon exhibits a large variation in ΔR in a small angular range.

A differential reflectance measurement was attempted with TE-polarized light. The detected signal was more than an order of magnitude lower than that with TM light, as expected [121], and consequently it was very noisy. No attempt was made to analyze the angular dependence of the TE signal.

Ferromagnetic materials exhibit a hysteresis in magnetization vs applied magnetic field when the field is increased to values greater than the coercivity of the material, saturating the magnetization. However, for initially non-magnetized samples, as were the nickel films of this study, the magnetization should be linear with applied field for field strengths much less than the coercivity. To test for linearity in the present study, the differential reflectance was measured for values of

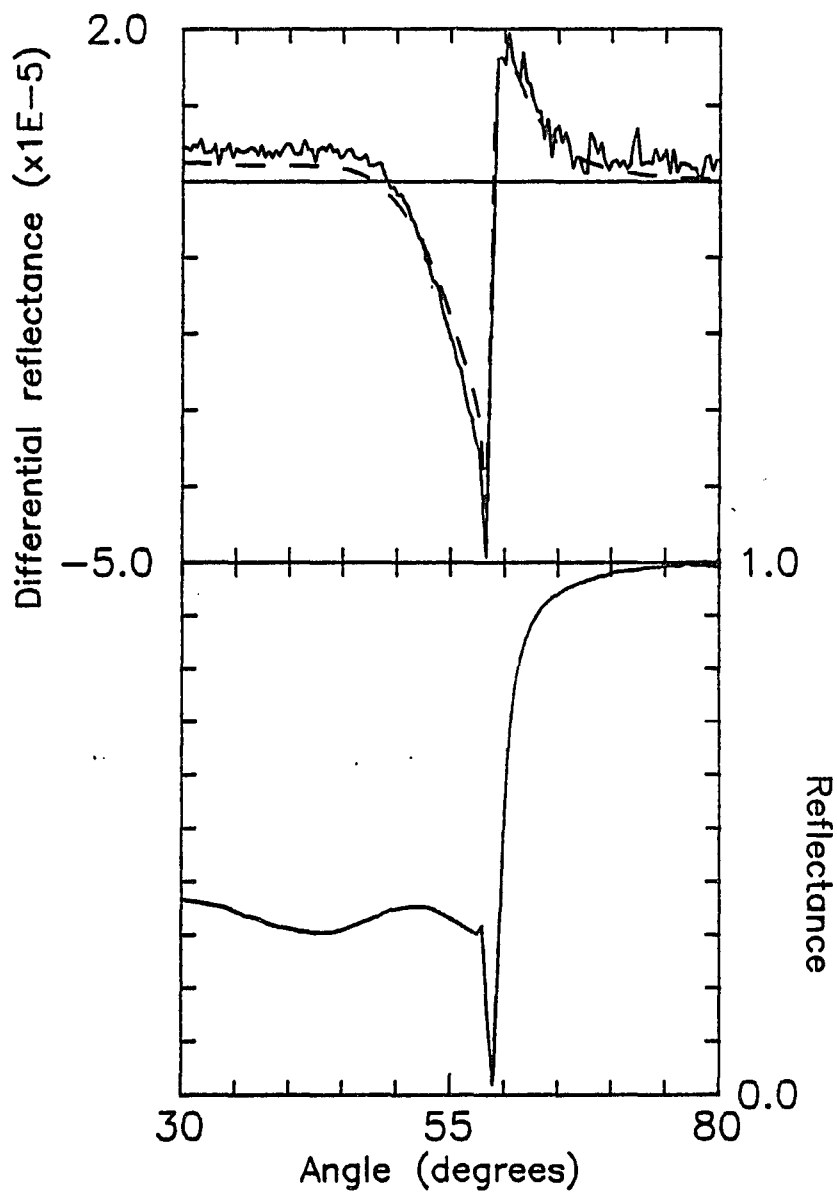


Fig. 6.6. Prism-coupled excitation of long-range surface magnetoplasmon polariton
-- wide angular reflectance scan

data set #2b; TM-polarized light; peak, applied magnetic field is approximately 0.0060 times saturation strength.

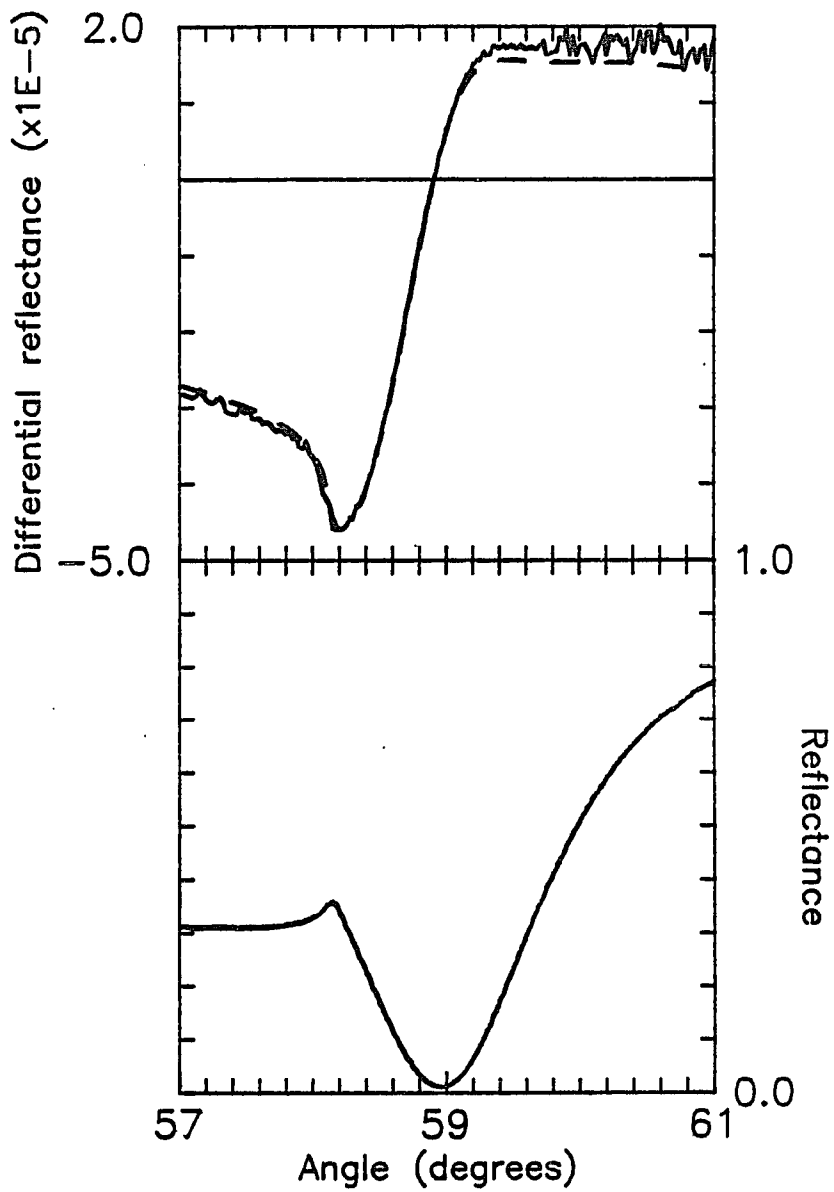


Fig. 6.7. Prism-coupled excitation of long-range surface magnetoplasmon polariton
-- narrow angular reflectance scan

data set #2b; TM-polarized light; peak applied magnetic field is approximately 0.0060
times saturation strength.

the ac current ranging from 0.5 to 5.0-amps-rms amplitude in the copper strip. These measurements are plotted in Fig. 6.8, after scaling to the equivalent of a 5.0-amp current. The ΔR curves show essentially the same angular profile, to within 10%, but decrease in magnitude at the lower currents. This seems to imply a nonlinear magnetic susceptibility. However, it was discovered that the waveforms generated at the lower currents were non-sinusoidal and dc-biased. A distorted waveform would partially explain the deviations between measurements at different currents, but it was difficult to quantify. Since it is the angular profile of ΔR and not the absolute magnitude which is of interest here, and since the 5.0-amps-rms waveform used for most of the measurements in this study was a non-biased sinusoid, the discrepancy was not a problem.

The fact that the angular profile of the ΔR signal near the surface magnetoplasmon resonance does not change with applied field strength reiterates experimentally what was derived theoretically -- that the resonant behavior of ΔR is due to the difference between surface magnetoplasmon resonances which have been shifted by the applied magnetic field. The angular positions of the extrema of ΔR are virtually independent of the strength of the magnetic field, but depend on the phase, ϕ , of the magneto-optic coefficient, in contrast with the conclusions of Refs. 126 - 129. By matching theoretical and experimental differential reflectance curves, ϕ can be inferred, as is discussed in the following section.

6E. Measurement of the Phase of the Magneto-Optic Coefficient

Analysis of the phase of the magneto-optic coefficient begins with the determination of the thickness and dielectric constants of each of the layers in a sample using the Fresnel reflectance data. Theoretical curves of differential

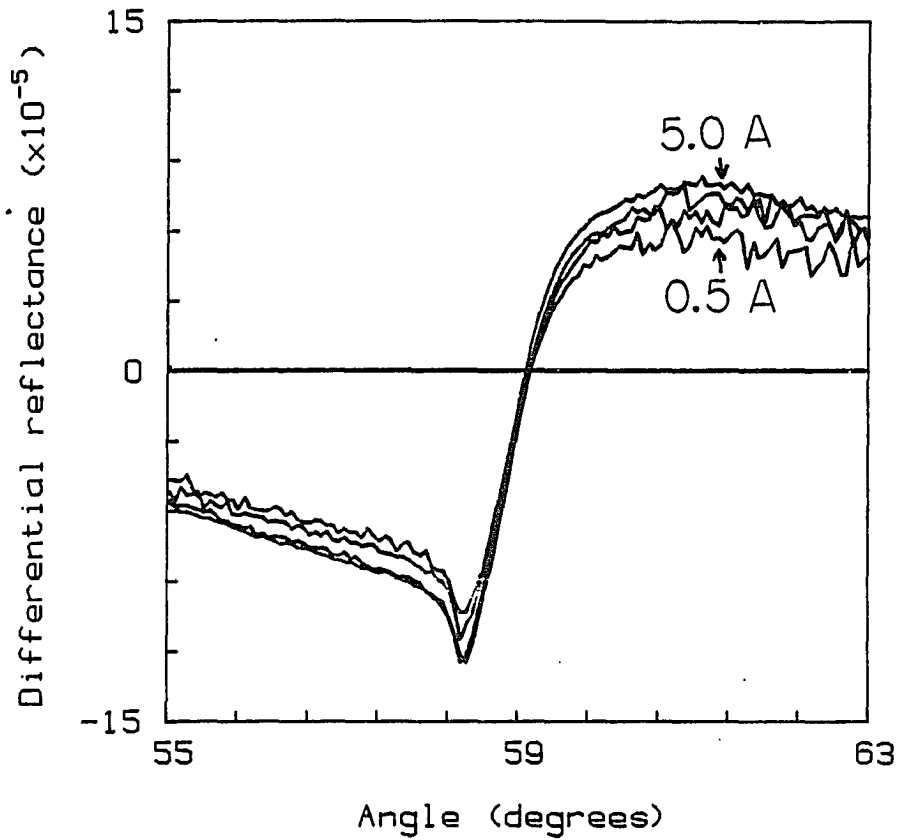


Fig. 6.8. Linearity of differential reflectance with applied magnetic field

data sets #3f - i; set of curves are for ac currents of 0.5, 1.0, 2.5, and 5.0 amps rms in the copper conducting strip, scaled to the equivalent of a 5.0 amp current; the slight mismatch of curves is due partially to nonsinusoidal current waveform; peak, applied magnetic field is approximately 0.021 times saturation strength.

reflectance are then calculated from the multilayer model using various values of ϕ for the nickel film. The magnitude, Q_0 , of the magneto-optic coefficient is adjusted to scale the size of ΔR_{\pm} to that of the experimental curve. Using the data of set #3, the experimental ΔR is plotted in Fig. 6.9 overlaid with scaled, theoretical curves of ΔR_{\pm} for $\phi = -25^\circ$, -35° , and -45° . None of the curves shown, nor those for other values of phase, matches exactly, and the discrepancy was enough to warrant further investigation into the material system.

It is well known that some degree of roughness exists at the surfaces of a deposited film due to an initially rough substrate, disorder in the growth process, and/or impurities in the film. Although an exact analysis of the optical properties of a rough metal surface is complicated, fairly accurate modelling of the reflective behavior has been accomplished by treating the roughness as a cermet layer on the metal surface [135]. A cermet exhibits dielectric properties intermediate between those of the film and the bounding medium, as derived from an appropriate theory such as the Maxwell Garnett approach [136]. While studying the reflectance from prism-coupled surface plasmon polaritons, Kovacs found that by replacing part of the metal film with a cermet layer, the theoretical reflectance resonance was shifted, broadened and brought into coincidence with his experimental data [39].

Plotted in Fig. 6.10 and 6.11 are theoretical curves of the differential reflectance of measurement #3b when the nickel film is modelled with a cermet at its interface with the coupling layer. The dielectric constant, ϵ_c , of the cermet layer is given by the Maxwell Garnett theory according to the expression [136]

$$\epsilon_c = \frac{(1+2q) \epsilon_d \epsilon_m + 2(1-q) \epsilon_d^2}{\epsilon_m(1-q) + \epsilon_d(2+q)} \quad (6.1)$$

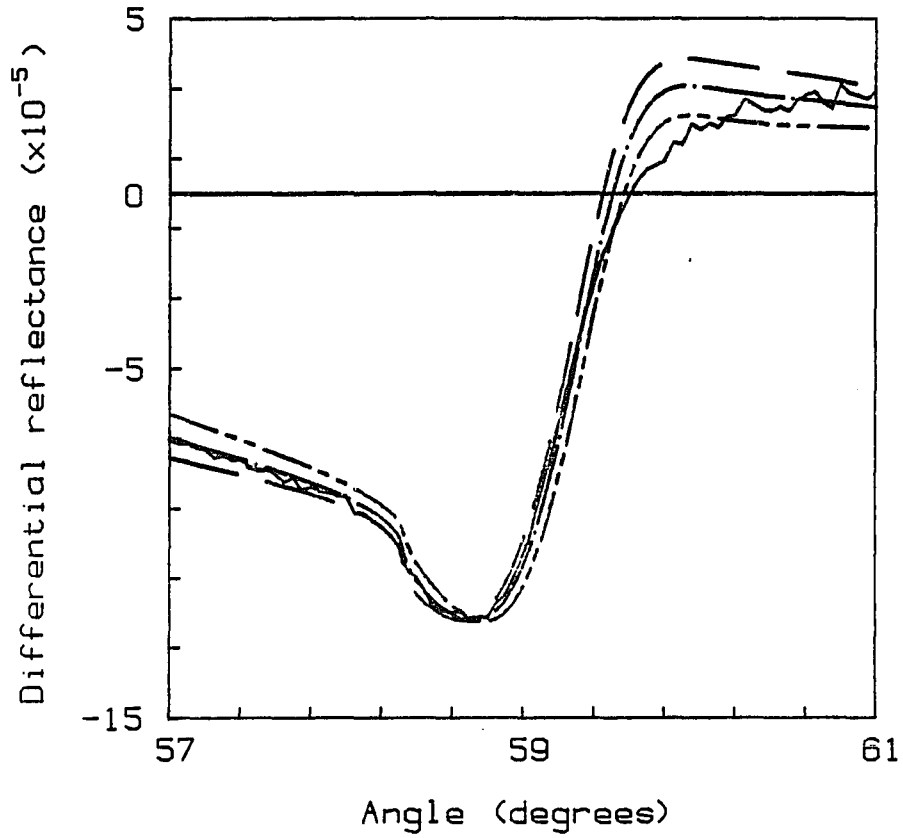


Fig. 6.9. Differential reflectance as a function of magneto-optic coefficient phase

long-range surface magnetoplasmon of data set #3b; experimental curve is solid; theoretical curves are for phases $\phi = -25^\circ$ (long- and short-dashed), $\phi = -35^\circ$ (dot-dashed), and $\phi = -45^\circ$ (dashed).

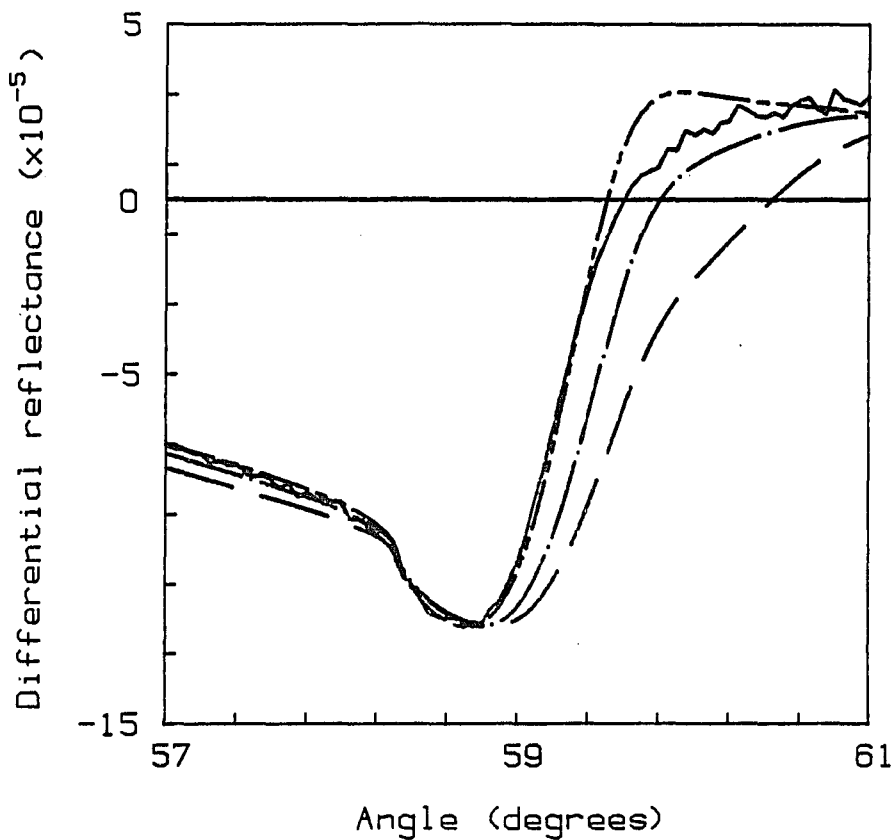


Fig. 6.10. Cermet-layer model of nickel differential reflectance -- cermet layer added to reflectance-determined nickel thickness

long-range surface magnetoplasmon of data set #3b; experimental curve is solid; theoretical curves are for nickel thickness of 24.5 nm, $\phi = -35^\circ$, cermet layer of fill-factor $q = 0.4$, and cermet-layer thickness of 0 nm (long- and short-dashed), 1.2 nm (dot-dashed), and 2.4 nm (dashed).

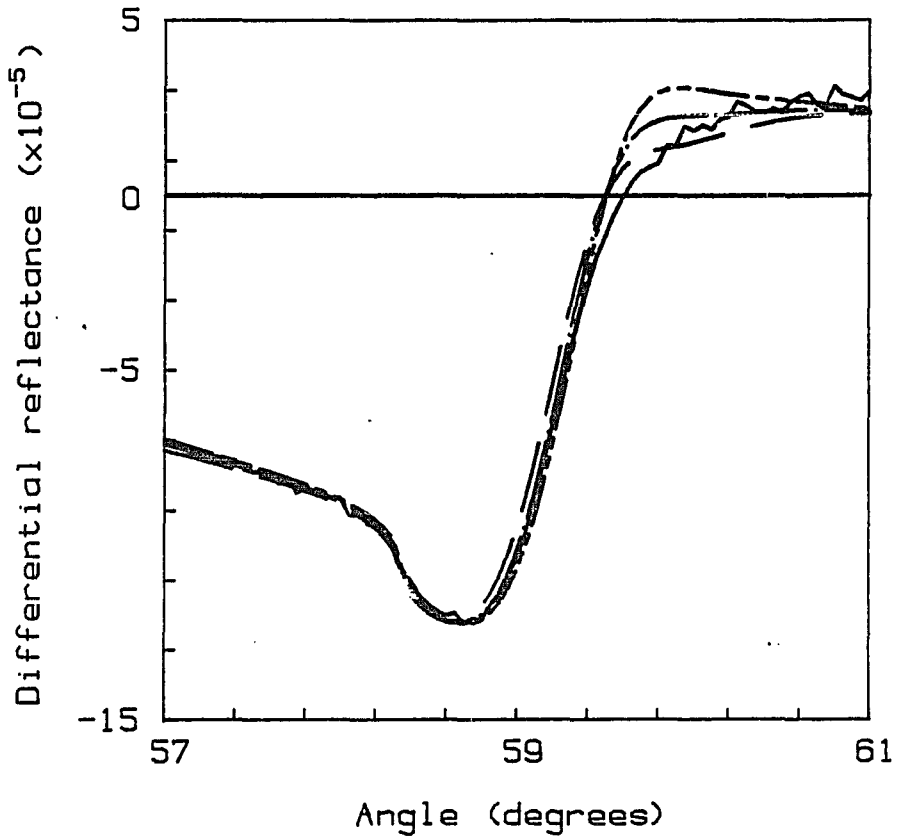


Fig. 6.11. Cermet-layer model of nickel differential reflectance - model matches prism-coupled, Fresnel reflectance

long-range surface magnetoplasmon of data set #3b; experimental curve is solid; theoretical curves are for nickel $\phi = -35^\circ$, cermet layer of fill-factor $q=0.4$, and other thicknesses and index as follows: $d_{Ni} = 24.5$ nm, $n_{COU} = 1.507$, and $d_{cer} = 0$ nm (long- and short-dashed); $d_{Ni} = 23.5$ nm, $n_{COU} = 1.505$, and $d_{cer} = 1.2$ nm (dot-dashed); and $d_{Ni} = 22.5$ nm, $n_{COU} = 1.503$, and $d_{cer} = 2.4$ nm (dashed).

where ϵ_m is the dielectric constant of the metal, ϵ_d is the dielectric constant of the dielectric matrix, and q is the fill-fraction of the metal in the dielectric. A nickel fill-fraction of $q = 0.4$ was used, yielding a cermet dielectric constant of $\epsilon_c = 7.4 + i3.1$. Note that with a cermet layer added to the original nickel thickness determined from Fresnel reflectance measurements, the shape of the differential reflectance curve near 61° becomes more like the experimental data in some respects, but the resonance also broadens (see Fig. 6.10). This is due to a broadening of the theoretical Fresnel reflectance resonance, which no longer matches the experimental resonance. With the additional degrees of freedom that the cermet layer provides to the model, the Fresnel reflectance can be matched fairly well by adjusting the nickel thickness and the coupling-layer index and thickness. Shown in Fig. 6.11 are plots of ΔR for different multilayer models, including a cermet layer, which were adjusted to match the Fresnel reflectance of the prism-coupler stack. The bare sample reflectances of theory and experiment did not match, and the figure indicates that neither do the prism-coupled differential reflectances. Apparently, the theoretical differential reflectance, prism-coupled reflectance, and bare reflectance cannot simultaneously agree with their experimental counterparts for a multilayer which includes a cermet layer. A thorough investigation of the cermet model with different filling factors and thicknesses supported the conclusion that the perturbed shape of the ΔR curves is not the result of nickel surface properties which can be modelled as a cermet layer.

Another possible explanation for the mismatch of differential reflectance theory and data is a magnetically inert layer at the surface of the nickel films. In an inert or "dead" layer, the magnetic dipole moment of the material is destroyed

locally or the magnetic domains are fixed in a random orientation so that cooperative alignment does not occur. Existence of a layer of this type has been used to explain the loss of read and write efficiency in magnetic tape heads with use [137]. The presence of an inert layer at nickel surfaces was a hotly debated issue in the 1970's after Liebermann et al. measured a deficiency in the magnetization of very thin nickel films which corresponded to two atomic layers at 0 K and four atomic layers at room temperature [138]. Although the behavior was explained with a theoretical model, theoretical research since then has shown that no inert layer exists on a free nickel surface [139]. A more plausible explanation is that water from the aqueous solution in which the films were deposited was chemisorbed onto the surface of the nickel [112, p. 25]. The lone electrons of disassociated hydrogen atoms paired with the unpaired electrons in the 3d band of nickel and destroyed the magnetic moment at the surface. A similar chemisorption and electron pairing takes place with organic molecules [112]. The system most widely studied has been the chemisorption of hydrogen gas on nickel. In a systematic investigation, hydrogen gas was introduced into the high-vacuum evaporation chamber of deposited nickel films with thicknesses ranging from 3 to 20 nm [140]. It was found that all films exhibited roughly the same maximum decrease in magnetization, corresponding to an inert nickel layer of between 0.4 and 1.5 nm. The lattice spacing of bulk nickel atoms is approximately 0.35 nm [141].

If a magnetically inert surface layer does exist, the magneto-optic properties of the material can be predicted by modelling a surface layer with a null magneto-optic coefficient. This method has been used to optically determine the thickness of inert layers on magnetic tape heads by analyzing the shape and magnitude of the longitudinal Kerr effect as a function of incident angle [142].

To test the hypothesis of an inert layer in the present study, a thin section of the nickel film was modelled to have a null magneto-optic coefficient. The remainder of the film was given a non-zero coefficient with an adjustable phase, and the diagonal element of the dielectric constant for the entire film was kept identical to the value inferred from reflectance measurements. For different thicknesses of the inert layer, the differential reflectance is plotted theoretically and compared with the experimental data in Fig. 6.12. The theoretical and experimental match of ΔR was much closer with a phase ϕ of -35° and an inert layer of approximately 1.2-nm thickness at the metal-coupling-layer interface than with no inert layer. When the inert layer was modelled at the metal-substrate interface, it had the opposite effect on the shape of ΔR , and no match was possible. It is important to note that setting the off-diagonal, dielectric tensor element to zero for part of a magnetic layer affects the Kerr reflectance but does not affect the Fresnel reflectance. This is in contrast to the insertion of a cermet layer, which affects both.

Oxidation at the surface of the nickel films has been suggested as an explanation for the magnetically inert layer. However, nickel oxide differs from nickel in the diagonal elements of its dielectric tensor as well as the off-diagonal elements. The experimental data implies a deviation only in the off-diagonal elements in order for the theoretical and experimental Fresnel reflectance measurements to remain consistent. In the prism-coupling measurement, the oxide layer would act only as an additional coupling layer, optically blending into the rest of the structure. Hence, an oxide is precluded as a cause for the measured magneto-optic properties.

After a detailed theoretical investigation, the conclusion of the author is that an inert layer at the exposed interface of the nickel film is the explanation most

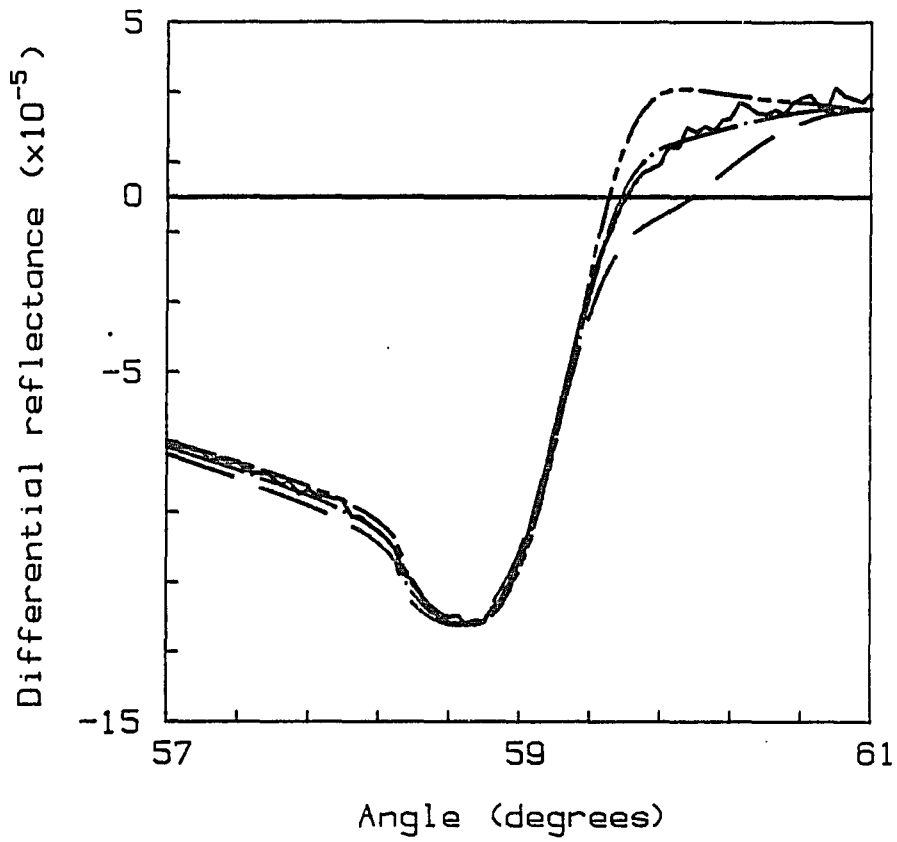


Fig. 6.12. Inert-layer model of nickel differential reflectance

long-range surface magnetoplasmon of data set #3b; experimental curve is solid; theoretical curves are for a magnetically inert section of the top nickel surface, having a thickness of 0 nm (long- and short-dashed), 1.2 nm (dot-dashed), or 2.4 nm (dashed).

consistent with the observed angular profile of ΔR . Since an organic coupling liquid was used for the prism-coupling measurements, it is conceivable that chemisorption of the liquid occurred and the pairing of hydrogen and nickel electrons negated the magnetic moment of nickel atoms. The existence of a 1.2-nm layer in the model was determined independently for all measurements made with sample #3. A similar layer was inferred from measurements made with sample #4, indicating an inert layer thickness of 1.3 nm, and with sample #5, indicating a thickness of 1.8 nm. Measurements of sample #2 did not suggest an inert layer, but neither could a close match of experimental and theoretical data be made with other models. In Figs. 6.6 and 6.7 are plotted theoretical curves for a magneto-optic phase coefficient of -31.5° and no inert layer. Sample #2 proved to be an enigma in several of the measurements in this study, which reminded the author that reality is always more complex than any model.

As illustrated in Figs. 6.9 - 6.11, possible causes of the observed ΔR other than the presence of an inert layer perturb the ΔR curves differently, and they do not adequately account for the angular profile. Differential reflectance measurements on bare nickel films were inconclusive since similar theoretical curves were obtained by varying the inert-layer thickness or the phase of the magneto-optic coefficient. The presence of an inert layer should be verified by other non-optical surface measurements.

6F. Effect of sample Parameters on Reflectance and Differential Reflectance

In order to provide more evidence which confirms the theoretical results of chapter 4, and to explore the variety of transverse Kerr reflectance curves accompanying excitation of the long-range surface magnetoplasmon polariton, prism-

coupled reflectance measurements were made of several nickel films for a range of sample parameters. The accessible parameters were the nickel film thickness, which was different for different films; the coupling-layer thickness, which could be changed by adjusting the micrometer on the prism holder; and the coupling-layer refractive index, which was different for different index-matching liquids. Although the substrate index could not be easily varied, its effect was inferred from its value relative to the coupling-layer index. Data set #3b was used as a standard for comparison. It exhibited a ΔR signal which was 0.021 times that expected with the nickel magnetization saturated at the peak of the ac magnetic field. The ratio of detected ΔR to saturation ΔR varied between other measurements, most likely due to variations in the applied magnetic field strength. Except for the measurements of sample #2, the same copper conducting strip was transferred to the back of each substrate to induce the magnetic field, but it became somewhat kinked with use. Another factor which may have affected the strength of the field was the alignment of the laser beam spot over the strip. In the cases where the difference in magnitude was greater than 10%, the experimental data was scaled to the standard in order to make comparisons easier; this is noted in the discussion. In all cases, the experimental measurements of the angular profile of ΔR agreed with the theoretical model, with most of the deviation being random noise in the detection process.

6F.1. Nickel Thickness

The characteristics of the long-range surface-plasmon resonance as a function of nickel thickness are depicted in Fig. 6.13. The distinguishing features of the long-range surface plasmon are seen in the figure: the refractive and absorptive parts of the propagation constant increase with increasing metal thickness as

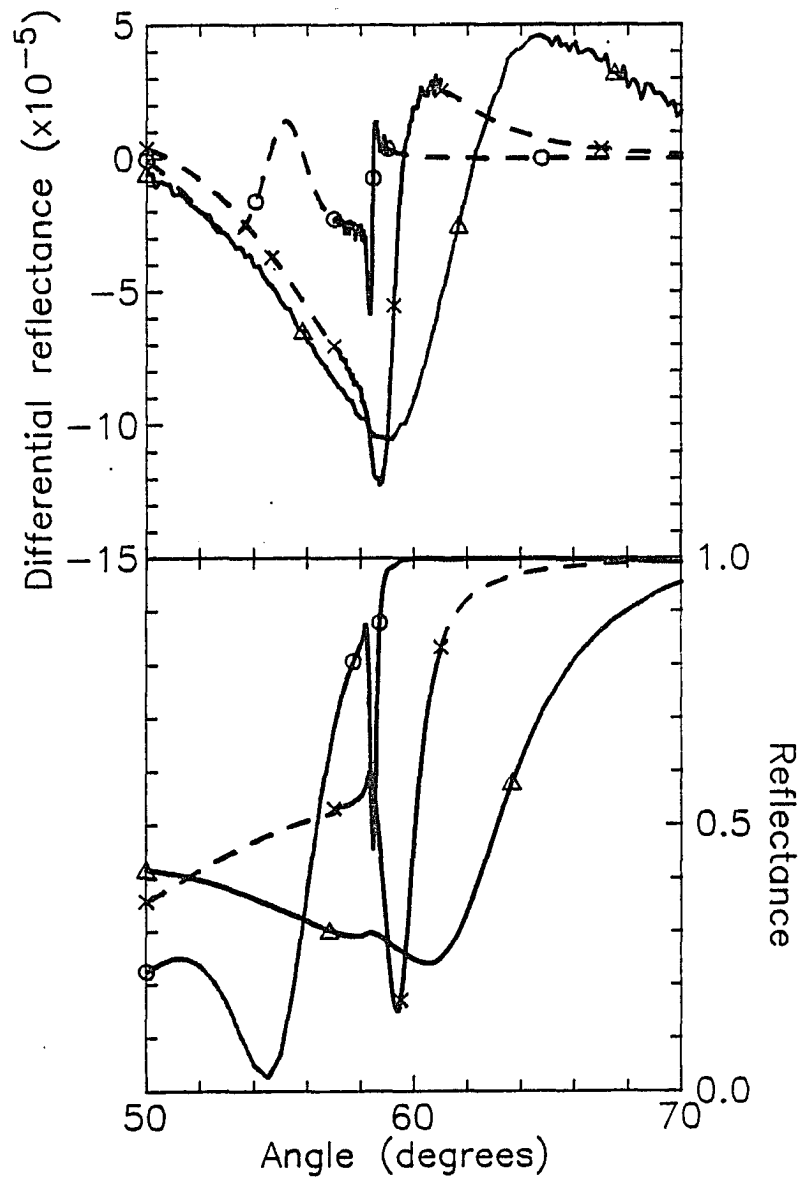


Fig. 6.13. Prism-coupled, long-range surface magnetoplasmon as a function of nickel thickness

data sets #4a with $d_{Ni} = 13$ nm - o, #3b with $d_{Ni} = 24.5$ nm - x, and #5a with $d_{Ni} = 45$ nm - Δ ; dashed curves are theoretical extensions of solid, experimental curves.

evidenced by the increase in the angular position and width of the Fresnel reflectance resonance with increasing metal thickness. All other parameters are approximately identical except the coupling-layer thickness, which was adjusted to accommodate the different evanescent wing lengths of the plasmon fields. Small differences in substrate or coupling-layer index were due to variations in the temperature or the substrate composition.

Differential reflectance measurements are also plotted in Fig. 6.13. Assuming that the applied field and the magnetic susceptibility were the same for all samples, the ΔR data from the 13-nm-thick film was 37% smaller in magnitude than the theoretical expectation. The data from the 44-nm-thick film was smaller by 13%. A partial explanation lies in a thickness-dependent susceptibility. The coercivity of thin nickel films deposited on rock-salt substrates has been found to depend inversely on film thickness in the 20-100 nm range [134]. This would imply a smaller susceptibility and therefore a smaller ΔR from the thinner film, but would not explain the smaller ΔR from the thicker film. Lacking the apparatus to measure the susceptibility and saturation magnetization of the samples, the ΔR data from the 13 nm and 44 nm films were scaled to be in accordance with theory so that the dependence of ΔR on thickness would be illustrated.

Figure 6.13 indicates that with increasing nickel thickness there is an increase in the magnitude of the differential reflectance for the long-range surface magnetoplasmon. The magnetic field-induced change in the position and width of the reflectance resonance is larger for the thicker films and is not completely counteracted by the larger absorptive loss. Agreement with relationship (4.33) is only qualitative for these experimental curves, as the coupling efficiency was not the same for the three samples. A theoretical study was made in which the coupling

factor $h \equiv \exp(-k_0 \kappa_1 d_1)$ was held constant at a value of $1/e$ at the resonance angle for nickel thicknesses of between 10 and 40 nm. Relationship (4.33) then predicted to within 5% the dependence of $|\Delta R|_{\max}$ on nickel thickness.

6F.2. Coupling-Layer Thickness

The series of experimental curves in Fig. 6.14 depicts the behavior of reflectance with a change in the coupling-layer thickness, d_{cou} . As d_{cou} was decreased from $0.56 \mu\text{m}$ to $0.13 \mu\text{m}$ for sample #3, fewer coupling-layer resonances were allowed, and the reflectance oscillations below the critical angle spread out according to expectation. The reflectance dip above the critical angle, which is associated with the long-range surface plasmon, shifted toward the critical angle and eventually disappeared. For the thinnest coupling layer, a new dip appeared at a larger angle. Reference to Fig. 2.9 suggests that the new dip signalled the excitation of the single-surface plasmon at the nickel-substrate interface as the coupling geometry approached the Kretschmann case of no coupling layer. Actually, the calculated profile of the optical fields in the sample layers is fairly similar for the different d_{cou} . Because nickel is a lossy metal, the field enhancement upon excitation of the long-range surface plasmon is small. Consequently, the sum of incident and reflected fields decaying towards the center of the coupling layer from its two interfaces gives rise to a sine-like profile. The peak field strengths at the two interfaces of the nickel film remain within 40% of each other for a wide range of coupling layer thicknesses down to the absence of a coupling layer. The interfacial fields are maximally excited at an angle above the critical angle which changes only slightly with d_{cou} . Little indication is given of the transition between the double-interface and single-interface mode.

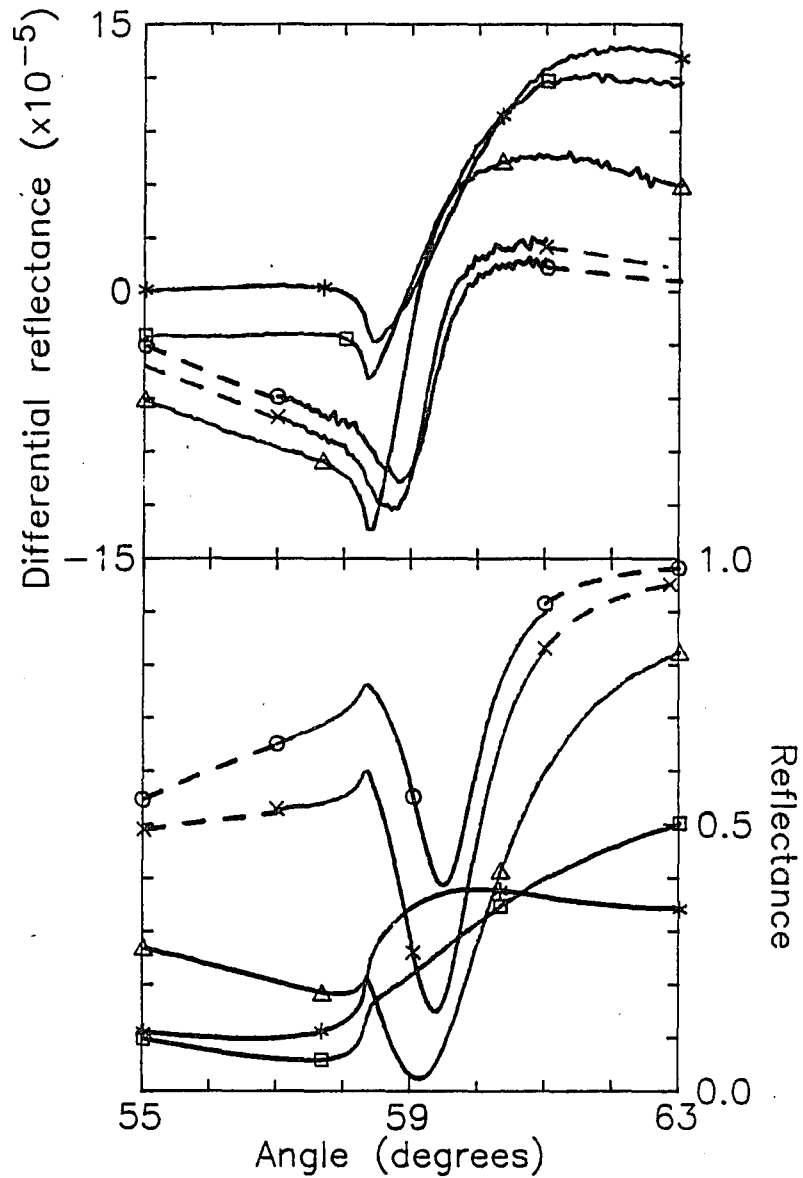


Fig. 6.14. Prism-coupled, long-range surface magnetoplasmon as a function of coupling-layer thickness

data sets #3a - e; Fresnel reflectance is plotted in lower curve; coupling-layer thicknesses are $0.56 \mu\text{m}$ - o; $0.46 \mu\text{m}$ - x; $0.30 \mu\text{m}$ - Δ ; $0.18 \mu\text{m}$ - \square ; $0.13 \mu\text{m}$ - *; dashed curves are theoretical extensions of solid, experimental curves.

In Fig. 6.14 the differential reflectance exhibits the usual resonant shape with two local extrema near the angle of surface-plasmon excitation. The resonances of R and ΔR broaden with the increase in loss accompanying a smaller d_{COU} . Coupling to the single-interface plasmon and re-radiation are the sources of the loss increase. The ΔR curve for the thinnest coupling layer has an appearance similar to that for the Kretschmann geometry (see Fig. 4.5). As d_{COU} decreases, the field-induced perturbation in the resonance width, proportional to $\Delta\beta_p''$, increases faster than the resonance width increases. According to Eq. (4.33), $|\Delta R|_{\text{max}}$ for $d_{\text{COU}}=0.13 \mu\text{m}$ should be more than three times larger than that for $d_{\text{COU}}=0.56 \mu\text{m}$. The contrast shown by experimental and theoretical data is much smaller. It is moderated by the obvious differences in coupling efficiency which are not accounted for by Eq. (4.33).

6F.3. Coupling-Layer Refractive Index

The long-range surface plasmon resonance is affected by the refractive indices of the layers bounding the metal film. Reflectance and differential reflectance data for a coupling-layer index greater than the substrate index are compared to the near-symmetric case in Fig. 6.15. The resonance position shifts to larger angles with the increase in index, in agreement with the discussions of Chapter 2 and Appendix A. For a coupling-layer index greater than the substrate index by more than about 0.04, the optical field is no longer evanescent on the coupling-layer side of the metal film since its modal index is smaller than the coupling-layer index. The mode has evolved into a single-interface plasmon at the metal-substrate interface, accompanied by a broadening of the resonance due to an increase in the absorptive part of the modal propagation constant. The experimental

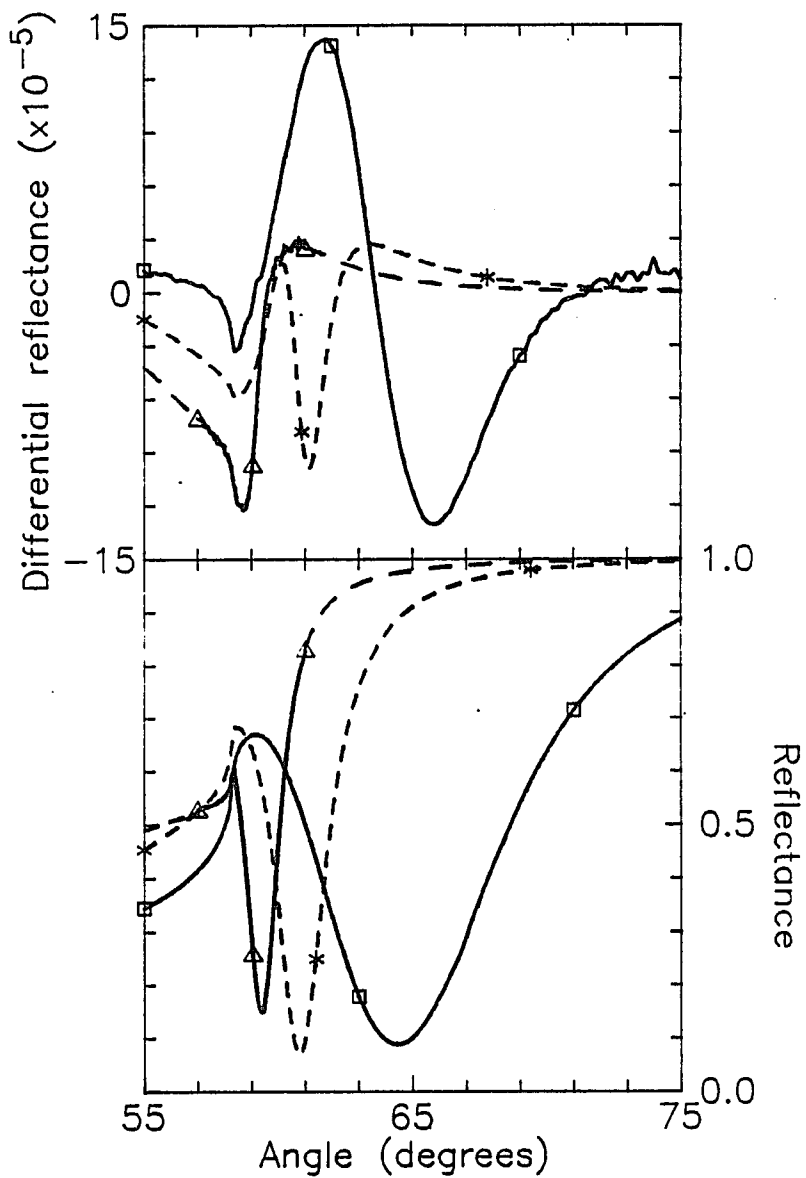


Fig. 6.15. Prism-coupled reflectance and differential reflectance as a function of bounding asymmetry: $n_{\text{cou}} > n_{\text{sub}}$.

coupling-layer refractive index is 1.507 - Δ (data set #3b), 1.55 - * (theoretical), and 1.647 - \square (data set #3j); substrate index is 1.514.

ΔR curve for $n_{\text{COU}}=1.647$ in Fig. 6.15 resembles the Kretschmann geometry curve of Fig. 4.5 because the coupling geometry is effectively the same; the role of the coupling layer has become like that of the prism. As in the case of decreasing coupling-layer thickness, discussed in the previous section, the transition between exciting the long-range surface plasmon and exciting the single-interface plasmon is more a question of definition than of experimental demarcation. For the long-range mode, $\kappa'' > \kappa'$ in the coupling layer, indicating critical damping of the fields perpendicular to the metal interface.

A boundary-index difference, $n_{\text{COU}} - n_{\text{SUB}}$, of between 0.04 and -0.05 does allow for the excitation of the long-range mode. ΔR for a coupling-layer index of 1.55 is plotted in Fig. 6.15 from a theoretical calculation; it has four local extrema near the plasmon resonance, in contrast to the pair of extrema for the near-symmetric case. A combination of the shifts in position, width, and depth of the quasi-Lorentzian reflectance resonance truncated at the critical angle causes this unique shape. Because of the oscillation of ΔR with angle, $|\Delta R|_{\text{MAX}}$ for $n_{\text{COU}} = 1.55$ is not larger than that for the near-symmetric case, as would be expected from relationship (4.33).

When the coupling-layer index is less than the substrate index, the reflectance behaves as illustrated in Fig. 6.16. The long-range surface plasmon resonance is located at smaller angles, and for a sufficiently large asymmetry, $n_{\text{COU}} - n_{\text{SUB}} \lesssim -0.05$, the mode is cut off from being bound at the metal-substrate interface. Figure 6.16 contains a theoretical curve plotted for a coupling-layer index of 1.4. The resonance features of surface plasmon excitation are absent from both the reflectance and differential reflectance, although there remains a non-zero ΔR at

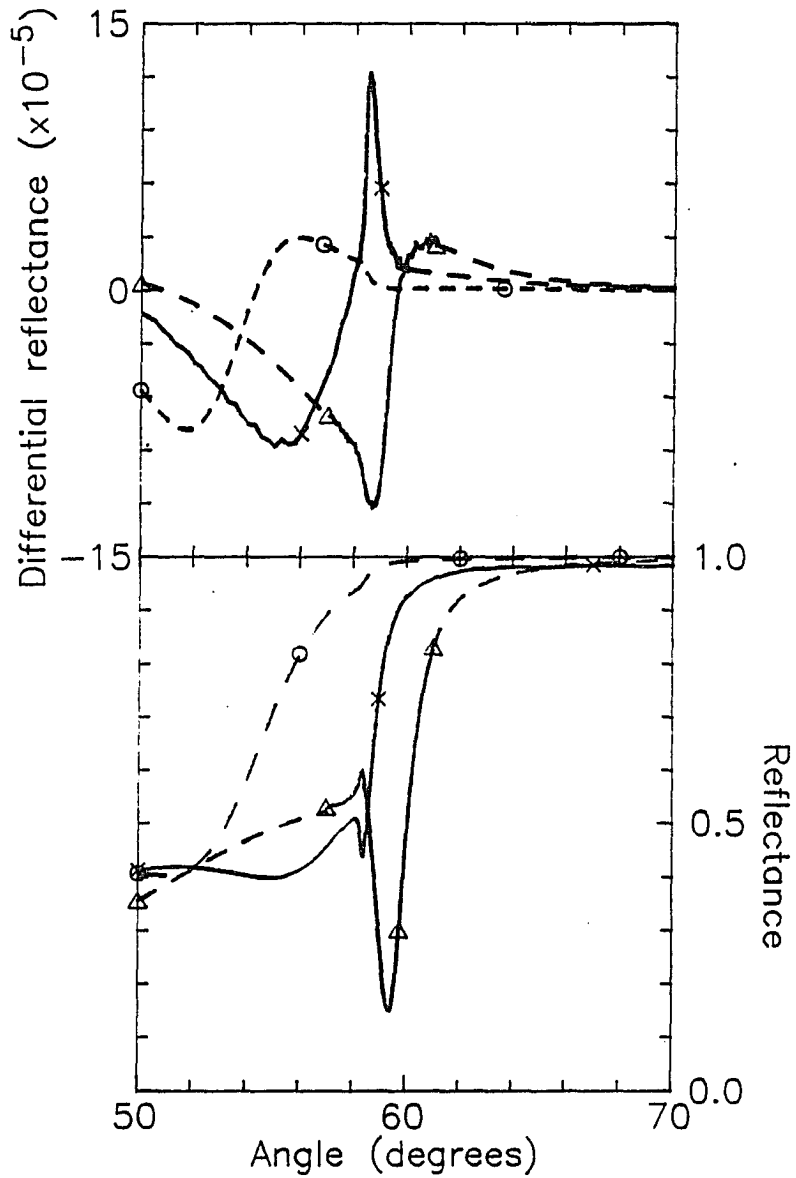


Fig. 6.16. Prism-coupled reflectance and differential reflectance as a function of bounding layer asymmetry: $n_{\text{cou}} < n_{\text{sub}}$.

coupling-layer refractive index is 1.507 - Δ (data set #3b), 1.457 - x (data set #3k), and 1.40 - o (theoretical); substrate index is 1.514.

angles lower than the critical angle due to the coupling-layer resonances. The experimental curve of ΔR for $n_{\text{COU}}=1.457$ is about 20% smaller than that expected for the applied field strength of this experiment, but its shape follows the theory. Alignment of the incident laser beam in a weaker part of the fringing field from the copper conducting strip is suspected as the cause of this discrepancy. The curve was scaled accordingly for plotting in Fig. 6.16, and it has a larger magnitude than that of the near-symmetric case.

CHAPTER 7

CONCLUSIONS

The purpose of this investigation has been to develop a unified theoretical framework for surface plasmon polaritons in layered media which can be applied to the special cases of a surface-active medium bounded by optically nonlinear media or a surface-active medium which is magnetic. Two types of surface plasmon modes were treated: modes which are bound to the interfaces of the surface-active medium, not interacting with bulk radiation; and modes which are coupled to bulk radiation in an optically dense medium acting as a prism. The properties of both types of modes are derived from the expression for reflection from a multiple-layered stack, depending fundamentally on the optical impedance of each layer. The propagation constant of a bound mode is the complex pole of reflectance. A prism-coupled mode is detected by a resonant minimum in the reflectance, and its resonance properties depend on the complex pole and zero of the reflectance.

By appropriate modification of the expression for optical impedance, the properties of surface magnetoplasmon polaritons and nonlinear surface plasmon polaritons are presented in a form similar to that of the properties of linear, nonmagnetic surface plasmon polaritons. The theory is generally applicable to TM-polarized plane waves in multilayered, dielectric media which exhibit the forms of the dielectric tensor given in the text. A particular emphasis in this work was placed on the long-range surface plasmon polariton of a thin metal film bounded by non-metallic media. The long-range mode has smaller losses than the short-range

surface plasmon of a thin metal film or the single-interface plasmon. Consequently, the nonlinear effects and, in some cases, the magneto-optic effects on reflected radiation from the prism-coupled, long-range surface plasmon are enhanced relative to the effects on other plasmon modes and on bulk reflectance.

The nonlinear wave theory was developed for prism coupling to the TM guided waves of a thin film bounded by a substrate whose dielectric constant is proportional to the square of the electric field. Modelling the incident beam as an infinite plane wave, a uniaxial approximation which assumes a dielectric constant dependent on the square of the field normal to the film is justified for the case of surface plasmon excitation. The reflectance and electromagnetic fields of the prism-coupled surface plasmon are expressed in terms of a nonlinear optical impedance, and the incident and reflected intensities are calculated parametrically from the field in the nonlinear substrate. A long-range surface-plasmon geometry demonstrates switching between high and low reflectance at intensities almost two orders of magnitude less than those needed for the switching of an equivalent single-surface plasmon geometry.

As the wavelength of excitation is increased, and the plasmon modes become less confined and less lossy, the nonlinear behavior becomes more sensitive to the multilayer geometry. An additional power-limited branch of the reflectance curve is expected for moderate prism-loading, due to self-focussing in a substrate with a positive nonlinearity. A positive nonlinearity requires higher switching intensity than a negative nonlinearity. Based on perturbation theory, a nonlinearity in the coupling layer requires a higher switching intensity than a nonlinearity in the substrate. Nonlinear wave theory was compared to perturbation theory and homogeneous index approaches to the problem, and was found to apply to a wider

variety of material parameters. However, the simple homogeneous index approach is helpful in gaining a qualitative understanding of the switching behavior of prism-coupled, nonlinear guided waves.

When the metal film in a surface plasmon geometry is magnetic, the properties of the surface plasmon are perturbed. A transverse magnetization induces non-zero, off-diagonal elements in the dielectric tensor, which couple the components of the electric field in the plane of incidence. Equivalently, the Lorentz force on the oscillating surface charges induces motion normal to the oscillation. A shift of the dispersive and absorptive parts of the surface plasmon propagation constant results from the magnetization. The dispersion relation for the surface magnetoplasmon polariton is derived from the Fresnel reflectance coefficient when the optical impedance is replaced by a transverse, magneto-optical impedance. The shift of the propagation constant of the bound, long-range surface magnetoplasmon polariton depends on the metal-film thickness, and is generally much smaller than that of the single-interface magnetoplasmon polariton. Reflectance perturbations at the two metal interfaces are opposite, and for a symmetrically-bounded metal film they are equal in magnitude to first order in the magnetization, such that they tend to cancel. The shift of the propagation constant is increased for an asymmetrically-bounded metal film.

Surface magnetoplasmon polaritons can be studied experimentally using prism coupling. The shifts of the dispersive and absorptive parts of the propagation constant are manifested by angular shifts in the position and width of the reflectance resonance, respectively. Because the shifts are very small, the effect is detected by modulating an applied magnetic field and measuring the transverse Kerr differential reflectance. Perturbation of the surface-plasmon resonance produces an enhanced

differential reflectance signal near the resonance, the angular shape of which depends on the shape of the quasi-Lorentzian reflectance dip and the magnitude and sign of the propagation constant shift. Contrary to the conclusions of past research, the shape of the differential reflectance signal does not depend on the magnitude of the magneto-optic coefficient, but does depend on its phase. Prism coupling to the long-range surface magnetoplasmon magnifies the effect of a small shift in propagation constant because of the mode's narrow resonance. The differential reflectance signal from the long-range surface plasmon geometry is comparable in magnitude to that from single-interface plasmon geometries, and it exhibits much narrower angular features.

Prism-coupling measurements were made of thin nickel films on glass substrates. The long-range surface plasmon polariton was observed as a resonance in the angular reflectance, and the corresponding surface magnetoplasmon polariton was observed as a resonance in the differential reflectance from the prism coupler. Material parameters of the nickel samples were inferred by matching the experimental measurements to a multilayer model. Although the applied magnetic field was significantly weaker than the coercivity of the nickel films, the phase of the magneto-optic coefficient was determined from the angular shape of the differential reflectance signal. To obtain satisfactory agreement between theory and experiment, a magnetically inert, nickel surface layer was hypothesized. It was on the order of several atomic layers thick, and is believed to be due to a destruction of the local magnetic moment of nickel via the adsorption of coupling liquid on the exposed nickel surface. Other material models did not adequately explain the observed differential reflectance signal.

A wide variety of samples were investigated to substantiate the theoretical conclusions. The magnitude of the differential reflectance signal increased with nickel film thickness in the 13 - 45-nm range, accompanied by an increase in the resonance angle and width. For a significant difference between the refractive indices of the coupling layer and the glass substrate, the strength of the differential reflectance was increased relative to that of the near-symmetric structure. The single-interface magnetoplasmon polariton was excited by using a large index-matching liquid or by making the coupling-layer thickness very small. In all cases, the angular shape of the differential reflectance was consistent with the expectations of theory, and the measured material constants agreed with values cited in the literature.

Future research will expand upon the present work in several areas. As of this writing, there has been no experimental observation of the nonlinear, long-range surface plasmon polariton. Optical bistability from a prism-coupled waveguide with an electronic nonlinearity is also of current interest, but has not been observed. Conclusive experimental evidence will settle the question of whether hysteresis occurs in the reflected intensity as a function of prism-coupled, incident intensity from a real source. The whole field of nonlinear waveguides is still in its infancy, and much work is necessary to develop suitable materials and device concepts in order to reach its potential. The stability of nonlinear guided modes, grating and endfire coupling, and optical logic require further research from both physics and engineering viewpoints.

The study of surface magnetoplasmon polaritons is part of the larger field of magneto-optics, which has experienced a resurgence of interest recently due to its potential in erasable optical recording. Of great importance to efficient and reliable

devices are the properties of magnetic materials and surfaces. Surface magnetoplasmon research offers tools for studying the optical properties of materials and their surfaces, particularly small impurity layers such as the inert layer. The polar and longitudinal, long-range surface magnetoplasmon polaritons should be investigated experimentally, since these configurations are of greater practical interest. Magneto-optics also holds promise in the area of optical sensing. Electric-current, magnetic-field, and impurity sensing are examples of the applications which merit further inquiry.

While the study of surface plasmon polaritons may appear on the surface to have limited scope, the theoretical basis and experimental techniques on which it relies are applicable to the broad realm of layered-media research. Since the early investigations at the turn of the century, interest in the subject has resurfaced again and again. When the interest is coupled with the imagination of future scientists, the long-range outlook for surface plasmon polaritons looks bright.

APPENDIX A

MATERIAL CHARACTERIZATION USING EXPERIMENTAL PRISM-COUPLER REFLECTANCE

The linear, nonmagnetic properties of the nickel film samples and adjacent layers used in the study of surface magnetoplasmons were determined primarily by analysis of the TM reflectance measurements reported in Chapter 6. This appendix provides details of the analysis. A set of theoretical reflectance curves is presented for a variation in each relevant sample parameter to identify its primary and secondary effects. Using the key features of the typical reflectance curve as a monitor, a systematic procedure is developed which aids in theoretically matching the experimental data with a multilayer model of a sample. Although the metal properties given here as an example are close to those of nickel, and the wavelength is 632.8 nm, the method of analysis can generally be applied to other surface plasmon experiments. The discussion of magneto-optic properties is given in Chapter 6.

Assuming that the sample materials studied in Chapter 6 are homogeneous and have low optical loss (except for the metal), and that the interfaces of the four-layer prism-coupler stack are planar and parallel, the seven unknown sample parameters are listed in Table A.1. The expression for the TM reflectance as a function of these parameters and the angle in the prism, Eq. (2.23), is not separable into terms depending on individual parameters. However, the reflectance as a function of angle has several distinct features which can be used to monitor the effect of the sample parameters (for example, see Fig. A.3); they are also listed in

Table A.1. Unknown sample parameters and features of TM reflectance curves

Unknown sample parametersreal part of metal dielectric constant, ϵ'_{Ni} imaginary part of metal dielectric constant, ϵ''_{Ni} metal thickness, d_{Ni} prism refractive index, n'_{pr} coupling layer refractive index, n'_{cou} coupling layer thickness, d_{cou} substrate refractive index, n'_{sub} Distinct features of TM reflectance vs incident angle

Air-sample reflectance:

reflectance minimum, R_{min} angle of reflectance minimum, θ_{min}

reflectance slope with angle

Prism-coupled, long-range surface plasmon (LRSP) reflectance:

number of coupling-layer resonances, #FP

average reflectance of Fabry-Perot coupling-layer resonances, R_{FP} critical angle, θ_c angle of LRSP resonance, θ_{sp} minimum reflectance of LRSP resonance, R_{sp} LRSP resonance width, $\delta\theta_{sp}$

Table A.1. In addition to the prism-coupled reflectance, the reflectance of the bare nickel film samples (air-nickel-substrate) was measured in this study, and its features are listed as well (for example, see Fig. A.1). Altogether there are nine measurable reflectance features to determine the seven unknowns. It appears from numerical studies that the seven unknowns can be uniquely specified by matching theoretical reflectance curves to the experimental data, although a strict mathematical analysis has not been applied.

To study the effects of the sample parameters on the reflectance features, each sample parameter is varied separately around its typical value, and a set of reflectance curves is plotted as a function of angle. The typical sample is a nickel film of 20-nm-thickness with a dielectric constant $\epsilon_{Ni} \equiv \epsilon' + i\epsilon'' = -13 + i16$, and a substrate with a refractive index of 1.5. Figure A.1 consists of sets of theoretical, bare sample reflectance curves for different values of nickel ϵ' (-11 to -17) and of nickel ϵ'' (12 to 24), and Figure A.2 consists of sets of curves for values of nickel thickness (15 nm to 30 nm) and of the substrate index (1.48 to 1.54). Certain observations can be made from these plots: 1) the effects of nickel thickness and ϵ' on reflectance are virtually identical, shifting the reflectance almost uniformly over a wide angular range; these parameters cannot be independently determined based on this measurement alone; 2) the effect of nickel ϵ'' is primarily on the angular position of the pseudo-Brewster reflectance minimum and on the average slope of the reflectance curve; 3) the effect of the substrate index on reflectance is minimal -- less than a 0.0028 reflectance change for all angles between 10° and 85° if the index is varied by 0.06.

Standard values of the additional parameters involved in prism-coupler reflectance measurements are the prism refractive index of 1.7788, the coupling-layer

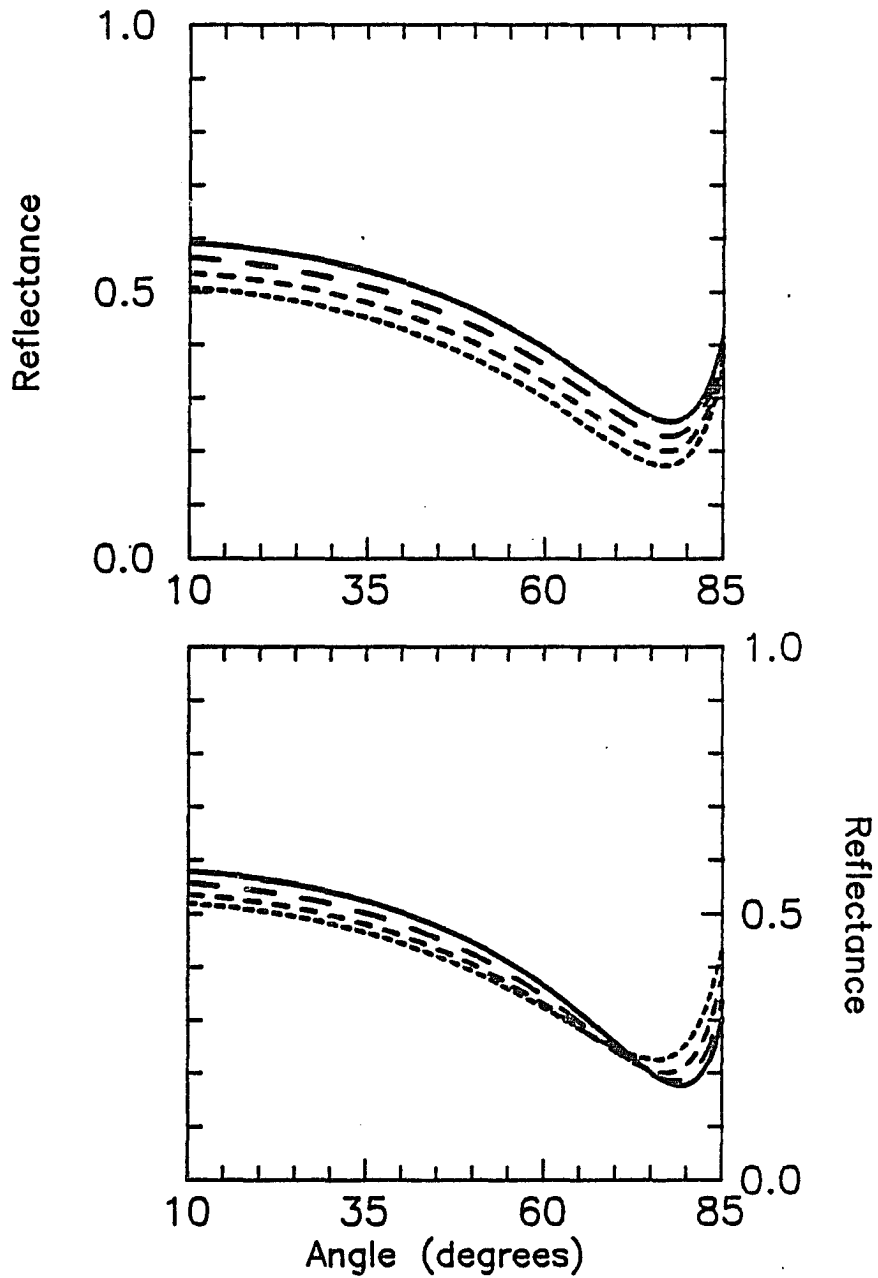


Fig. A.1. Theoretical dependence of bare sample reflectance on nickel dielectric constant

top plot: $\epsilon''=16$, $\epsilon'=-17$ (solid), $\epsilon'=-15$ (long-dashed), $\epsilon'=-13$ (medium-dashed), $\epsilon'=-11$ (short-dashed); bottom plot: $\epsilon'=-13$, $\epsilon''=24$ (solid), $\epsilon''=20$ (long-dashed), $\epsilon''=16$ (medium-dashed), $\epsilon''=12$ (short-dashed); other parameters are standard.

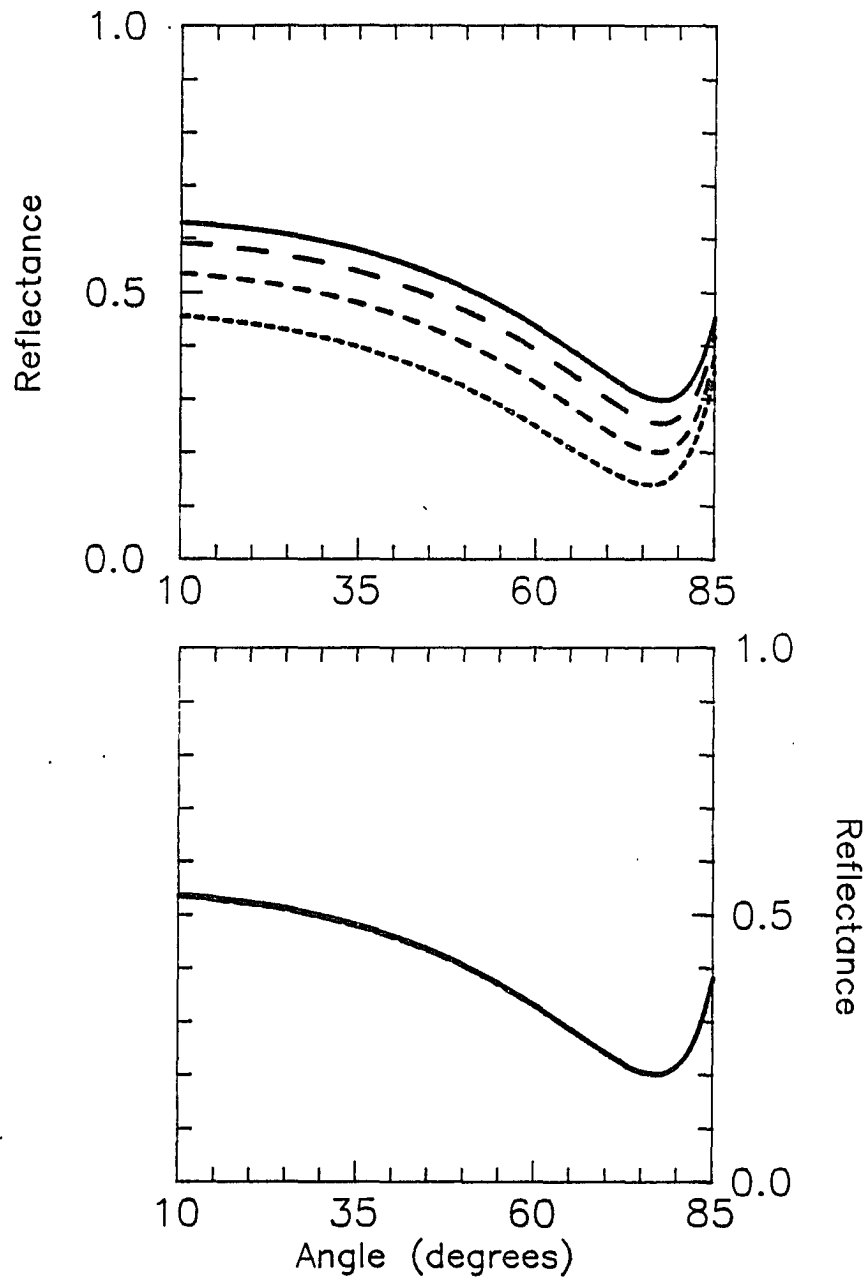


Fig. A.2. Theoretical dependence of bare sample reflectance on nickel thickness and substrate refractive index

top plot: $d_{Ni}=30$ nm (solid), $d_{Ni}=25$ nm (long-dashed), $d_{Ni}=20$ nm (medium-dashed), $d_{Ni}=15$ nm (short-dashed); bottom plot (note that all curves overlap): $n_{sub}=1.54$ (solid), $n_{sub}=1.52$ (long-dashed), $n_{sub}=1.50$ (medium-dashed), $n_{sub}=1.48$ (short-dashed); other parameters are standard.

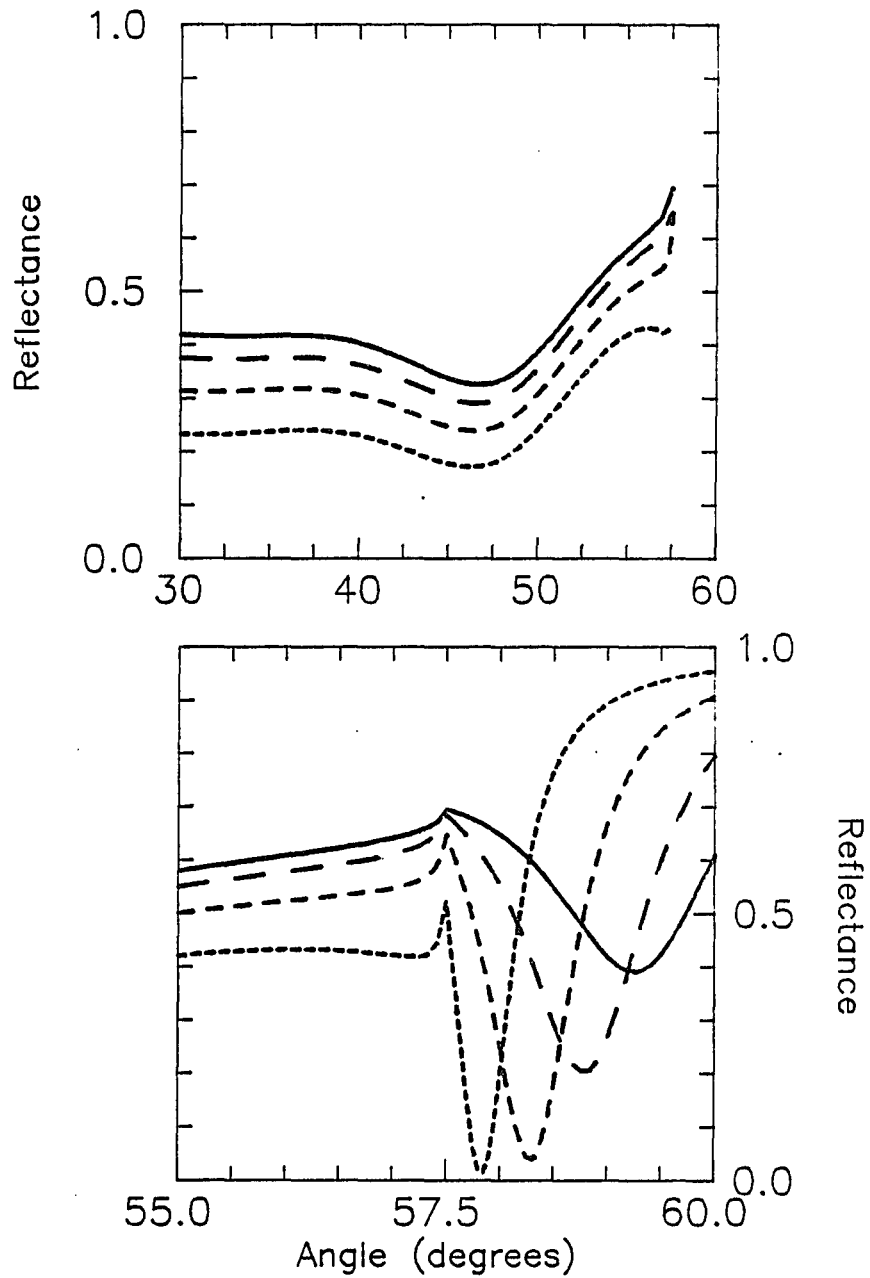


Fig. A.3. Theoretical dependence of reflectance from prism-coupled, long-range surface plasmon on nickel thickness

$d_{Ni}=30$ nm (solid), $d_{Ni}=25$ nm (long-dashed), $d_{Ni}=20$ nm (medium-dashed), $d_{Ni}=15$ nm (short-dashed); other parameters are standard.

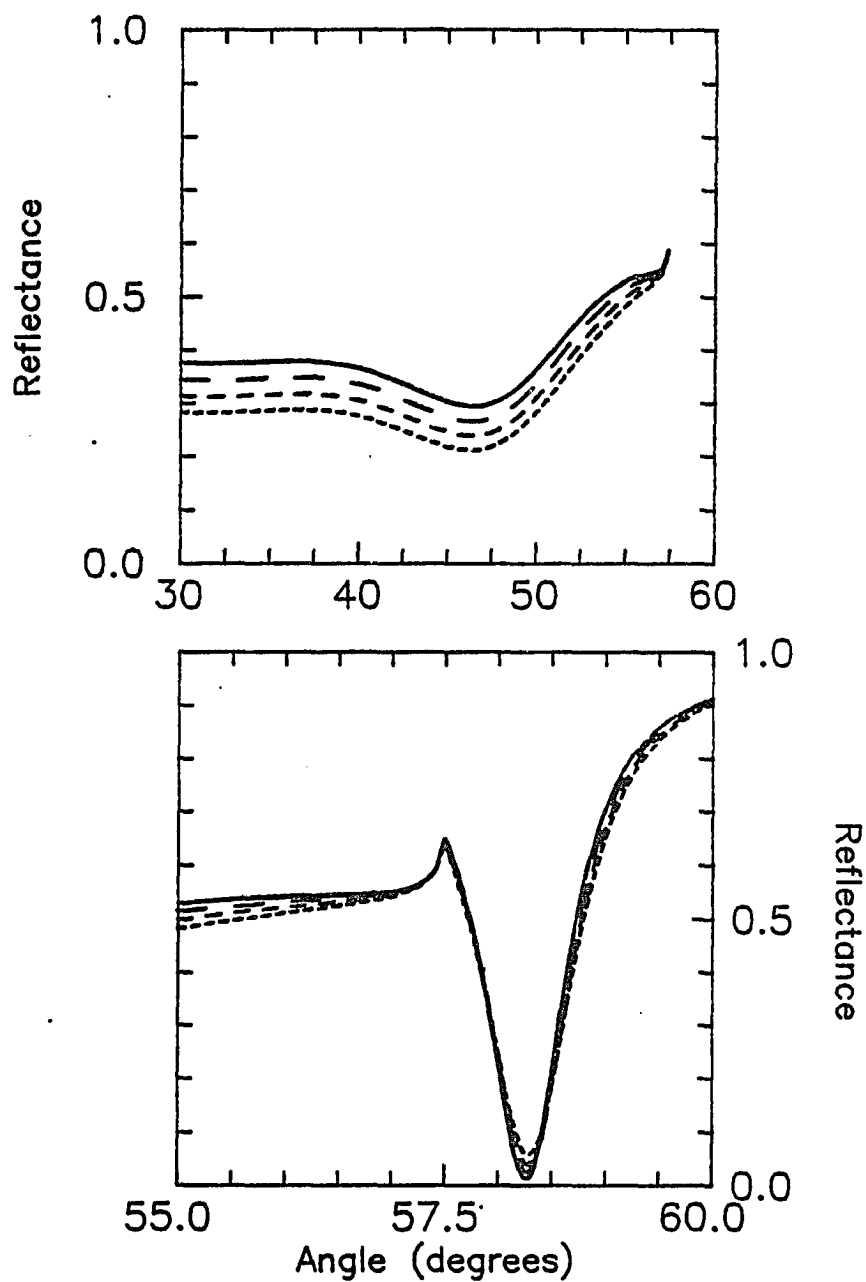


Fig. A.4. Theoretical dependence of reflectance from prism-coupled, long-range surface plasmon on real part of nickel dielectric constant

$\epsilon' = -17$ (solid), $\epsilon' = -15$ (long-dashed), $\epsilon' = -13$ (medium-dashed), $\epsilon' = -11$ (short-dashed); other parameters are standard.

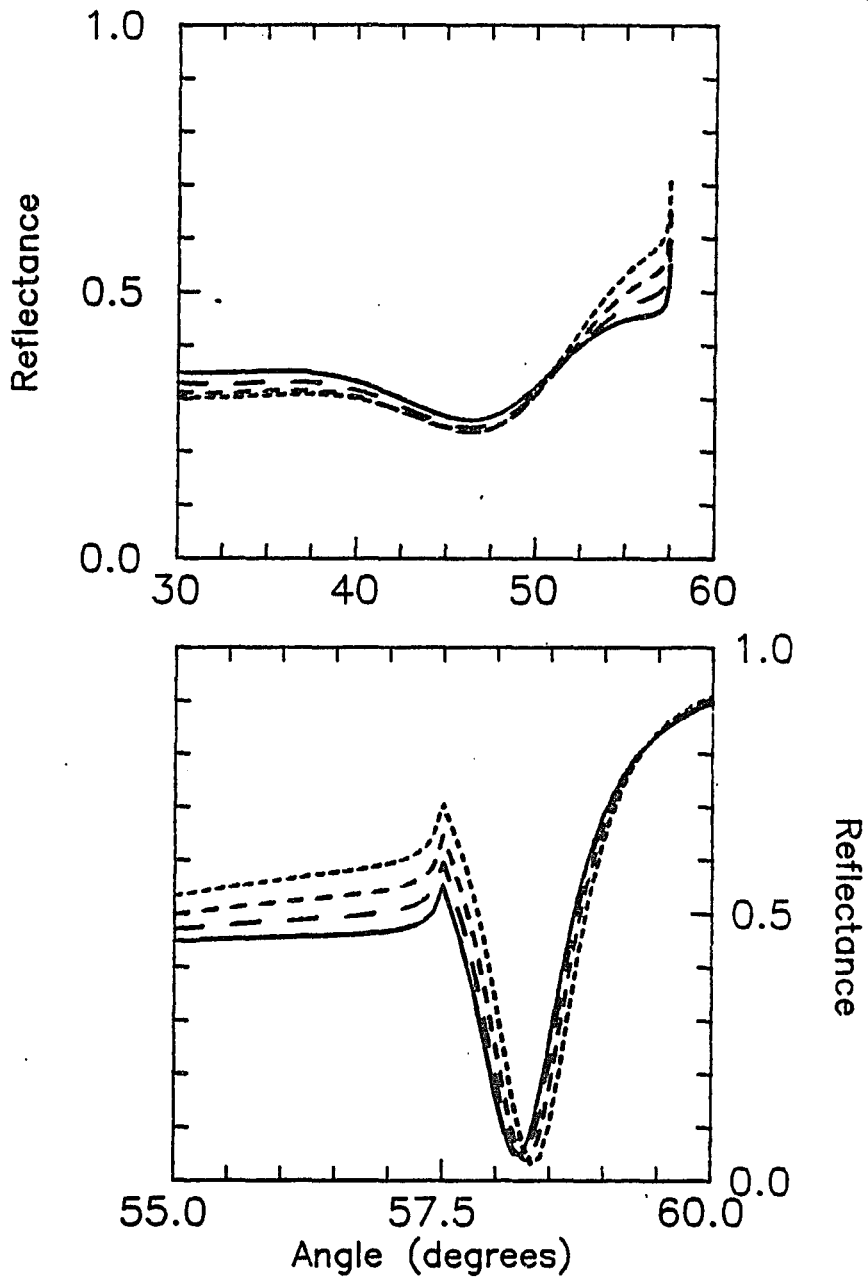


Fig. A.5. Theoretical dependence of reflectance from prism-coupled, long-range surface plasmon on imaginary part of nickel dielectric constant

$\epsilon''=24$ (solid), $\epsilon''=20$ (long-dashed), $\epsilon''=16$ (medium-dashed), $\epsilon''=12$ (short-dashed); other parameters are standard.

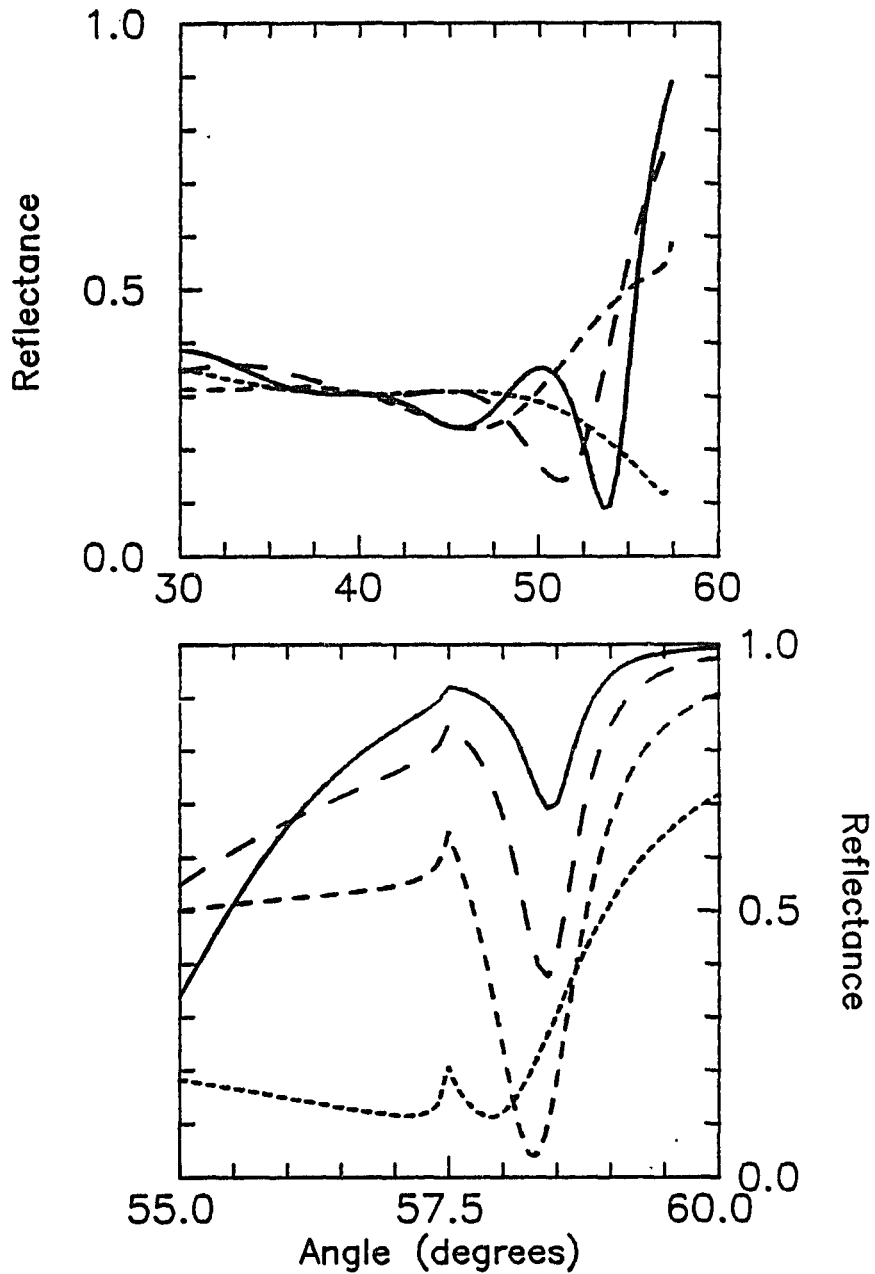


Fig. A.6. Theoretical dependence of reflectance from prism-coupled, long-range surface plasmon on coupling-layer thickness

$d_{\text{COU}}=0.9 \mu\text{m}$ (solid), $d_{\text{COU}}=0.7 \mu\text{m}$ (long-dashed), $d_{\text{COU}}=0.5 \mu\text{m}$ (medium-dashed), $d_{\text{COU}}=0.3 \mu\text{m}$ (short-dashed); other parameters are standard.

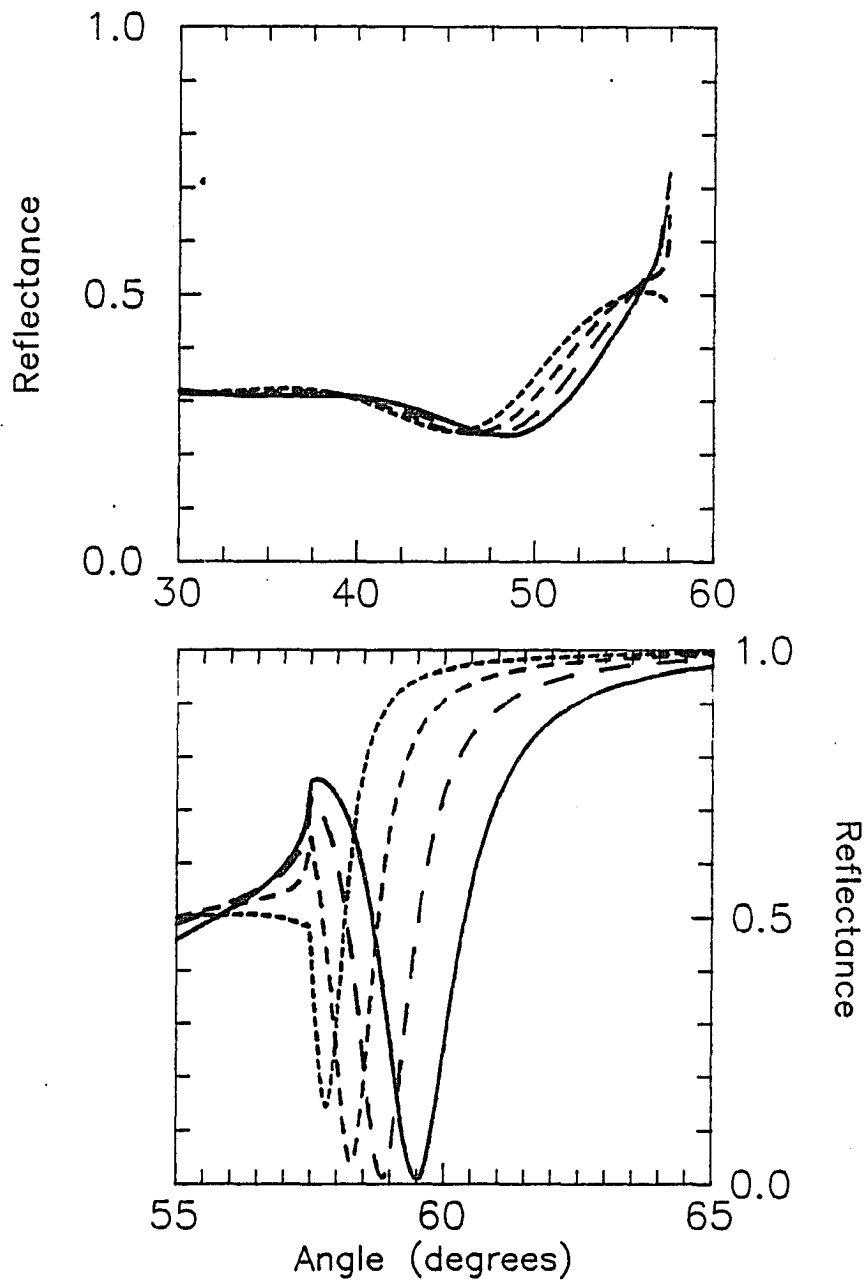


Fig. A.7. Theoretical dependence of reflectance from prism-coupled, long-range surface plasmon on coupling-layer refractive index

$n_{\text{cou}}=1.54$ (solid), $n_{\text{cou}}=1.52$ (long-dashed), $n_{\text{cou}}=1.50$ (medium-dashed), $n_{\text{cou}}=1.48$ (short-dashed); other parameters are standard.

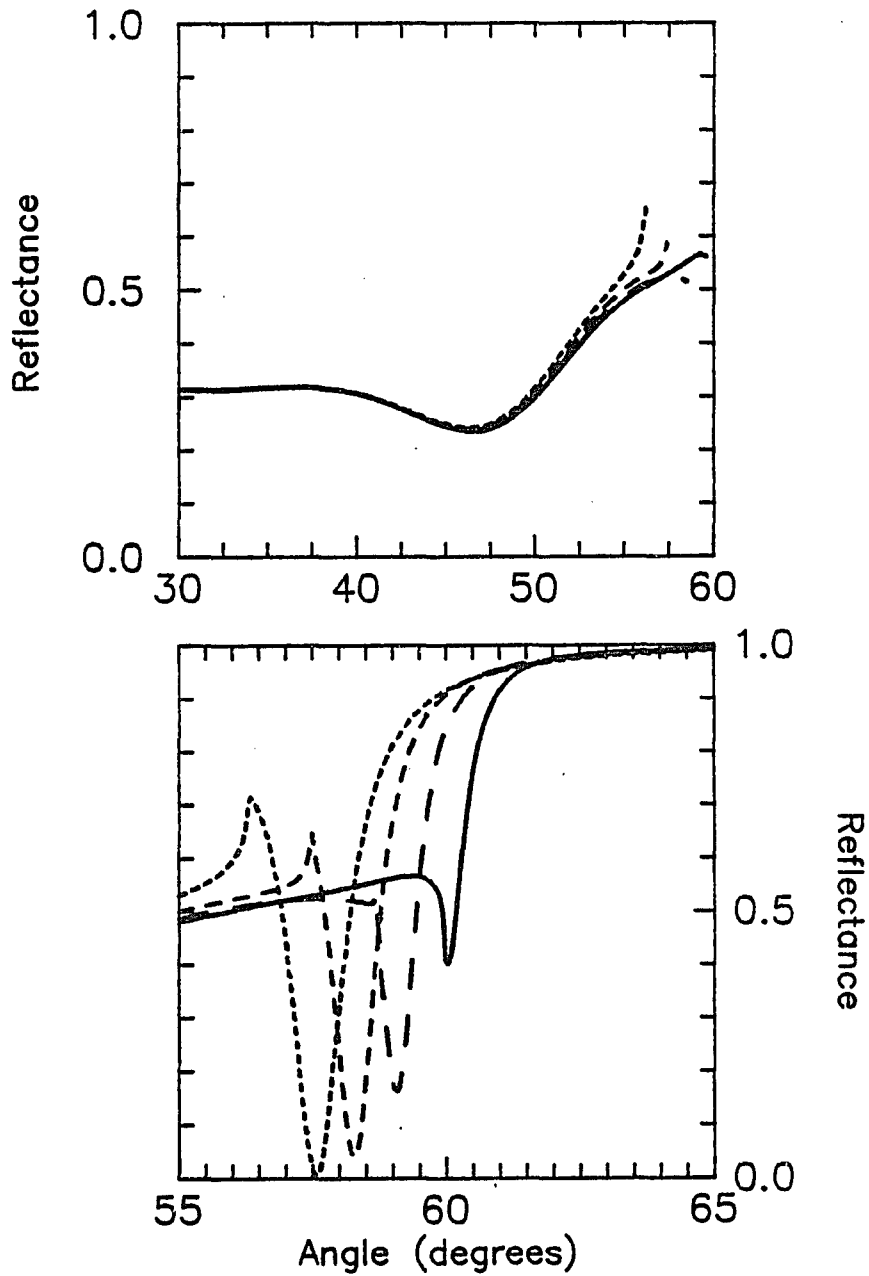


Fig. A.8. Theoretical dependence of reflectance from prism-coupled, long-range surface plasmon on substrate refractive index

$n_{\text{sub}}=1.54$ (solid), $n_{\text{sub}}=1.52$ (long-dashed), $n_{\text{sub}}=1.50$ (medium-dashed), $n_{\text{sub}}=1.48$ (short-dashed); other parameters are standard.

thickness of $0.5 \mu\text{m}$, and the coupling-layer refractive index of 1.5. Figures A.3 - A.8 illustrate the changes in reflectance caused by variations in nickel thickness (15 nm to 30 nm), ϵ' (-11 to -17), and ϵ'' (12 to 24), coupling layer thickness ($0.3 \mu\text{m}$ to $0.9 \mu\text{m}$) and index (1.48 to 1.54), and substrate index (1.48 to 1.54), respectively. Since the same prism was used for all measurements in the experimental study, and in this study its index of refraction was already known [138], a variation in the prism index was not considered. In each figure, a plot from an angle of 30° to the critical angle is shown to highlight the coupling-layer resonances, and a plot of narrower range, either $55 - 60^\circ$ or $55 - 65^\circ$, is shown to highlight the surface plasmon resonance. The effects of each parameter on the reflectance features are clearly seen in the figures and have been explained to some degree in chapter 2. The degree to which each parameter affects a certain feature can be classified as primary or secondary. This classification is presented in Table A.2.

Table A.2 suggests a systematic procedure for matching the experimental reflectance data with a theoretical model in order to determine the unknown sample parameters. The features of the reflectance curves are considered one at a time, and by varying a parameter of the four-layer stack theoretically, the best match of theoretical to experimental reflectance is found. The cycle is repeated until it converges on a solution within the accuracy of the data. To accelerate the procedure, the features which are affected by the least number of parameters are matched first. For example, the sharp feature in the prism-coupled reflectance at the critical angle is determined solely by the substrate index and the known prism index, as discussed in Section 5B.2; therefore, one of the first steps is a determination of the substrate index. An outline of the complete procedure follows:

Table A.2. Degree of dependence of prism-coupled TM reflectance features on sample parameters

| <u>feature</u> | <u>primary dependence</u> | <u>secondary dependence</u> |
|----------------------------|---|---|
| #FP | d_{cou} | n_{cou} |
| RFP | $d_{\text{Ni}}, \epsilon'_{\text{Ni}}$ | ϵ''_{Ni} |
| θ_{c} | n_{sub} | |
| θ_{sp} | $d_{\text{Ni}}, n_{\text{cou}}, n_{\text{sub}}$ | $\epsilon''_{\text{Ni}}, d_{\text{cou}}$ |
| R_{sp} | $d_{\text{Ni}}, d_{\text{cou}}$ | $\epsilon'_{\text{Ni}}, n_{\text{cou}}, n_{\text{sub}}$ |
| $\delta\theta_{\text{sp}}$ | $d_{\text{Ni}}, n_{\text{cou}}$ | $\epsilon'_{\text{Ni}}, \epsilon''_{\text{Ni}}, d_{\text{cou}}, n_{\text{cou}}, n_{\text{sub}}$ |

- 1) Set all sample parameters to their estimated values.
- 2) Determine ϵ''_{Ni} approximately from θ_{min} of the bare sample reflectance.
- 3) Determine n_{sub} from the critical angle, θ_c , based on the prism-coupled reflectance.
- 4) Adjust d_{cou} to approximate the number of coupling-layer resonances, #FP.
- 5) Adjust d_{Ni} to approximate the average reflectance, R_{FP} , of the coupling-layer resonances.
- 6) Adjust n_{cou} to approximate the surface plasmon resonance angle, θ_{sp} .
- 7) Adjust d_{Ni} to fit the minimum reflectance of the surface plasmon resonance, R_{sp} .
- 8) Adjust ϵ'_{Ni} to fit R_{FP} .
- 9) Adjust ϵ''_{Ni} to fine tune features of the prism-coupled reflectance.
- 10) Repeat steps 4 through 9, noting the effect of each sample parameter on all of the reflectance features, until the best match of theoretical and experimental reflectance is obtained.
- 11) Confirm the inferred values of nickel parameters by comparing theoretical and experimental bare sample reflectance curves.

The procedure is interactive, and it was automated on an IBM personal computer for plotting and comparing theoretical and experimental reflectance curves and calculating the deviation between them. The accuracy to which the sample parameters could be determined is given in Table 6.1.

REFERENCES

1. E. Burstein, *Comments on Solid State Physics* 1, 202 (1969).
2. E. Burstein, in *Polaritons*, edited by E. Burstein and F. de Martini (Pergamon, New York, 1974), p. 1.
3. J.J. Hopfield, *Phys. Rev.* 112, 1555 (1958).
4. D.L. Mills and E. Burstein, *Rep. Progr. Phys.* 37, 817 (1974).
5. see *Polaritons*, edited by E. Burstein and F. de Martini (Pergamon, New York, 1974).
6. R. Ruppin and R. Englman, *Rep. Progr. Phys.* 33, 149 (1970).
7. E. Burstein, W.P. Chen, Y.J. Chen, and A. Harstein, *J. Vac. Sci. Technol.* 11, 1004 (1974).
8. J. Zenneck, *Ann. Physik* 23, 846 (1907).
9. A. Sommerfeld, *Ann. Physik* 28, 665 (1909).
10. U. Fano, *J. Opt. Soc. Amer.* 31, 213 (1941).
11. E. Burstein, A. Harstein, J. Schoenwald, A.A. Maradudin, D.L. Mills and R.F. Wallis, in *Polaritons*, edited by E. Burstein and F. de Martini (Pergamon, New York, 1974), p. 89.
12. A. Otto, *Advan. Solid State Phys.* 14, 1 (1974).
13. P. Halevi, in *Electromagnetic Surface Modes*, edited by A.D. Boardman (John Wiley & Sons, New York, 1982), p. 249.
14. T. Tamir, in *Electromagnetic Surface Modes*, edited by A.D. Boardman (John Wiley & Sons, New York, 1982), p. 521.
15. F. Goos and H. Haenchen, *Ann. Phys. Lpz.* (6) 1, 333 (1947) and (6) 5, 251 (1949).
16. P. Leurgans and A.F. Turner, *J. Opt. Soc. Am.* 37, 983 (1947).
17. A. Otto, *Z. Physik* 216, 398 (1968).
18. E. Kretschmann and H. Raether, *Z. Naturforsch.* 23a, 2135 (1968).

19. E. Kretschmann, Z. Phys. 241, 313 (1971).
20. P.K. Tien, Appl. Opt. 10, 2395 (1971).
21. P.K. Tien, R. Ulrich and R.J. Martin, Appl. Phys. Lett. 14, 291 (1969).
22. D. Bohm and D. Pines, Phys. Rev. 92, 609 (1953); D. Pines, Phys. Rev. 92, 626 (1953).
23. R.H. Ritchie, Phys. Rev. 106, 874 (1957).
24. E.A. Stern, quoted by R.A. Ferrell, Phys. Rev. 111, 1214 (1958).
25. C.J. Powell and J.B. Swan, Phys. Rev. 115, 869 (1959); 116, 81 (1959).
26. P. von Blackenhagen, H. Boersch, D. Fritsche, H.G. Seifert and G. Sauerbrey, Phys. Lett. 11, 296 (1964).
27. Y.-Y. Teng and E.A. Stern, Phys. Rev. Lett. 19, 511 (1967).
28. S.N. Jasperson and S.E. Schnatterly, Phys. Rev. 188, 759 (1969); Bull. Amer. Phys. Soc. 12, 399 (1967).
29. K.L. Kliewer and R. Fuchs, Advan. Chem. Phys. 27, 355 (1974).
30. A. Otto, in: Optical Properties of Solids, New Developments, edited by B.O. Seraphin (North-Holland, Amsterdam, 1975), p. 677.
31. H. Raether, in Surface Polaritons, edited by V.M. Agranovich and D.L. Mills (North-Holland, Amsterdam, 1982), p. 331.
32. W.H. Weber and S.L. McCarthy, Appl. Phys. Lett. 25, 396 (1974).
33. K.L. Kliewer and R. Fuchs, Phys. Rev. 153, 498 (1967).
34. E.N. Economou, Phys. Rev. 182, 539 (1969).
35. H. Raether, Surf. Sci. 8, 233 (1967).
36. F. Abèles and T. Lopez-Rios, Opt. Comm. 11, 89 (1974).
37. G.J. Kovacs and G.D. Scott, Phys. Rev. B 16, 1297 (1977).
38. A.B. Buckman and C. Kuo, J. Opt. Soc. Am. 69, 343 (1979).
39. G.J. Kovacs, "Optical Excitation of Resonant Electromagnetic Oscillations in Thin Films", Doctoral Dissertation, University of Toronto, 1977.
40. G.J. Kovacs, Thin Solid Films 60, 33 (1979).

41. M. Fukui, V.C.Y. So and R. Normandin, *Phys. Stat. Sol. B* 91, K61 (1979).
42. Dror Sarid, *Phys. Rev. Lett.* 47, 1927 (1981).
43. Dror Sarid, R.T. Deck, A.E. Craig, R.K. Hickernell, R.S. Jameson and J.J. Fasano, *Appl. Opt.* 21, 3993 (1982).
44. Dror Sarid, R.T. Deck and J.J. Fasano, *J. Opt. Soc. Am.* 72, 1345 (1982).
45. G.I. Stegeman, J.J. Burke and D.G. Hall, *Appl. Phys. Lett.* 41, 906 (1982).
46. L. Wendler and R. Haupt, *J. Appl. Phys.* 59, 3289 (1986).
47. G.I. Stegeman, J.J. Burke and D.G. Hall, *Opt. Lett.* 8, 383 (1983).
48. G.I. Stegeman, *Appl. Opt.* 22, 2243 (1983).
49. G.I. Stegeman and J.J. Burke, *Appl. Phys. Lett.* 43, 221 (1983).
50. A.E. Craig, G.A. Olson and Dror Sarid, *Opt. Lett.* 8, 380 (1983).
51. Y. Kuwamura, M. Fukui, and O. Tada, *J. Phys. Soc. Japan* 52, 2350 (1983).
52. J. C. Quail, J. G. Rako, and H. J. Simon, *Opt. Lett.* 8, 377 (1983).
53. R.T. Deck, Dror Sarid, G.A. Olson and J.M. Elson, *Appl. Opt.* 22, 3397 (1983).
54. R.A. Booman, G.A. Olson and Dror Sarid, *Appl. Opt.* 25, 2729 (1986).
55. D. Maystre, in *Electromagnetic Surface Modes*, edited by A.D. Boardman (John Wiley & Sons, New York, 1982), p. 661.
56. G.I. Stegeman, R.F. Wallis and A.A. Maradudin, *Opt. Lett.* 8, 386 (1983).
57. P. Drude, *Theory of Optics* (Longmans, Green, New York, 1922; Dover, New York, 1968).
58. J. Schoenwald, E. Burstein and J.M. Elson, *Solid State Comm.* 12, 185 (1973).
59. H.E. Bennett and J.M. Bennett, in *Optical Properties and Electronic Structure of Metals and Alloys*, edited by F. Abeles (Elsevier North-Holland, New York, 1966), p. 175.
60. P.B. Johnson and R.W. Christy, *Phys. Rev. B* 6, 4370 (1972).
61. P.B. Johnson and R.W. Christy, *Phys. Rev. B* 9, 5056 (1974).
62. A. Otto, in *Polaritons*, edited by E. Burstein and F. de Martini (Pergamon, New York, 1974), p. 117.

63. A. Craig, "Surface plasmon waves on thin metal films", Doctoral Dissertation, Univ. of Arizona, Tucson, 1984.
64. G.C. Aers, A.D. Boardman and P. Clark, Phys. Stat. Sol. B 85, 171 (1978).
65. R.D. Olney, R.J. Romagnoli and P.E. Ferguson, J. Opt. Soc. Am. B 3, 1526 (1986).
66. Dror Sarid and G.I. Stegeman, J. Appl. Phys. 52, 5439 (1981).
67. B. Crosignani, C.H. Papas, and P. Di Porto, Optics Letters 6, 61 (1981).
68. H. Winful, J.H. Marburger, and E. Garmire, Appl. Phys. Lett. 35, 379 (1979).
69. Dror Sarid, Proc. SPIE 317, 132 (1981).
70. G.I. Stegeman, IEEE J. Quantum Electron. QE-18, 1610 (1982).
71. B. Bosacchi and L.M. Narducci, Opt. Lett. 8, 324 (1983).
72. G.M. Wysin, H.J. Simon, and R.T. Deck, Opt. Lett. 6, 30 (1981).
73. Y.J. Chen and G.M. Carter, Solid State Commun. 45, 277 (1983).
74. P. Martinot, S. Laval, and A. Koster, J. Phys. 45, 597 (1984).
75. P. Vincent, N. Paraire, M. Nevriere, A. Koster, and R. Reinisch, J. Opt. Soc. Am. B 2, 1106 (1985).
76. P.W. Smith, J.-P. Hermann, W.J. Tomlinson, and P.J. Maloney, Appl. Phys. Lett. 35, 846 (1979).
77. A.E. Kaplan, JETP Lett. 24, 114 (1976).
78. A.E. Kaplan, Sov. Phys. JETP 45, 896 (1977).
79. W.J. Tomlinson, Opt. Lett. 5, 323 (1980).
80. A.A. Maradudin, Z. Phys. B 41, 341 (1981).
81. N.N. Akhmediev, Sov. Phys. JETP 56, 299 (1982).
82. U. Langbein, F. Lederer, and H.-E. Ponath, Opt. Commun. 46, 167 (1983).
83. A.A. Maradudin, in Optical and Acoustic Waves in Solids - Modern Topics, edited by M. Borissov, (World Scientific, Singapore, 1983), pp. 72.
84. D.J. Robbins, Opt. Commun. 47, 309 (1983).

85. A.D. Boardman and P. Egan, *IEEE J. Quantum Electron.* QE-22, 319 (1986).
86. V.J. Montemayor and R.T. Deck, *J. Opt. Soc. Am. B* 2, 1010 (1985).
87. V.M. Agranovich, V.S. Babichenko, and V.Y. Chernyak, *JETP Lett.* 32, 512 (1980).
88. V.K. Fedyanin and D. Mihalache, *Z. Phys. B* 47, 167 (1982).
89. F. Lederer, U. Langbein, and H.-E. Ponath, *Appl. Phys. B* 31, 187 (1983).
90. D. Mihalache, R.G. Nazmitdinov, and V.K. Fedyanin, *Phys. Scr.* 29, 269 (1984).
91. A.D. Boardman and P. Egan, *J. Phys. Colloq.* C5, 291 (1984).
92. C.T. Seaton, J.D. Valera, B. Svenson, and G.I. Stegeman, *Opt. Lett.* 10, 149 (1985).
93. G.I. Stegeman, C.T. Seaton, J. Ariyasu, R.F. Wallis, and A.A. Maradudin, *J. Appl. Phys.* 58, 2453 (1985).
94. J. Ariyasu, C.T. Seaton, G.I. Stegeman, A.A. Maradudin, and R.F. Wallis, *J. Appl. Phys.* 58, 2460 (1985).
95. K.M. Leung, *Phys. Rev. B* 32, 5093 (1985).
96. R.K. Hickernell and Dror Sarid, *J. Opt. Soc. Am. B* 3, 1059 (1986).
97. G.S. Agarwal and S. Dutta Gupta, in *Optical Bistability 3*, edited by H.M. Gibbs, P. Mandel, N. Peyghambarian, and S.D. Smith (Springer, Berlin 1986), p. 117.
98. G.S. Agarwal and S. Dutta Gupta, *Phys. Rev. B* 34, 5239 (1986).
99. V.J. Montemayor and R.T. Deck, *J. Opt. Soc. Am. B* 3, 1211 (1986).
100. C. Liao, G.I. Stegeman, C.T. Seaton, R.L. Shoemaker, and J.D. Valera, *J. Opt. Soc. Am. A* 2, 590 (1985).
101. M.J. Moran, C.Y. She, and R.L. Carman, *IEEE J. Quantum Electron.* QE-12, 259 (1975).
102. D.A.B. Miller, C.T. Seaton, M.E. Prise, and S.D. Smith, *Phys. Rev. Lett.* 47, 197 (1981).
103. C.K.R.T. Jones and J.V. Moloney, *Proc. of Topical Meeting on Optical Bistability (OB3)*, Tucson, AZ, Dec. 1985.
104. Wayne M. Gibbons and Dror Sarid, *Opt. Lett.*, to be published, August 1987.

105. P. Martinot, A. Koster, and S. Laval, *IEEE J. Quantum Electron.* QE-21, 1140 (1985).
106. Y.J. Chen and G.M. Carter, *Appl. Phys. Lett.* 41, 307 (1982).
107. G. Assanto, B. Svensson, D. Kuchibhatla, U.J. Gibson, C.T. Seaton, and G.I. Stegeman, *Opt. Lett.* 11, 644 (1986).
108. G. Vitrant and P. Arlot, *J. Appl. Phys.* 61, 4744 (1987).
109. Walter G. Driscoll, ed., Handbook of Optics (McGraw-Hill, New York, 1978), p. 7-106.
110. for a survey of magneto optic effects, see M.J. Freiser, *IEEE Trans. Mag.* MAG-4, 152 (1968).
111. P.S. Pershan, *J. Appl. Phys.* 38, 1482 (1967).
112. P.W. Selwood, Chemisorption and Magnetization (Academic Press, New York, 1975).
113. G.S. Krinchik and V.A. Arteme'ev, *Sov. Phys. JETP* 26, 1080 (1968).
114. N.V. Smith, R. Lasser, S. Chiang, *Phys. Rev. B* 25, 793 (1982).
115. C. Kittel, Introduction to Solid State Physics, Fifth Edition (John Wiley & Sons, New York, 1976), p. 223.
116. K.W. Chiu and J.J. Quinn, *Il Nuovo Cim.* 10, 1 (1972).
117. K.W. Chiu and J.J. Quinn, *Phys. Rev. B* 5, 4707 (1972).
118. H. Kaplan, E.D. Palik, R. Kaplan, and R.W. Gammon, *J. Opt. Soc. Am.* 64, 1551 (1974).
119. P.E. Ferguson, O.M. Stafsudd, and R.F. Wallis, *Physica* 86-88B, 1403 (1977).
120. P.E. Ferguson, O.M. Stafsudd, and R.F. Wallis, *Physica* 89B, 91 (1977).
121. G.S. Krinchik, E.E. Chepurova, and T.I. Kraeva, *JETP Lett.* 40, 776 (1984).
122. G.S. Krinchik, E.E. Chepurova, and T.I. Kraeva, *Sov. Phys. JETP* 62, 156 (1984).
123. R.K. Hickernell and Dror Sarid, *Opt. Lett.*, to be published, August 1987.
124. Dror Sarid, *Phys. Rev. B* 29, 2344 (1984).
125. Dror Sarid, *IEEE J. Quant. Elect.* QE-20, 943 (1984).

126. L.D. Landau and E.M. Lifschitz, Electrodynamics of Continuous Media, (Addison-Wesley, Reading, Mass., 1960).
127. R.F. Wallis, in Electromagnetic Surface Modes, edited by A.D. Boardman (John Wiley & Sons, New York, 1982), p. 575.
128. H. Burkhard and J. Jaumann, *Z. Phys.* 235, 1 (1970).
129. T. Tamir and H.L. Bertoni, *J. Opt. Soc. Am.* 61, 1397 (1971).
130. P.H. Lissberger, *J. Opt. Soc. Amer.* 51, 948 (1961).
131. A.E. Craig, G.A. Olson, and Dror Sarid, *Appl. Opt.* 24, 61 (1985).
132. M.A. Ordal, L.L. Long, R.J. Bell, S.E. Bell, R.R. Bell, R.W. Alexander, Jr., and C.A. Ward, *Appl. Opt.* 22, 1099 (1983).
133. F.S. Hickernell, personal communication.
134. L.E. Collins and O.S. Heavens, *Phil. Mag.* 45, 283 (1954).
135. R.S. Sennett and G.D. Scott, *J. Opt. Soc. Am.* 40, 203 (1950).
136. J.C. Maxwell Garnett, *Phil. Trans. R. Soc. London Ser. A* 203, 385 (1904); A 205, 237 (1906).
137. J.A.L. Potgiesser and J. Koorneef, *IERE Conf. Proc.* (1973).
138. L. Liebermann, *Phys. Rev. Lett.* 25, 232 (1970).
139. M.C. Desjonqueres and F. Cyrot-Lackmann, *Solid State Commun.* 20, 855 (1976).
140. H.J. Bauer, D. Blechschmidt, and M.V. Hellermann, *Surface Sci.* 30, 701 (1972).
141. D.W. Gray, ed., American Institute of Physics Handbook (Mc-Graw Hill, New York, 1972), Ch. 9, p. 6.
142. Dror Sarid, M. Deeter, and V. Kahwaty, *Appl. Opt.*, to be published, August 1987.